The Intercoupling of Thermal Transport and Mechanical Properties in Colloidal Nanocrystal Assemblies

by

Zhongyong Wang

A Dissertation Presented in Partial Fulfillment
of the Requirements for the Degree
Doctor of Philosophy

Approved January 2021 by the
Graduate Supervisory Committee:

Robert Wang, Chair
Nathan Newman
Liping Wang

ARIZONA STATE UNIVERSITY

May 2021

ABSTRACT

Colloidal nanocrystals (NCs) are promising candidates for a wide range of applications (electronics, optoelectronics, photovoltaics, thermoelectrics, etc.). Mechanical and thermal transport property play very important roles in all of these applications. On one hand, mechanical robustness and high thermal conductivity are desired in electronics, optoelectronics, and photovoltaics. This improves thermomechanical stability and minimizes the temperature rise during the device operation. On the other hand, low thermal conductivity is desired for higher thermoelectric figure of merit (ZT).

This dissertation demonstrates that ligand structure and nanocrystal ordering are the primary determining factors for thermal transport and mechanical properties in colloidal nanocrystal assemblies. To eliminate the mechanics and thermal transport barrier, I first propose a ligand crosslinking method to improve the thermal transport across the ligand-ligand interface and thus increasing the overall thermal conductivity of NC assemblies. Young's modulus of nanocrystal solids also increases simultaneously upon ligand crosslinking. My thermal transport measurements show that the thermal conductivity of the iron oxide NC solids increases by a factor of 2-3 upon ligand crosslinking. Further, I demonstrate that, though with same composition, long-range ordered nanocrystal superlattices possess higher mechanical and thermal transport properties than disordered nanocrystal thin films. Experimental measurements along with theoretical modeling indicate that stronger ligand-ligand interaction in NC superlattice accounts for the improved mechanics and thermal transport. This suggests that NC/ligand arranging order also plays important roles in determining mechanics and thermal transport properties of NC assemblies. Lastly, I show that inorganic ligand functionalization could lead to tremendous mechanical enhancement (a factor of ~60)

in NC solids. After ligand exchange and drying, the short inorganic $Sn_2S_6^{4-}$ ligands dissociate into a few atomic layers of amorphous SnS2 at room temperature and interconnects the neighboring NCs. I observe a reverse Hall-Petch relation as the size of NC decreases. Both atomistic simulations and analytical phase mixture modeling identify the grain boundaries and their activities as the mechanic bottleneck.

ACKNOWLEDGMENTS

Over the last five years I had the opportunity to pursue my PhD at Arizona State University. I meet a lot of nice people that have shaped my perspectives over research and life. I received tremendous help from many kind professors, university staff members, lab mates, and friends. Now it's time to acknowledge them, say good-bye to our shared journey, and continue to the next adventure.

First, I would like to express my great thanks to my advisor, Prof. Robert Wang for offering me the opportunity to work with him for the last 5 years. He has trained me into an independent researcher with his great patience and experience during my PhD. I learned not only how to design, conduct experiments, but more importantly how to think ahead and be organized regarding my research life. He is always open to new thoughts and proposals. He encourages me to bring up new ideas, learn new knowledge, and collaborate with teams in different fields. I'm also grateful to Prof. Liping Wang and Prof. Nathan Newman, who also serves on my committee. Your knowledge and experience will definitely help improve this dissertation.

I had wonderful memories interacting with coworkers, colleagues, and collaborators for the last 5 years. I would especially thank Minglu Liu, Yuanyu Ma, Seid Sadat, and Prathamesh Vartak for teaching me on experiments with their experience. I wouldn't have quickly been accustomed to the lab life without their guidance. I would also like to thank Ashish Rana, Wilson Kong, Yanan Zhang, and Najam Shah, I really enjoyed the time we spent together and the wonderful talks, laugh we had in the office and the lab. I have got tremendous help from our collaborators. I would like to thank Prof. Newman, Cameron, Prof. Chawla, Arun Sundar, Prof. Qiong Nian, Rui Dai, Prof. Kiran Solanki, Soundarya Srinivasan at Arizona State University for their support over my

research or papers. I'm also thankful to Prof. Jonathan Malen, Lingyun Dai, Alex Christodoulides from Carnegie Mellon University and Prof. Junlan Wang and Yang Zhou from University of Washington. Though some of them I haven't met in person, we had great collaborations and I appreciate all the contributions from you all to my research at ASU.

I have also met a lot of friends with whom I shared a lot of wonderful memories during my stay at Arizona. Specially, I would like to thank Lei Liu, Yuqi Guo for our shared experiences as roommates. I would also express my thanks to Siying Liu, Linyu Cao, Pu Han, Dini Wang, Hangkun Jing, and Yichen Yao. We know each other from classes and then start to hang out together and eventually become good friends. I thank them for their companionship during my PhD life.

Finally, I would like to express my great gratefulness to my family. Their unconditional love accompanies me through many many days and nights across the Pacific ocean. I wouldn't have survived my lengthy PhD life without their strong support. I dedicate this dissertation to them.

TABLE OF CONTENTS

Page

CHAPTER Page

CHAPTER Page

LIST OF TABLES

LIST OF FIGURES

Figure Page

Figure Page

Figure Page

Figure Page

Figure Page

Figure Page

1 OVERVIEW AND OUTLOOK

1.1 Overview

Colloidal nanocrystals are promising building blocks for lots of advanced devices due to their unique properties. However, their mechanical and thermal transport properties was not studied thoroughly for now. In-depth study into this not only helps the devices robustness and meets thermal management requirements, but helps fundamental understanding of mechanical response, heat transfer and their intercoupling in these unique nanostructures.

This dissertation presents efforts to study the origin of poor mechanical and thermal transport properties both experimentally and computationally, and tune these properties with ligands crosslinking, ligand alignment, and ligand exchange approaches.

In chapter 2, we present a detailed introduction and overview of both experimental and theoretical studies of thermal transport and solid mechanics of colloidal nanocrystal assemblies. Thermal transport and mechanical response of colloidal nanocrystal assemblies has been studied separately in the literature. Previous thermal transport study on nanocrystal assembly indicates that surface chemistry of colloidal nanocrystals mediates thermal transport in nanocrystal assembly. Specifically, they found that thermal conductivity of nanocrystal assembly is not sensitive to the core material, but rather sensitive to volumetric fraction change of ligand matrix that induced by either core size change or ligand exchange. Additionally, they demonstrated that interface thermal conductance is also a key parameter that determines thermal transport, which is usually linked to interfacial bond length and overlap of their vibrational density of states. On the other hand, previous studies on mechanical properties of colloidal nanocrystal assemblies show that soft ligand matrix

that arise from that weak van der Waals ligand-ligand interaction bottlenecks mechanical response of colloidal nanocrystal assemblies. Specifically, they found nanocrystal core size, packing order, and ligand composition all play roles in determining mechanical properties of nanocrystal assemblies. There have been several approaches proposed to tune the mechanical properties of nanocrystal assemblies. Representative approaches including ligand removal via plasma etching, polymer grafting, organic ligand crosslinking, and DNA functionalization is covered to exhibit how the mechanical properties is tuned in nanocrystal assemblies. Clearly there are might some inherent connection between thermal transport and mechanical properties of colloidal nanocrystal assemblies. So, studying mechanics and thermal transport in parallel in nanocrystal assemblies could help elucidate the underlying mechanism, and further potentially provides guidance on coupling and decoupling of mechanics and thermal transport in colloidal nanocrystal assemblies. Past studies have successfully correlated thermal conductivity with Young's modulus and sound speed in various solid material system including polymers, superatomic crystals, and lead halide perovskite crystals.

In chapter 3, we reported 200-300% increase of thermal conductivity of iron oxide nanocrystal assemblies accompanied by significantly increased Young's modulus of the nanocrystal assemblies via facile ligand crosslinking approach. Using oleic acid capped iron oxide nanocrystal as an example, we showed that a mild temperature treatment of the nanocrystal assembly leads to the ligand desorption and ligand crosslinking at the same time. This further verifies by thermogravimetric analysis, x-ray photoelectron spectroscopy, and gas-chromatography mass spectroscopy analysis on the iron oxide nanocrystal solids before and after annealing. We then performed thermal transport measurements on the iron oxide nanocrystal solids. Specifically, we found thermal conductivity of 20nm iron oxide nanocrystal solids increase significantly from 0.6

W/mK to 1.7 W/mK. We further performed nanoindentation measurements to uncover the effects of Young's modulus and sound speed change on the overall thermal conductivity change. Our results show that the non-crosslinked iron oxide nanocrystal solids exhibit decent linear relation between the thermal conductivity and sound speed. This suggests that non-crosslinked nanocrystal solids of various core sizes share similar mean free path of heat carrier. Nonetheless, crosslinked iron oxide nanocrystal solids show a surprisingly inverse linear between thermal conductivity and sound speed, which indicates thermal transport in nanocrystal solids has shifted from sound speed dominated regime to heat carrier scattering or heat carrier mean free path dominated regime. In addition to the observed thermal transport enhancement, this ligand crosslinking approach also presents an effective way of decoupling thermal transport and mechanical response of colloidal nanocrystal solids.

In chapter 4, we present the 1st thermal transport measurements on single domain colloidal nanocrystal superlattices of various core sizes and found that, though with similar compositions, long-range-ordered nanocrystal superlattice possess higher mechanical and thermal transport properties as compared to disordered nanocrystal thin film. Specifically, we performed thermal transport measurements along with the nanoindentation measurements on both long-range-ordered PbS nanocrystal superlattice and short-ranged-ordered/disordered nanocrystal solids thin film for a variety of core sizes (3 – 6 nm). We found both the ordered superlattice and disordered thin film show similar linear relation between thermal conductivity and sound speed, though with different slopes. This means nanocrystal superlattice possesses a higher heat carrier mean free path as compared to that of disordered thin film. We further conducted theoretical simulations and drew a conclusion that both of the observed thermal conductivity increase and Young's modulus enhancement arise from the

improved ligand-ligand interaction that facilitated by improved ligand packing in nanocrystal superlattice.

In chapter 5, we demonstrate a mechanical property enhancement of colloidal nanocrystal solids by a factor of 60 through a ligand exchange process. We measured Young's modulus and hardness of organically capped CdSe nanocrystal solids and inorganically capped CdSe nanocrystal solids as well. We observed a similar increasing trend of mechanical properties with nanocrystal core size increase for both the cases. However, deeper theoretical understanding points to that the similar increasing trend, however, has different origins. Specifically, Young's modulus and hardness of organically capped CdSe nanocrystal solids increase with size increasing as a result of stronger ligand-ligand interaction in larger nanocrystals. Comparatively the increasing trend of Young's modulus and hardness in inorganically functionalized CdSe nanocrystal solids results from the softer interfacial bonds and boundary activity dominated plastic deformation mechanism, respectively. This new nanocrystalline material is specially promising for mechanical coating applications.

1.2 **Outlook**

As an outlook of this dissertation, the thorough understanding of thermal transport and mechanics in colloidal nanocrystal assemblies motivates future in-depth phononic properties study on colloidal nanocrystal assemblies. Here we demonstrate a few interesting directions on investigation of phononic properties of colloidal nanocrystal assemblies. We hope this motivates future efforts towards this direction.

In chapter 6, we briefly show that colloidal nanocrystal and magic-sized cluster assemblies are promising phonon-engineered solids due to tight control over their size, surface chemistry, and periodicity. A few recent computational studies have demonstrated the potential of utilizing colloidal nanocrystal assemblies as phononic

crystals. We also present a few state-of-the-art experimental techniques for studying the phononic properties of these nanomaterials, which includes inelastic neutron scattering, phonon spectroscopy, and x-ray-based techniques. Among all of them, phonon spectroscopy presents a promising route towards studying the phonon transmission in these nanomaterials. Future work of this dissertation involves preparation high quality nanocrystal/nanocluster assemblies and investigation of activation and transmission of "coherent phonon" in these superstructures.

Additionally, the experimental results along with computational results presented here pave the way for future studies to realize mechanical robustness and efficient heat dissipation in colloidal nanomaterial-based devices. Below we briefly introduce some examples to show how the findings of this dissertation could benefit other mechanics and thermal transport studies.

Our study on enhanced thermal transport via ligand crosslinking motivates future efforts on boosting thermal transport in nanostructure system with molecular crosslinking approach. The crosslinking of organic ligand induced by temperature treatment might not be applicable to some delicate nanomaterial systems. So, alternatively, polymer crosslinking with molecular crosslinkers, crosslinking with UV treatment, have presented great potential for improving thermal transport in these more delicate systems. On the other hand, it would also be interesting to investigate the effect of crosslinking density on both solid mechanics and thermal transport. The crosslinking density can be potentially tuned by number of covalent bonds presented in the molecular chain.

Our work on combined mechanical and thermal transport measurements on colloidal nanocrystal superlattice highlights the importance of ligand alignment and interdigitation on determining their mechanical and thermal transport properties. It

would be interesting to continue to study how surface chemistry change affects mechanics and thermal transport in colloidal nanocrystal superlattice. Although we realized that "coherent phonon", or collectively motion of nanocrystals, doesn't contribute to thermal transport at room temperature. However, low temperature measurements could potentially detect the presence of coherent phonons, which contribute more to thermal transport at low temperature due to their long mean free path. Furthermore, magic-sized cluster, which has small while identical core, presents a more promising way of studying coherent phonon at low temperature via thermal transport measurements. In addition to thermal transport measurements, inelastic neutron scattering, phonon spectroscopy, and X-ray based techniques, can be further used to study the fundamental phononic properties of colloidal nanomaterial assemblies.

Our mechanical measurements on inorganically functionalized nanocrystalline CdSe inspires future mechanical property study upon these new group of nanocrystalline materials. Our computation study also motivates future experimental efforts on varying mechanical properties of nanocrystalline material via interface design and engineering. Additionally, inorganic functionalization has been reported to greatly improve the charge transport. Obviously decoupling of charge transport/mechanics and thermal transport presents great potential for robust thermoelectric devices. So, it would be very interesting to systematically investigate the thermoelectric performance of inorganic functionalized nanocrystal solids at full temperature ranges.

2 THERMAL TRANSPORT AND MECHANICAL PROPERTIES OF COLLOIDAL NANOCRYSTALS

2.1 Colloidal Nanocrystals

Colloidal nanocrystals[1-3] are solution-grown, nanometer-sized, inorganic particles that are stabilized by a layer of ligands attached to the particle surface. A schematic is shown in Figure 2.1 to describe the micro-morphology for nanocrystals. The inorganic cores are comprised of metal, metal oxide, semiconductor, and magnetic materials, which possesses various electronic, optical and magnetic properties.[4-6] Such as superparamagnetism of magnetic nanocrystals, surface plasmon resonance in noble metal nanoparticles, and the size-dependent band gap of semiconductor nanocrystals due to the quantum confinement effect. The surface-capped ligands ensure these structures are easy to fabricate and process further into more complex structures. This combination of features makes colloidal nanocrystals attractive and promising building blocks for many applications.

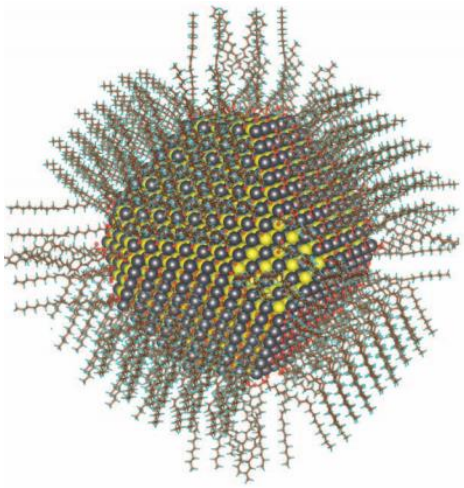

Figure 2.1 Schematic illustration of PbS nanocrystal passivated with oleic acid as the ligand. Figure adapted from Reference[7].

2.1.1 **Colloidal Nanocrystal Synthesis**

Colloidal synthesis of inorganic nanocrystals is developing into a new branch of synthetic chemistry. Scientists have successfully synthesized the nanocrystals with controlled size, shape and high monodispersity with a variety of techniques. Typically, colloidal nanocrystals are synthesized through reacting appropriate molecular precursors, such as inorganic salts or organometallic compounds. The colloidal synthesis generally involves several consecutive stages: nucleation from the initial homogeneous solution, further growth of the nuclei, isolation of particles reaching the desired size, which is illustrated in Figure 2.2d. In this section, three representative chemical methods are briefly discussed: reduction, thermal decomposition, and the nonhydrolytic sol-gel process.

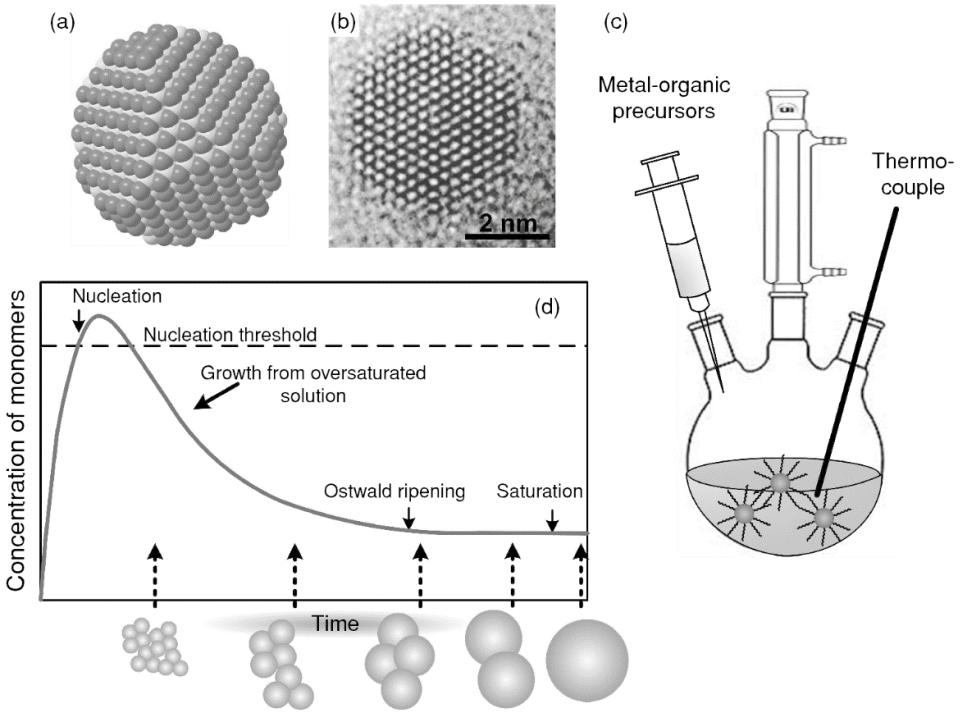

Figure 2.2 (a) schematic illustration and (b) High-Resolution TEM characterization for nanocrystal. (c) schematic illustration of the hot injection method. (d) Nanocrystal nucleation and growth as a function of time. Figure adapted from reference[8].

Reduction method involves a variety of reductants such as sodium borohydride, hydrogen, and alcohols. This method was first used for preparing metal nanoparticles. As early as 1853, Faraday prepared the gold nanoparticle from the reduction of $HAuCl_4$ with phosphorous[9]. Enustun et al.[10] synthesized uniform 13 nm gold nanoparticles by using sodium citrate as both a reductant and a stabilizer. Organic phase reduction became more popular because it possesses the following advantages: highly crystalline due to relatively high synthesis temperature, high yield, and highly-monodispersity. Sun et al.[11] synthesized the Co nanoparticles by the reduction of a cobalt salt with superhydride at high temperature with presence of surfactants such as oleic acid. Many metallic nanoparticles, in particular of platinum group metals, has been successfully synthesized by reduction of metals salts with high boiling-point alcohols such as diols and ethylene glycol, which is known as the polyol process.[12]

Thermal decomposition is another widely used method for synthesizing nanocrystals. Usually the thermal decomposition reaction of organometallic compounds and surfactant complex were performed in hot solution phase to synthesizing nanoparticles. One typical example for thermal decomposition is the hot-injection method. The experimental set-up of the hot-injection method is shown in Figure 2.2c. This so-called hot-injection method was used a lot for synthesizing semiconductor nanocrystals. Murray et al.[13] synthesized cadmium chalcogenides nanocrystals by rapid injection of organometallic precursors such as dimethyl cadmium and trioctyphosphine selenide into a hot coordinating solvent. This rapid injection induces a short burst of nucleation and the nanocrystals would further grow into desired size through aging at slightly lower temperature.

The nonhydrolytic sol-gel process is one of the most popular routes for synthesizing oxide nanomaterials. The most well-known hydroxylation reaction is the thermal

decomposition of metal alkoxides or carboxylates. In this process, hydroxyl groups are produced on metal cations along with alkene side products through thermal decomposition.

2.1.2 **Colloidal Nanocrystals Assembly**

Crystals are formed with different lattices through arrangement of different atoms based on the strong atom interactions, which is also known as metallic bonding, ionic bonding and covalent bonding. Similarly, when nanocrystals start to approach each other, they will also form periodic arrays due to van der Waals interaction between the adjacent nanocrystals. This process is also termed as the self-assembly process for these nanomaterials. The self-assembled nanomaterial structure possesses unique optical, magnetic, electronic, and catalytic properties. For instance, Lee et al.[14] reported fabrication of field-effect-transistor channels using semiconductor nanocrystal arrays. Choi et al.[15] constructed plasmonic circuits and magnetic inductors utilizing assemblies of metallic and magnetic nanocrystals.

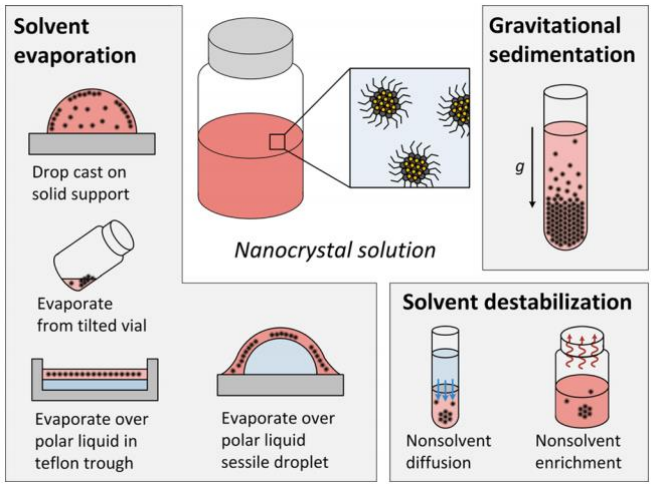

Figure 2.3 Experimental approaches to prepare nanocrystal superlattices include solvent evaporation method (left), and destabilization or sedimentation techniques (right). Figure adapted from reference[16].

We start with the preparation and structural characterization of superlattices, which can be seen as the foundation for study of nanocrystal superlattices. Overall, there are three representative methods for nanocrystal superlattice preparation: solvent evaporation, gravitational sedimentation, and solvent destabilization. The schematic illustration of these three methods is shown in Figure 2.3. Controlled-solvent-Evaporation usually leads to nanocrystal superlattice thin films.

Solvent evaporation is a facile way for getting nanocrystal superlattices. Talapin et al.[17] simply dropped cast a smaller volume of nanocrystal solution onto the supporting substrate and allow it to dry over a few minutes to get closed-packed PbSe nanocrystal solids. Bigioni et al.[18] prepared 2-dimensional superlattice membranes by gentle deposition of a droplet of nanocrystal solution at the air-liquid interface. Dong et al.[19] reported a preparation of binary nanocrystal superlattice membranes self-assembled at the liquid-air interface. As is shown in Figure 2.4f, a drop of mixed nanocrystal solution comprised of Fe_3O_4 and FePt nanocrystals was deposited on the surface of diethylene glycol (DEG) in a Teflon well. A glass slide was placed on top of the Teflon well to slow down the solvent evaporation rate. Figure 2.4g, h showed TEM overview of (100) projection and (110) projection of an AB_2 binary nanocrystal superlattice, respectively.

Destabilization-based assembly[20, 21] is an effective way for forming 3-dimensional nanocrystal superlattices, which promotes gradual clustering of nanocrystals in solution. Colloidal nanocrystals are usually capped with hydrocarbon ligands, which tend to approach each other and form clusters with slowly increased polarity of the solution. In practice, this is accomplished by adding a layer of non-solvent to the top of the nanocrystal solution in a sealed container. The solution polarity would slowly

change as the diffusion of non-solvent molecules into the solvent phase and gradually destabilize the nanocrystals.

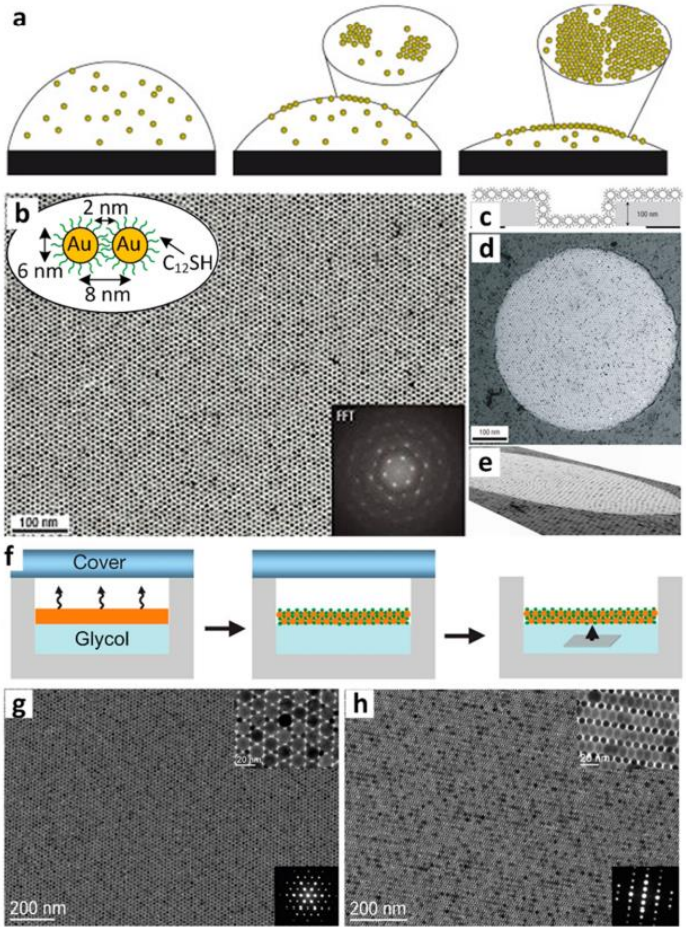

Figure 2.4 (a) Schematic illustration of Au nanocrystal captured by a quickly receding interface, which leads to monolayer island growth. (b) TEM overview of a long-range-ordered monolayer with hexagonal symmetry. (c) Sketch of the freestanding superlattice membrane formed by evaporation over a polar liquid subphase. (d) Top view and (e) tilted projection of TEM image of a superlattice membrane draped over a 0.5 um hole. (f) Schematic illustration of nanocrystal interfacial assembly and the substrate transfer process. TEM overview of (g) (100) projection and (h) (110) projection of an AB2 binary nanocrystal superlattice. Figure adapted from reference[16].

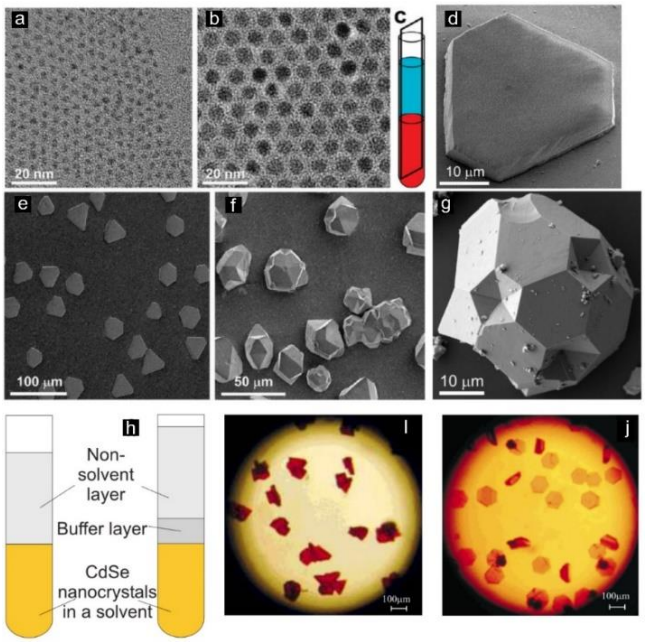

Figure 2.5 TEM images of (a) 3.1 and (b) 8.0 nm PbS nanocrystals. (c) A scheme demonstrating the experimental set-up for growing superlattices. (d, e) High magnification and low magnification SEM image for single domain superlattice grown from 3.1nm PbS nanocrystals. (f, g) High magnification and low magnification SEM image for multiply twinned superlattice grown from 8 nm PbS nanocrystals. (h) Scheme illustrating the concept of the nucleation procedure. (i) Optical image of faster nucleation, irregular shaped crystals. (j) Slower nucleation, perfectly faceted hexagonal platelets. Figures adapted from references[20, 21].

As is shown in Figure 2.5a, b, the first important thing for forming superlattices is monodispersity of the colloidal nanocrystal. Only highly monodispersed colloidal nanocrystals would be arranged in order and grow nanocrystal superlattice. The morphology of superlattices self-assembled from colloidal PbS nanocrystals was highly dependent on the particle size, as is evidenced in Figure 2.5e, f, superlattices from large (>7nm) PbS nanocrystals tend to form multiply twinned fcc superlattices. While superlattices from smaller (<4nm) PbS nanocrystals showed a strong tendency of

forming single domain superlattices. Finally, the superlattice morphology was also greatly affected by the nucleation speed. As is illustrated in Figure 2.5i, j, the nucleation speed was controlled by the diffusion rate of the non-solvent molecules to the solvent phase. With the presence of the buffer layer in between, the diffusion rate of the non-solvent molecule was slowed down due to longer path from the top phase to the bottom phase, in this case, the nucleation might consume more time and generate single-domain nanocrystal superlattices, which is shown in Figure 2.5j.

Gravitational sedimentation is a less common approach for assembling nanocrystals, since it only works for bigger nanocrystals with diameter approaching 1 um or nanocrystals comprised of high-density metals. In this report, most nanocrystals involved fall below this size limit and exhibit assembly behavior which is not significantly influenced by gravitational forces.

2.2 Phonon Theory and Transport Backgrounds

2.2.1 Phonons and Heat Capacity

In a crystalline solid, the constituent atoms would vibrate about their equilibrium positions when the temperature is higher than absolute 0 K. The thermal vibration extent is determined by the interatomic forces they exert on each other. These vibrations are quantized elastic waves, which are phonons. The lattice vibrations with angular frequency ω are treated as quantum harmonic-oscillators. The average energy ε' of a harmonic oscillator (lattice vibration with angular frequency ω) at finite temperature of T

$$\varepsilon' = \sum_n P_n \varepsilon_n = \frac{1}{2}\hbar\omega + \frac{\hbar\omega}{e^{\hbar\omega/k_B T} - 1}$$

Where P_n corresponds to the probability of the oscillator being in nth level, which is given by the Boltzmann factor $\exp(-\varepsilon_n/k_BT)$, while ε_n equals to the energy of the nth energy level of the oscillator. At the low temperature limit, where $\hbar\omega \gg k_BT$, ε' is equals to $1/2\,\hbar\omega$, while at the high temperature limit, $\hbar\omega \ll k_BT$, ε' is equals to k_BT.

To demonstrate some general features of these elastic waves, we start with the Newtonian multibody equation of motion for one dimensional monoatomic lattice.

$$\mathrm{m}\frac{d^2x^j}{dt^2} = k(x^{j+1} + x^{j-1} - 2x^j)$$

while the solution for the elastic wave has the following expression, noting that the equilibrium locations of atoms have discrete values, $\mathrm{x} = \mathrm{ja}$, where j is the unit cell designation, x is the atom displacement, a is the lattice parameter.

$$x^j = x_0 exp[i(\kappa ja)]exp[-i(\omega t)]$$

Through combining the Newtonian motion equation and the elastic wave equation, we are able to derive the phonon dispersion for the one-dimensional monoatomic lattice

$$\omega^2(\kappa) = \frac{4k}{m} sin^2\left(\frac{1}{2}\kappa a\right)$$

Now we consider two different atoms in the primitive unit cell with masses m_1 and m_2, respectively. Here we also begin with the linear lattice for simplification. Similarly, the external force exert on the atoms can be expressed as a spring force ($\mathrm{F} = -\mathrm{kx}$), where k is the force constant, then we get the one-dimensional equation of motion based on the harmonic oscillator.

$$\mathrm{m1}\frac{d^2x_1^j}{dt^2} = -k\left(x_1^j - x_2^j\right) + k\left(x_2^{j-1} - x_1^j\right) = k\left(x_2^j + x_2^{j-1} - 2x_1^j\right)$$

$$\mathrm{m}2\frac{d^2x_2^j}{dt^2} = k\left(x_1^{j+1} + x_1^j - 2x_2^j\right)$$

Noting that the equilibrium locations of atoms have discrete values, $\mathrm{x} = \mathrm{ja}$, where j is the unit cell designation, the solutions for elastic wave has the following expression

$$x_1^j = x_{0,1}exp[i(\kappa ja)]exp[-i(\omega t)]$$

$$x_2^j = x_{0,2}exp[i(\kappa ja)]exp[-i(\omega t)]$$

Combining the Newtonian motion equation and the expression for elastic waves, we get the phonon dispersion relation for this one-dimensional two-atom lattice

$$\omega^2(\kappa) = \frac{2k(m_1 + m_2) \pm [4k^2(m_1 + m_2)^2 - 8k^2m_1m_2(1 - \cos\kappa a)]^{1/2}}{2m_1m_2}$$

Apart from the acoustic branch, there is another phonon branch which is called the optical branch. More specifically, overall, in acoustic phonons, the neighboring atoms m_1 and m_2 are vibrating towards the same direction, which leads to smaller interatomic displacement and smaller restoring force and hence low energy phonons. While in optical phonon vibration wave, the neighboring atoms m_1 and m_2 are vibrating towards the opposite way, which leads to bigger interatomic displacement and bigger restoring force and hence high energy phonons. This phonon dispersion relation for a diatomic chain, also shows that the phonon group velocity ($\mathrm{v} = \partial\omega/\partial\kappa$) is not a constant and depends on the wave number κ. In general, the total number of branches is equal to the number of dimensions of motion times the number of atoms per primitive cell.

The wave number density of states (DOS) D_κ of phonons is defined as the reciprocal of the interspacing between adjacent k values allowed in k space. The phonon angular frequency density of states D_ω is the total number of modes in the frequency range ω

to $\omega + d\omega$, divided by volume V. D_ω converts the number of phonons of wave number k to those of frequency ω, using the dispersion relation.

$$D_p(\omega) = \frac{1}{L^3}\left(\frac{L}{2\pi}\right)^3 \sum_\alpha \frac{1}{\nabla_\kappa \omega_\alpha} = \left(\frac{1}{2\pi}\right)^3 \sum_\alpha 4\pi\kappa^2 \frac{d\kappa}{d\omega_\alpha}$$

Where α is the branch index (the acoustic branches has 3 branches, two transverse, and one longitudinal).

For acoustic phonons, Debye used a constant phonon speed v_s, which equals to ω/κ. From this relation, we get the following form for D_ω

$$D_p(\omega) = \frac{1}{2\pi^2}\frac{\omega^2}{{v_s}^3}$$

Where v_s is a single acoustic phonon speed. Using the Debye model of the phonon DOS, we get the following expression for total energy of all the phonons modes in a monatomic, isotropic crystal per unit volume

$$E_p = \int_0^\infty \hbar\,\omega \frac{1}{exp\left(\frac{\hbar\,\omega}{k_B T}\right) - 1} D_p(\omega) d\omega$$

The lattice specific heat capacity of a solid at constant volume can be derived by differentiating E_p with respect to temperature T

$$c_v = \frac{\partial E_p}{\partial T} = \int_0^\infty \hbar\,\omega \frac{\partial}{\partial T}\left(\frac{1}{exp\left(\frac{\hbar\,\omega}{k_B T}\right) - 1}\right) D_p(\omega) d\omega$$

As is described previously, there are 3n phonon modes for a monatomic, single-atom lattice crystal.

$$3\mathrm{n} = \int_0^{\infty} D_p(\omega)\, d\omega \approx \int_0^{\omega_D} D_p(\omega)\, d\omega = \int_0^{\omega_D} \frac{3\omega^2}{2\pi^2 {v_s}^3} d\omega$$

From this integral, we get the expression for the cutting-off angular frequency ω_D

$$\omega_D = (6\pi^2 n {v_s}^3)^{1/3}$$

Using the Debye cut-off frequency, we have

$$c_v = 9k_B \left(\frac{T}{T_D}\right)^3 \int_0^{T_D/T} \frac{x^4 e^x}{(e^x - 1)^2} dx$$

Where T_D equals to $\hbar\, \omega_D / k_B$. From this expression, we can also shed light on temperature dependence of the specific hear capacity. At the low temperature limit, $c_v \propto T^3$, while at the high temperature, $c_v \approx 3nk_B = 3R$.

2.2.2 **Phonon Transport Theory**

In classical particle dynamics, particles in a system can be described using particle position and momentum space (i.e., phase space). For a dilute gas, Boltzmann defined a particle probability distribution function that denotes the fraction of particles (gas atoms or molecules) with a location x and a momentum p at certain time t. This Boltzmann transport equation (BTE) is also used for phonons, as phonons can be seen as quasi-particles. In the Boltzmann transport equation (BTE) derivation of the phonon conductivity, the single-mode relaxation time (SMRT) hypothesis for a mode in phonon system is used. In the SMRT approximation, each phonon mode has a single, effective relaxation time. Callaway and Holland were the first to derive the phonon conductivity by combining BTE and SMRT.

The heat flux generated by a change in the population of energy carriers can be expressed as the following form:

$$\mathrm{q} = \sum_{\alpha} \frac{1}{8\pi^3} \int E_p v_p f_p'(k) dk$$

where E_p is the phonon energy, v_p is the phonon group velocity and f_p' is the deviation of the phonon population from the equilibrium distribution. This heat flux vector was directly compared with Fourier law ($\mathrm{q} = -k_p \nabla T$) to get an expression for thermal conductivity. The steady-state BTE (with no external force and source) for a single-phonon mode is

$$v_p \cdot \nabla f_p = \left(\frac{\partial f_p}{\partial t}\right)_{\tau}$$

Assuming the phonon population is only related to temperature, then

$$v_p \cdot \nabla f_p = v_p \cdot \frac{\partial f_p}{\partial T} \nabla T$$

As $f_p = f_p^{\circ} + f_p'$, where f_p° is the equilibrium phonon distribution, the deviation from equilibrium f_p' can be assumed to be independent of temperature, then

$$\frac{\partial f_p}{\partial T} \approx \frac{\partial f_p^{\circ}}{\partial T}$$

For the collision term, the relaxation time approximation was used, whereby

$$\left(\frac{\partial f_p}{\partial t}\right)_{\tau} = \frac{f_p^{\circ} - f^p}{\tau_p} = -\frac{f_p'}{\tau_p}$$

Based on assumptions shown above, deviation from equilibrium f_p' can be expressed as following

$$f_p' = -\tau_p \frac{\partial f_p^{\circ}}{\partial T} v_p \cdot \nabla T$$

Then the heat flux expression can be changed into the following,

$$\mathrm{q} = -\sum_{\alpha} \frac{1}{8\pi^3} \int E_p \tau_p \frac{\partial f_p^{\circ}}{\partial T} v_p v_p dk \cdot \nabla T$$

Assuming E_p to be independent of temperature, the phonon mode specific heat capacity is given as following

$$c_{v,p} = \frac{\partial \left(E_p f_p^{\circ}\right)}{\partial T} = E_p \frac{\partial f_p^{\circ}}{\partial T}$$

Then the heat flux can be further expressed as

$$\mathrm{q} = -\sum_{\alpha} \frac{1}{8\pi^3} \int c_{v,p} \tau_p \, v_p v_p dk \cdot \nabla T$$

After comparison with the Fourier law q=-Kp · ∇T, the phonon thermal conductivity can be expressed as

$$K_p = \sum_{\alpha} \frac{1}{8\pi^3} \int c_{v,p} \tau_p \, v_p v_p dk$$

Callaway made more assumptions to get more specified phonon conductivity expression, he assumed all phonons has a single speed v_p, used the debye specific heat capacity expression and treated the three modes as the same, his expression was shown below

$$K_p = (48\pi^2)^{1/3} \frac{1}{a} \frac{k_B^3}{h_p^2} \frac{T^3}{T_D} \int_0^{T_D/T} \tau_p \, (x) \frac{x^4 e^x}{(e^x - 1)^2} dx$$

Where $\mathrm{x} = h\omega/(2\pi k_B T)$, a is the lattice constant. It should be pointed out that Callaway's single-mode relaxation-time model only works for low-temperature thermal conductivity prediction. As he didn't consider the phonon dispersion and difference between longitudinal and transverse polarizations.[22]

2.2.3 **Phonons Scattering Mechanism**

The crystal boundary scattering relies on diffusive boundary absorption/emission mechanism. The phonon mean free path equals to the length of travel of the phonon before the boundary absorption/re-emission. If we assume the phonons have a single speedv_p, the relaxation time is

$$\tau_{p-b} = L/v_p$$

This represents ballistic transport within the crystal if the phonon-boundary scattering is the dominated mechanism, which is true for crystalline microparticles and nanoparticles at low temperature.

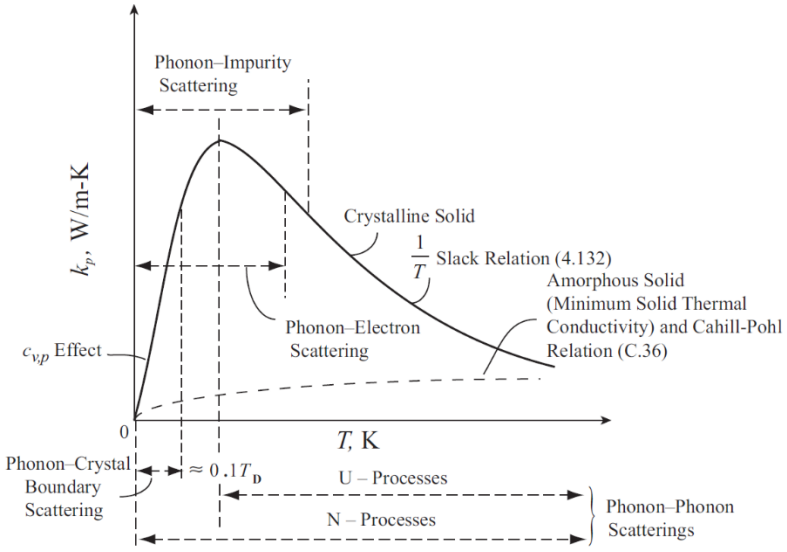

Figure 2.6 Regimes of dominant phonon-scattering mechanisms in variations of phonon conductivity with respect to temperature. Figure adapted from reference[22].

Phonon-impurity scattering can be analogous to Rayleigh scattering of the transverse electromagnetic waves. Based on the classic theory, the phonon-impurity scattering should also be proportional to ω_p^4. Obviously, the phonon relaxation time for phonon-impurity scattering would be related to the mass difference between the

impurity atom and the host atom, which is shown as atom B and atom A in Figure 7b, respectively. Klements derived the relaxation time expression for phonon-impurity scattering

$$\tau_{p-im} = \frac{4\pi v_p^3}{V_c \sum_i x_i \left(1 - \frac{M_i}{M}\right)^2} \omega^{-4}$$

Here the impurity i has an atomic mass M_i and mass fraction x_i. The lattice constant is a, and the host atomic mass is M. From this expression, we would see stronger scattering and smaller phonon relaxation time with bigger atomic mass difference between the impurity atom and the host atom. Phonon angular frequency has similar effect on phonon-impurity scattering, which means higher energy phonons are easier to be scattered by the impurity and leads to smaller phonon relaxation time.

As is shown in Figure 2.7c, the inter-phonon scattering has been assumed to be dominated by the three-phonon scattering processes. The three-phonon scattering is divided into N (normal) and U (umklapp) processes, and the U-processes are dominant at high temperature. Obviously, these three-phonon scattering changes the energy of each phonon involved, so it is hard to describe this scattering using a relaxation-time approximation. In N-processes, the crystal momentum and energy are conserved. While in U-processes, the crystal momentum is no longer conserved. Even though the energy still is. In Figure 2.7c, g is the reciprocal lattice vector.

The phonon-electron relaxation time is expressed as following:

$$\frac{1}{\tau_{p-e}} = \frac{3v_p^2}{\mu_e^2} \frac{\sigma_e}{c_{v,p} T}$$

Where σ_e and μ_e are the electrical conductivity and mobility, and $c_{v,p}$ is the phonon specific heat of the phonons allowed to interact with free electrons. From the phonon-

electron relaxation time expression shown above, we can tell how the free electron mobility and concentration would affect the phonon-electron scattering relaxation time. Basically, scattering between phonon and free electron with higher mobility will have a longer phonon relaxation time. And the phonon relaxation time is inversely proportional to carrier concentration, which means phonons have high changes to be scattered by free electrons with higher electron concentration. And this is easily understood. In general, phonons affect conduction electron transport more than electrons affecting the phonon transport. So, for insulators and semiconductors, this phonon-electron scattering can be neglected for thermal conductivity prediction.

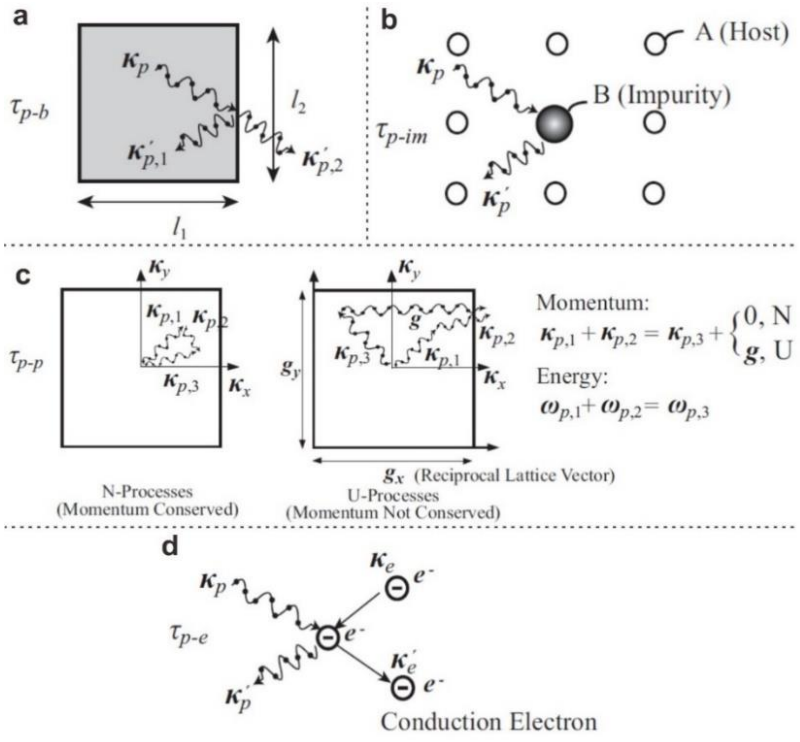

Figure 2.7 Phonon Scattering Mechanism. (a) Phonon-boundary scattering; (b) Phonon-impurity scattering; (c) Three-phonon scattering; (d) Phonon-electron scattering. Figure adapted from reference[22].

The Matthiessen rule can be applied to combining the phonon scattering from various scattering mechanisms, which is shown below

$$\frac{1}{\tau_p} = \sum_j \frac{1}{\tau_{p,j}} = \frac{1}{\tau_{p-im}} + \frac{1}{\tau_{p-b}} + \frac{1}{\tau_{p-e}} + \frac{1}{\tau_{p-p,N}} + \frac{1}{\tau_{p-p,U}} + \cdots\cdots$$

Finally, the $k_p - T$ behavior is investigated and the dominating phonon scattering mechanism at different temperature is summarized in Figure 2.6. At 0 K, atoms are frozen and thus $k_p = 0$. As the temperature increases, k_p would increase due to a specific heat effect. As was discussed in previous section, the specific heat capacity is proportional to T^3 at low temperature. If we assume the phonon speed to be not temperature-dependent, the phonon relaxation time is dominated by phonon-boundary scattering. As the temperature further increases, the impurity, electron and interphonon U-processes start to dominate. Usually the highest thermal conductivity occurs at a temperature of around 0.1 T_D. As is also shown in the figure, at high temperature, the thermal conductivity is inversely proportional to temperature. This is because at these temperatures, the specific heat reaches a plateau value (3R), the phonon relaxation time is inversely proportional to phonon population, which is proportional to the temperature at this stage. This relation is also known as Slack Relation. Finally, with further increase of the temperature, the thermal conductivity would eventually reach its lower limit-amorphous solid thermal conductivity. This is also known as Cahill-Pohl relation. Cahill and Pohl extend the Einstein solid thermal conductivity model to include a range of frequencies and arrive at

$$k_{p,C-P} = \left(\frac{\pi}{6}\right)^{1/3} k_B n^{2/3} \sum_\alpha v_{p,\alpha} \left(\frac{T}{T_\alpha}\right)^2 \int_0^{T_\alpha/T} \frac{x^3 e^x}{(e^x - 1)^2} dx$$

Where $v_{p,\alpha}$ and $T_{D,\alpha}$ are the phonon acoustic speed and the Debye temperature for polarization α, x equals to $h\omega/k_B T$, and $\tau_{p,\alpha}$ equals to ω/π. It is generally accepted that

$k_{p,C-P}$ is the lowest thermal conductivity for a solid. In this case, the phonon mean free path is $\lambda_p = \pi\, v_{p,\alpha}/\omega$, this mean free path is 1/2 of the wave length $\lambda = 2\pi\, v_{p,\alpha}/\omega$. This $k_{p,C-P}$ is used for thermal conductivity of amorphous solids and polymers. Figure 2.6 also shows the $k_{p,C-P}$ with respect to temperature. This thermal conductivity will increase with increased temperature at low temperature range ($T<T_D$), while it reaches a plateau at temperature higher than T_D.

2.2.4 **Phonon Transport at Nanoscale**

At the nanoscale, the interface thermal conductance between two materials are of primary significance in the study of its thermal properties. The thermal boundary resistance is a measure of an interface's resistance to heat flow, which exists even at the atomically perfect interfaces due to the vibrational properties in different materials. When phonons attempt to traverse the interface, it will scatter at the interface. The probability of transmission after scattering will depend on the available energy states on different sides of the interface. The Acoustic Mismatch Model (AMM) and the Diffusive Mismatch Model (DMM) are widely used for predicting the boundary thermal resistance. The AMM model assumes geometrically perfect interface and phonon transport process is entirely elastic, where phonons are treated as waves in a continuum. On the other hand, the DMM model assumes scattering at the interface is diffusive, which is usually more accurate for interfaces with characteristic roughness at elevated temperature. One crucial factor in determining the interface thermal resistance is the overlap of phonon states. Assume the overlap between phonon dispersions in two materials is small, there are less modes to allow for heat transport in the material, giving at a high thermal resistance relative to materials with a high degree of overlap. In the AMM model, there is no phonon scattering at the boundary as the interface is assumed to be perfect. Thus, the phonons propagate elastically across the interface. The wavevectors that propagate across the interface are

determined by conservation of momentum. This assumption of elastic scattering makes it more difficult for phonons to transmit across the interface, which results in low phonon transmission. It is noteworthy that both AMM model and DMM model don't consider phonon-phonon interaction at the interface. But in reality, 3-phonon or even 4-phonon interaction plays an important role for phonon propagation across the interface.

When the sample dimension decreased to nanoscale, one of the prominent changes is the surface atoms ratio as compared to the interior. We know the surface atoms would vibrate different from the interior atoms because of their different atomic environment. The surface atoms lose their neighboring atoms, which leads to different bond strengths and bond angles. As for nanomaterials, the surface atoms ratio is significantly increased, which cannot be neglected as compared to the bulk material. Similarly, we would anticipate the deviation of the lattice vibration properties for nanomaterials as compared to bulk materials. Ruan et al.[23] reported vibrational spectra broadening in nanomaterials due to surface effect using lattice dynamics calculations and MD simulations. As can be seen from Figure 2.8, the phonon density of states (DOS) of nanocrystals is distinct from that of the bulk crystal. Overall, the vibrational spectra of bulk material showed sharp, well-defined peaks, which should relate to its rigorous periodic structure. While the nanocrystal showed broadened peaks and extended tails at low and high frequencies. This is attributed to the loss to some extent of the periodicity. More specifically, they believe the surface atoms contribute to the high frequency tail in the nanocrystal phonon DOS. As these atoms have contracted bonds due to the loss of the attraction from their outer neighbors, which leads to harder surface and thus increased vibrational frequencies.

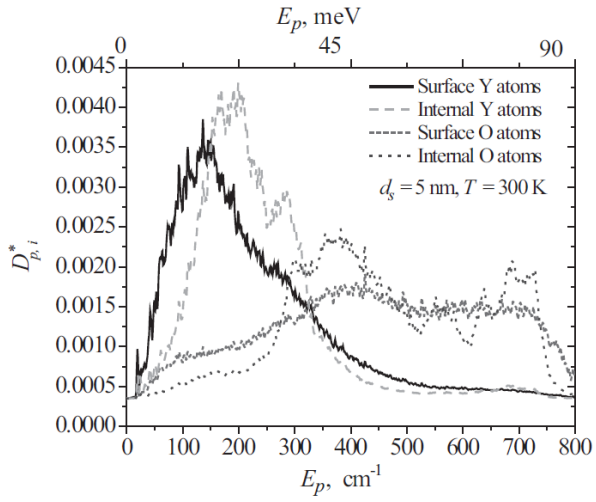

Figure 2.8 Normalized particle phonon DOS of the surface Y atoms, internal Y atoms, surface O atoms, and internal O atoms. Figure adapted from reference[23].

2.2.5 **Thermal Transport Across the Self-assembled Molecular Junctions**

As is discussed previously, colloidal nanocrystal solids have been widely applied to different applications due to its unique electronic, optical and magnetic properties. It is well known that the performance and lifetime of devices degrade with increased operating temperature, which can be caused by low heat dissipation rate of the device materials. Thus, thermal energy transport in these nanosolids needs to be studied thoroughly as all the nanocrystal solids-based devices must meet the thermal management requirements in industry. Compared to the bulk crystals, nanocrystal solids have numerous hard/soft interfaces in between the inorganic core and the organic ligand shell. The presence of these interfaces creates a complex and uncharted vibrational landscape for thermal energy transport in nanocrystals solids.

Losego et al.[24] studied the effects of chemical bonding on heat transport across the interfaces of two inorganic substrates connected by a self-assembled monolayer (SAM) with systematically varied termination chemistries. As is shown in Figure 2.9a and b, to achieve an interface with variable binding chemistry, they prepared self-assembled

monolayers sandwiched between z quartz (Qz) substrate and a gold (Au) film. The bond strength between the Au and the SAM was controlled by varying the SAM's end-group functionalities. Time-domain thermoreflectance (TDTR) technique was used for measuring the thermal conductance. They used SAMs of the same length and end-groups of methyl and thiol as the example. As thiol is known to form a strong covalent-like bond to the gold film, whereas methyl group is only weakly attached to the gold film through van der Waals attraction. As is shown in Figure 2.9d, the thermal conductance across the Au/SH-C11-Si-Qz interface was measured to be 65 MW m^{-2} K^{-1}. This value decreased to 36 MW m^{-2} K^{-1} when the end group of the SAM changed into methyl group. In summary, they showed that the strength of a single bonding layer directly controls phonon heat transport across an interface. Although transitioning from van der Waals interaction to covalent bonding increased conductance by ~80% for Au/Qz interfaces, they also proposed that much greater contrast could be achieved in systems that have more similarity in their vibrational properties.[25, 26]

Still, the SAM molecular configuration is quite different from nanocrystal/ligand interface. In SAMs, the organic molecules are attached to the flat gold surface, whereas ligands are attached to a surface with high curvature. Experiments[27] and simulations[28] results have proved that alkanethiols are more densely-packed on curved nanocrystal cores, which gives higher grafting density.

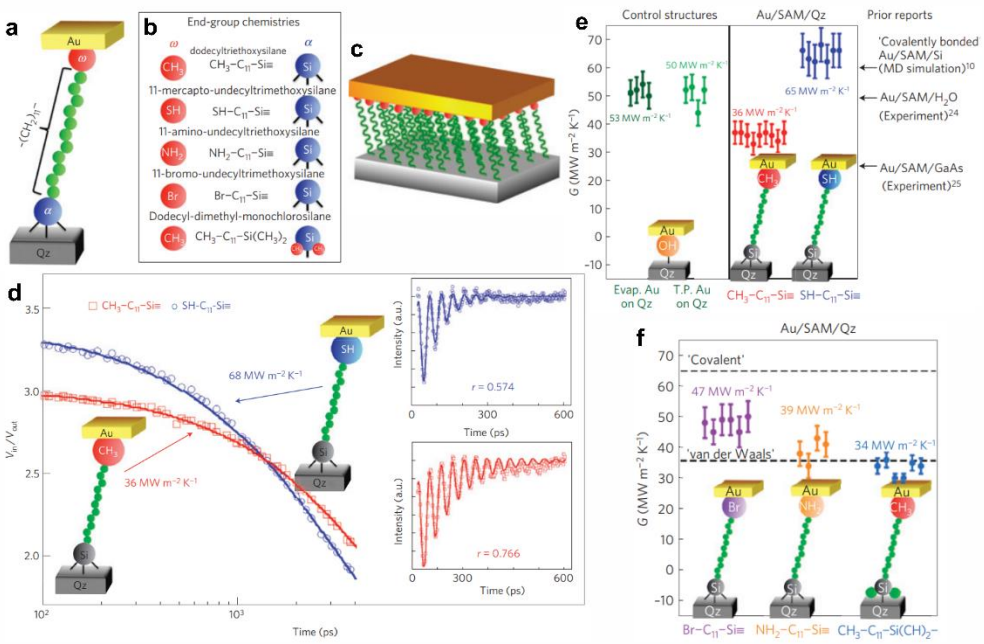

Figure 2.9 (a) Schematic illustration of experimental systems which consists of a quartz substrate, bifunctional SAM, and Au layer. (b) List of all SAM chemistries that are studied and abbreviations used. (c) Schematic illustration of the finial test structure. (d) TDTR thermal transport measurements along with fits for representative Au/CH_3-C_{11}-Si-Qz and Au/SH-C_{11}-Si-Qz structures. Inset shows picosecond acoustic data collected from an offset pump-probe beam geometry. (e) Control structures consist of gold evaporated on Qz and gold transfer-printed to Qz. Experimental structures consist of Au/CH_3-C_{11}-Si-Qz and Au/SH-C_{11}-Si-Qz structures. Literature data was also included for comparison. (f) Interfacial thermal conductance measured for other interfacial chemistries including Au/Br-C_{11}-Si-Qz, Au/NH_2-C_{11}-Si-Qz and Au/CH_3-C_{11}-Si(CH_3)$_2$-Qz structures. Figure adapted from reference[24].

2.2.6 **Thermal Transport in Colloidal Nanocrystal Solids**

Ong et al.[29] measured the thermal conductivity of three-dimensional nanocrystal solids using the frequency-domain thermoreflectance (FDTR) technique, and found that the thermal energy transport in nanocrystal arrays is mediated by density and

chemistry of the inorganic/inorganic interfaces, and the volume fractions of nanocrystal cores and surface ligands. Overall, the thermal conductivities of nanocrystal arrays are controllable within the range of 0.1-0.3 $Wm^{-1}k^{-1}$, and only weakly depend on the thermal conductivity of the inorganic core material.

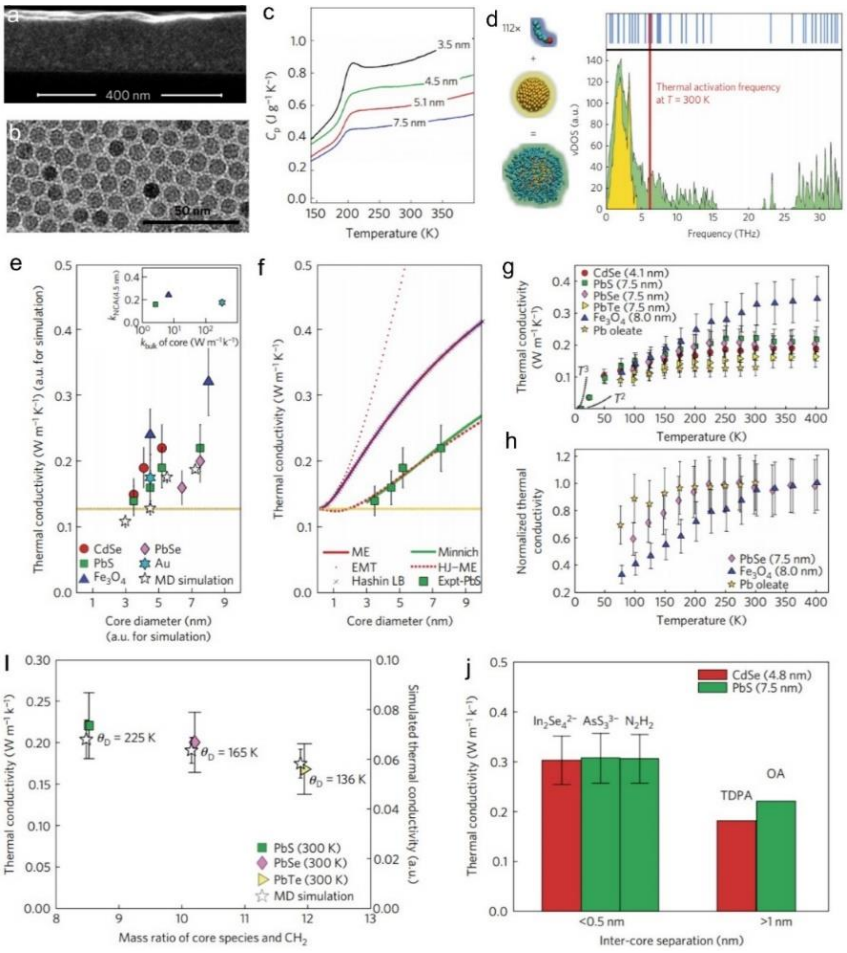

Figure 2.10 (a) SEM cross-sectional image of a 7.5 nm diameter PbS NCA film. (b) Planar TEM image of an 8 nm diameter Fe_3O_4 NCA film showing a regular close-packed arrangement. (c) Specific heat capacity data as a function of temperature for a diameter series of PbS nanoparticles coated with oleic acid ligands. (d) Vibrational density of states (vDOS) of a 2.8-nm-diameter Au nanocrystal and its individual constituents. The blue vertical lines represent the vibrational spectrum of one ligand.

The yellow region in the vDOS of the Au core, which is enclosed in the green vDOS of the nanocrystal. (e) Diameter series data for various NCAs have increasing thermal conductivity with core diameter regardless of core composition. (f) EMA model, HJ-ME and Minnich models comparison with experimental data. (g) Temperature series for CdSe, PbS, PbSe, PbTe and Fe_3O_4 NCAs, and Pb oleate ligands. (h) Normalized temperature series for Pb oleate ligands and PbSe and Fe_3O_4 NCAs. (i) Oleate-capped lead chalcogenide NCAs show a decrease in thermal conductivity with large mass ratio. (j) NCA thermal conductivity for different inorganic and organic ligands on CdSe and PbS nanocrystals. Figure adapted from reference[29].

They first prepared nanocrystal array (NCA) thin film via spin-coating of nanocrystal solution. The nanocrystals were closely packed with a face-centered-cubic lattice structure, which is shown in Figure 2.10a, b. Specific heat capacity of NCAs were measured using DSC and shown in Figure 10c. They also performed molecular dynamics simulations and harmonic lattice dynamics calculations to elucidate how the vibrational structure of a nanocrystal is related to its constituent core and ligands. From Figure 2.10d, we can see all core vibrational states overlap with ligands states below the thermal activation frequency at 300 K, while higher-frequency ligands states have no corresponding core states to overlap at higher temperatures.

Thermal conductivity as a function of core diameter for CdSe, PbS, PbSe, Au and Fe_3O_4 NCAs is shown in Figure 2.10e, NCA thermal conductivity increases with increasing diameter. They first tried effective medium approximation to help understand the trend, which is shown in Figure 2.10f, the effective medium approximation (EMA) model assumes a random distribution of two phases, captures the increasing trend due to increasing core volume fraction, yet severely overestimates the thermal conductivity. A modified EMA model[30] with inclusion of thermal interface

conductance by Hasselman and Johnson (HJ-ME) was then employed to fit the experimental data, which turned out to agree well. They further performed temperature-dependent thermal conductivity measurements and found thermal conductivities of PbS, PbSe, PbTe and CdSe NCAs increases from 10 to 200K and plateau above 200K. This data is shown in Figure 2.10g, h. They believe this behavior suggests that interfacial vibrational energy transport at the measured temperatures is dominated by elastic events, whereby the frequencies of the interacting states are the same. If inelastic scattering is present at the interface, the thermal interface conductance will continue to increase due to increased phonon population with temperature increase. Vibrational density of states (vDOS) was considered here to understand this phenomenon. Below a temperature of 200K, which is near the Debye temperature of CdSe (182K), PbS (225K), PbSe (175K) and PbTe (136K), increasing the temperature increases the populations of vibrational states with frequencies that are common to the cores and ligands. While at higher temperature, the vibrational frequencies common to the cores and ligands are fully activated. Additional higher-frequencies ligand states continue to be activated, but the thermal conductivity plateaus as these high frequency states do not have core states to couple with elastically. This is again proved by the temperature-dependent measurement on Fe_3O_4 NCAs, which plateaus above 300k due to much higher Debye temperature (>350K). Lead chalcogenide nanocrystals solids of the same size and ligand with cores of different compositions were prepared and measured and shown in Figure 2.10i, from this plot we see a decrease of thermal conductivity with large mass ratio of the core species. They ascribed this thermal conductivity decrease to a decrease of debye temperature. The 30% decrease from PbS NCAs to PbTe NCAs cannot be solely explained as a reduced core thermal conductivity, which actually amounts to only a 5 % decrease. They believe lower Debye temperature would cause the shift of the core

phonons to lower frequencies, which leads to less overlap with the high frequency ligand states. This would decrease the interface thermal conductance from ~140 MW $m^{-1}K^{-1}$ to ~72 MW $m^{-1}K^{-1}$. Electronic conductivity of the nanocrystal solids recorded a ten order of magnitude by exchanging the oleic acid ligands with shorter hydrazine ligands[17, 31]. To determine whether thermal transport parallels charge transport, the original long organic oleate ligands were exchanged with shorter inorganic ligands (N_2H_4, AsS_3^{3-}, $In_2Se_4^{2-}$) for thermal conductivity measurement. As is shown in Figure 2.10 j, thermal conductivity increased by 50% after ligand exchange. To evaluate the electronic thermal conductivity contribution before and after ligand exchange, electronic conductivity was measured and converted into electronic thermal conductivity using Wiedemann-Franz law. It turns out that the electronic thermal conductivity contribution was still an order of magnitude smaller than measured values even after ligand exchange. This verifies that thermal energy transport in nanocrystal solids was dominated by phonons.

Liu et al.[32] used PbS NCs as a model system and varied ligand binding group (thiol, amine, and atomic halides), ligand length (ethanedithiol, butanedithiol, hexanedithiol, and octanedithiol), and NC diameter (3.3-8.2 nm). This work also reveals several findings: (i) The thermal conductivity of the NC solids can be increased by up to a factor of 2.5 with varying ligand choices. (ii) ligand binding strength to the core does not significantly affect the thermal conductivity. (iii) shorter ligands lead to shorter inter-particle distance and increases the thermal conductivity. (v) Surface chemistry effect could exceed the effects of NC diameter and becomes more pronounced as NC diameter decreases.

Figure 2.11a-c shown the PbS nanocrystal morphology, nanocrystal solids thin film, and ligands used of different molecular structure. They first studied the thermal

conductivity of PbS nanocrystals solids with ethylenediamine (EDA) and 1,2-ethanedithiol (EDT) ligands. These two ligands have identical backbones, but different ending groups: amine group for EDA and thiol group for EDT. These groups form covalent bonds to the PbS NC surface with different binding strength: it was believed thiol groups forms a stronger bond than the amine group.[33] As is shown in Figure 2.11d, PbS NC solids with EDT ligands have a lower thermal conductivity than with EDA ligands, this is quite counter-intuitive as usually we would believe thiol group with stronger bonding should have higher thermal interface conductance, which has been reported in SAM junctions. To further expand this binding group motif, PbS NC solids with halide ligands which form much stronger ionic bonds than thiol group and amine group shown above, was measured and also shown in Figure 2.11d, it turns out thermal conductivity of these nanocrystal solids with much stronger ionic bonds are essentially equivalent. This further proves that thermal conductance of the NC core ligand interface does not dominate thermal transport in nanocrystal solids.

The thermal conductivity of NC solids of varying core diameter was also studied and shown in Figure 2.11g. As the Core diameter increased from 3.3 nm to 8.2 nm, thermal conductivity increases from 0.13 $Wm^{-1}K^{-1}$ to 0.27 $Wm^{-1}K^{-1}$, which agrees well with measurements by Ong et al.[29] Nanocrystal inter-particle distance was determined by ligand shell length. In order to understand how ligand length impact the thermal conductivity, PbS nanocrystal of fixed size with ligands of different length are measured and shown in Figure 2.11e. Thermal conductivity decreased from 0.27 $Wm^{-1}K^{-1}$ to 0.2 $Wm^{-1}K^{-1}$ when ligand backbone carbon atoms increased from 4 to 8. This again proves that interparticle distance is an important parameter affecting the thermal conductivity of nanocrystal solids.

Effective medium approximation (EMA) modified by Hasselman and Johnson, which included the thermal interface conductance, was used to fit the experimental data.[30] As is shown in Figure 2.11i, the PbS NC solids with oleic acid (OA) ligands of different sizes matched well with the prediction of EMA model. To study the relative impact of each parameter on NC solid thermal conductivity in EMA.

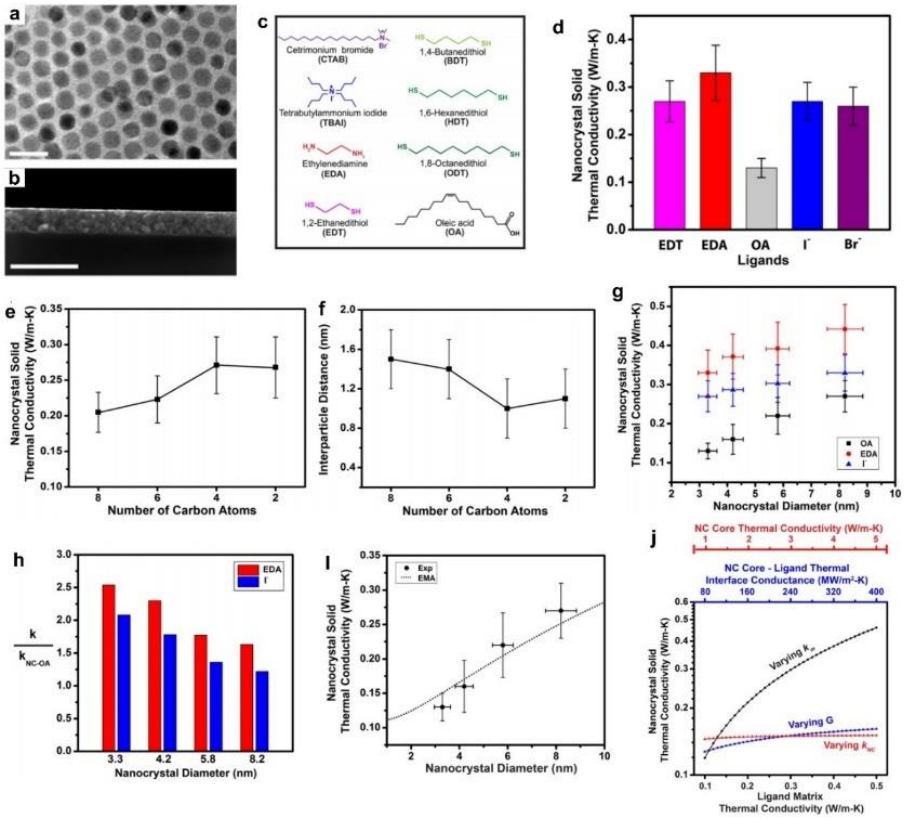

Figure 2.11 (a) TEM image of ~8.2 nm PbS nanocrystals with oleic acid ligands, the scale bar is 20 nm. (b) Cross-sectional SEM image of the nanocrystal solid thin film, the scale bar is 500 nm. (c) the chemical structure of the molecules used during the ligand exchange. (d) Thermal conductivity of 3.3 nm PbS nanocrystal solids with ethanedithiol (EDT), ethylenediamine (EDA), oleic acid (OA), I-, and Br- ligands. (e) Thermal conductivity of 3.3 nm PbS nanocrystal solids with alkanedithiol ligands of varying backbone length. (f) Interparticle distance of 3.3 nm PbS nanocrystal solids

with alkanedithiol ligands of varying backbone length. (g) Thermal conductivity pf PbS nanocrystal solids with oleic acid (OA), ethylendiamine (EDA), and I- ligands as a function of nanocrystal diameter. (h) The relative increase of thermal conductivity in PbS nanocrystal solids with ethylendiamine (EDA), and I- ligands and varying nanocrystal diameter. (i) Effective medium approximation model results. (j) Sensitivity analysis on the EMA model with three independent parameters: NC core thermal conductivity, NC core-ligand thermal interface conductance, and ligand matrix thermal conductivity. Figure adapted from reference[32].

The nature of thermal transport in colloidal nanocrystal solids is a complex combination of different effects. Such as phonon/electron coupling in the nanocrystal, electronic band structure, and vibrational density of states. All of these factors could play roles in thermal energy transport in nanocrystal solids, which make it difficult to develop a systematic theoretical understanding of thermal energy transport in nanocrystal solids.

Effective medium approximation (EMA) was first developed by Maxwell and Eucken to model the effective thermal conductivity of heterogeneous or composites materials. This Maxwell-Eucken model assumes a dispersion of small spheres within a continuous matrix of a different components, with the spheres being far apart such that the local distortions to the temperature distributions around each of the spheres do not interfere with their neighbors' temperature distributions. The effective thermal conductivity of the composites can be expressed by

$$\mathrm{K} = \frac{k_1 V_1 + k_2 V_2 \frac{3k_1}{2k_1 + k_2}}{V_1 + V_2 \frac{3k_1}{2k_1 + k_2}}$$

Where k_1 and k_2 corresponds to the thermal conductivity of the continuous phase and dispersed phase, respectively. V_1 and V_2 corresponds to the volume ratio of the continuous phase and dispersed phase, respectively. This model predicted that effective thermal conductivity of the composites was a function of the thermal conductivity of the constituents, the geometric distribution and the volume fraction of each component, but independent of their dimensions. Experiments results indicated that the effective thermal conductivity of the composites can be affected by a thermal barrier resistance at the interface between the individual components.[34, 35]

Hasselman and Johnson[30] modified the original effective medium approximation (EMA) and include the interface thermal conductance into the model. Some key derivation steps will be shown below to better understand the model. The temperature T_2 within the spherical dispersion of radius a and the temperature T_1 in the surrounding matrix are assumed to be of the general form:

$$T_2 = rAcos\theta$$

$$T_1 = (\nabla T)rcos\theta + (B/r^2)cos\theta$$

Where ∇T is the temperature gradient at large distances away from the dispersion, A and B are constants to be solved and r and θ are spherical coordinates with θ being the angle between the radius vector r and the temperature gradient. Equations shown above are subject to the boundary conditions at r=a:

$$K_2\left(\frac{\partial T_2}{\partial r}\right) = K_1\left(\frac{\partial T_1}{\partial r}\right)$$

$$T_2 - T_1 = -\left(\frac{\partial T_1}{\partial r}\right)$$

Solving for A and B and substitution into equation, which yields:

$$T_2 = (\nabla T) r cos\theta \frac{1 + \left[\frac{K_1}{ah_c} + \frac{K_1}{K_2} - 1\right]\left[1 + \frac{2K_1}{K_2}\left(\frac{K_2}{ah_c} + 1\right)\right]^{-1}}{\frac{K_2}{ah_c} + 1}$$

$$T_1 = (\nabla T) r cos\theta + \frac{(\nabla T) a cos\theta}{r^2} \frac{\left[\frac{K_1}{ah_c} + \frac{K_1}{K_2} - 1\right]}{\left[1 + \frac{2K_1}{K_2}\left(\frac{K_2}{ah_c} + 1\right)\right]}$$

With the volume fraction of spheres, $V_2=na^3/b^3$ and for b very large such that $K_m/b_{hc}=K_{eff}/b_{hc}=0$, equating these last terms yields:

$$K_{eff} = K_1 \frac{\left[2\left(\frac{K_2}{K_1} - \frac{K_2}{ah_c} - 1\right)V_2 + \frac{K_2}{K_1} + \frac{2K_2}{ah_c} + 2\right]}{\left[\left(1 - \frac{K_2}{K_1} + \frac{K_2}{ah_c}\right)V_2 + \frac{K_2}{K_1} + \frac{2K_2}{ah_c} + 2\right]}$$

This equation agrees with the expression of Maxwell for effective thermal conductivity in absence of an interfacial thermal barrier resistance.

Minnich et al.[36] further modified the HJ-ME model and included the reduction of the thermal conductivities of the particle inclusions and matrix due to boundary scattering. When the characteristic length of inclusion is on the order of or smaller than the phonon mean free path. This formulation takes into account the increased interface scattering in the different phases of the nanocomposites and the thermal boundary resistance between the phases.

In nanocomposites, where the inclusion size is smaller than the phonon mean free path (MFP), the EMA model failed to match with those from more rigorous solutions. This is because the host and particle thermal conductivities in nanocomposites are not equal to their bulk values due to increased interface scattering.

As is shown previously in the phonon transport kinetic theories,

$$k = \frac{1}{3}\int C(\omega)\, v(\omega)\Lambda(\omega)d\omega \approx \frac{1}{3}Cv\Lambda$$

Where C is the volumetric specific heat, v is phonon group velocity, and Λ is the phonon MFP. For the host phase, they expect the effective thermal conductivity to be a function of the bulk MFP and a characteristic length that accounts for the nanoparticle density. The interface density, defined as the surface area of the nanoparticles per unit volume of composites, is a primary factor in determining the effective thermal conductivity. The interface density for spherical particle is defined as

$$\Phi = \frac{4\pi(d/2)^2}{a^3} = \frac{6\varphi}{d}$$

$$\varphi = \frac{(\frac{4}{3})\pi(d/2)^2}{a^3} = \frac{(1/6)\pi d^3}{a^3}$$

Where φ is the volume fraction of nanoparticles, a is the unit cell effective length. The effective area of collison for a phonon and spherical nanoparticle is $\pi d^2/4$; thus, if a phonon travels a distance L it will encounter $\mathrm{N} = \pi d^2 Ln/4$ inclusions. The MFP is the distance traveled divided by the number of collisions,

$$\Lambda_{coll} = \frac{L}{\pi d^2 Ln/4} = \frac{4a^3}{\pi d^2} = \frac{2d}{3\varphi}$$

We can now relate the collision MFP and Φ,

$$\Lambda_{coll} = \frac{4}{\Phi}$$

Applying Matthiessen's rule, the effective MFP of the host phase is

$$\frac{1}{\Lambda_{eff,h}} = \frac{1}{\Lambda_{b,h}} + \frac{1}{\Lambda_{coll}} = \frac{1}{\Lambda_{b,h}} + \frac{4}{\Phi}$$

Where $\Lambda_{eff,h}$ and $\Lambda_{b,h}$ are the effective and bulk MFPs of the host phase, respectively.

They next consider the inclusion phase. The MFP of the particle phase should only be a function of the bulk MFP and the characteristic length of the particle phase. Using the Matthiessen's rule, we get an effective MFP,

$$\frac{1}{\Lambda_{eff,p}} = \frac{1}{\Lambda_{b,p}} + \frac{1}{d}$$

Using this MFP they got the effective thermal conductivity of the particle phase. Based on all the derivations shown above, they got an expression for effective thermal conductivity of a nanocomposite as a function of the interface density Φ and the particle diameter d.

$$k_{eff}(\Phi; d) = \frac{1}{3} C_h v_h \frac{1}{\frac{1}{\Lambda_{b,h}} + \frac{4}{\Phi}} \times \frac{k_p(d)\big(1 + 2\alpha(\Phi, d)\big) + 2k_h(\Phi) + 2(\frac{\Phi d}{6})\big[k_p(d)(1 - \alpha(\Phi, d) - k_h(\Phi))\big]}{k_p(d)\big(1 + 2\alpha(\Phi, d)\big) + 2k_h(\Phi) - (\frac{\Phi d}{6})\big[k_p(d)(1 - \alpha(\Phi, d) - k_h(\Phi))\big]}$$

2.3 Mechanics of Nanostructured Materials

2.3.1 Background of Nanoindentation

Indentation has been the most widely used technique for determining the mechanical properties of materials. However, traditional indentation test requires imaging the indent, which imposes a lower limit on the length scale of the indentation. While nanoindentation[37], which is capable of continuously measuring nanonewton level load and nanometer level displacement, becomes a very powerful technique of measuring mechanical properties of small volume of materials at the nanometer scale. After obtaining the load-displacement curve, we can retrieve many mechanical properties such as Young's modulus, hardness, and fracture toughness.

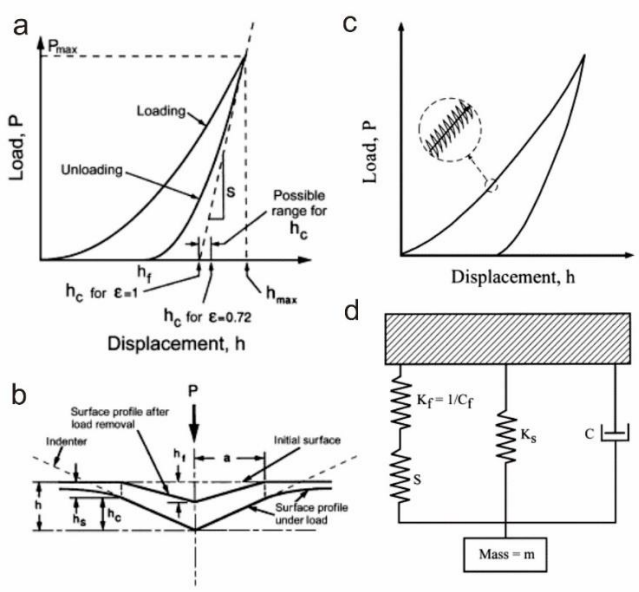

Figure 2.12 (a) A representative load-displacement curve and (b) the deformation pattern of an elastic-plastic sample during and after an indentation; a schematic illustration of the (c) CSM loading cycle and the (d) dynamic indentation model. Figure adapted from reference[37].

Young's modulus and hardness are the two most frequently measured mechanical properties using nanoindentation. During a typical nanoindentation test, as the probe penetrates through the sample, which induces both elastic and plastic deformation, eventually leads to the formation of a hardness impression. Once the ultimate displacement is reached, the probe withdraws and only the elastic portion of the displacement is recovered. Figure 2.12a, b shows a representative load-displacement curve and the deformation pattern of an elastic-plastic sample during and after indentation. Nanoindentation hardness is defined as the indentation load divided by the projected contact area of the indentation. We can derive the hardness from the peak load as

$$H = \frac{P_{max}}{A}$$

where P_{max} is the peak load from the load-displacement curve, A is the projected contact area. For an indenter with a known geometry, A is obtained as a function of contact length h_c. For a perfect Berkovich indenter, A_c is given by

$$A_c = 24.56h_c^2$$

Young's modulus of the sample can be derived from the initial unloading contact stiffness, $S = dP/dh$, as S can be correlated to Young's modulus by the following expression

$$S = 2\beta\sqrt{\frac{A}{\pi}}E_r$$

Where β is a constant that dependent on the geometry of the indenter. Specifically, β=1.034 for a Berkovich indenter. And E_r is the reduced elastic modulus, which accounts for the fact that elastic deformation occurs in both the sample and the indentor. E_r is further related to E of the sample by the following equation

$$E_r = \frac{1-v^2}{E} + \frac{1-v_i^2}{E_i}$$

Where E and E_i are elastic modulus of the sample and the indenter, respectively. While v and v_i are Poisson's ratio for the sample and the indenter, respectively. Specifically, for diamond indenter, E_i = 1141 GPa and v_i = 0.07.

Recently, continuous stiffness measurement (CSM) has been developed to further improve nanoindentation test.[37] Specifically, CSM is accomplished by imposing a small, sinusoidally varying signal on top of a DC signal that drives the motion of the indenter. This technique allows the measurement of the contact stiffness at any point along the loading curve, which enables continuous measurements of mechanical properties. This offers an effective route towards measuring the mechanical properties of nanometer-

thick films. As shown in figure 2.12c, a small harmonic force is imposed and further added to the nominally increasing load on the indenter. The displacement response of the indenter at the excitation frequency and the phase angle between the two are measured continuously as a function of depth. By solving for the in-phase and out-of-phase portions of the response, one can explicitly determine the contact stiffness as a function of depth. To calculate the contact stiffness, the dynamic response of the indentation system needs to be determined. As shown in figure 2.12d, 3 main components need to be considered, that are mass, m, of the indenter, the spring constant, K_s of the leaf springs, and the stiffness, K_f of the indenter frame, where $K_f = 1/C_f$, and the damping coefficient, C. Assumes the imposed driving force is $P = P_{os}\exp(i\omega t)$ and the displacement response of the indenter is $h(\omega) = h_0\exp(i\omega t + \emptyset)$. Then, the contact stiffness can be obtained from the expression below

$$\left|\frac{P_{os}}{h(\omega)}\right| = \sqrt{\left\{\left(S^{-1} + K_f^{-1}\right)^{-1} + K_s - m\omega^2\right\}^2 + \omega^2 C^2}$$

Alternatively, contact stiffness can also be derived from the phase difference between the force and the displacement signals via the following equation

$$\tan(\emptyset) = \frac{\omega C}{\left(S^{-1} + K_f^{-1}\right)^{-1} + K_s - m\omega^2}$$

Where P_{os} is the magnitude of the force oscillation, $h(\omega)$ is the magnitude of the resulting displacement oscillation, ω is the frequency of the oscillation, and $\emptyset$ is the phase angle.

2.3.2 **Mechanical Property of Colloidal Nanocrystal Assemblies**

Colloidal nanocrystal assemblies possess fascinating mechanical behavior and unique thermal, optical, and electronic properties, which arise from the collective response of inorganic nanocrystals that are in close proximity yet separated by

molecular ligands. Studying mechanics is of great importance for realization of strong and stiff membranes, films and strong and tough nanocomposites. More importantly, study of the mechanical properties of nanocrystal assemblies provides fundamental insight into the cohesion and dynamics at the nanoscale. Mechanical properties study on colloidal nanocrystal assemblies is still scarce in the literature. Here we briefly introduce some representative studies in this field.

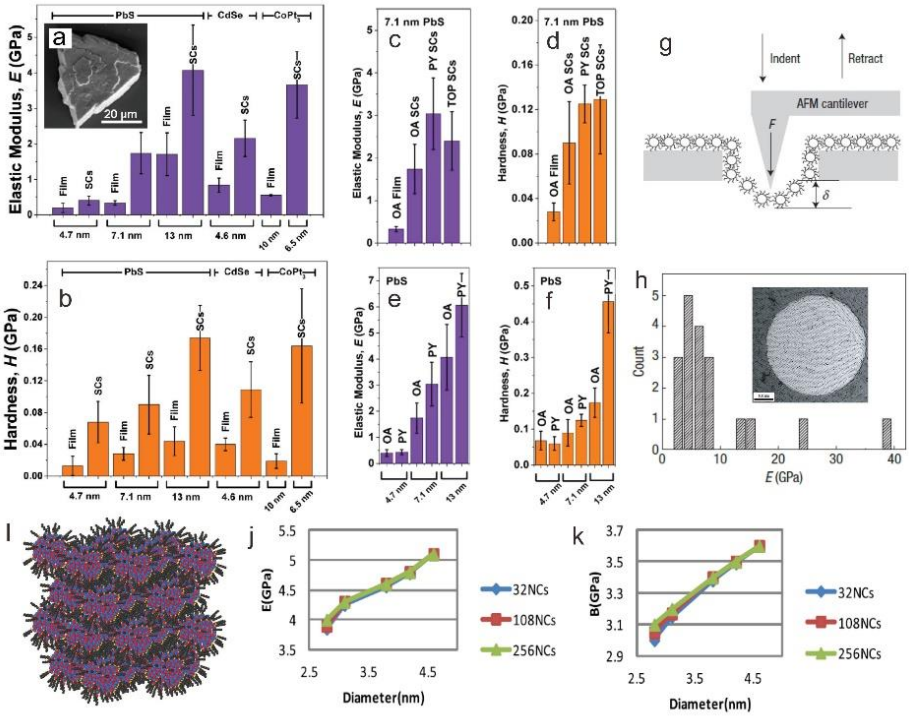

Figure 2.13 Summary of nanoindentation mechanical results for NCs films with short-ranged order and SCs: (a) elastic moduli and (b) hardness. The error bars represent standard deviations of the results for at least 10 indentations. Comparison of (c) elastic moduli and (d) hardness for 7.1 nm PbS NCs with different ligands. Comparison of (e) elastic moduli and (f) hardness of PbS NCs with addition of pyridine. The error bars represent standard deviations of the results for at least 10 indentations. (g) Schematic diagram: as an AFM tip exerts a force on the membrane the vertical displacement is

measured. (h) Histogram of Young's moduli derived from large-displacement asymptotes. The inset shows a TEM image of a gold nanoparticle monolayer freely suspended over a hole with a 250 nm radius in the silicon nitride substrate. (i) Atomistic model of hexylthiol capped CdSe nanocrystal superlattice with an FCC packing order. (j) Young's modulus and (k) bulk modulus calculated from MD simulations for NCSL arrays of different sizes. Figures adapted from references[38-40].

Podsiadlo et al.[38] systematically studied mechanical properties of colloidal nanocrystal assemblies of varied packing order, nanocrystal size, and capping ligands. In general, they found that colloidal nanocrystal assemblies have elastic modulus and hardness in the range of ~0.2-6 GPa and 10-450 MPa, respectively. These values are analogous to strong polymers, which indicates that the organic ligands present in the assemblies dominate the mechanical response. Specifically, as shown in Figure 2.13a, b, Young's modulus and hardness of colloidal PbS nanocrystal thin film increases with respect to nanocrystal size increase. This is generally understood as a result of higher volume fraction of ligand matrix with increase of size increase. Additionally, they found nanocrystal arranging order also affects mechanical properties of nanocrystal assemblies significantly. Nanocrystal superlattice possesses higher modulus and hardness, which results from its stronger ligand-ligand interaction within the ligand matrix. They further found ligand exchange also significantly change the mechanical properties of colloidal nanocrystal solids. As demonstrated in Figure 2.13c, d, e, f, colloidal PbS nanocrystals with pyridine or trioctylphosphine ligands exhibit higher modulus and hardness than that of PbS nanocrystals with original oleic acid ligand.

Mueggenburg et al.[39] reported 1st mechanical measurements on two-dimensional arrays of close-packed nanoparticles and showed that this nanocrystal array can be stretched across micrometer-size holes. They measured elastic properties of Au

nanocrystal array with force microscopy (Figure 2.13g). Specifically, as shown in Figure 2.13h, for dodecanethiol-capped 6-nm-diameter Au nanocrystal monolayer, they obtained a Young's modulus of ~6 GPa. They claimed that Au nanocrystal monolayer also possesses high flexibility in addition to remarkable strength. They also found the nanocrystal array remains intact and able to withstand tensile stress up to temperature around 370K. The exceptional robustness and resilience at high temperatures of nanocrystal monolayer present great potential for a wide range of sensor applications.

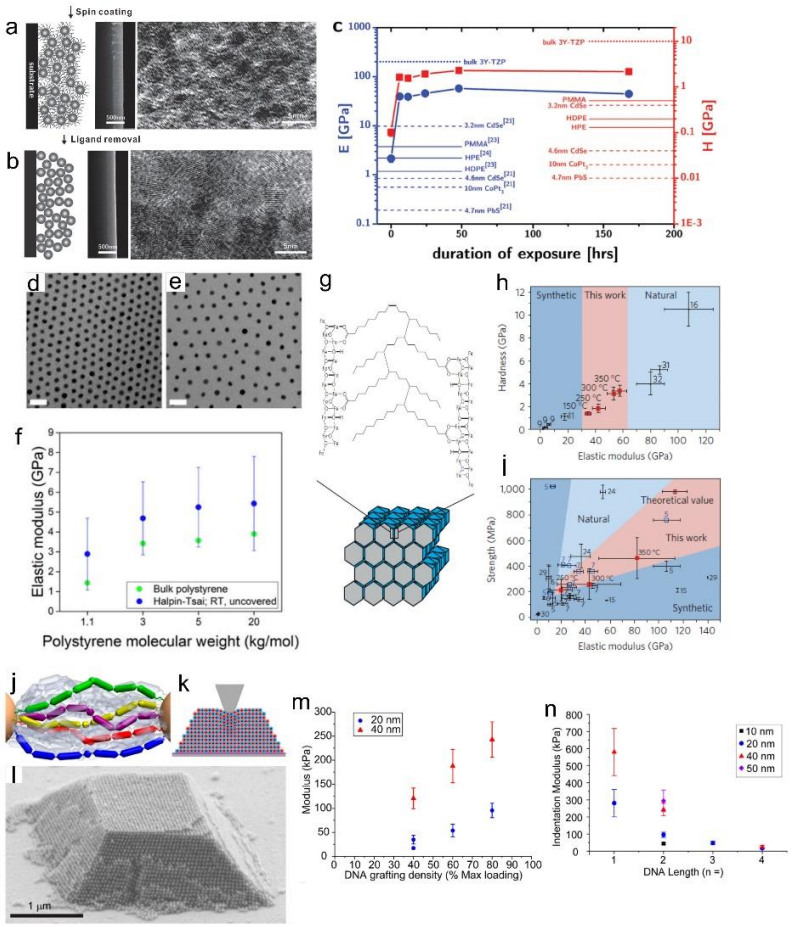

Figure 2.14 (a) 3.7 nm ZrO2 nanoparticle thin film prepared by spin coating which leads to a disordered assembly that prevents cracking. Cross-sectional SEM displays

uniform and smooth film and TEM imaging shows the nanostructure. (b) The ligands separating the nanoparticles are removed by plasma etching, leading to a crack-free all-inorganic polycrystal. Cross-sectional SEM displays the reduction in thickness after ligand removal and TEM imaging show the homogeneous grain size. (c) Modulus and hardness of the films as a function of processing time. TEM images of Au nanocrystal with polystyrene ligands of various molecular weights, (d) 5-kg/mol, (e) 20-kg/mol. (f) Comparison of the elastic modulus of bulk polystyrene with various molecular weights and the elastic modulus of the polymeric component of the superlattice. (g) Schematic illustration of organically linked iron oxide nanocrystal supracrystal. (h, i) Mechanical properties of crosslinked iron oxide nanocrystal supracrystal, and its comparison with other materials. (j) Scaled depiction of DNA conformation between particles for n = 2 linkers at 50% loading. (k) Cartoon showing nanoindentation of a BCC crystal assembled from two complementary particle types. (l) SEM image of a DNA linked nanocrystal superlattice. (m) DNA grafting density effect on the indentation modulus. (n) Indentation modulus for different lengths of DNA on different nanoparticle sizes. Figures are adapted from references[41-44].

In addition to experimental studies, computational work has also been done to elucidate the original of mechanical response of colloidal nanocrystal assemblies. Zanjani et al.[40] presented both coarse-grained and atomistic simulations of elastic modulus of CdSe nanocrystal superlattices. The molecular atomistic simulations yield Young's moduli in the 4-5 GPa range. As is shown in Figure 2.13j, k, they found Young's modulus and bulk modulus increases with increasing nanocrystal size. This is in line with experimental results. They also found the coarse-grained calculations, which doesn't account for the ligand ligand attraction, also showed similar increases with core sizes but predict moduli that are two orders of magnitude lower than the present atomistic simulation results and previous experiments.

Both the experiments and simulations point to a fact that organically capped inorganic nanocrystals possess very limited range of moduli and hardness as a result of weak ligand ligand van der Waals interaction. Various approaches have been proposed in the literature to further improve the mechanical properties of organically capped colloidal nanocrystal solids. Shaw et al.[41] studied structural, chemical, and mechanical evolution of films of colloidal ZrO_2 nanocrystals upon exposure to an O_2 plasma. As shown in Figure 2.14a, b, the original ligands (trioctylphosphine oxide) that separates the neighboring nanocrystals were removed via the plasma etching without obvious nanocrystal sintering. Figure 2.14c presents the mechanical property evolution with increase of duration of O_2 plasma exposure. Specifically, for 3.7 nm ZrO_2 nanocrystal assemblies, its Young's modulus and hardness increases from 2.2 GPa and 0.1 GPa to 44.5 GPa and 2.2 GPa, respectively. Gu et al.[42] investigated the mechanical behavior of polymer-grafted nanocrystal superlattices and explored the role of polymer structural conformation, nanocrystal packing, and superlattice dimensions. They found polymer-grafted nanocrystal superlattices containing 3-20 vol % Au have an elastic modulus of ~6-19 GPa, and hardness of ~120-170 MPa. As showed in Figure 2.14f, polymer extension, interdigitation, and grafting density are found to be critical for superlattice elastic and plastic deformation. Dreyer et al.[43] proposed a facile ligand crosslinking method to boost the mechanical response of iron oxide nanocrystal supracrystals. Using oleic acid capped iron oxide nanocrystal as a demonstration example, they showed that self-assembly of spherical iron oxide nanoparticles in supracrystals linked together by a thermally induced crosslinking reaction of oleic acid molecules leads to a nanocomposite with exceptional bending modulus of 114 GPa, hardness of up to 4 GPa and strength up to 630 MPa. With a simple nanomechanical model, they ascribed the exceptional mechanical properties to the covalent backbone of the linked organic molecules. Very recently, Lewis et al.[44] reported that mechanical

properties of DNA-grafted nanoparticle superlattices can be easily tuned overly nearly 2 orders of magnitude. Specifically, they prepared nanoparticle superlattice via DNA-programmed assembly. As shown in Figure 2.14 j, nanoparticles use a standard DNA motif where a brush of oligonucleotides is first directly grafted to nanoparticles and subsequently functionalized with DNA linkers that drive the nanocrystal assembly via duplex formation. Interestingly, the superlattice can be assembled such that they possess a flat top parallel to the substrate, which significantly aids in mechanical characterization (Figure 2.14k, l). They systematically studied how nanoparticle core size, DNA length, and DNA grating density affects indentation modulus. As is shown in Figure 2.14m, when the number if DNA linkers attached to a particle was reduced, the nanoparticle superlattice also had a proportional reduction in the indentation modulus. As predicted by theory and measured by nanoindentation, increasing DNA length decreased the superlattice modulus, and increasing nanoparticle size increased lattice modulus (Figure 2.14 n).

2.3.3 Intercoupling of Thermal Transport and Mechanical Properties

Classical physics indicates that thermal transport and elastic moduli is linked to atomic and/or intermolecular bonding strength. Kinetic theory further correlates thermal conductivity and elastic moduli with average sound speed. This has been proved to be true in a variety of solid material systems. Choy et al.[45] measured the axial and transverse Young's modulus and thermal conductivity of gel and single crystal polyethylene at a temperature range of 160 to 360 K. They found axial Young's modulus increases sharply with increasing draw ratios. As shown in Figure 2.15a, axial Young's modulus increases linearly with thermal conductivity. More recently, Xie et al.[46] measured the thermal conductivity, heat capacity and sound speed of thin films of five polymers, nine polymer salts, and four caged molecules. As shown in Figure 2.15b, a nearly linear relationship between thermal conductivity and sound speed is

observed. They further found that minimum thermal conductivity calculated from the measured sound velocity and effective atomic density is in good agreement with the thermal conductivity measurements. This presents theoretical insight towards the linear relation between thermal conductivity and sound speed of amorphous macromolecules.

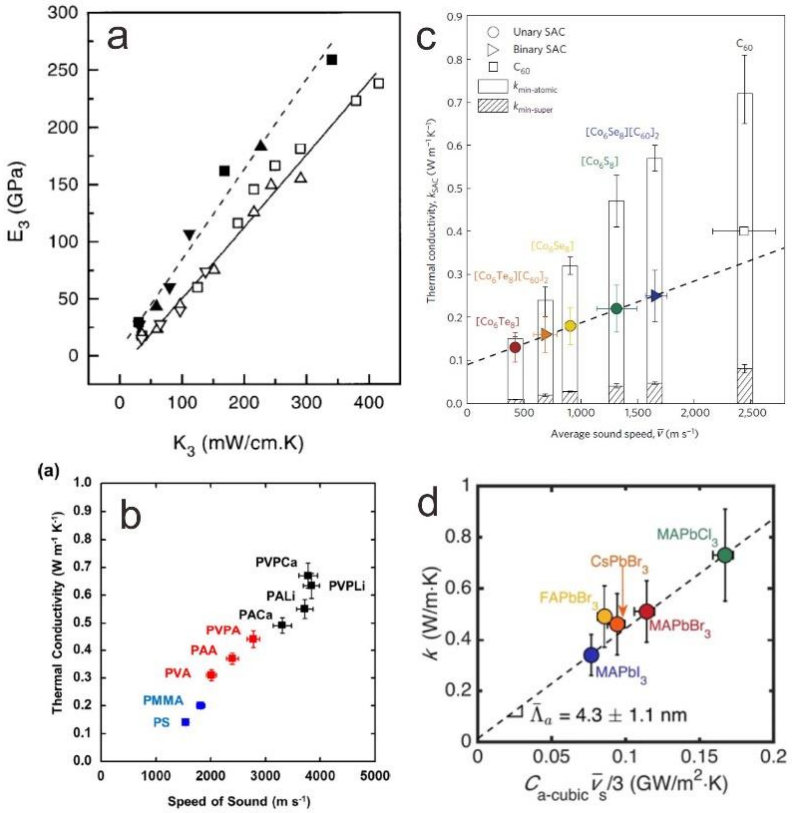

Figure 2.15 (a) Relation between the axial Young's modulus and thermal conductivity of drawn polyethylene. (b) Measured thermal conductivity as a function of average sound speed for several polymers and polymer salts with the same backbone structures and varying interchain bonds. (c) Thermal conductivity of superatomic crystals as a function of average sound speed. (d) thermal conductivity as a function of the product of volumetric heat capacity and average sound speed. Figures adapted from references[45-48].

In additional to polymers, Ong et al.[47] found average elastic modulus and sound speed plays a predictive role for thermal conductivity of superatomic crystals. Superatomic crystals are three-dimensional periodic arrays in which preformed sub-nanometer molecular clusters emulate the role of atoms in traditional solid-state compounds. The strong linearity between thermal conductivity and average sound speed (Figure 2.15c) indicates that thermal transport in superatomic crystals arises from the acoustic phonons that emerge due to the collective inter-superatom vibrations. Elbaz et al.[48] measured thermal conductivity, elastic modulus, and sound speed of lead halide perovskites and found the room temperature thermal conductivity of lead halide perovskites range from 0.34 to 0.73 W/mK and scale with sound speed (Figure 2.15d). They conclude that transport in lead halide perovskites arises form acoustic phonons having similar mean free path distributions.

3 LIGANDS CROSSLINKING BOOSTS THERMAL TRANSPORT IN COLLOIDAL NANOCRYSTAL SOLIDS

3.1 Abstract

The ongoing interest in colloidal nanocrystal solids for electronic and photonic devices necessitates that their thermal transport properties be well understood because heat dissipation frequently limits performance in these devices. Unfortunately, colloidal nanocrystal solids generally possess very low thermal conductivities. This very low thermal conductivity primarily results from the weak van der Waals interaction between the ligands of adjacent nanocrystals. We overcome this thermal transport bottleneck by crosslinking the ligands, which exchanges a weak van der Waals interaction with a strong covalent bond. We obtain thermal conductivities of up to 1.7 W m^{-1} K^{-1} that exceed prior reported values by a factor of 4. This improvement is significant because the entire range of prior reported values themselves only span a factor of 4 (i.e., 0.1 – 0.4 W m^{-1} K^{-1}). We complement our thermal conductivity measurements with mechanical nanoindentation measurements that demonstrate ligand crosslinking increases Young's modulus and sound velocity. This increase in sound velocity is a key bridge between mechanical and thermal properties because sound velocity and thermal conductivity are linearly proportional according to kinetic theory. Control experiments with non-crosslinkable ligands as well as transport modeling further confirm ligand crosslinking boosts thermal transport.

3.2 Introduction

Colloidal nanocrystals (NCs) are solution-grown, nanometer-sized, inorganic particles that are stabilized by a layer of molecular ligands attached to the particle surface. Upon deposition onto a substrate, these particles assemble into a solid material commonly referred to as a NC solid. NC solids have been used in a wide range

of applications including electronics[14, 49, 50], optoelectronics[49, 51], photovoltaics[52, 53], and thermoelectrics[54]. Thermal properties of the active material play an important role in all of these applications. A high thermal conductivity is desired in electronics, optoelectronics, and photovoltaics because this minimizes the temperature rise during device operation, which improves device performance and lifetime. On the other hand, a low thermal conductivity is desired in thermoelectric materials because this leads to large temperature gradients that are important to device function. Research on thermal transport in NC solids[29, 32] shows that these materials have very low thermal conductivities of approximately 0.1 - 0.4 W m^{-1} K^{-1}. While beneficial for thermoelectrics, this low thermal conductivity is problematic for the primary NC applications of interest, which include electronics, optoelectronics, and photovoltaics. Determining methods to obtain high thermal conductivity in these materials are consequently important.

Prior research on NC solids[29, 32] collectively point to the ligand chemistry as the main thermal transport bottleneck. These works[29, 32] studied the effect of varying ligand volume fraction in the NC solid by changing the NC size and/or exchanging the native ligands for shorter ligands. Ong *et al.*[29] showed that NC solid thermal conductivity is largely insensitive to the thermal conductivity of the NC core, which indicates that the NC-ligand interface and/or the ligand matrix is limiting thermal transport. Additional experiments by our group[32] investigated a variety of NC-ligand binding groups, ligand lengths, and NC sizes. Our studies narrowed down the source of the low thermal conductivity to the ligand matrix itself. Within the ligand matrix, we identified the ligand-ligand interface between adjacent colloidal NCs as the key thermal transport bottleneck.

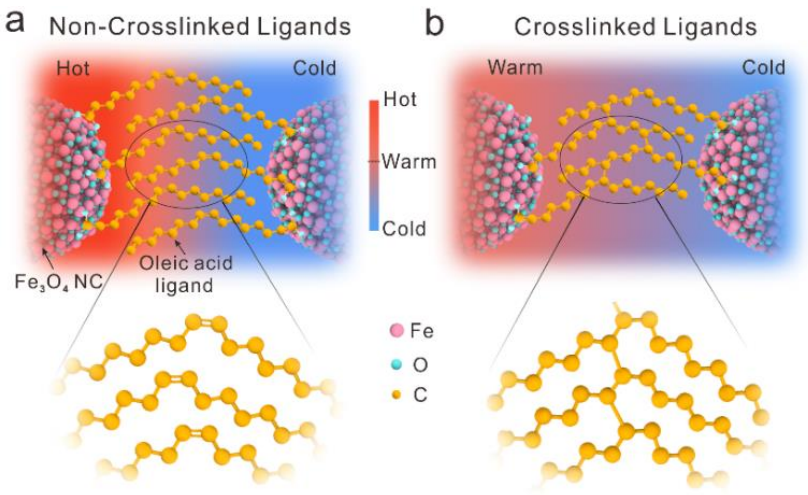

Figure 3.1 Schematic illustrations of ligand structure and the corresponding effect on thermal transport. The insets show zoomed-in views of the ligands before and after crosslinking (hydrogen atoms are omitted for improved clarity). (a) Nanocrystal solids without ligand crosslinking have a low thermal conductivity and require large temperature gradients to move a given quantity of heat. This leads to a high temperature that is "hot" as represented by the bright red background. (b) After ligand crosslinking, nanocrystal solids have a high thermal conductivity and require smaller temperature gradients to move a given quantity of heat. This leads to a high temperature that is just "warm" as represented by the moderately red background.

In this work, we demonstrate that the thermal transport bottleneck in NC solids can be overcome by crosslinking the molecular ligands on the NC surface through a moderate annealing treatment (Figure 3.1). This ligand crosslinking process effectively exchanges the weak van dew Waals (vdW) interactions with strong covalent bonds, and leads to a significant thermal conductivity increase. We demonstrate this process on iron oxide NCs with oleic acid ligand molecules. Control experiments with non-crosslinkable stearic acid ligands confirm the impact of crosslinking on thermal transport. We complement our thermal conductivity measurements with corresponding

materials characterization, mechanical measurements, and thermal transport modeling. Nanoindentation measurements demonstrate that crosslinking also increases Young's modulus and sound velocity. This increase in sound velocity is a key bridge between mechanical and thermal properties because sound velocity and thermal conductivity are linearly proportional according to kinetic theory.

3.3 Results and Discussion

We synthesized monodisperse 8-20 nm iron oxide NCs with either oleic acid (OA) ligands or stearic acid (SA) ligands using a modified thermal-decomposition recipe[55]. Transmission electron microscopy (TEM) imaging and size distribution histograms confirm uniform NC morphology and narrow size distributions (Figure 3.7). Thin films of nanocrystal solids were prepared by spin-coating and then heating to 150 °C to drive off residual solvent. Figure 3.2a-c and Figure 3.8 demonstrate that spin-coating results in ordered assemblies of iron oxide NCs. We crosslinked the ligands of adjacent NCs using the heat treatment reported by Dreyer *et al*.[43] The crosslinking process is carried out by heating the NC assembly to 350 °C for 30 minutes and is illustrated in Figure 1d, e. The crosslinking process binds two adjacent ligands together by splitting the C=C double bond of the OA molecule into saturated C-C single bonds (Figure 3.1).[43] This effectively exchanges the weak vdW interactions between neighboring ligands with strong covalent bonds. The annealing process also causes a portion of the OA ligands to desorb and a corresponding decrease in interparticle spacing (edge-to-edge spacing) between the NCs. High-resolution TEM images (Figure 3.2f, g) show that the individual NCs remain isolated from one another before and after the crosslinking procedure and that the ligand matrix remains intact (*i.e.*, the NCs do not sinter together). In addition to localized TEM imaging, we also interrogated the ligand matrix over a large area using X-ray reflectivity (XRR). By combining these measurements with a geometric model, we conclude that the interparticle spacing

between NCs is ~1 nm and ~0.4 nm before and after annealing, respectively (see section 3.5 of this chapter).

Gas chromatography-mass spectrometry (GC-MS) data on ligands extracted from the NC surface provides direct evidence of ligand crosslinking (Figure 3.3a). The mass spectra data of the crosslinked ligands contain fragments with molecular weights that substantially exceed the molecular weight of OA. This is typically not possible unless the starting material (*e.g.*, cross-linked OA) has a molecular mass exceeding that of OA. More specifically, we detect the presence of large *m/z* peaks (400 - 500) that are 1.4- to 1.8-times more massive than OA itself (282). Control measurements on pure OA and non-crosslinked NC solids are identical to each other and distinctly different from the crosslinked ligands. Furthermore, these measurements on control samples do not yield heavy molecular fragments in the 400 – 500 *m/z* range that are present in the crosslinked samples.

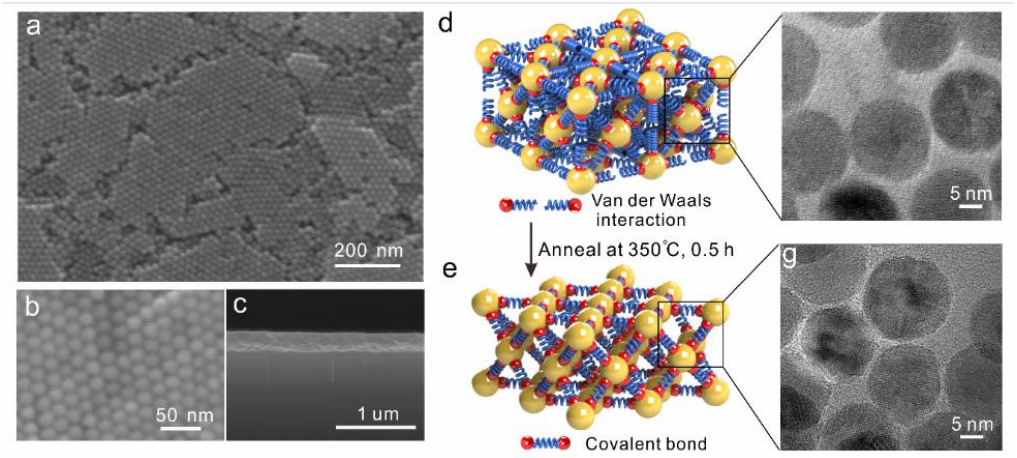

Figure 3.2 Iron oxide NC thin film characterization before and after ligand crosslinking. (a) Scanning electron microscopy (SEM) image of a non-crosslinked iron oxide NC thin film; (b) High-resolution SEM image showing that the non-crosslinked iron oxide NCs form ordered assemblies; (c) cross-sectional view SEM image of iron oxide NC thin film; schematic illustrations of (d) non-crosslinked iron oxide NC solids and (e)

crosslinked iron oxide NC solids, where the adjacent OA ligands are interacting through weak vdW forces and strong covalent bonding, respectively; High-resolution TEM images of (f) non-crosslinked and (g) crosslinked samples show that the annealing process does not lead to NC sintering.

X-ray photoelectron spectroscopy (XPS) characterization confirms the absence of C=C double bonds in annealed samples and provides additional evidence for OA crosslinking. Figures 3.3b-d show high-resolution XPS scans in the C1s, Fe2p, and O1s regions. In the C1s region, a C sp2 peak is observed at 284 eV that can be attributed to the C=C double bonds in the OA ligands of unannealed NC solids. After annealing at 350 °C, the peak corresponding to the C=C double bond disappears. This observation is in agreement with the ligand crosslinking mechanism described by Dreyer *et al.*,[43] wherein the C=C double bond splits and forms a new bond that crosslinks adjacent ligands. We identify the strongest peak at 284.8 eV as the aliphatic C from the OA molecules. The peaks observed at 286 eV and 288.5 eV correspond to the carboxylate that binds the OA molecule to the iron oxide NC surface. The annealing process does not induce any notable changes in the peaks of the Fe2p region, which indicates that the iron oxide NC cores are not affected by the annealing treatment. The O1s region features two prominent peaks at 530.5 eV and 531.5 eV, which correspond to the lattice oxygen in the iron oxide core and oxygen in the carboxylate that bind the OA molecules to the iron oxide NC surface, respectively. The carboxylate peaks in the C1s and O1s regions remain generally unchanged by the annealing process and indicate that organic ligands remain on the NC surface. The annealing also causes OA ligands that were weakly bound to desorb and a corresponding decrease in the interparticle (edge-to-edge) spacing of the NC solid. We probed this partial desorption of ligands using thermogravimetric analysis (TGA, Figure 3.9) and XRR analysis (see section 3.5 of this chapter). Assuming a basic geometric model, uniform ligand

coverage, and an absence of unbound ligands, we calculate that the annealing process decreases the organic ligand capping density from 2 nm^{-2} to 0.8 nm^{-2}. These ligand capping densities are in agreement with prior work by Dreyer *et al.*[43] and indicate that approximately 40% of the ligands remain on the surface after the annealing treatment that crosslinks the OA ligands.

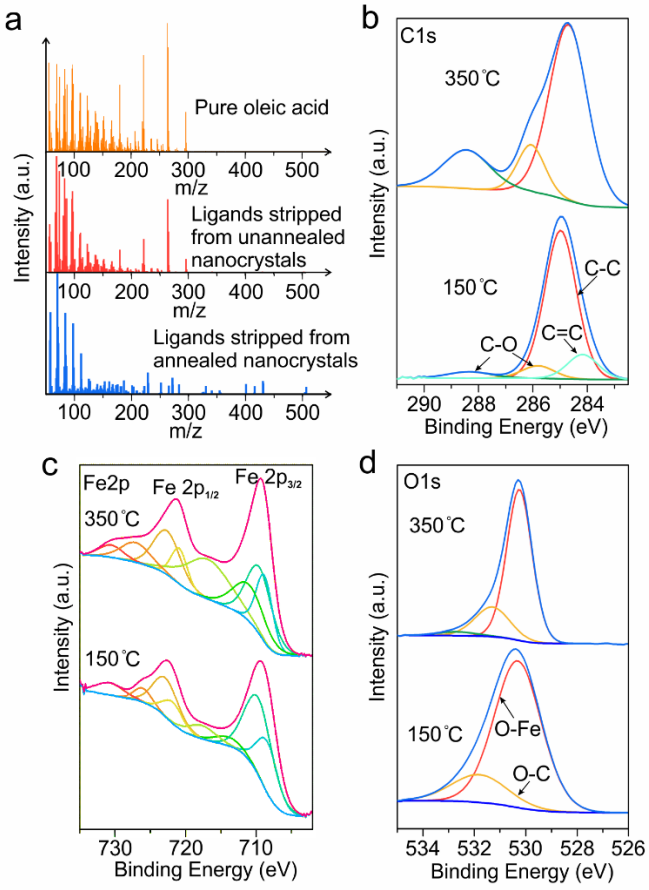

Figure 3.3 Characterization of ligands crosslinking upon annealing. (a) Mass-spectra of pure oleic acid (OA, orange) and organic components extracted from the iron oxide NC surface before (red) and after (blue) annealing; high-resolution x-ray photoelectron spectroscopy scan of C1s (b), Fe2p (c), and O1s (d) regions before and after annealing at 350 °C.

We measured the cross-plane thermal conductivity of the NC solid films using the differential 3ω method.[56-58] Figure 3a-b is a schematic illustration and cross-sectional SEM image of a NC solid sample that is ready for measurement by the 3ω method (*i.e.*, a NC solid sandwiched by a top SiO_2 layer and a bottom Si substrate. A detailed description of our 3ω thermal conductivity measurement system is in Supporting Information and also in our previous work[32].

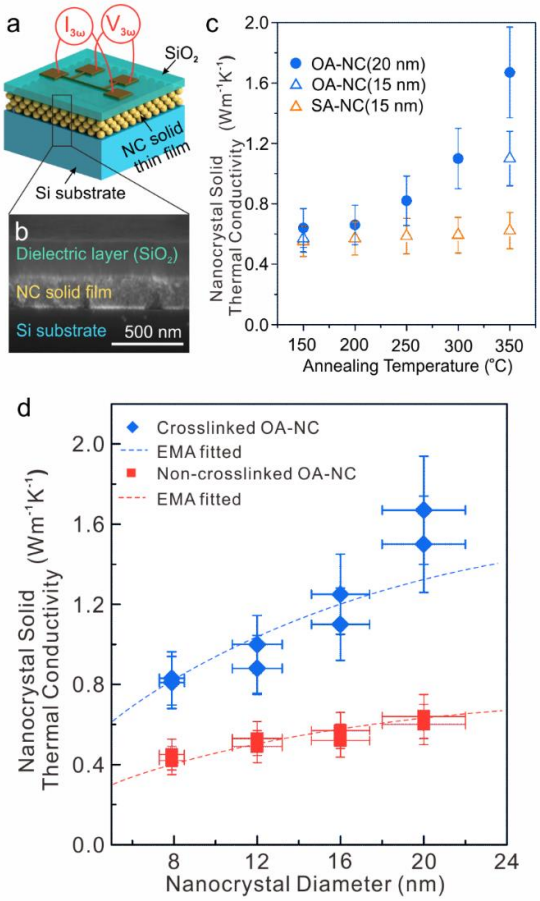

Figure 3.4 Thermal conductivity measurements of NC solid films before and after ligand crosslinking. (a) Schematic of a sample prepared for thermal conductivity measurement via the 3ω method; (b) Cross-sectional SEM image illustrating the substrate – NC solid film – dielectric SiO_2 stack in the measurement samples; (c) Thermal conductivity of oleic acid (OA)-capped NC solids and stearic acid (SA)-capped

iron oxide NC solids as a function of annealing temperature for both 15 and 20 nm diameter NCs; (d) Room temperature thermal conductivity measurement results on OA-capped iron oxide NC solids of different NC sizes before and after annealing at 350 °C. The dash lines in (d) are fitted results based on an effective medium approximation (EMA) model.

Thermal transport measurements show that a thermal conductivity increase of up to ~260% accompanies the annealing process that crosslinks the NC ligands. Figure 3.4d shows the thermal conductivity of non-crosslinked and crosslinked iron oxide NC solids as a function of core diameter at room temperature. The thermal conductivity of non-crosslinked iron oxide NC solids increased from 0.42 - 0.64 $Wm^{-1}K^{-1}$ as the core diameter increased from 7.9 - 20 nm. NC solids can be approximated as a nanocomposite consisting of high thermal conductivity NC cores embedded in a low thermal conductivity ligand matrix. This trend of increasing thermal conductivity with increasing NC diameter is consistent with prior reports[29, 32], and occurs because the volume fraction of the high thermal conductivity component (NC cores) is increasing relative to the low thermal conductivity component (ligand matrix). We next crosslinked the OA ligands of the NCs and observed a substantial thermal conductivity increase for all NC diameters (Figure 3.4d). The thermal conductivity of crosslinked iron oxide NC solids increased from 0.81 - 1.7 $Wm^{-1}K^{-1}$ as the diameter increased from 7.9 - 20 nm.

Our measured value of 1.7 $Wm^{-1}K^{-1}$ exceeds the highest reported thermal conductivity in a colloidal NC solid by a factor of ~4 (i.e. Liu *et al.*[32] measured a thermal conductivity of 0.4 $Wm^{-1}K^{-1}$ for 8 nm diameter PbS NCs with short ethylenediamine ligands). This difference cannot be attributed to a difference in the thermal conductivity of the NC cores (Fe_3O_4[59] and PbS[60]) because Ong *et al.*[29] showed that thermal conductivity is insensitive to this parameter. Ong[29] and Liu[32] both showed that the NC

solid thermal conductivity is directly related to the volume fraction of the ligand matrix. Consequently, a partial explanation for this thermal conductivity difference is our larger 20 nm NC cores (*i.e.*, smaller ligand volume fraction). However, this diameter difference by itself is insufficient to explain the observed thermal conductivity difference. Our 7.9 nm diameter samples provide a more suitable comparison to the prior work on 8 nm samples by Liu *et al.*[32] In this comparison, our measured value of 0.81 $Wm^{-1}K^{-1}$ is still double that of the value reported by Liu *et al.*[32]

Annealing the NC solids with oleic acid in this work leads to two effects, partial ligand desorption and ligand crosslinking, both of which can increase thermal conductivity. Consequently, we performed control experiments using stearic acid (SA) ligands to experimentally confirm that ligand crosslinking is the dominant factor that causes the increased thermal conductivity. SA is chemically identical to oleic acid (OA), except that it lacks the C=C double bond in its carbon backbone. This means that SA ligands cannot crosslink. GC-MS, TGA, TEM, and SEM analysis on SA-capped NCs further confirm that they behave like OA-capped NCs except for their inability to crosslink (see section 3.5 of this chapter and Figure 3.11). Consequently, we can use OA ligands to infer the combined effects of ligand crosslinking and partial ligand desorption, whereas we can use SA ligands to infer the effect of partial ligand desorption only.

Figure 3c shows the thermal conductivity of OA-capped and SA-capped NC solids as a function of annealing temperature. For an annealing temperature of 150 °C, which is too low to induce ligand crosslinking, the thermal conductivity of 15 nm NCs is ~0.55 $Wm^{-1}K^{-1}$ regardless of whether OA or SA ligands are used. Beyond this annealing temperature, the thermal conductivity of the OA-capped NC solids rapidly rises, but the thermal conductivity of the SA-capped NC solids increases only slightly. After annealing at 350 °C, the thermal conductivity values for 15 nm NCs reach 1.1 and 0.62

$Wm^{-1}K^{-1}$ for OA and SA ligands, respectively. Using the OA-case as a proxy for combined ligand crosslinking and ligand desorption, and the SA-case as a proxy for ligand desorption only, we estimate that ligand crosslinking and ligand desorption account for 87% and 13% of the total change in thermal conductivity. This experiment confirms that ligand crosslinking is the dominant effect that increases thermal conductivity from the annealing process.

It is worth noting that our iron oxide diameter series partially overlaps with the iron oxide diameter series studied by Ong[29] and this provides a means to check the accuracy of our measurements. Our measurement of 0.42 ± 0.08 W m^{-1} K^{-1} for 7.9 nm NCs and their measurement of 0.32 ± 0.05 W m^{-1} K^{-1} for 8 nm iron oxide NCs are within experimental uncertainty of each other and validate our results. We also investigated the possible effects of sample contact resistance and/or free electrons carriers on our thermal conductivity measurements and found that these are negligible (see section 3.5 of this chapter).

To more thoroughly interrogate the origins of our increased thermal conductivity, we performed Young's modulus measurements on the NC solids. According to kinetic theory, thermal conductivity is proportional to sound velocity ($k = 1/3 C v_s \Lambda$), where k, C, v_s, and Λ are thermal conductivity, volumetric heat capacity, sound velocity, and mean free path of acoustic vibrations, respectively. Furthermore, solid mechanics dictates that sound velocity is proportional to the square root of Young's modulus ($v_{s,ave} \propto \sqrt{E/\rho}$), where $v_{s,ave}$, E, and ρ are the average sound speed, Young's modulus, and density, respectively. Consequently, changes in thermal conductivity can correlate to changes in Young's modulus and vice versa. This relationship has been recognized by other researchers, and we now use it here to investigate the effects of ligand crosslinking.

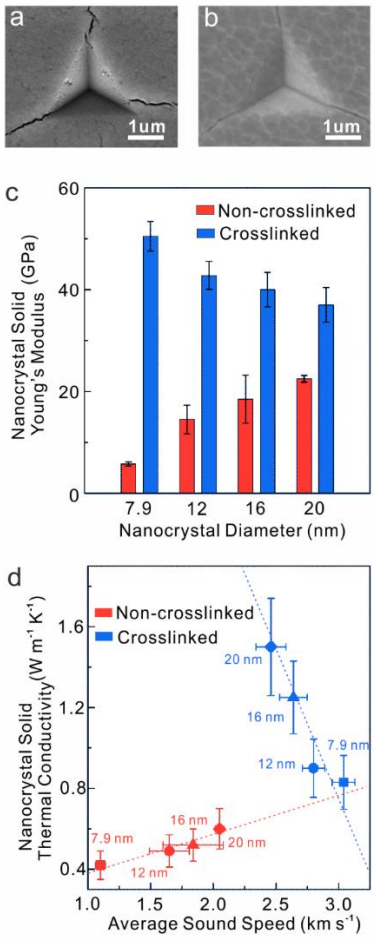

Figure 3.5 Representative SEM images of nanoindented iron oxide NC solids (a) before and (b) after annealing; (c) Young's modulus of non-crosslinked and crosslinked iron oxide NC solids with varying NC core diameter. (d) Thermal conductivity of non-crosslinked and crosslinked iron oxide NC solids as a function of derived average sound speed and varying NC core diameter.

We used nanoindentation to measure the Young's modulus of our NC solid films. Figure 3.5a and 3.5b shows the indented surfaces of non-crosslinked and crosslinked NC solids, respectively. These SEM images show no pileup of displaced material at the edge of the indent, which allows us to derive the elastic modulus using the Oliver-Pharr method[61]. We then use Hay's model[62] to subtract the effect of the substrate in

our Young's modulus measurements (Figure 3.14c, d). As shown in Figure 3.5c, the Young's modulus of the non-crosslinked thin films increases monotonically from 5.75 – 22.5 GPa as the NC diameter increases from 7.9 - 20 nm. This trend is due to the declining volume fraction of the soft organic ligands and stronger interaction between nanocrystal cores,[63] and has been previously observed for OA-capped PbS NC thin films.[38]

In all cases, the Young's modulus of the NC solid increases after ligand crosslinking. The relative change in Young's modulus is greatest for the 7.9 nm diameter NCs, which is intuitive since that sample has the largest volume fraction of ligand matrix. Interestingly a Young's modulus trend reversal with NC diameter occurs after crosslinking. The Young's modulus of the crosslinked NC solid decreases monotonically from 50.5 – 36.0 GPa as the core diameter increases from 7.9 - 20 nm. We speculate that this trend reversal in Young's modulus arises from variations in the effectiveness of the crosslinking procedure as the NC diameter is changed (see section 3.5 of this chapter), but also acknowledge that this trend merits further study.

Further dissection of our nanoindentation data allows us to calculate the mechanical properties of the individual components for the NC solid (*i.e.*, NC cores versus ligand matrix). We assume a constant Young's modulus for the iron oxide NC core (E_{NC}=163 GPa)[64] and utilize Halpin-Tsai theory[65] to derive the modulus of the ligand matrix (E_m, Section III in Supporting Information). The resulting average Young's modulus of the OA ligand matrix is ~0.3 GPa and ~1.8 GPa for non-crosslinked and crosslinked ligand matrices, respectively.

Figure 3.5d shows that the thermal conductivity of non-crosslinked NC solids is linearly proportional to the average speed of sound in the NC solid. We calculated the average sound speed (one longitudinal and two transversal polarizations) of NC solids using the Young's moduli from nanoindentations, densities from X-ray reflectivity

measurements, and an assumed Poisson ratio of 0.3 (Table 3.1, 3.2).[66] Plotting these average sound speeds against NC thermal conductivity reveals a linear proportionality (Figure 3.5d) that is in line with kinetic theory. Additional analysis shows that changes in heat capacity[67-69] and/or mean free path do not have meaningful impacts on thermal conductivity as the NC size is changed (see section 3.5 of this chapter). Hence we conclude that the thermal conductivity dependence on NC size for non-crosslinked samples is dominated by changes in sound velocity.

As the NC diameter is varied, the thermal conductivities of crosslinked NC solids exhibit an opposing dependence on average sound speed than that of non-crosslinked NC solids (Figure 3.5d). Rather than increasing linearly with average sound speed, the thermal conductivity of crosslinked NC solids decreases linearly with average sound speed. Kinetic theory predicts a linear proportionality of thermal conductivity to sound speed, volumetric heat capacity, and carrier mean free path. Consequently, this trend in thermal conductivity with sound velocity can only be explained if changes in volumetric heat capacity and/or carrier mean free path are overpowering changes in sound velocity. As mentioned earlier, changes in volumetric heat capacity are negligible as the NC diameter is varied (see section 3.5 of this chapter). This indicates that changes in average sound speed are being overpowered by changes in mean free path when it comes to the thermal conductivity of crosslinked NC solids. In short, we conclude that the thermal conductivity of non-crosslinked NC solids is dictated by the speed of sound whereas the thermal conductivity of crosslinked NC solids is dictated by mean free path.

We further calculate the average sound speed for the ligand matrix using the modulus derived from the Halpin-Tsai model and the density estimated from geometric modeling and our XRR data (see section 3.5 of this chapter). The average sound speed of the ligand matrix is calculated to increase from ~600 to ~1700 m/s for non-

crosslinked and crosslinked nanocrystal solids, respectively (Table 3.3). This indicates that acoustic vibrations travel ~2.8x faster within the crosslinked ligand matrix and naturally leads to a thermal conductivity increase.

In order to interpret the effect of the individual NC solid components on the overall NC solid thermal conductivity, we use effective medium approximation (EMA) modeling to fit our thermal conductivity data (Figure 3.4d). Thermal interface conductance is an important parameter when modeling the thermal conductivity of nanocomposites and so we use an EMA model[30] that explicitly accounts for this parameter. The overall NC solid thermal conductivity is then a function of the thermal conductivity of the NC core (k_{NC}), thermal conductivity of the ligand matrix (k_m), volume fraction of the NC cores (V_{NC}), radius of the NC core (a), and the core-ligand interface thermal conductance (G). For non-crosslinked OA-capped iron oxide NC solids, we set k_{NC} and k_m to 7 $Wm^{-1}K^{-1}$ and 0.13 $Wm^{-1}K^{-1}$ as based on literature values. We utilize the interparticle distance, L, of 1.0 nm from our TEM and XRR data to determine our model input for V_{NC}. We vary G to fit our experimental data and find that find that 400 $MWm^{-2}K^{-1}$ yields good agreement (Figure 3.4d).

To fit our thermal conductivity on crosslinked NC solids, we use the same k_{NC} and G values as the non-crosslinked NC solids. We use these same values because the NC core is unchanged by the crosslinking process. We acknowledge that in reality G might change slightly after annealing due to possible carboxylate binding states change upon annealing (See Supporting Information and Figure 3.10). However, we expect any changes in G to be small as this possible carboxylate binding states change doesn't alternate their covalent bond nature. Additional EMA analysis on crosslinked NC solids also points to k_m rather than G as the dominate contributor to enhanced thermal transport (See section 3.5 of this chapter and Figure 3.20). We change L from 1.0 to 0.4 nm in accordance with our materials characterization data and analysis. The

crosslinking process also changes the intrinsic properties of the ligand matrix itself, and so we change k_m from 0.13 to 0.37 $Wm^{-1}K^{-1}$. This change in k_m was chosen in accordance with the ~2.8x change in ligand sound velocity for non-crosslinked and crosslinked ligands mentioned earlier, and the linear proportionality between thermal conductivity and sound velocity dictated by kinetic theory. Figure 3.4d shows that these rational and simple changes to the EMA model inputs yield reasonable agreement with our experimental thermal conductivity data on crosslinked NC solids for all diameters.

Our EMA model allows us to decouple the effects of ligand crosslinking and partial ligand desorption on thermal conductivity that both occur during the annealing process. These effects manifest themselves in the EMA model as an increase in k_m and a decrease in L, respectively. Figure 3.6a shows the relative effects of increasing k_m and decreasing L on NC solid thermal conductivity while all other EMA model parameters remain fixed. The steepness of the k_m curve versus the L curve in Figure 3.6a indicate that the overall thermal conductivity of the NC solid is much more sensitive to k_m. Additional EMA analyses are shown in the Supporting Information (Figures 3.18 and 3.19a). Based on these EMA analyses, we estimate for 7.9 nm NC solids that changes in k_m and L account for 76% and 24% of the total change in thermal conductivity induced by annealing, respectively. These number change slightly as the NC size increases, and for 20 nm NC solids, we estimate that changes in k_m and L account for 85% and 15% of the total change in thermal conductivity, respectively. Compellingly, these EMA predictions are in reasonable agreement with our experimental data on iron oxide NCs with OA and SA ligands (Figure 3.4c). As discussed earlier, that experimental data indicated that ligand crosslinking and ligand desorption (i.e., changes in k_m and L) account for 87% and 13% of the total change in thermal conductivity, respectively. Consequently, we conclude that ligand

crosslinking (and a corresponding change in k_m) is the dominant contributor to the thermal conductivity increase from annealing.

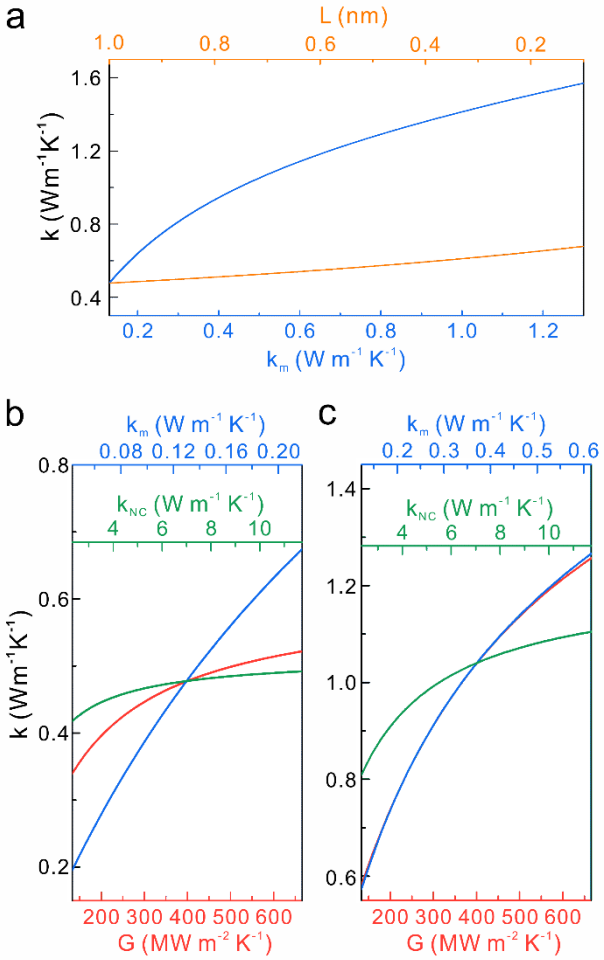

Figure 3.6 Sensitivity analysis on the effective medium approximation (EMA) model for NC solids with NC cores of 12 nm diameter. (a) EMA sensitivity towards k_m (blue) and L (orange). In both curves we hold k_{NC} and G fixed at 7 $Wm^{-1}K^{-1}$ and 400 MW $m^{-2}K^{-1}$, respectively. We hold L fixed at 1 nm while varying k_m and we hold k_m fixed at 0.13 $Wm^{-1}K^{-1}$ while varying L. EMA sensitivity analysis for a NC solid (b) before and (c) after annealing towards three independent parameters: k_{NC} (green), G (red), and k_m (blue). Unless a parameter is explicitly varied in part (b), we hold L, k_{NC}, k_m, and G fixed at 1.0 nm, 7 $Wm^{-1}K^{-1}$, 0.13 $Wm^{-1}K^{-1}$ and 400 $MWm^{-2}K^{-1}$, respectively. Unless a

parameter is explicitly varied in part (c), we hold *L*, k_{NC}, k_m, and *G* fixed at 0.4 nm, 7 $Wm^{-1}K^{-1}$, 0.37 $Wm^{-1}K^{-1}$ and 400 $MWm^{-2}K^{-1}$, respectively.

While prior work demonstrated that overall thermal transport was dominated by ligand matrix thermal conductivity, our data on crosslinked NC solids show that this is no longer the case. Figure 3.6b shows an EMA sensitivity analysis on a non-crosslinked 12 nm NC solid for varying k_m, G, and k_{NC}. The center point on the figure indicates the nominal values for each of these parameters and the corresponding thermal conductivity of the NC solid. Each input parameter is then varied by a factor of 5 while keeping the other parameters constant. Figure 3.6b clearly shows that varying k_m leads to the largest changes in overall thermal conductivity and that the effects of varying k_{NC} and/or G are much smaller. This is true for other NC sizes as well (Figure 3.19b-g) and indicates that the k_m is the bottleneck in thermal transport for non-crosslinked NC solids. This result agrees with prior work. Figure 3.6c shows a similar sensitivity analysis, but instead considers crosslinked samples. In this case, the effects of varying G and k_m are nearly identical. Consequently, meaningful increases in thermal conductivity should be achievable by either increasing the interface conductance at the NC-ligand interface or by increasing the ligand matrix thermal conductivity itself. Interestingly, Figure 3.6c also shows that changing k_{NC} could now lead to detectable changes in overall thermal conductivity (whereas changing this parameter in non-crosslinked NC solids has a near-negligible effect). These trends also hold for other NC sizes (Figures 3.19b-g).

While prior work demonstrated that overall thermal transport was dominated by ligand matrix thermal conductivity, our data on crosslinked NC solids show that this is no longer the case. Figure 5b shows an EMA sensitivity analysis on a non-crosslinked 12 nm NC solid for varying k_m, G, and k_{NC}. The center point on the figure indicates the nominal values for each of these parameters and the corresponding thermal

conductivity of the NC solid. Each input parameter is then varied by a factor of 5 while keeping the other parameters constant. Figure 3.6b clearly shows that varying k_m leads to the largest changes in overall thermal conductivity and that the effects of varying k_{NC} and/or G are much smaller. This is true for other NC sizes as well (Figure 3.19b-g) and indicates that the k_m is the bottleneck in thermal transport for non-crosslinked NC solids. This result agrees with prior work. Figure 3.6c shows a similar sensitivity analysis, but instead considers crosslinked samples. In this case, the effects of varying G and k_m are nearly identical. Consequently, meaningful increases in thermal conductivity should be achievable by either increasing the interface conductance at the NC-ligand interface or by increasing the ligand matrix thermal conductivity itself. Interestingly, Figure 3.6c also shows that changing k_{NC} could now lead to detectable changes in overall thermal conductivity (whereas changing this parameter in non-crosslinked NC solids has a near-negligible effect). These trends also hold for other NC sizes (Figures 3.19b-g).

Lastly, we performed molecular dynamics (MD) simulations on two simplified models of NC solids to investigate the effect of crosslinking (Supporting Information). This analysis shows that given the same steady state heat flux, the magnitude of the temperature gradient in the NC solid with vdW ligand interactions is much greater than the NC solid with a covalent bond between ligands (Figure 3.21). This indicates that the NC solid with covalent bonding has a higher thermal conductivity. We next focused on the temperature distribution along a single NC pair and the ligand molecules between them (Figure 3.22). In the vdW ligand interactions, there is a sharp drop in temperature at the ligand-ligand interface. This indicates that the ligand-ligand interface is the thermal transport bottleneck and is in agreement with the findings of our prior work. After exchanging the vdW interaction with a covalent bond, the temperature drop across the ligand-ligand interface substantially diminishes, which is

indicative of a large increase in thermal conductivity of the NC solid. These MD simulations corroborate our earlier conclusions that ligand crosslinking substantially increases thermal conductivity.

3.4 Conclusion

We used a combination of materials characterization, thermal transport measurements, mechanical measurements, and modeling to show that ligand crosslinking significantly increases thermal transport in colloidal NC solids. This work also demonstrates thermal transport in non-crosslinked NC solids is primarily controlled by the speed of sound, whereas thermal transport in crosslinked NC solids is primarily controlled by the mean free path of acoustic vibrations. This work sheds light on ligand design for thermal transport in NC solids. This will in turn play an important role in NC solid devices where thermal transport can crucially effect device performance and lifetime (*e.g.*, electronics, optoelectronics, and photovoltaics). Future studies on additional crosslinking chemistries to boost thermal transport would also be interesting. For example, molecular crosslinking can be achieved via non-thermal means such as exposure to UV light[70]. These approaches could greatly expand the applicability of ligand crosslinking to systems beyond the iron oxide - OA ligand system studied in this work.

3.5 Method and Supporting Information

3.5.1 Materials Synthesis and Characterization

3.5.1.1 *Nanocrystal synthesis*

Iron oxide NCs with 20 + 2.0 nm diameter and oleic acid (OA) ligands were synthesized using the following recipe. 0.62 g FeO(OH) (0.00695 mol), 14.7 g OA (0.052 mol) and 25 g 1-octadecene were mixed in a 50 ml flask and degassed for 0.5 h. The mixture was then gradually heated in a nitrogen environment to 320 °C and

kept at this temperature for 2 hours. The resulting particles were then precipitated by adding acetone, centrifuged, and stored in toluene. In this synthesis, nucleation and growth of iron oxide NCs is strongly affected by the starting ligand concentration. Consequently we varied the molar ratio of OA to FeO(OH) to obtain monodisperse NCs with diameters ranging from 7.9 - 20 nm (Figure 3.7). For syntheses of iron oxide NCs with stearic acid (SA) ligands, SA was substituted for OA during the synthesis procedure. Monodisperse nanocrystals of varying size were obtained by varying the molar ratio of SA to FeO(OH). Specifically, for 15 nm NC synthesis, the molar ratio of SA to FeO(OH) is 4:1.

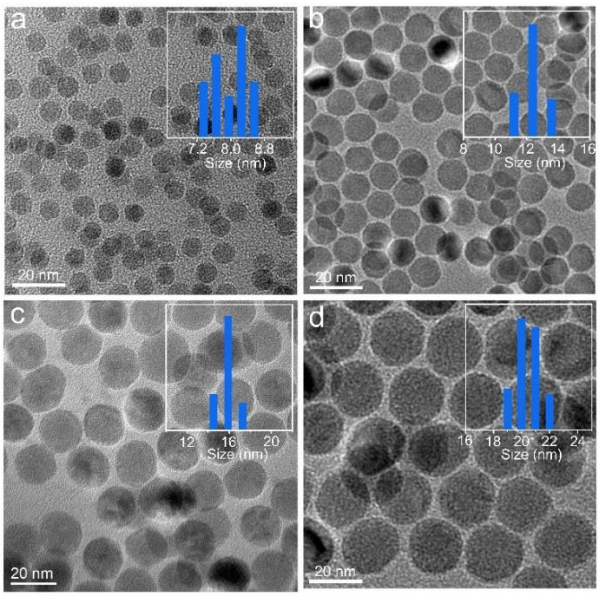

Figure 3.7 TEM images of monodisperse iron oxide NCs with OA ligands and with varying diameters: (a) 7.9 $\pm$ 0.6 nm, (b) 12 $\pm$ 1.2 nm, (c) 16 $\pm$ 1.4 nm, (d) 20 $\pm$ 2.0 nm. The insets in parts a-d show histograms of the particle size distribution in each image.

3.5.1.2 ***NC thin film preparation***

NC solid thin films were prepared by spin-casting the NC solid solution onto ~1 x ~1 cm silicon substrate inside a nitrogen-filled glovebox. The NC concentration in the solution was ~100 mg/mL. In a typical film preparation, 45 μL of iron oxide NC solution was deposited onto the silicon substrate and then spun at 1800 RPM for 25 s. After spin-coating, the substrate was covered by a petri-dish to slow the evaporation rate. After evaporation, all samples were annealed at 150 °C in a nitrogen atmosphere for 30 minutes to drive off any residual solvent. For crosslinked samples, an additional annealing step at 350 °C for 30 minutes was then conducted.

NC solid thin films prepared in this manner result in locally ordered nanocrystal assemblies (Figures 3.2a-c in the main text). NC ordering in these films were also inspected via TEM by scratching the film from the substrate, crushing it into a small powder in solvent, and then drop-cast onto a carbon-coated TEM grid. TEM images of these samples (Figure 3.8) further illustrate that NCs exhibited a locally well-ordered structure in the spin-coated samples.

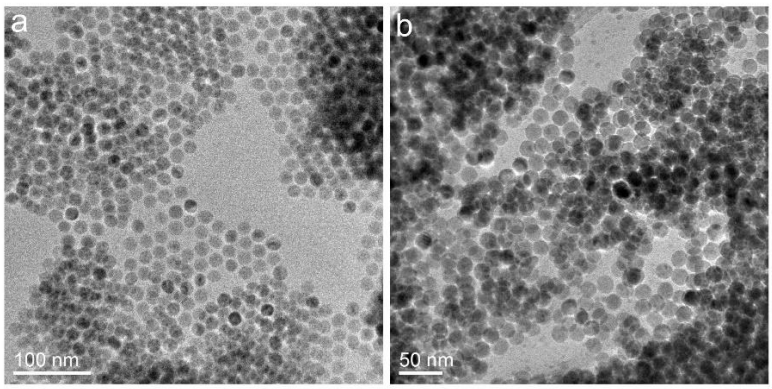

Figure 3.8 TEM image of (a) non-crosslinked and (b) crosslinked NC solid fragments extracted from a spin-coated NC solid thin film. These images demonstrate the high degree of local ordering in these NC structures.

3.5.1.3 ***Materials characterization***

Transmission Electron Microscopy (TEM) and Scanning Electron Microscopy (SEM): Iron oxide NC morphology and size were characterized using a FEI CM-200 TEM operated at 120 kV. This same TEM instrument was also used for HRTEM on samples before and after annealing (crosslinking). To conduct HRTEM, the NC solid film was scratched from the substrate, crushed into a small powder in solvent, and then drop-cast onto a carbon-coated TEM grid. The micro-morphology of the NC solid thin films was characterized using a FEI XL-30 SEM. Profilometry: NC solid film thickness was determined by scratching the film and then conducting profilometry using a Bruker XT profilometer.

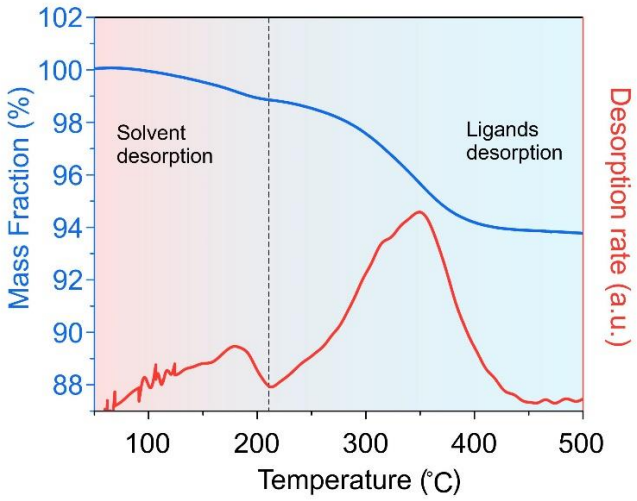

Figure 3.9 (a) Thermogravimetric analysis (TGA) of NC solids consisting of 20 nm diameter iron oxide NCs with surface capped OA ligands.

X-ray Photoelectron Spectroscopy (XPS): XPS measurements were carried out in a VG 220i-XL instrument with a monochromated Al K-alpha X-ray as the source. The analysis was done in an ultra-high vacuum system (10^{-9} Torr). Figure 3.3c in the main text shows the high-resolution XPS scan of the Fe2p region. This region features two

separate peaks at 709 eV and 722.5 eV that correspond to Fe $2p_{3/2}$ and Fe $2p_{1/2}$, respectively. The annealing process does not induce any notable changes in these peaks, which suggests that the iron oxide NC cores are not affected by the annealing treatment. The absence of Fe $2p_{3/2}$ satellite peak also suggests that the iron oxide NC cores are in the magnetite phase. Figure 3.3d in the main text shows the high-resolution XPS scan of the O1s region. The strongest peak in this region is at 530.5 eV and corresponds to lattice oxygen in the iron oxide NC core. Another peak centered at 531.5 eV corresponds to the oxygen in carboxylate. The carboxylate peaks in the C1s and O1s regions remain generally unchanged by the annealing process and indicate that organic ligands remain on the NC surface.

Gas chromatography-mass spectrometry (GC-MS): GC-MS was used to characterize the ligand structure. Ligand samples were prepared via extraction from the NC surface using methanol. If needed, the resulting organic solution can be further concentrated by flowing nitrogen across the sample to evaporate excess solvent. For crosslinked samples, ~100 mg of iron oxide NC solid was heated to 350 ºC and kept at that temperature for 30 min. The crosslinked ligands were then extracted using methanol.

3.5.1.4 ***Thermogravimetric analysis***

Thermogravimetric Analysis (TGA)analysis was used to determine ligand capping density of our NC solids and was done using a Labsys Evo instrument. TGA samples were prepared in a nitrogen-filled glovebox by drop-casting the NC solution onto a pre-cleaned silicon substrate and then drying at room temperature for 48 h. The solidified composites were then scratched off the substrate and sealed in a vial inside the glovebox for transport to the TGA. During TGA, the sample was heated from room temperature to 500 ºC at a heating rate of 2 ºC min^{-1} in a helium atmosphere.

Figure 3.9a shows a typical TGA curve of the NC solids and two major steps are observed. The solid blue TGA curve for OA capped iron oxide NCs is consistent with the results reported by Dreyer *et al.* The first step occurs between room temperature and ~200 ºC. This step corresponds to a ~1% mass loss of the sample and we assign this step to desorption of residual solvent in the sample. The second step occurs between ~200 ºC and 450 ºC and corresponds to a ~5% mass loss of the sample. As described by Dreyer *et al.,*[43] we assign the mass loss throughout the ~200-450 ºC region to desorption of OA ligands. We do not observe any additional mass loss between 450 and 500 ºC, which indicates that all of the OA has desorbed by ~ 450 ºC.

The ligand capping density on the NCs can be calculated by combining the TGA data with our known NC core diameter, NC core chemical composition, and ligand chemical composition. For example, in the analysis of the non-crosslinked 20 nm NCs, the OA mass fraction (i.e. mass loss between 200 ºC and 450 ºC) and Fe_3O_4 mass fraction is determined to be 5.32% and 94.68%, respectively. This OA mass fraction can be converted into the number of OA molecules (N_{OA}) via the molecular weight (282.47 g mol^{-1}) and Avogadro's number. Similarly, the Fe_3O_4 mass fraction can be converted into volume fraction via the Fe_3O_4 density (5.17 g cm^{-3}). This volume fraction is then converted into surface area (S_{NC}) using the known NC diameter. Finally, the OA ligand capping density (ρ_{OA}) is calculated as N_{OA}/S_{NC}. Based on this approximation, ρ_{OA} was determined to be 2 nm^{-2} and 0.8 nm^{-2} for OA capped Fe_3O_4 NC solids before and after annealing, respectively. This capping density of 2 nm^{-2} for pristine NC solids is in line with the reported results for 16 nm iron oxide NC.[43]

Our crosslinking process of OA ligands consists of a sample anneal at 350 ºC. Consequently, if we partition the 5.32% mass loss into two separate regions (i.e. 200

– 350 ºC and 350 - 450 ºC), we can estimate the amount mass fraction of OA ligands that crosslink. Using this analysis, we estimate that during the crosslinking process, 3.20% of the mass is lost in the form of desorbed weakly bound OA (i.e. the 200 – 350 ºC region) and 2.12% of the OA remains on the NC surface. We hypothesize that the OA remaining on the surface comes in two forms: (i) crosslinked OA and (ii) strongly bound OA ligands that aren't crosslinked (*i.e.,* as described in Section IIIc, physical tethering to the NC surface and proximity to other OA ligands can likely cause some OA ligands to not crosslink).

3.5.1.5 ***X-ray reflectivity measurements***

X-ray Reflectivity Measurements: XRR measurements were used to determine the mass density of the NC solid, $\rho_{NCsolid}$, and the interparticle spacing, *L*. XRR measurements were carried out using a PANalytical X-ray diffractometer, fitted with an x-ray mirror using a 1/32° slit and a parallel plate collimator. XRR measures the electron density of the sample and this information can then be converted into mass density when combined with the sample's elemental ratio (Fe:O:C:H). The elemental ratio used for these calculations were determined via the TGA measurements.

The interparticle spacing was determined using the mass density output of the XRR measurements using the following equation:

$$\frac{\frac{4}{3}\pi\left(a+\frac{L}{2}\right)^3\rho_{NCsolid}}{\eta}=\frac{4}{3}\pi a^3\rho_{Fe_3O_4}+m_{ligand}$$

where *a* is the NC radius, ρ_{Fe3O4} is the mass density of Fe_3O_4 phase, and m_{ligand} is the ligand mass per NC. Additionally, η is the volume fraction of the close-packed spheres in a face-centered lattice (0.74). This assumption of close-packed spheres is reasonable based on the SEM and TEM images of the NC solids. Combining XRR and

TEM with a geometric model, we calculated L decreased from ~1nm to ~0.4 nm after annealing at 350 °C.

3.5.1.6 *Fourier-transform infrared spectroscopy*

Fourier-transform infrared spectroscopy was utilized to characterize the carboxylate binding states change before and after annealing at 350 ºC. A commercial Thermo Nicolet 6700 FTIR system was used.

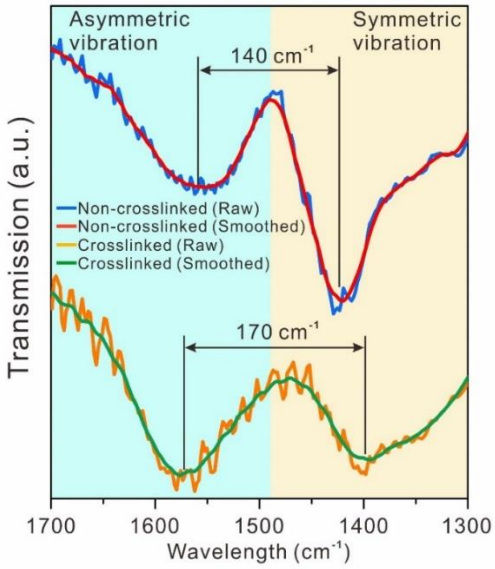

Figure 3.10 Raw and smoothed FTIR spectra of non-crosslinked and crosslinked OA capped iron oxide nanocrystal solids.

As was reported by Deacon et al.[71] that the type of interaction between the carboxylate head and the metal atoms can be categorized by the wavenumber separation Δ, between the asymmetric ϑ_{as}(COO$^-$) stretch vibrations and symmetric ϑ_s (COO$^-$) stretch vibrations IR bands into four types: 1, Δ (200-320 cm^{-1}) monodentate; 2, Δ (140-190 cm^{-1}) bridging bidentate; 3, Δ (110-140 cm^{-1}) bridging and/or chelating bidentate; 4, Δ (<110 cm^{-1}) chelating bidentate; 5, ionic bonding. According to Figure 3.10, Δ was determined to be 140 cm^{-1} and 170 cm^{-1} for non-

crosslinked and crosslinked iron oxide nanocrystal solids, respectively. The shift of Δ upon ligands crosslinking might suggest minor carboxylate binding state change from chelating bidentate to bridging bidentate. Nonetheless, the possible carboxylate binding states change doesn't alternate its covalent bond nature, thus theoretically leads to little change in its thermal interface conductance.

3.5.1.7 ***Nanocrystal with SA ligands***

Annealing the NC solids with oleic acid in this work leads to two effects, partial ligand desorption and ligand crosslinking, both of which can increase thermal conductivity. In order to experimentally confirm that ligand crosslinking is the dominant origin of increased thermal conductivity, we performed control experiments using iron oxide NCs with stearic acid (SA) ligands. SA is chemically identical to oleic acid (OA), except that it lacks the C=C double bond in its carbon backbone, which means that SA ligands cannot crosslink. Like OA ligands, SA ligands partially desorb from the annealing process. Consequently, we use OA ligands to infer the effects of combined ligand crosslinking and partial ligand desorption, whereas we use SA ligands to infer the effects of partial ligand desorption only. The effect of ligand crosslinking only can be inferred via the difference between the OA ligand and SA ligand cases.

Figure 3.11 compiles a range of materials characterization experiments on NC solids with SA ligands. These characterizations confirm that SA-capped NCs behave like OA-capped NCs, except for their inability to crosslink. TEM and SEM characterizations show that iron oxide NCs with SA ligands are monodisperse and form compact ordered assemblies (Figures 3.11b, c, and d). Figure 3.11c is a TEM image after annealing the SA-capped NCs, and demonstrates that no NC sintering occurs from the annealing process. Figure 3.11e shows TGA data for NCs with SA ligands and a two-step desorption process that is similar to NCs with OA ligands. We attribute the

first mass loss of ~1.5% between room temperature and 200 ºC to desorption of residual solvent. The second mass loss occurs between 200 and ~450 ºC. This mass loss is ~11% and we attribute it to desorption of SA ligands. Combining this data with a geometric model as in the OA case, we determine the SA ligand capping density (ρ_{SA}) to be 3.4 nm^{-2} and 1.1 nm^{-2} for SA capped Fe_3O_4 NC solids before and after annealing at 350 °C, respectively.

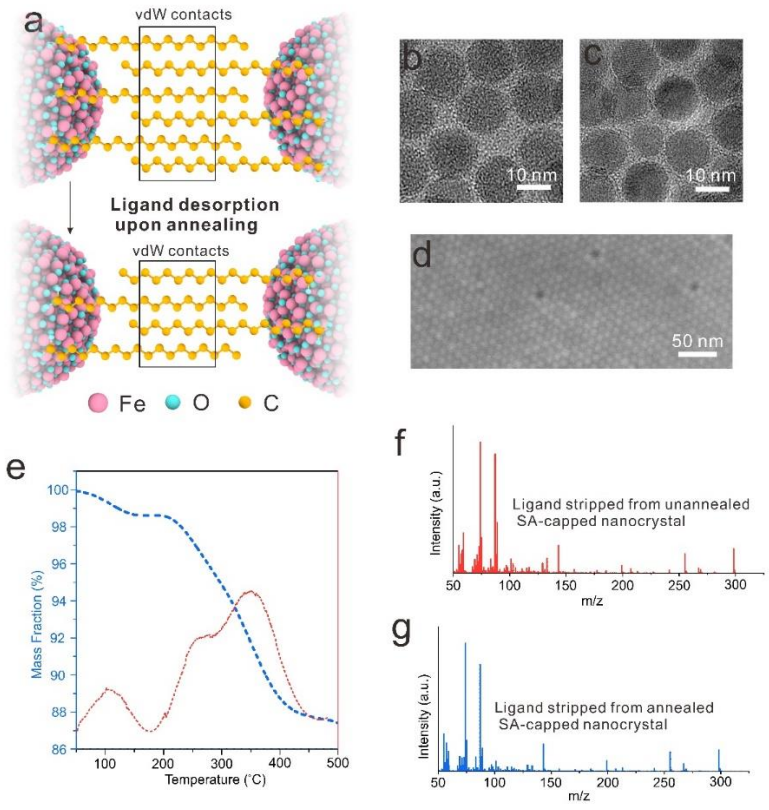

Figure 3.11 Materials characterization on iron oxide nanocrystals (NCs) with stearic acid (SA) ligands both before and after annealing. (a) Schematic illustrations of ligand structure for SA-capped iron oxide NCs before and after annealing (hydrogen atoms are omitted for improved clarity). Annealing results in partial ligand desorption, but no ligand crosslinking occurs; TEM images of SA-capped iron oxide NCs (b) before and (c) after annealing at 350 °C show no sintering; (d) monodispersed SA-capped iron

oxide NCs shows a similar close-packed arrangement as OA-capped iron oxide NCs; (e) Thermogravimetric analysis of NC solids consisting of 15 nm diameter iron oxide NCs with surface capped SA ligands; mass-spectra of organic components extracted from SA-capped iron oxide NCs (f) before and (g) after annealing at 350 °C verifies the absence of crosslinking for SA ligands.

We note that the initial SA capping density of 3.1 nm^{-2} is higher than that of OA. This likely occurs because SA is a saturated hydrocarbon chain that tends to form ordered ligand assemblies and facilitates ligand interdigitation (*i.e.*, the C=C double bond in OA leads to a kink in the ligand backbone that inhibits ligand ordering and interdigitation). Analogously to the OA case discussed earlier, we partition the temperature region of the second mass loss for SA capped NCs into two regions (i.e. temperatures below 350 °C and above 350 °C). Using this analysis, we estimate that for SA capped iron oxide NCs annealed at 350 °C, 7% of the mass is lost in form of desorbed weakly bound SA and 4% of the mass remains on the surface in form of strongly bound SA ligands. GC-MS analysis on the organics extracted from these nanocrystals before and after annealing confirm that no ligand crosslinking occurs for SA ligands (Figure 3.11f and g). Unlike the OA-case, the mass spectra before and after annealing are identical. Furthermore, no large *m/z* molecular fragments consistent with crosslinking are observed.

3.5.2 **3ω Thermal Conductivity Measurements**

3.5.2.1 ***Basic principle and experimental setup***

The 3ω method[57, 58] is widely-used for determining the thermal conductivity of thin film and bulk samples and was used in this study. Measuring thermal conductivity essentially boils down to applying a known heat flux and measuring the corresponding temperature gradient. In the 3ω method, a narrow metal line is patterned on top of

the sample and this metal line functions as both a Joule heater and a resistive thermometer. A thorough description of our lab's implementation of the 3ω technique along with benchmark control measurements on six different materials with thermal conductivities ranging from ~0.15 – 150 W/m-K is provided in our prior publication. We have also used this technique in several other works as well.[72-75]

3.5.2.2 *NC thin film sample preparation*

To prepare the NC solid thin films for measurement, a dielectric layer of SiO_2 of ~ 150 nm was first deposited on top of the samples via magnetron sputtering. An Au heater line of 5 μm width, 800 μm length, and 80 nm thickness was then deposited using standard photolithography techniques. In accordance with the differential 3ω thermal conductivity measurement technique, an identical reference sample (but without the NC solid thin film) was prepared alongside the experimental samples. This reference sample allows the temperature drop across the NC solid thin film to be isolated and the corresponding thermal conductivity to be calculated.

NC solid thin films used for thermal conductivity measurements were typically 150 – 400 nm thick. We also varied film thickness outside of this range and did not observe any variations in thermal conductivity (see Figure 3.23). This lack of a variability is expected since thermal conductivity is an intrinsic property. It also indicates that thermal transport in these samples is diffusive and that our measurements are not affected by thermal contact resistances to the NC solid thin films.

3.5.2.3 *Temperature coefficient of resistance (TCR)*

The TCR of the 3ω metal line, β, is needed to convert the voltage signal of the metal line into a temperature signal. TCR is defined as:

$$\beta = \frac{1}{R_0}\frac{dR}{dT}$$

where R_0 is the resistance of the heater line at room temperature. TCR is a measure of change in resistance with changing temperature and was measured using a home-built measurement setup. Sample temperature was controlled with a thermoelectric device sandwiched in between a copper sample holder and aluminum heat sink. TCR was determined by measuring the 4-point electric resistance of the heater line at 7 different temperatures from 20°C to 50°C. A linear fit was used for determining dR/dT. Figure 3.12 shows representative data of the TCR measurement.

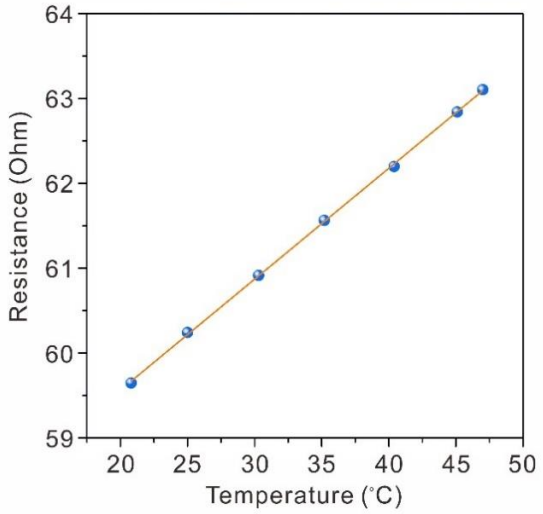

Figure 3.12 4-point electrical resistance of the 3ω metal line as a function of temperature. This curve is used to determine the temperature coefficient of the 3ω metal line and convert the 3ω voltage signal into a temperature signal.

3.5.2.4 ***Data analysis***

We used the differential 3ω method[56] to determine the thermal conductivity of the NC solid thin films. This technique requires parallel preparation of the sample of interest (i.e. the NC solid thin film) and a reference sample. The reference sample is prepared is identically to the sample of interest, except that a NC solid thin film is never deposited on the reference sample. The temperature drop of the NC solid film,

ΔT_f, was then determined by comparing the actual experimental sample to the reference sample.

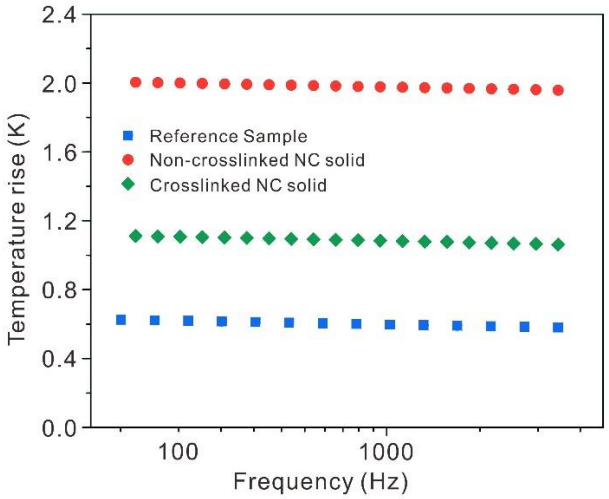

Figure 3.13 Representative data collected from the differential 3ω method. The temperature drop across the NC solid film is the difference in temperature rise between the experimental sample and the reference sample.

Figure 3.13 shows representative data from the reference sample, non-crosslinked experimental sample, and crosslinked experimental sample. Since the NC solid film thickness (~200 nm) is much less than the width of the 3ω line (~5 μm), heat conduction along the thin film can be approximated as 1-dimensional. The thermal conductivity of the NC solid film, k_f, is then calculated as:

$$k_f = \frac{Pt_f}{wl\Delta T_f}$$

where P is the excitation power of heater line, t_f is the NC solid thin film thickness, w is the heater line width, and l is the heater line length.

3.5.3 **Mechanical Measurements and Analysis**

3.5.3.1 ***Nanoindentation***

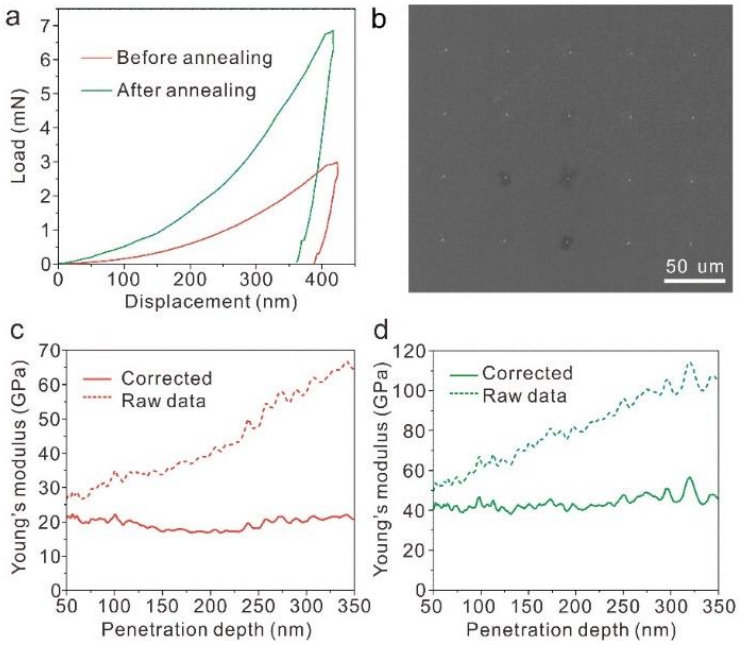

Figure 3.14 Nanoindentation characterizations on iron oxide NC solids film before and after annealing (i.e. non-crosslinked and crosslinked, respectively). (a) Representative nanoindentation curves of the loading and unloading of indents on 16 nm iron oxide NC solids before and after annealing; (b) SEM image of a 4×5 indents pattern made on the surface of iron oxide NC solids film; Representative Young's modulus as a function of displacement on 16 nm iron oxide NC solids for (c) before and (d) after annealing with raw data and data corrected for substrate effects.

Young's modulus of the NC solid film is evaluated using nanoindentation. A commercial nanoindenter system (Nanoindenter XP-II, Agilent) equipped with a diamond Berkovich tip is utilized to perform the test. The tip area function was first calibrated using a standard silica sample. Then nanoindentation was carried out on the film surface to an indentation depth of 400 nm. Tests were conducted in strain rate

control mode (0.05 s^{-1}). Our experiments were conducted using the continuous stiffness measurement technique, which enabled an accurate measurement of instantaneous contact stiffness, with increasing indentation depth, by superimposing a small harmonic force on the applied load.[37] 20 indents (4 x 5 array, Figure 3.14b) were made to get an average Young's modulus of each NC solid film. Figure 3.14a shows a representative load-displacement curve for the loading and unloading of indents on the thin film with 16 nm diameter NCs. The maximum loads obtained are quite different between the non-crosslinked and crosslinked NC solids, which indicate a difference in hardness. Young's modulus, *E*, can also be inferred from this load-displacement curve. The modulus calculated based on the conventional Oliver-Pharr method (dash line in Figure 3.14c, d) increased with the indentation depth, which is due to the effect of the stiffer and harder Si substrate. We corrected the modulus data using Hay's model[62] to deduct the substrate effect. The corrected modulus is shown as the solid line in Figure 3.14c, d, which exhibits a plateau for indentation depths exceeding ~50 nm.

The modulus of crosslinked 16 nm diameter iron oxide NCs has been measured by Dreyer *et al.*[43] and provides a useful reference point to our measurements; we measured a value of 40 GPa whereas they measured 57.5 GPa. This difference in mechanical properties can likely be attributed to the difference in the domain size of the NC ordering between their samples and our samples. The samples in Dreyer *et al.*[43] consisted of large domains in a three-dimensional supercrystal whereas the domain sizes in our thin film samples are comparatively smaller. Similar mechanical property dependencies on NC assembly domain size has been previously reported by Podsiadlo *et al*.[38] for CdSe NCs. The Young's modulus in their NC superlattices was twice as large as the Young's modulus in their NC films.

Table 3.1 Properties of Non-Crosslinked NC Solids

NC size (nm)	Young's Modulus (GPa)	Density (gcm^{-3})	Longitudinal sound speed (m/s)	Transversal sound speed (m/s)	Average sound speed (m/s)	Thermal conductivity (W/mK)
7.9+0.6	5.75±0.43	3.04	1590±60	850±30	1100±40	0.42±0.08
12+1.2	14.5±2.8	3.28	2400±230	1300±120	1680±160	0.53±0.08
16+1.4	18.5±4.7	3.41	2700±350	1430±190	1840±240	0.57±0.09
20+2.0	22.5±0.67	3.49	2950±50	1600±30	2030±30	0.64±0.11

We calculated the average sound velocity (v_s) using the following equations[66]:

$$v_L = \sqrt{\frac{E}{\rho}\left[\frac{(1-\sigma)}{(1+\sigma)(1-2\sigma)}\right]}$$

$$v_T = \sqrt{\frac{E}{2\rho(1+\sigma)}}$$

$$v_s = \frac{v_L + 2v_T}{3}$$

Where:

v_L: longitudinal sound speed

v_T: transversal sound speed

E: Young's modulus of NC solid

ρ: density of NC solid

σ: Poisson ratio (a universal Poisson ratio of 0.3 is used)

Table 3.2 Properties of Crosslinked NC Solids

NC size (nm)	Young's Modulus (GPa)	Density (gcm^{-3})	Longitudinal sound speed (m/s)	Transversal sound speed (m/s)	Average sound speed (m/s)	Thermal conductivity (W/mK)
7.9+0.6	50.5±2.9	3.44	4410±240	2360±70	3040±90	0.81±0.13
12+1.2	42.8±2.7	3.59	4060±290	2170±70	2800±90	0.88±0.13
16+1.4	40±3.4	3.65	3830±160	2050±90	2640±110	1.1±0.18
20+2.0	36±3.4	3.68	3600±170	1900±100	2500±120	1.67±0.27

3.5.3.2 ***Mechanical properties of ligand matrix***

We use Halpin-Tsai theory[65], which is developed for polymer nanocomposites, to calculate the effective modulus of the OA ligand matrix in non-crosslinked and crosslinked iron oxide NC solids. Previous work on mechanical properties of NC solids has successfully applied this theoretical model to a variety of NC systems. In accordance with Halpin-Tsai composite theory, we use the following two equations used to calculate the modulus of the ligand matrix:

$$\frac{E}{E_m} = \frac{1 + \delta\eta\varphi_{NC}}{1 - \eta\varphi_{NC}}$$

$$\eta = \frac{\frac{E_{NC}}{E_m} - 1}{\frac{E_{NC}}{E_m} + \delta}$$

Where:

E: is the modulus of the NC solid composite

E_m: is the modulus of the ligand matrix

E_{NC}: is the modulus of the NC core

δ: is the shape parameter for spherical fillers ($\delta = 2 + 40 * \varphi_{NC}$)

φ_{NC}: is the volume fraction of the NC cores

Halpin-Tsai theory also allows us to independently study the relative sensitivities of the NC solid's Young's modulus to E_m and E_{NC}. For non-crosslinked NC solids, varying E_m leads to large changes in overall NC solid Young's modulus while varying E_{NC} leads to much smaller changes (Figure 3.15a). Evidently the Young's modulus of non-crosslinked NC solids is dominated by E_m. However, after crosslinking, the overall Young's modulus is similarly sensitive to both E_{NC} and E_m (Figure 3.15b). For simplicity, we have utilized the average values of our measured E_m for the nominal values in the sensitivity analyses shown in Figures 3.15a and 3.15b (*i.e.*, 0.42 GPa and 1.53 GPa for non-crosslinked and crosslinked NC solids, respectively).

The density of the ligand matrix before and after annealing was estimated based on the following assumptions: (i) the NCs are arranged into a face-centered cubic structure with inter-particle spacings of 1.0 nm and 0.4 nm for non-crosslinked and crosslinked NC solids, respectively. (ii) the OA ligands are uniformly dispersed in the gap between the NCs. The ligand matrix density can then be derived using the following equation:

$$\rho_{ligand} = \frac{\varphi 16\pi a^2 \frac{M_{OA}}{N_A}}{\left(\frac{4a + 2L}{\sqrt{2}}\right)^3 - \frac{16\pi a^3}{3}}$$

where a is the NC radius, L is the interparticle spacing, φ is the OA capping density, M_{OA} and N_A are molecular weight of OA and Avogadro's number, respectively. We note

that the OA capping density was already determined to be 2 nm^{-2} and 0.8 nm^{-2} for non-crosslinked and crosslinked NC solids, respectively. Table 3.3 below shows the average sound velocity for the ligand matrix using the measurements and equations described above.

Table 3.3 Parameters of Non-Crosslinked and Crosslinked Ligand Matrices

	Non-Crosslinked Ligands			Crosslinked Ligands		
NC size (nm)	Young's modulus of ligand (GPa)	Density (gcm^{-3})	Average sound speed (m/s)	Young's modulus of ligand (GPa)	Density (gcm^{-3})	Average sound speed (m/s)
7.9+0.6	0.23	0.76	440	2.4	0.40	1960
12+1.2	0.45	0.65	660	1.5	0.38	1600
16+1.4	0.48	0.57	730	1.1	0.32	1500
20+2.0	0.5	0.52	780	1.1	0.26	1650

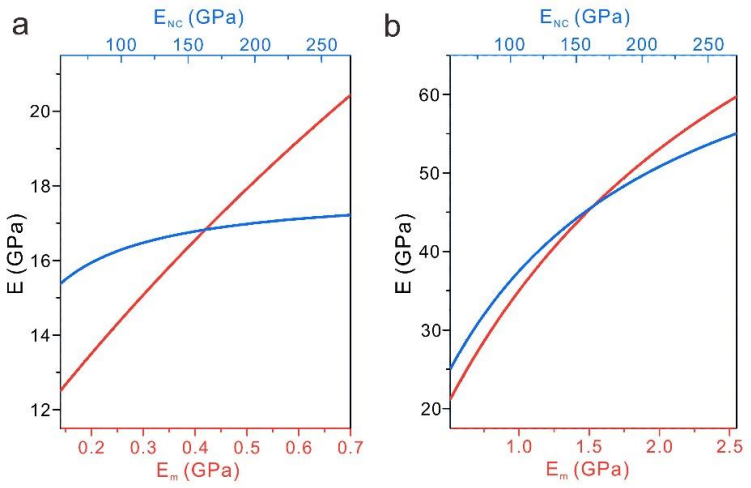

Figure 3.15 Sensitivity analysis on the Halpin-Tsai model for NCs solids with 12 nm diameter NC cores that have (a) non-crosslinked ligands and (b) crosslinked ligands.

The centerpoint on the x-axis indicates the nominal values for each of these parameters whereas the y-axis shows the corresponding Young's modulus of the NC solid. Each of these parameters are then varied by a factor of 5 which keeping the other parameters constant. Unless a parameter is explicitly varied in part (a), we hold E_{NC}, E_m, and L fixed at 163 GPa, 0.42 GPa, and 1 nm, respectively. Unless a parameter is explicitly varied in part (b), we hold E_{NC}, E_m, and L fixed at 163 GPa, 1.53 GPa, and 0.4 nm, respectively.

3.5.3.3 *Ligand crosslinking effectiveness*

Our mechanical analysis shows that the Young's modulus of the crosslinked ligand matrix increases as NC size is decreased (Table 3.3). We hypothesize that this trend arises due to variations in crosslinking effectiveness as the NC diameter is changed.

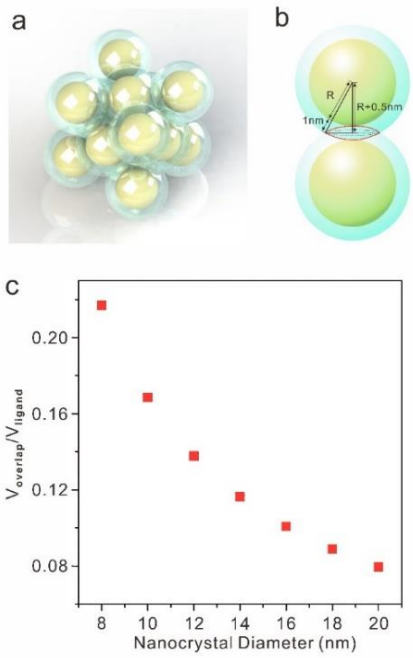

Figure 3.16 Ligand crosslinking effectiveness analysis based on a simple geometry model. (a) A schematic illustration of dense face-centered-cubic packing of NCs with an assumed 1 nm thick ligand shell. (b) The effective crosslinking volume ($V_{overlap}$) was

defined as the overlapping volume of two neighboring ligand shells; (c) The ratio of $V_{overlap}$ to the ligand shell volume (V_{ligand}) in a unit cell plotted as a function of NC core diameter.

In Figure 3.16, we illustrate a simple geometric model that possibly explains this trend. This model approximates each colloidal NC as a homogenous core (i.e., iron oxide) of arbitrary diameter with a homogenous shell (i.e., OA ligands) that is 1 nm thick. The overall NC solid is modeled as a densely packed face-centered-cubic lattice. In this lattice, we allow the ligand shells to overlap one another, but do not allow any overlap with the cores themselves (Figure 3.16b). We conjecture that the primary driving force for our observed change in thermal and mechanical properties is crosslinking in the regions of ligand overlap between adjacent NCs. This is because crosslinking in these regions lead to NCs connected together via strong covalent bonds. Figure 3.16c graphs the volume of overlapping ligand regions ($V_{overlap}$) divided by the total ligand shell volume (V_{ligand}). This graph shows that as the NC core size is decreased, the ratio of $V_{overlap}$ to V_{ligand} substantially increases. This should correlate to an increase in crosslinking effectiveness as the NC size is decreased and consequently a higher ligand matrix Young's modulus for smaller diameter NCs that are crosslinked.

3.5.4 Specific Heat Capacity and Mean Free Path

3.5.4.1 *Specific heat capacity of NC solids*

For non-crosslinked NC solids, the specific heat capacity of the iron oxide NC core[69] and the OA ligands[76] are reported to be 0.6534 J g^{-1} K^{-1} and 2.043 J g^{-1} K^{-1}, respectively. We assume these parameters to be constant regardless of NC core sizes. The gravimetric specific heat capacity (C_p) of the NC solids can then be calculated based on a simple mixture rule as shown in Table S4. These mass-based specific heat capacities are then converted into volumetric heat capacities by multiplying with

density. As is indicated in Table 3.4, the volumetric heat capacity of the non-crosslinked NC solids changes from 2.50 to 2.54 J cm^{-3} K^{-1} as the NC diameter is varied. This change is negligible.

Table 3.4 Volumetric Heat Capacity Estimation for Non-Crosslinked and Crosslinked NC Solids

NC Size (nm)	C_{core} (J g^{-1} K^{-1})	C_{ligand} (J g^{-1} K^{-1})	$C_{non\text{-}crosslinked}$ (J cm^{-3} K^{-1})	$C_{crosslinked}$ (J cm^{-3} K^{-1})
7.9+0.6	0.6534	2.043	2.50	2.45
12+1.2	0.6534	2.043	2.52	2.52
16+1.4	0.6534	2.043	2.53	2.52
20+2.0	0.6534	2.043	2.54	2.52

Note: Volumetric heat capacity (C_V) of NC solid is derived as the product of gravimetric specific heat capacity (C_p) and density (ρ). We estimate C_p as a function of the gravimetric specific heat capacities of the NC cores (C_{core}) and ligands (C_{ligand}), respectively, through the formula: $C_p = C_{core}m_{core} + C_{ligand}m_{ligand}$, where m_{core} and m_{ligand} are the mass fractions of the NC cores and ligands, respectively.

For crosslinked NC solids, we continue to use the 0.6534 J g^{-1} K^{-1} value for the gravimetric specific heat of the NC core as no discernable changes are observed in the XPS data. We further assume specific heat capacity of crosslinked OA to be the same as that of the non-crosslinked OA. We believe this assumption is reasonable because reports show that the specific heat capacity of normal alkanes reach a constant value once the number of carbon atoms exceeds 10.[67] In addition, the heat capacity of polymers do not vary with crosslinking.[68] We then calculate the volumetric heat

capacities for crosslinked NC solids as described above. These values are listed in Table 3.4. Changes in volumetric heat capacity for crosslinked NC solids as a function with NC diameter is also negligible.

3.5.4.2 ***Mean free path of acoustic vibrations***

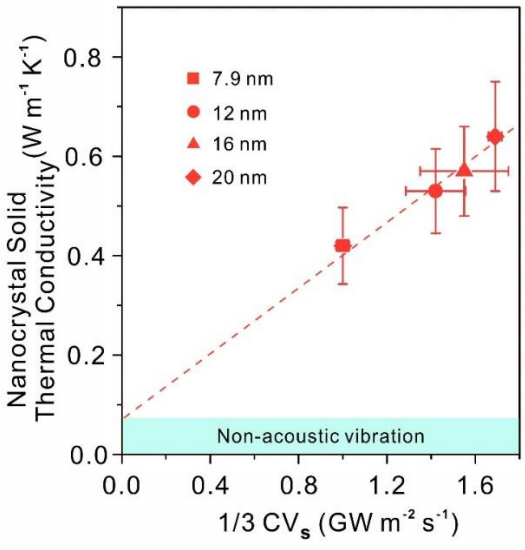

Figure 3.17 Thermal conductivities of non-crosslinked NC solids plotted against $(1/3)Cv_s$ where *C* is the volumetric heat capacity and v_s is the speed of sound. The fact that all of the data fall along a linear line indicates that the samples have a constant mean free path for acoustic vibrations. The slope of this line indicates that this mean free path is ~ 0.3 nm. Extrapolation of the linear fit to the y-intercept indicates a parallel contribution to thermal transport from non-acoustic vibrations.

Figure 3.17 shows the thermal conductivity of non-crosslinked NC solids plotted against the quantity $(1/3)Cv_s$ where *C* is the volumetric heat capacity and v_s is the speed of sound. Graphing the data in this manner mirrors the kinetic theory result for thermal conductivity, $k = (1/3)Cv_s\Lambda$, where Λ is the mean free path of acoustic vibrations. Figure 3.17 shows that the data fall along a line with constant slope. This

indicates that these samples all have an equivalent mean free path for acoustic vibrations (mean free path ~ 0.3nm). Extrapolation of this line to $(1/3)Cv_s = 0$ reveals a non-zero y-intercept. This indicates a parallel contribution to thermal transport in the NC solid that occurs from non-acoustic vibrations (*e.g.*, optical vibrations, diffusons, and/or locons) and that is equivalent to ~ 0.07 W m^{-1} K^{-1}. It is not surprising that these NC solids exhibit thermal transport from non-acoustic vibrations since they have a non-crystalline nature. The non-crystalline nature of the NC solids arises from many different sources. While the NC cores themselves are crystalline, the cores within the NC solid exhibit orientational disorder (*i.e.*, within the NC solid, the crystallographic axes of individual NC cores are pointed in random directions). The ligands on the NC surface are also not crystalline and impart additional disorder in the system. Lastly, there is some translational disorder in the system because the NCs have a finite size distribution.

3.5.5 **Effective Medium Approximation (EMA) Modeling**

We use the modified EMA model by Hasselman and Johnson[30] to model the thermal conductivity of our NC solids. The EMA model by Hasselman and Johnson explicitly accounts for the interface thermal conductance between the dispersed phase (NC cores) and continuous phase (ligand matrix), which is an important parameter in nanoscale heat conduction. This EMA model is given by the following expression:

$$k_{eff} = k_m \frac{\left[2\left(\frac{k_{NC}}{k_m} - \frac{k_{NC}}{aG} - 1\right)V_{NC} + \frac{k_{NC}}{k_m} + \frac{2k_{NC}}{aG} + 2\right]}{\left[\left(1 - \frac{k_{NC}}{k_m} + \frac{k_{NC}}{aG}\right)V_{NC} + \frac{k_{NC}}{k_m} + \frac{2k_{NC}}{aG} + 2\right]}$$

where k_m and k_{NC} corresponds to the thermal conductivity of the ligand matrix and NC core, respectively. V_{NC} corresponds to the volume fraction of the NC core. a and G are the NC core radius and the core-ligand thermal interface conductance, respectively. From this expression, we see that the effective thermal conductivity of the NC solid is

determined by the thermal conductivities and volume fractions of the individual components, the interface conductance between the individual components, and the radius of NC core.

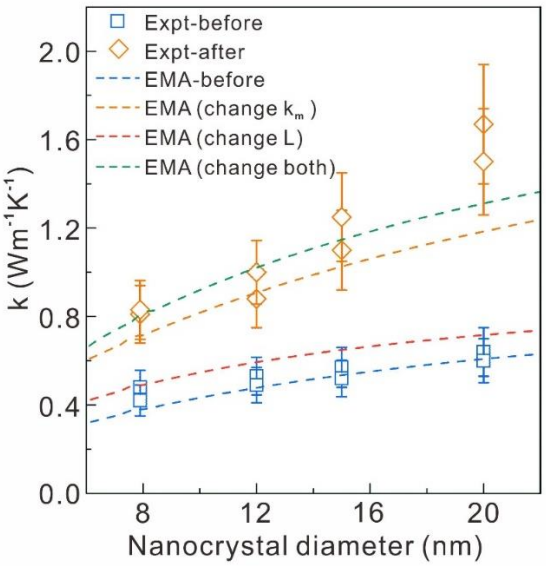

Figure 3.18 EMA sensitivity analysis towards interparticle distance (L) and ligand matrix thermal conductivity (k_m) for a series of NC sizes. The experimental thermal conductivity measurements are shown as hollow blue squares and hollow orange diamonds for iron oxide NC solids before and after annealing, respectively. Annealing the samples leads to two different effects. One of these effects is ligand crosslinking, which manifests as a change in k_m. The other effect is the partial desorption of NC ligands, which manifests as a change in L. The effect of changing k_m and changing L can be independently assessed using the effective medium approximation (EMA). If we only consider an increase of k_m from 0.13 to 0.37 W m^{-1} K^{-1}, we obtain the orange dashed line. If we only consider a decrease of L from 1.0 nm to 0.4 nm, we obtain the red dashed line. If we consider changes in both k_m and L, the EMA fit is shown as the green dash line. This analysis shows that ~80% of the change in thermal conductivity that arises from annealing originates from ligand crosslinking (*i.e.*, a change in k_m).

This EMA model allows us to decouple the effects of ligand crosslinking and ligand desorption on thermal conductivity, both of which occur during the annealing process. Both of these effects should increase the overall thermal conductivity of the NC solid. In the EMA model, these effects manifest themselves as an increase in k_m and a decrease in interparticle distance L, respectively. Figure 3.18 shows the relative effects of increasing k_m and decreasing L on NC solid thermal conductivity as all other EMA model parameters remain fixed. Changing L from 1.0 nm to 0.4 nm (i.e., values before and after the annealing process) leads to only a small change in the thermal conductivity (red dashed curve in Figure 3.18). In contrast, changing k_m from 0.13 to 0.37 W m^{-1} K^{-1} (i.e., values before and after the annealing process as dictated by the changes in ligand matrix sound velocity that were calculated from mechanical measurements) leads to a large change in thermal conductivity (orange dashed curve in Figure 3.18). Changing both k_m and L leads to the best match to our thermal conductivity data for crosslinked NC solids (green dashed curve in Figure 3.18).

A G value of 400 $MWm^{-2}K^{-1}$ is derived from our EMA fitting on non-crosslinked OA capped iron oxide nanocrystals solids. The same G value was used for our EMA fitting on cross-linked OA capped iron oxide nanocrystal solids. We acknowledge that G could change upon annealing due to possible carboxylate binding states and ligand capping density changes. However, we don't believe G would change significantly upon annealing.

Our EMA model as well as our mechanical measurements suggests that increased k_m rather than possible significant change in G leads to enhanced thermal transport. On one hand, as is shown in Figure 3.20a-c, for relatively smaller k_m (0.13-0.23 W/mK), varying G from 300 $MWm^{-2}K^{-1}$ to 800 $MWm^{-2}K^{-1}$ leads to poor overall EMA

fitting that significantly deviates from most of the experimental data. On the other hand, as is indicated in Figure 3.20d-f, for relatively larger k_m (0.28-0.37 W/mK), varying G from 300 $MWm^{-2}K^{-1}$ to 800 $MWm^{-2}K^{-1}$ leads to much better overall EMA fitting. This suggests that increased k_m is more likely to be the major contributor. And this is in line with our mechanical measurements where a k_m of 0.37 W/mK is derived due to 3-fold increase in sound speed of crosslinked ligand matrix. As was recognized by the reviewer, G starts to affect thermal conductivity more with a larger k_m. Specifically, as is evidenced in Figure 3.20f, varying G from 400 $MWm^{-2}K^{-1}$ to 800 $MWm^{-2}K^{-1}$ leads to overestimation of nanocrystal solids thermal conductivity for smaller nanocrystal diameters (8-12nm).

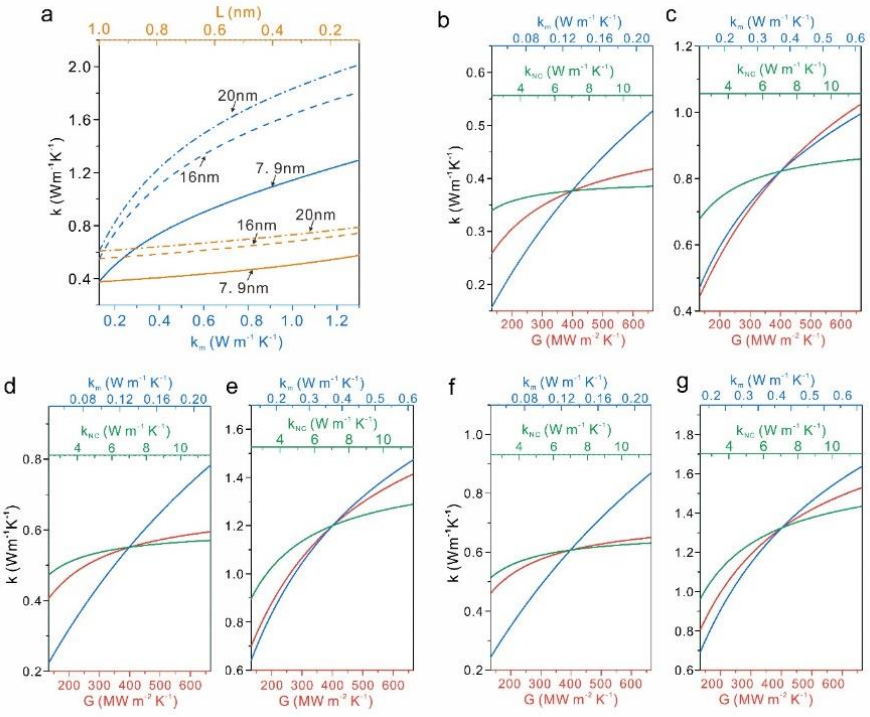

Figure 3.19 Sensitivity analysis on the effective medium approximation (EMA) model for 7.9 nm, 16 nm, and 20 nm NC solids. (a) EMA sensitivity towards k_m (blue) and L (orange). We hold k_{NC} and G fixed at 7 W m^{-1} K^{-1} and 400 MW m^{-2} K^{-1}, respectively. We

hold L fixed at 1 nm while varying k_m and we hold k_m fixed at 0.13 W m^{-1} K^{-1} while varying L. EMA sensitivity for (b, d, f) non-crosslinked and (c, e, g) crosslinked NC solid towards three independent parameters: k_{NC} (green), G (red), and k_m (blue); (b, c), (d, e), and (f, g) are for 7.9 nm, 16 nm, 20 nm NC solids, respectively. Unless a parameter is explicitly varied in parts (b, d, f), we hold L, k_{NC}, k_m, and G fixed at 1.0 nm, 7 W m^{-1} K^{-1}, 0.13 W m^{-1} K^{-1} and 400 MW m^{-2} K^{-1}, respectively. Unless a parameter is explicitly varied in part (c, e, g), we hold L, k_{NC}, k_m, and G fixed at 0.4 nm, 7 W m^{-1} K^{-1}, 0.37 W m^{-1} K^{-1} and 400 MW m^{-2} K^{-1}, respectively.

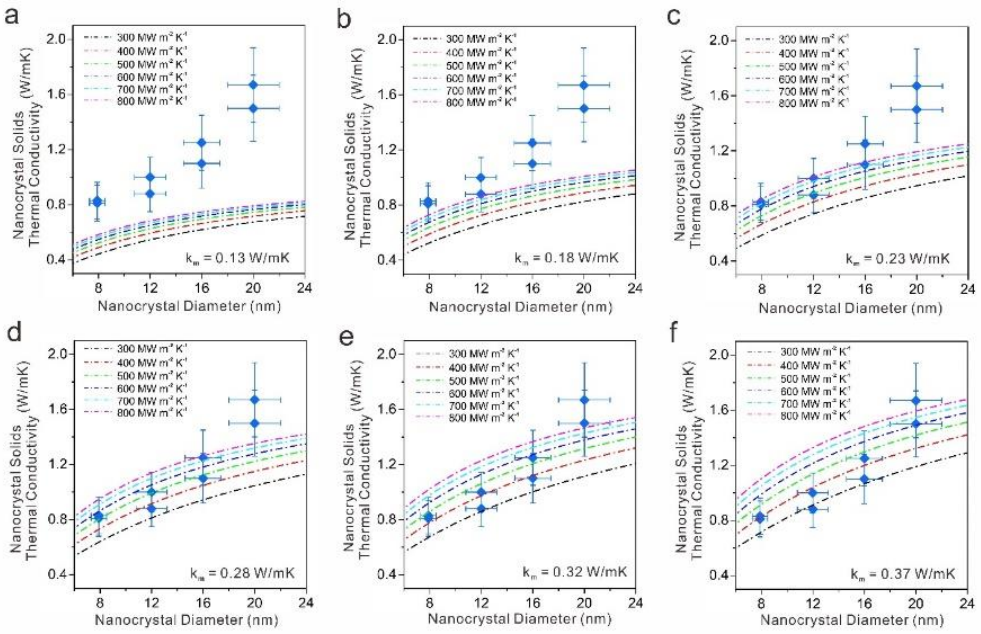

Figure 3.20 Room temperature thermal conductivity measurement results on OA-capped iron oxide NC solids of different NC sizes after annealing at 350 °C. The dash lines are fitted results based on an effective medium approximation (EMA) model. we hold k_m fixed at 0.13 $Wm^{-1}K^{-1}$, 0.18 $Wm^{-1}K^{-1}$, 0.23 $Wm^{-1}K^{-1}$, 0.28 $Wm^{-1}K^{-1}$, 0.32 $Wm^{-1}K^{-1}$, and 0.37 $Wm^{-1}K^{-1}$ for (a), (b), (c), (d), (e), and (f), respectively. While G is varied from 300 $MWm^{-1}K^{-1}$ to 800 $Wm^{-1}K^{-1}$ for all the EMA fittings in (a-f).

In addition, interfacial bond strength is reported to be the dominator for thermal interface conductance, for example, Losego et al.[24] reported that thermal conductance of Au/Self-assembled monolayer (SAM) interface can be enhanced by a factor of 2 through exchanging van der Waals contact interface with covalent bonded interface. Although we acknowledge that carboxylate binding state might change slightly upon annealing, we don't believe binding states change alternates the covalent bond nature of carboxylate binding to the iron oxide nanocrystal surface, thus we don't anticipate a significant change in G upon annealing.

3.5.6 **Molecular Dynamics (MD) Modeling**

MD simulations were conducted using the LAMMPS package. A simple one-dimensional NC solid model proposed by Ong et al.[29] was utilized to calculate the temperature gradients in the NC solids. In this simplified model, a spherical core was crafted from an FCC lattice structure with 135 atoms and 6 linear chains were perpendicularly grafted to the sphere surface in six different directions (± x, ± y, ± z). The atoms within the sphere interact via a standard 12-6 Lennard-Jones (LJ) potential of length scale σ and energy scale ε. The ligands are simplified as a straight chain of atoms that are bonded to their nearest neighbors with a Hookean spring type force of stiffness of 118ε and equilibrium distance of 1.1σ. We also apply an additional three-body bending energy term to constrain the ligand linearly. The ligand atom closest to the NC core was bonded to the four closest core atoms via the same set of Hookean springs. The vdW interaction between two neighboring ligands was described by a 12-6 LJ potential with length scale σ, energy scale 0.2ε, and a "soft cutoff", which refers the damping of ligand to ligand atom interaction as the distance approaches $\sim 7\sigma$. Ligands were offset in the y-direction by $1.3\,\sigma$ to avoid direct overlap of the ligand ends. The ligand overlap in the x-direction was 2 atoms and 1 atom for the non-crosslinked (vdW) and crosslinked (covalent) models, respectively. The ends of the

ligands along the y- and z-axis are tethered to their initial positions using a weak Hookean spring with stiffness 4ε and equilibrium distance of 1.1σ (Figure 3.21a, b). This weak tethering prevents the rotational and translational movement of the NC cores and ligands. The stiffness of this Hookean spring is set to be identical to the weak LJ interaction between the neighboring ligands along the x-axis. For simulating the NC solids with crosslinked ligands, the interaction between two overlapping ligand atoms are exchanged with a covalent bond, which we modeled with a single Hookean spring without the bending energy term (Figure 3.21b).

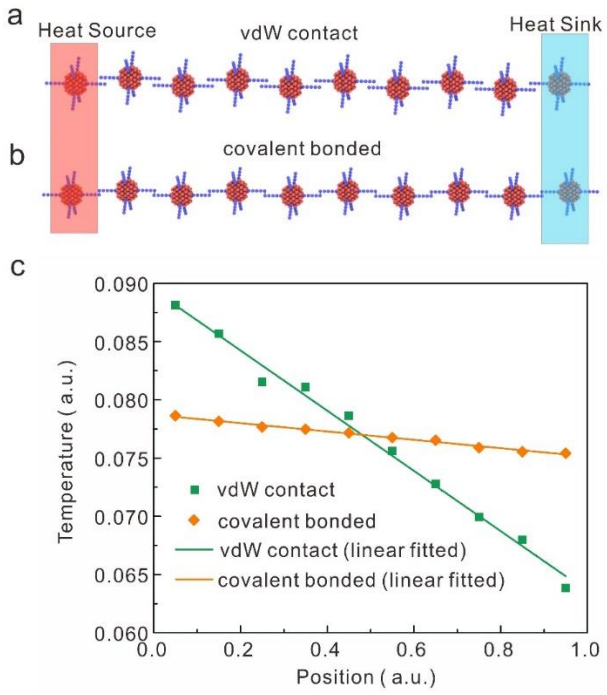

Figure 3.21 Molecular dynamics simulation result. (a) Schematic illustration of a simplified non-dimensionalized NC solid model with vdW interactions between neighboring ligands; (b) Schematic illustration of a simplified non-dimensionalized NC solid model with covalent bonds between neighboring ligands; (c) Steady-state temperature profiles after the heat flux and the heat sink are applied to the NC solid

models. Each point represents the average temperature of one NC core at their respective position.

We applied fixed boundary conditions to all three directions. This system is first thermalized to a dimensionless temperature of 0.070 and then allowed to relax and reach equilibrium. This process was run for 10 million steps with a dimensionless time-step of 0.001. We then employed a non-equilibrium molecular dynamics (NEMD) simulation to impose a constant heat flux to one end of the system and a heat sink to the other end of the system. After running for 60 million steps, the temperature profile reaches steady state. We further ran the program for another 70 million steps to allow us to calculate the average temperature distribution after reaching steady state.

The temperature distribution along a chain of 10 NC cores was extracted from the MD simulation and is shown in Figure 3.21c. The temperature of each core after reaching steady state was determined by averaging the temperature of all the core atoms. This analysis shows that given the same steady state heat flux input, the magnitude of the temperature gradient in the NC solid with vdW ligand interactions is much greater than the NC solid with a covalent bond between ligands (Figure 3.21c). This indicates that the NC solid with covalent bonding has a higher thermal conductivity.

We also examine the temperature distribution along a single NC pair and the ligand molecules between them (Figure 3.22). In this case, each temperature data point corresponds to a core or ligand atom at that position. In the vdW ligand interactions, there is a sharp drop in temperature at the ligand-ligand interface. This indicates that the ligand-ligand interface is the thermal transport bottleneck. After exchanging the vdW interaction with a covalent bond, the temperature drop across the ligand-ligand interface substantially diminishes. This reflects a large increase in thermal conductance

at the ligand-ligand interface and consequently a large increase in thermal conductivity of the NC solid.

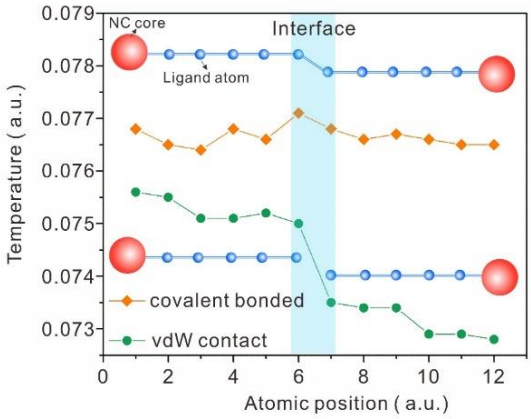

Figure 3.22 Temperature profiles from MD simulations along two adjacent NCs with vdW interactions between neighboring ligands as well as covalent bonds between neighboring ligands. A very large temperature drop appears at the vdW contact, which indicates large thermal interface resistance. This large temperature drop disappears in the case of the covalent bond, which means that the thermal conductance across the ligand-ligand interface has greatly increased. Each temperature data point corresponds to the temperature of the core or ligand atom at that location.

3.5.7 **Thickness Dependent Thermal Conductivity**

NC solids thin films of different thicknesses (100, 150, 200, 300, and 500 nm) were prepared by spin-coating NC solutions of different concentrations. To prepare these samples for thermal conductivity measurements, SiO_2 films were deposited on these samples using sputtering. Metal 3ω lines were then patterned using standard lithography techniques. Figure 3.23 shows the resulting thermal conductivity as a function of sample thickness for non-crosslinked and crosslinked samples. The thermal conductivity is independent of sample thickness which indicates that the contact

resistances (Si substrate – NC interface, NC-SiO_2 interface, and Au-SiO_2 interface) in the 3ω sample stack are negligible.

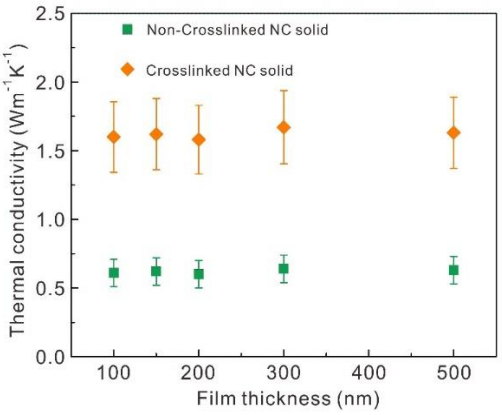

Figure 3.23 The measured thermal conductivity of NC thin films as a function of film thickness. The NCs in these samples consisted of iron oxide NCs of 20 nm diameters.

3.5.8 **Electronic Contribution to Thermal Conductivity**

Heat transfer in solid materials occurs via the transport of electrons and mechanical vibrations (e.g. phonons). We used the Wiedemann-Franz law to estimate the contribution of electrons to the overall thermal conductivity in our samples. The Wiedemann-Franz law relates the electronic contribution to thermal conductivity to the electrical conductivity via the following equation:

$$\frac{k_e}{\sigma T} = L$$

where k_e is the electronic contribution to thermal conductivity, σ is the electrical conductivity, T is the absolute temperature, and L is the Lorentz number ($2.44*10^{-8}$ W Ω K^{-2}).

We measured the electronic conductivity of non-crosslinked and crosslinked iron oxide NC solid thin films using the van der Pauw method. We first measured the

electrical sheet resistance using a Keithley 2400 sourcemeter by taking current-voltage data at 10 points for currents ranging from -50 to +50 μA. The sample thickness was then determined by profilometry. The sheet resistance was then divided by the sample thickness to get the electronic conductivity. The electrical conductivity of the pristine and annealed NC solids was measured to be ~ 0 and 1.64 S m^{-1}, respectively.

Using these measured electrical conductivities and the Wiedemann-Franz law, we estimate that the electronic contribution to thermal conductivity is ~0 and ~1x10^{-5} W m^{-1} K^{-1} for non-crosslinked and crosslinked samples, respectively. These contributions are negligibly small compared to the experimentally measured thermal conductivity (e.g. ~ 1 W m^{-1} K^{-1}) and so we conclude that mechanical vibrations dominate thermal transport in both crosslinked and non-crosslinked NC solids.

4 STRONGER LIGAND-LIGAND INTERACTION LEADS TO ENHANCED MECHANICS AND THERMAL TRANSPORT IN COLLOIDAL NANOCRYSTAL SUPERLATTICES

4.1 Abstract

Colloidal nanocrystals (NCs) are promising candidates for a wide range of applications (electronics, optoelectronics, photovoltaics, thermoelectrics, etc.). Mechanical and thermal transport property play very important roles in all these applications. On one hand, mechanical robustness and high thermal conductivity is desired in electronics, optoelectronic, and photovoltaics. As this improves thermomechanical stability and minimizes the temperature rise during the device operation. On the other hand, a low thermal conductivity is desired for a higher thermoelectric figure of merit (ZT). Colloidal nanocrystal solids have been identified to have very limit range of elastic moduli (30MPa-1GPa) and thermal conductivities (0.1-0.4 W/mK). Previous work identified the vdW contact of neighboring ligands in nanocrystal solids as the major mechanics and thermal transport bottleneck.

Here we report a combined mechanics and thermal transport measurement on single domain colloidal PbS nanocrystal superlattice. We found that, though with similar compositions, long-range ordered nanocrystal superlattices (NCSL) possess mechanical and thermal transport properties that are 2-3 times higher than that of disordered thin films. Our measurements along with theoretical modeling indicate that stronger ligand-ligand interaction in nanocrystal superlattice accounts for the improved mechanics and thermal transport. Our work indicates that, in addition to ligand composition, ligand interdigitation and arranging order play equivalent important roles in determining mechanical and thermal transport properties of NC assemblies.

4.2 Introduction

Colloidal nanocrystals with inorganic core and molecular ligand can assemble into a solid material that usually termed as NC solids. NC solids with tunable electronic and optical properties have shown great potential for electronics, optoelectronics, photovoltaics, and thermoelectrics. Mechanical and thermal transport properties of NC solids also play a very important role in the NC solids-based applications. As the active materials involved in these devices have to meet the mechanical robustness and thermal management demands. Unfortunately, NC solids has been reported to have very limited range of elastic moduli (30 MPa - 1 GPa) and thermal conductivity (0.1 - 0.4 W/mK) as results of weak vdW interaction of organic ligands. Previous work focus on modifying surface chemistry of the NCs to improve the mechanical or thermal transport properties. For example, Ong et al.[77] showed that thermal conductivity of NC solid is insensitive to thermal conductivity of NC core, but rather sensitive to core-ligand interface and ligand matrix. Liu et al.[78] further investigated effects of NC-ligand binding groups, ligand length, and NC sizes. Our recent work[79] demonstrated a simultaneous increase of Young's modulus and thermal conductivity in iron oxide NC solids with ligands crosslinking method.

Bulk polymers have very similar mechanical properties and thermal conductivities (0.1 W/mK) as that of NC solids. This is because defects in polymers act as stress concentration points and phonon scattering sites for heat transfer. However, alignment of polymer chains can result in significant increase of mechanical strength and thermal conductivity.[80] Similarly, several experimental studies showed that self-assembled monolayers (SAM) of aligned polyethylene chains also exhibits very high thermal conductance.[75, 81] Ligand matrix within NC solids is believed to be disordered, which was also believed to account for the poor mechanical and thermal transport properties

of NC solids. If the ligand order within the NC solids can be improved, will its mechanics and thermal transport be enhanced as well?

In this work, we demonstrate a 200-300% increase of mechanical and thermal transport properties of NC composites without changing surface chemistry. We find that mechanics and thermal transport behaviors of NC composites resemble that of polymers, where molecular chain interdigitation and alignment significantly affect mechanical strength and thermal conductivity. Using oleic acid capped PbS NC as an example, we varied the ligand interdigitation and arranging order in PbS NCs through controlled destabilization of NCs in solution phase. Specifically, quick drying of the NC solution (i.e. spin coating or drop-casting) yields NC solid thin films with disordered ligands (Figure 4.1a), while slow diffusion of non-solvent (i.e. ethanol) into NC solution leads to three dimensional NCSL with ordered ligands (Figure 4.1d). We then performed mechanical property and thermal conductivity measurements on both PbS NC solid thin films and PbS NCSLs with nanoindentation and Frequency Domain Thermo Reflectance (FDTR) techniques, respectively. Though with very similar compositions, NCSLs possess Young's modulus and thermal conductivity that is 2-3 times higher than that of NC solid thin films. In addition, Young's modulus and thermal conductivity of NCSL show more pronounced NC size dependence than that of NC solid thin films. This indicates that ligand-ligand interactions are dependent on NC core sizes in NCSLs. We suspect this variance in ligand-ligand interaction results from ligand interdigitation and arranging order to different extents when the NC core size is varied. We complement our mechanical and thermal transport measurements with material characterization and computationally modeling. Both of our coarse-grained simulations and atomistic MD simulations points to enhanced ligand alignment and interdigitation as the major contributor in enhanced mechanics and thermal transport that observed in NCSLs.

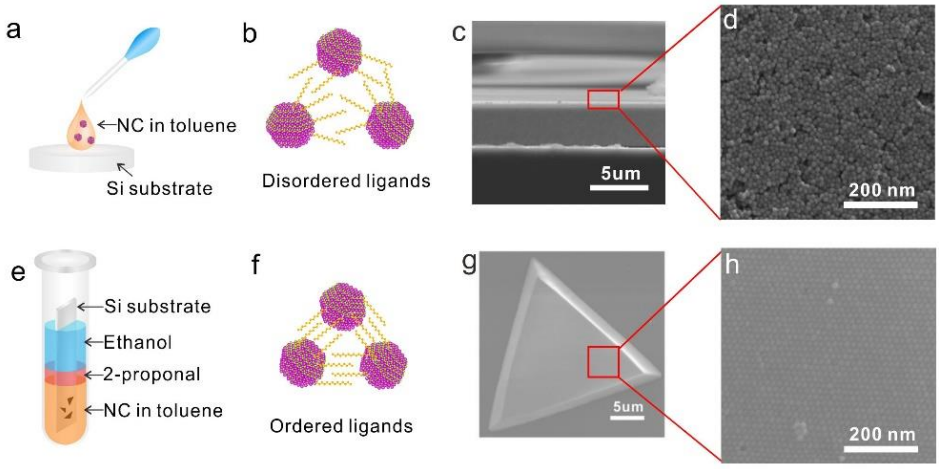

Figure 4.1 Materials characterizations of randomly packed PbS NC thin film and long-range ordered PbS NCSL. (a) Schematic illustration of quick drying of NC solution via drop-casting or spin-coating; (b) Schematic of adjacent PbS NCs with disordered ligands packing when solvent is quickly evaporated; (c) cross-sectional view SEM image of spin coated PbS NC thin films; (d) High-resolution SEM image of spin coated PbS nanocrystals shows disordered packing of NCs; (e) Schematic illustration of controlled destabilization of NC solution via slow diffusion of non-solvent; (f) Schematic of adjacent PbS NCs with ordered ligands packing when NC is slowly destabilized by non-solvent diffusion; (g) SEM image of a triangular shape single domain PbS NCSL prepared using non-solvent diffusion method; (h) High-resolution SEM image of PbS NCSL shows ordered packing of NCs with single orientations.

4.3 **Results and Discussion**

PbS NC solid thin film and NCSL are prepared and carefully characterized with a combination of scanning electron microscopy (SEM), transmission electron microscopy (TEM), and atomic force microscopy (AFM) techniques. Specifically, we synthesized monodispersed 3-6 nm PbS NC with oleic acid ligand using a modified Hines' method.[82] TEM images show that PbS NCs are uniform in size and shapes. The gap (~1.5 nm)

separating the adjacent PbS NCs originates from a bilayer of long OA molecular ligands that attached to the neighboring NC surfaces. The presence of thick OA shell also allows PbS NCs to assembled into macroscopic superstructures through ligand-ligand interaction. As is shown in Figure 4.1a, b, and c, drop-casting or spin-coating of concentrated PbS NC solution onto silicon substrates lead to loosely packed NC solid thin film after solvent is evaporated quickly. The NC solid thin film features disordered NCs and ligands arrangement, which leads to larger inter-NC spacing and weaker ligand-ligand interaction. This is due to the fact that NCs along with the attached OA ligands cannot re-orientate fully to reach their thermodynamically stable state during the short solvent drying process. On the other hand, destabilizing NCs through slow diffusion of non-solvent (i.e. ethanol) molecules usually lead to highly ordered and compact NCSL of finite sizes (50-200 um). PbS NCSL prepared using this method features triangular (Figure 4.1e) and hexagonal shapes. High resolution SEM image of NCSL shown in Figure 4.1f indicates that NC are orderly packed with single orientation, which suggests NCSL is in single domain. NCSL features ordered packing of ligands and further leads to smaller inter-NC spacing and stronger ligand-ligand interaction. And this has been characterized by Lee et al.[83] using small angle x-ray scattering (SAXS) in their study on PbS NCSL and NC thin films, where they found out there is ~20% decrease in internanocrystal spacing of NCSL as compared to disordered NC thin film. Thus, we derived an internanocrystal spacing of 1.2 nm for PbS NCSL. This decrease can be explained as follows: the NCs in the growth of NCSL are able to re-orientate freely to achieve more ligand interdigitation during the weeks long non-solvent diffusion process. In another word, NCSL reaches its thermodynamically stable state.

Intuitively we suspect that NCSL possesses different mechanical response towards stress applied as compared to its thin film state. As mechanical properties of colloidal

NC solids are believed to be dominated by the organic ligand-ligand interaction.[84] We continue to perform nanoindentation on PbS NC thin films and NCSLs to derive the Young's modulus and hardness. Our results shown in Figure 4.2f and Figure 4.7 indicate that NCSLs possess both higher Young's modulus and higher hardness than that of NC thin films. Specifically, schematic in Figure 4.2a illustrates the behavior of PbS NC solid thin film during the nanoindentation test, relatively smaller load is needed to break the vdW contacts of ligand molecules and displace neighboring NCs. While schematic in Figure 4.2c demonstrates that larger load is required to break the vdW contacts in NCSL because of stronger ligand-ligand interaction. Figure 4.2b, d show representative clean indents on PbS NC solid thin film and NCSL, respectively. Figure 4.2f shows that Young's modulus of PbS NC solid thin film increases from 110 MPa to 600 MPa when the NC core sizes increases from 3 nm to 6.1 nm. Similarly, we found Young's modulus of PbS NCSL increases from 360 MPa to 1.5 GPa when NC core sizes is varied from 3 nm to 6.1 nm. We attributed this variance to NC size dependent ligand-ligand interaction. We suspect this variance originates from surface curvature change when NC size is varied. He et al.[85] drew similar conclusions in their mechanical study on colloidal nanocrystal monolayer. More importantly, we noted that PbS NCSL has a Young's modulus that is 2-5 times higher than that of PbS NC solid thin films for a variety of NC core sizes. Per our previous discussion, we ascribed the enhancement observed to improved ligand-ligand interaction on account of more ligand interdigitation and better ligand alignment in PbS NCSL.

To quantitatively understand the varied mechanical properties between PbS NCSL and NC solid thin film, we employed a three-dimensional coarse-grained model of PbS NC assembly that constructed from an analytical NC pair potential to fit the experimental data. As was drawn in Figure 4.2a, c, there are 3 major contributions to the interaction between two neighboring NCs: vdW attraction between the cores,

dipole-dipole interactions, and ligand-ligand interactions. Additionally, we assume ligand-ligand interaction is proportional to the overlapped volume of the ligand shell in our NC pair model. Per our discussion above, the equilibrium position for internanocrystal spacing is set to be 1.5 and 1.2 nm for disordered PbS NC thin film and long range ordered PbS NCSL, respectively. The NC pair potential was further utilized to build a three-dimensional NC superlattice model of face-centered cubic lattice structure. This three-dimensional model further allows us to derive the mechanical properties of the superlattice structure by a "stress-strain" method.

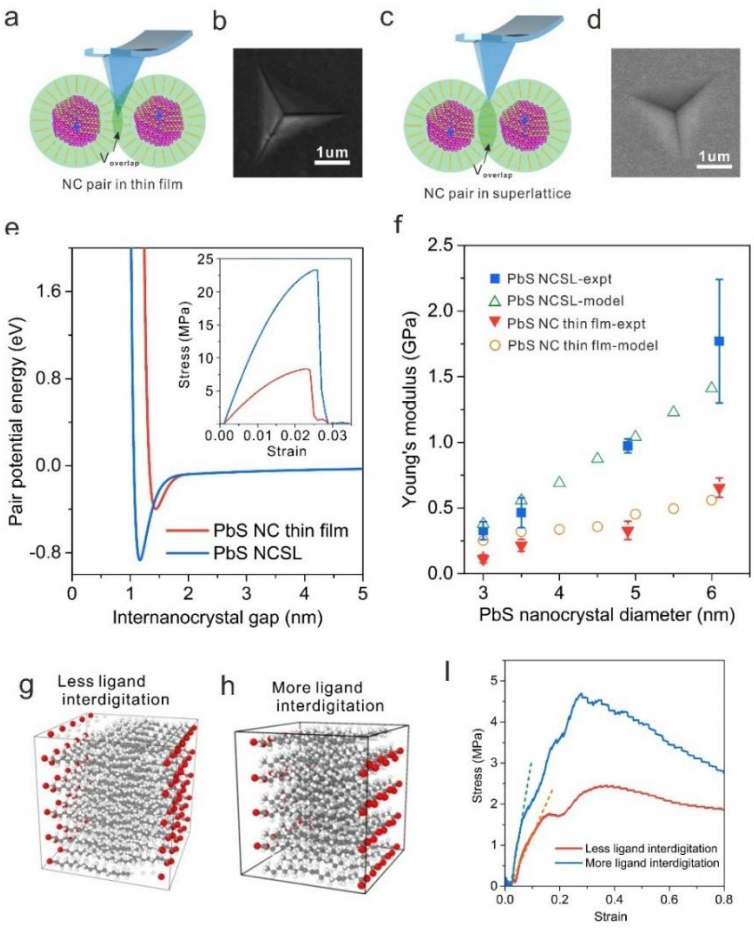

Figure 4.2 Mechanical property measurements and coarse-grained and atomistic MD model simulation. Schematic illustration of mechanical response of PbS NC pair of (a)

weaker and (c) stronger ligand-ligand interaction in PbS NC thin film and superlattice structure, respectively; SEM images of representative nanoindents on PbS NC (b) thin film and (d) NCSL, respectively; (e) NC pair that with higher ligand packing order and interdigitation leads to stronger NC-NC interaction and smaller interNC spacing; the inset shows calculated stress-strain curves of 3 dimensional NCSL model constructed using different pair potentials; (f) Young's modulus of PbS NC thin films and NCSLs of various core sizes measured with nanoindentation, the fitted results from the coarse-grained model matched well with experiments; Atomistic illustration of interdigitated oleic acid ligand-ligand bilayer with less (g) and more (h) interdigitation volume; (i) Representative stress-strain curve obtained by applying tensile strain onto atomistic models shown in (g) and (h), clearly a higher Young's modulus is predicted for interdigitated oleic acid ligand-ligand bilayer with higher interdigitation volume.

As was pointed out above, PbS NCSL features narrower inter-NC spacing and higher ligand packing order and thus better ligand interdigitation. Specifically, using 6 nm PbS NC as an example, by specifying an equilibrium position shift from 1.5 nm to 1.2 nm in the pair potential model, we observed a potential energy decrease and higher curvature of the energy curve near the equilibrium position. This further contributed to a Young's modulus increase from ~600 MPa to ~1750MPa, which was derived from stress-strain curves (inset of Figure 4.2e) calculated from the 3D coarse-grained model. As was shown in Figure 4.2f, our coarse-grained simulations fit the experiments well in both trend and magnitude for a range of NC core sizes.

Our atomistic MD simulations further directly verify that larger ligand-ligand interdigitation does lead to increased Young's modulus. We built up a fully atomistic model of ligand matrix using ReaxFF potential as implemented in LAMMPS package (detail in section 4.5.4). Specifically, we created an interdigitated OA-OA bilayer to

simulate the ligand-ligand interaction within colloidal nanocrystal solids. The ligand-ligand interface was pre-configured and relaxed at different overlap volume of molecular chains to simulate nanocrystal solid thin film and superlattice. The relaxed atomistic structures are shown in Figure 4.2g, h for ligand-ligand interface of less and more interdigitation volume, respectively. By applying tensile stress that is perpendicular to the ligand-ligand interface to the atomistic models, we obtained stress-strain curves which allows us to derive the Young's modulus by fitting the linear region. As shown in Figure 4.2i, a higher Young's modulus was derived for ligand-ligand bilayer of more interdigitation volume, which is in agreement with the conclusion we draw from experiments and coarse-grained modeling. However, the Young's modulus we derived from the atomistic model cannot be directly compared to experimental results due to the simplifications we made in this model (see section 4.5 of this chapter).

We measured heat capacity (C_p) of PbS NC solids of various core sizes (3 - 6.1 nm) via Differential Scanning Calorimetry (DSC). C_p of PbS NC solids as function of temperature and NC core sizes is shown in Figure 2b. We observed a similar abrupt slope change of C_p at around 200K as that of literature, which was further identified as a glassy transition of oleate ligands.[86] Ong et al.[77] reported that C_p of the NC composites can be estimated by adding up C_p of each constituent times its mass fractions. And the mass fraction of ligand matrix of 3-6.1 nm PbS NC solids and NCSLs were determined using thermogravimetric analysis (TGA) and shown in Table 4.1. Evidently both PbS NC solids and NCSLs composed of smaller NC cores possess higher ligand mass fractions as a result of higher interface density in smaller NCs. Additionally, NCSLs possess slightly lower ligand mass fractions, this is because ethanol strips some amount of ligand during NCSL growth.[83] We further estimated the

room temperature C_p of PbS NC solids and NCSLs using the mixture rule and the result is shown in Figure 4.3c. NCSL possesses slightly smaller C_p (~12% smaller) than that of NC solids as a result of smaller ligand mass fractions. And estimated C_p for NC solids and NCSLs using mixture rule are within 15% difference.

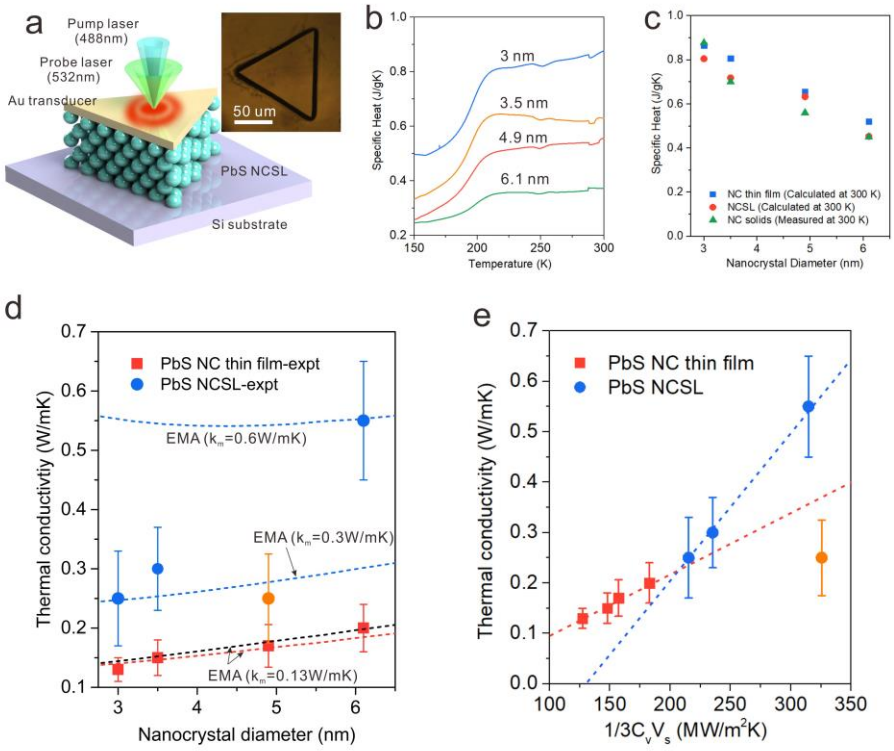

Figure 4.3 Heat capacity and thermal conductivity measurements of PbS NCSL and NC thin films of various NC sizes. (a) Schematic illustration of thermal conductivity measurement on gold-coated PbS NCSL using Frequency Domain Thermoreflectance (FDTR) technique; the inset shows an optical microscope picture of gold-coated PbS NCSL; (b) Temperature dependent specific heat capacity of oleic acid capped PbS nanocrystal solids of various NC core sizes; (c) Calculated room temperature specific heat capacity of PbS NCSL and NC thin films for a range of NC core sizes and its comparison with experimental measurement; (d) Thermal conductivity of PbS NCSLs

and NC thin films of various core sizes, the dash lines are Effective Medium Approximation (EMA) fittings; the result for 4.9nm PbS NCSL is highlighted in yellow. (e) Thermal conductivity of PbS NCSLs and NC thin films as a function of $1/3V_sC_v$; the dash lines are linear fittings. The result for 4.9nm PbS NCSL is again highlighted in yellow.

We continued to measure thermal conductivities of PbS NCSL and NC solid thin film using a Frequency Domain Thermoreflectance (FDTR) technique. As was illustrated is Figure 4.3a, all the samples were pre-deposited with 70 nm Au via electron-beam deposition. Au film on top of the NCSL was periodically heated with an intensity-modulated pump laser ($\lambda = 488\,nm$), and the probe laser ($\lambda = 532\,nm$) detects the temperature change via surface reflectivity change to derive thermal conductivity (details in section 4.5 of this chapter). Our results show that thermal conductivity of PbS NCSL increases by a factor of 2-3 than that of NC solid thin film for a variety of PbS NC core sizes (Figure 4.3d). Specifically, for PbS NC solid thin films, thermal conductivity increases from 0.13 W/mK to 0.18 W/mK when NC size is varied from 3 nm to 6.1 nm, this weak size-dependence of thermal conductivity generally understood as a result of decreased volume fraction of soft and thermally insulated ligand matrix when NC size varies from 3 nm to 6.1 nm. It is worth mentioning that our measurements on PbS NC solid thin films match well with previous literature reports.[77, 78] However, for PbS NCSL, we observed a thermal conductivity increase from 0.25 W/mK to 0.55 W/mK when NC sizes varies from 3 nm to 6.1 nm. On one hand, given the same NC size, thermal conductivity of PbS NCSL is 2-3 times of that of PbS NC solid thin film. On the other hand, thermal conductivity of PbS NCSLs show much more pronounced NC-size dependence as compared to PbS NC thin films. We acknowledge that the measurements on 4.9nm PbS NCSL is an outlier, and we suspect this might be a measurement artifact that has to do with the high surface roughness of 4.9 nm

PbS NCSL (Figure 4.5c and Figure 4.12). In fact, we observed excess diffuse scattering of laser light during our FDTR measurement on 4.9 nm PbS NCSL. This indicates that the uneven surface topography may be impeding the FDTR technique, which merits further study. Our FDTR measurement sensitivity analysis (Figure 4.14) showed that heat capacity change has a very minor effect on the thermal conductivity measured. Thus, we conclude that change in C_p is not responsible for the observed thermal conductivity increase in PbS NCSLs.

To our first approximation, this thermal conductivity enhancement was partly related to the Young's modulus increase. As classical kinetic theory suggests that thermal conductivity of solid is proportional to sound speed, while sound speed is linked to Young's modulus via relation ($v \propto \sqrt{E/\rho}$). Consequently, increase in Young's modulus could correlate to increase in thermal conductivity. We derived the average sound speed using Young's modulus from nanoindentation, density from geometric model, and an assumed Poisson ratio of 0.3. Plotting $1/3V_sC_v$ against the thermal conductivity reveals a linear proportionality (Figure 4.3e) that is in line with kinetic theory. In addition, evidently the linear fitted line for PbS NCSL exhibits a larger slope, which suggests larger average phonon mean free path (MFP) in PbS NCSL. Still, we acknowledge the data for 4.9 nm PbS NCSL is an outlier, which merits further study. The increase in phonon MFP for PbS NCSL results from the better alignment of ligand molecules. This behavior resembles that of polymers, where the alignment of polymer chains results in higher mechanical and thermal conductivity.[80]

To interpret the effects of the individual NC constituents on the PbS NC solid and NCSL's thermal conductivity, we employed an effective medium approximation (EMA) model to fit our thermal conductivity measurements (Figure 3.3d). According to this model, the NC composite's thermal conductivity is a function of thermal conductivity

of NC core (k_{NC}), ligand matrix (k_m), volume fraction of NC core (V_{NC}), radius of the NC cores (a), and core-ligand interface thermal conductance (G). For PbS NC solid thin films, we set k_{NC} and k_m to 2.3 W/mK and 0.13 W/mK as based on literature values. We vary G to fit our data and find that 100 $MWm^{-2}K^{-1}$ yields good agreement (Figure 3.3d). This finite G stems from the vibration density of states (vDOS) mismatch of PbS core and OA ligand. For PbS NCSL, we keep k_{NC} and G fixed as we don't anticipate these two parameters to change. We vary the universal k_m from 0.3 W/mK to 0.6 W/mK and find none of them could fit the experimental data. This indicates that we have to assign different values to k_m for different PbS NC sizes. Evidently k_m increases with increase of NC core sizes, which can be attributed to more pronounced NC size-dependent ligand-ligand interactions in NCSLs.

It has been reported[47, 87, 88] that the phonons that emerge from the periodicity of the superstructures could contribute to thermal transport. Coherent acoustic phonon in NCSL has also been probed successfully by picosecond acoustics[89] and inelastic neutron scattering[90], respectively. To elucidate whether coherent acoustic phonons contribute to thermal transport at room temperature, we employed a 3D mass-spring model (detail in section 4.5.5) to gain understanding of the phononic structure and energy scale of NCSL. In this mass-spring model, the energy of the phonon modes scales with $\sqrt{k/m}$, where k is effective spring constant between two neighboring NCs, and m is the core mass plus the ligand mass. Our calculations show that coherent phonon in our NCSL is of small energy (<0.2 meV) and group velocity (<1000 m/s) as a result of weak elastic coupling of adjacent NCs. Coherent phonon thermal conductivity per MFP of colloidal nanocrystal assemblies ranges from 3000 W m^{-2} K^{-1} to 20000 W m^{-2} K^{-1} (Figure 4.17b). This suggests coherent phonons won't contribute to room-temperature thermal conductivity significantly unless the average MFP exceeds ~6 um (Figure 4.17d), and this is very unlikely as coherent phonons will be

strongly scattered by core phonons, ligand vibrations, NC mass fluctuations, defects and grain boundaries at room temperature. However, specifically for smaller NC sizes, coherent phonon transport could play a role in thermal transport at low temperature, which merits future study.

4.4 Conclusion

In summary, we reported mechanics and thermal transport enhancement by a factor of 2-3 in ordered PbS NCSL as compared to disordered PbS NC thin film state. This increase magnitude in Young's modulus and thermal conductivity is very close to that achieved with recently proposed ligands crosslinking method. Nonetheless, unlike crosslinked iron oxide NCs, PbS NCSLs of various NC sizes still feature sound speed dominated thermal transport. We identified the improved ligand alignment and interdigitation in PbS NCSL as the major contributor to the enhanced NC-NC interaction and thus higher modulus and thermal conductivity. This conclusion was further confirmed by both coarse-grained and fully atomistic MD models simulations. Our work demonstrates the critical role of ligand alignment and interdigitation of NC assemblies in determining their mechanical and thermal transport properties. Our experimental data and theoretical model also suggest that more improvements could be achieved by further engineering ligand-ligand interactions in colloidal NC assemblies.

4.5 Method and Supporting Information

4.5.1 Materials Synthesis and Characterization

Colloidal oleic acid ligated PbS nanocrystal were synthesized and carefully characterized with a variety of techniques. Highly monodispersed PbS nanocrystals of 3-6.1 nm are further assembled into disordered thin film and long-range ordered superlattice. We conducted detailed characterizations on these assembled structures before proceeding with mechanical and thermal transport measurements.

4.5.1.1 ***PbS nanocrystal (NC) synthesis***

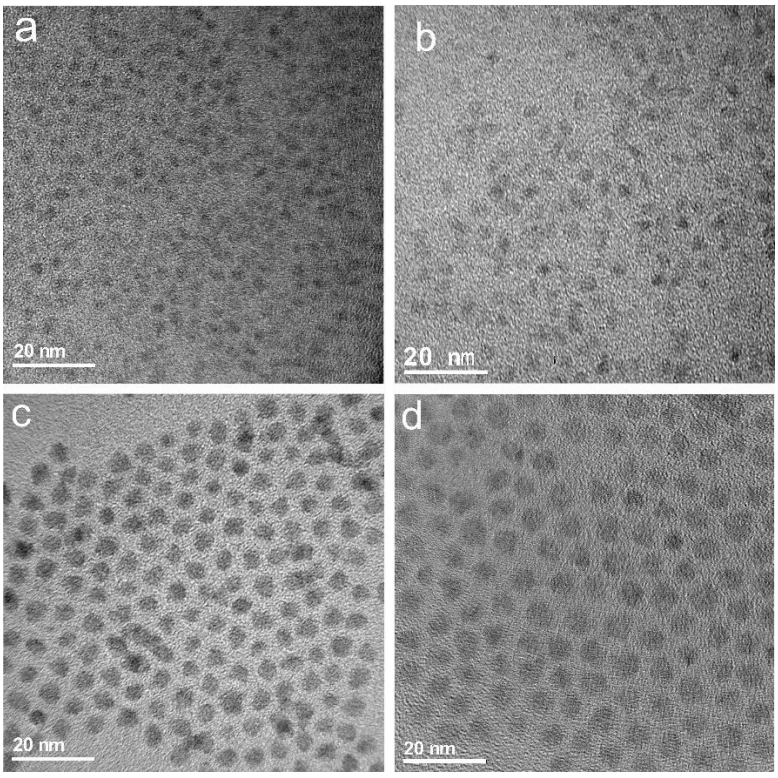

Figure 4.4 TEM images of (a) 3nm, (b) 3.5nm, (c) 4.9nm, (d) 6.1nm oleic acid capped PbS nanocrystals.

For 3-6.1 nm PbS-OA NC synthesis, we employed a modified "hot injection" method[82]. In a typical synthesis of 3nm PbS nanocrystal, we first prepared the Pb precursor solution by mixing lead oxide (450 mg, 99.99% Sigma Aldrich), oleic acid (2 g, 90% Sigma Aldrich), and 10ml Octadecene (ODE) in a 50 ml flask, degassing for 1h and then heat to 95 ℃ under N_2 until all lead oxide was dissolved. The sulfur precursor solution was prepared by mixing 210 ul TMS with 5 ml ODE, and then the S precursor solution was quickly injected. Then the heating mantle was removed and the flask was left naturally cool to room temperature. For cleaning, equal volume of ethanol were added to the flask, the NCs are precipitated by centrifuging and then re-dispersed in toluene. Afterwards, the particle solution was further purified twice by

repeating the precipitation and re-dispersing process. To vary the nanocrystal size, we tune the molar ratio of oleic acid to lead oxide and the injection temperature. In general, higher molar ratio of oleic acid and higher injection temperature favors the growth of PbS nanocrystal of larger sizes.

4.5.1.2 ***PbS NCSL preparation***

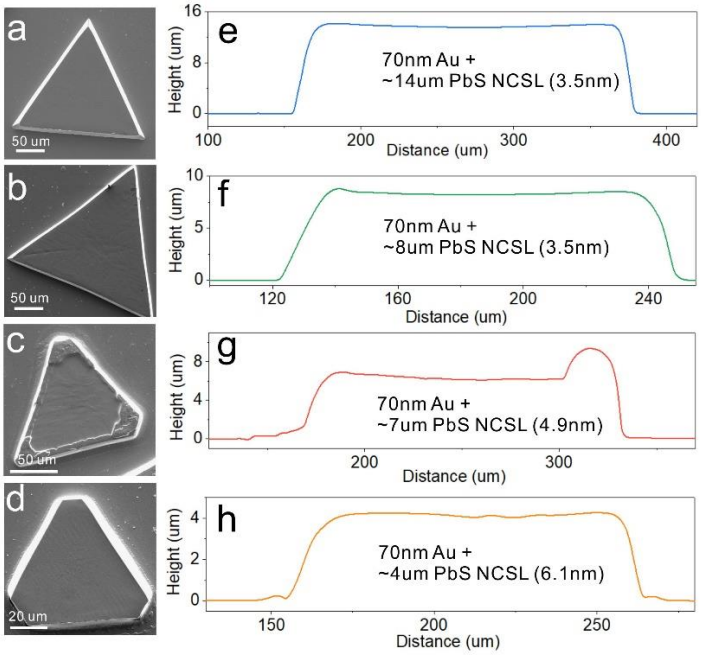

Figure 4.5 Surface morphology of gold coated PbS nanocrystal superlattices composed of (a) 3nm, (b) 3.5 nm, (c) 4.9 nm, and (d) 6.1 nm PbS nanocrystals. (e-h) The height profile obtained by scanning cross the superlattice with profilometry from a to d, respectively.

~300 ul PbS NC solution in toluene (~3.5 mg/ml) were placed at the bottom of a pre-cleaned glass tube (5cm long, 0.4cm in diameter). A pre-cut silicon wafer that fits the glass tube dimensions was inserted into the NC solution. Then 100 ul IPA (buffer layer) and 280 ul non-solvent (i.e. ethanol) were successively added to the surface of NC toluene solution slowly and gently with a syringe. The tube was sealed with parafilm

and left in the dark and undisturbed for 1-2 weeks for the nucleation and growth of PbS NCSL. After that the solution phases turn transparent, which suggests that the NCSL growth process is done. Then the Si substrate was carefully taken out, rinsed with ethanol and blow-dried with N_2. Randomly and densely packed "black dots" (NCSL) were seen on the polished side of the Si substrate.

Thickness of the PbS NCSLs of various core sizes are determined using profilometry. As shown in Figure 4.5, NCSL generally possesses thickness over 4um. Additionally, the lateral dimension of NCSL can also be roughly estimated based on SEM images and profilometry. Generally, the size of NCSL is limited to 100-200 um. These dimensions are critical for interpretating the nanoindentation and FDTR measurements, which will be discussed later.

4.5.1.3 ***PbS NC thin film preparation***

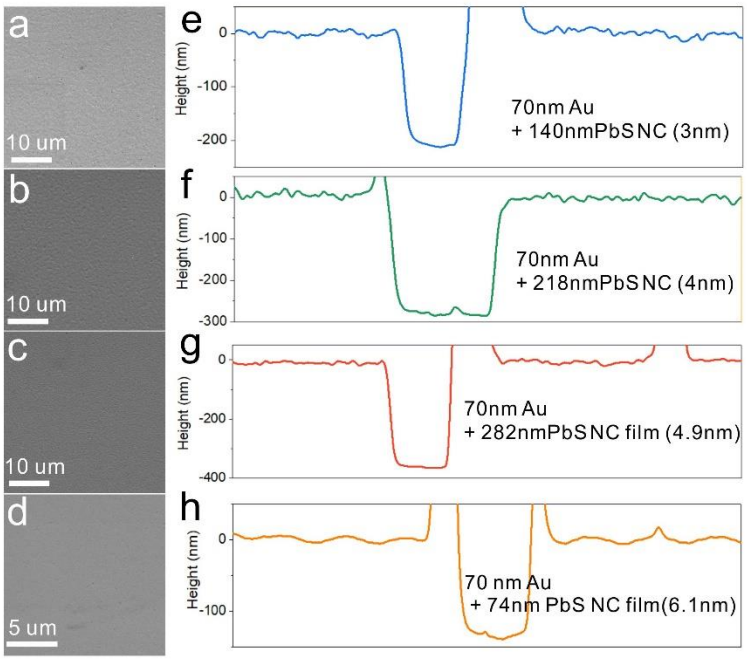

Figure 4.6 Surface morphology of gold coated PbS nanocrystal thin films composed of (a) 3nm, (b) 3.5 nm, (c) 4.9 nm, and (d) 6.1 nm PbS nanocrystals. (e-h) The height

profile obtained by scanning cross a pre-made scratch with profilometry from a to d, respectively.

~50 mg/ml PbS NC with OA ligand of various core sizes are drop-casted onto pre-cleaned Si substrates. After drying of the solvent at room temperature, the resulting thick film (>1 um) was further heated up to 100 ℃ for residual solvent removal. Similarly, the thickness of spin-coated thin films can also be derived through performing profilometry on gold-coated PbS NC thin films. As shown in Figure 4.6a-d, SEM images of gold-coated PbS NC thin films of various core sizes show very similar surface morphology. Thickness of PbS NC thin films are determined by subtracting the gold film thickness (~70 nm) from the overall thickness derived from profilometry profile (Figure 4.6e-h).

4.5.1.4 ***Material characterizations***

Transmission Electron Microscopy (TEM) and Scanning Electron Microscopy (SEM): PbS NC morphology and size were characterized using a FEI CM-200 TEM operated at 120 kV. This same TEM instrument was also used for HRTEM on samples before and after ligand exchange. To conduct HRTEM, the NC solution was drop-casted onto a carbon-coated TEM grid. The micro-morphology of the NC solid thin films was characterized using a FEI XL-30 SEM.

Atomic Force Microscopy (AFM) and Profilometry: Surface roughness of PbS NC thin films and NCSLs was characterized with a Bruker Multimode AFM using the tapping mode. The film thickness was measured by mapping the height profiles around a scratch. And the film thickness was further verified with profilometry characterizations around the scratch.

Thermogravimetric Analysis (TGA) on PbS NC Solids Thin Film and NCSL: TGA of the PbS NC thin films and NCSLs was carried out utilizing a TA instrument with a heating rate of 5 °C/min under a nitrogen flow.

Heat Capacity Measurements with Differential Scanning Calorimetry (DSC): DSC of PbS NC solids was carried out using a TA instrument. 10-20 mg of NC solids were sealed in Al pans. The DSC scans were collected from 77K to 400K with a heating and cooling rate of 20 °C/min. Aluminum oxide was used as a reference sample.

Table 4.1 Ligand mass fraction, ligand capping density, and composite density of oleic acid ligated PbS nanocrystals of various core sizes in both thin film (TF) sample form and superlattice (SL) sample form.

	3nm	3.5nm	4.9nm	6.1nm
TF_Ligand mass fraction (%)	36.4	33.3	25.07	17.8
SL_Ligand mass fraction (%)	33.2	28.5	23.9	14.2
TF_Ligand capping density (nm^{-2})	4.64	5.3	4.43	3.57
SL_Ligand capping density (nm^{-2})	4.03	4.3	4.15	2.73
TF_density (g cm^{-3})	2.62	2.89	3.37	3.54
SL_density (g cm^{-3})	3.07	3.25	3.83	3.83

Combining TGA analysis and a simple geometrical model (see section 3.5.3.2) allows us to estimate the ligand mass fraction and capping densities, and the densities of PbS NC thin films and NCSLs of various core sizes. As shown in Table 4.1, on one

hand, PbS NCSL possesses slightly smaller ligand capping density but higher density than that of PbS NC thin films. On the other hand, ligand capping density exhibits a weak NC size-dependence. And density of both PbS NCSL and NC thin films increases with increase of NC size.

4.5.2 Mechanical Measurements and Coarse-grained Modeling

4.5.2.1 *Nanoindentation*

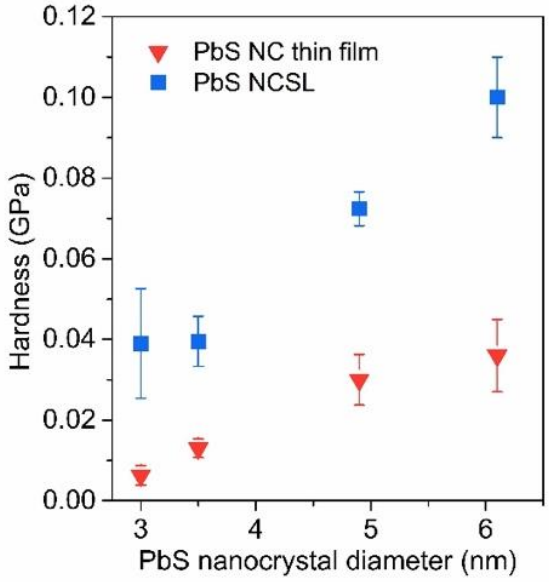

Figure 4.7 Hardness of PbS NC thin films and NCSLs of various NC core sizes measured with nanoindentation.

Young's modulus of the NC solid film is evaluated using nanoindentation. A commercial nanoindenter system (Nanoindenter XP-II, Agilent) equipped with a diamond Berkovich tip is utilized to perform the test. The tip area function was first calibrated using a standard silica sample. Then nanoindentation was carried out on the film surface to an indentation depth of 400 nm. Tests were conducted in strain rate control mode (0.05 s^{-1}). 20 indents were made to get an average Young's modulus of each NC solid film. Indentation was limited to 300 nm to avoid any potential substrate

effects. This indentation depth is within 10% of PbS nanocrystal thin film thickness (~3um) and PbS nanocrystal superlattice thickness (>4um). Load-displacement curves for the loading and unloading of indents on the NCSL and NC thin film were recorded. The maximum loads obtained are quite different between nanocrystal thin film and superlattice, which indicate a difference in hardness. Young's modulus, *E*, can also be inferred from this load-displacement curve.

We calculated the average sound velocity (v_s) using the following equations:

$$v_L = \sqrt{\frac{E}{\rho}\left[\frac{(1-\sigma)}{(1+\sigma)(1-2\sigma)}\right]}$$

$$v_T = \sqrt{\frac{E}{2\rho(1+\sigma)}}$$

$$v_s = \frac{v_L + 2v_T}{3}$$

Where:

v_L: longitudinal sound speed

v_T: transversal sound speed

E: Young's modulus of NC solid

ρ: density of NC solid

σ: Poisson ratio (a universal Poisson ratio of 0.3 is used)

4.5.2.2 ***Coarse-grained model***

PbS NC system was described using a coarse-grained model, where each NC plus the OA ligands are simplified as a spherical unit of diameter with a ligand shell of

certain length. The pairwise interaction energy for nanocrystals can be expressed as follows:

$$U(r) = U_{vdw}(r) + U_{electrostatic}(r) + U_{L-L}(r)$$

Where r is the interparticle distance. The attractive van der Waals interaction between two spherical nanocrystal cores can be expressed as:

$$U_{vdw}(r) = -\frac{A}{6}[\frac{2a_1a_2}{r^2-(a_1+a_2)^2} + \frac{2a_1a_2}{r^2-(a_1-a_2)^2} + \ln(\frac{r^2-(a_1+a_2)^2}{r^2-(a_1-a_2)^2})]$$

Where A is the Hamaker constant and a_1, a_2 are radius of two nanocrystals, respectively. Specifically, we set A to be 0.075 eV based on previous report.[91] We also set a_1 equals to a_2 as we are dealing with two identical NCs. The electrostatic interaction can be induced by charges, permanent and induced dipoles. PbS nanocrystals were reported[92] to possess a permanent dipole driven by ligand-induced tensile strain, and the magnitude is linearly related to the size of the PbS nanocrystals. Specifically, for 3.2 nm OA capped PbS NC, a net dipole moment of 190 D is used.[92] Thus, a dipole-dipole interaction energy was considered and calculated using equation below:

$$U_{dipole-dipole} = \frac{1}{4\pi\epsilon_0\epsilon_r r^3}[\boldsymbol{P_1}\cdot\boldsymbol{P_1} - 3(\boldsymbol{P_1}\cdot\boldsymbol{r})(\boldsymbol{P_2}\cdot\boldsymbol{r})]$$

Where $\boldsymbol{r}$ is the vector connecting two nanocrystals, $\boldsymbol{P_1}$ and $\boldsymbol{P_2}$ are dipole moments of nanocrystal 1 and 2. ϵ_0 and ϵ_r are vacuum permittivity and dielectric constant of OA matrix, which are further set to be 8.85E-12 F/m and 2[91], respectively. The ligand-ligand interaction can be described using the classical Lennard-Jones form, and is also assumed to be proportional to the overlap volume of two neighboring ligand shells:

$$U_{L-L} = 4\varepsilon[(\frac{\sigma}{r})^{12} - (\frac{\sigma}{r})^{6}]V_{overlap}\rho_L/M_L$$

$$V_{overlap} = \frac{\pi}{2}(2L - (r - 2a))^2 R + \frac{\pi}{6}\big(2L - (r - 2a)\big)^2 (2L + (r - 2a)/2)$$

Where ε is the depth of the potential well, σ is the finite difference at which the inter-particle potential is zero, ρ_L is the density of ligand shell, L is the ligand shell thickness (~1 nm), and M_L is the molar weight of OA ligand matrix. ρ_L is derived by combining thermogravimetric analysis (TGA) results and a simple geometrical model (see section 3.5.3.2). To determine the parameters in the Lennard-Jones potential for describing ligand-ligand interaction, we used Salem's theory[93] to calculate the attraction force between two parallel alkane chains at short distance:

$$W = A\frac{3\pi}{8\lambda^2}\frac{L}{D^5}$$

Where λ and L are the length of CH_2 and whole alkane chain, respectively. D is the distance between two adjacent alkane chains. In our case, D was related to ligand capping density ρ_c, which can be determined from TGA on the NC solids sample. Assuming a hexagonal array of interdigitated ligand molecules, D can be derived as $D = \sqrt{1/2\rho_c}$. In the end we calculated the molar-based attraction interaction of interdigitated ligand shells. The vdW interaction of ligands are assumed to decrease with decrease of nanocrystal size. This assumption is based on the fact that OA ligands from neighboring NCs are harder to interdigitate due to increased surface curvature. In our model, we multiply ε by a decay constant τ (<1) in LJ expression to account for the decrease of interaction energy of ligands on smaller nanocrystals. We further assumed τ linearly decreases with decrease of NC sizes. Additionally, we increase ε by 20% in LJ expression for ligand-ligand interaction in PbS nanocrystal superlattice as compared to that of PbS nanocrystal thin films. This increase by 20% is kind of arbitrary, but our control simulations suggest that the change in ε is not affecting the simulation results significantly. On the other hand, colloidal nanocrystal superlattice

tends to exhibit a smaller internanocrystal distance than that of disordered nanocrystal thin film. In our model, we use 1.2 nm and 1.5 nm as the equilibrium internanocrystal distance for nanocrystal superlattice and thin film, respectively.

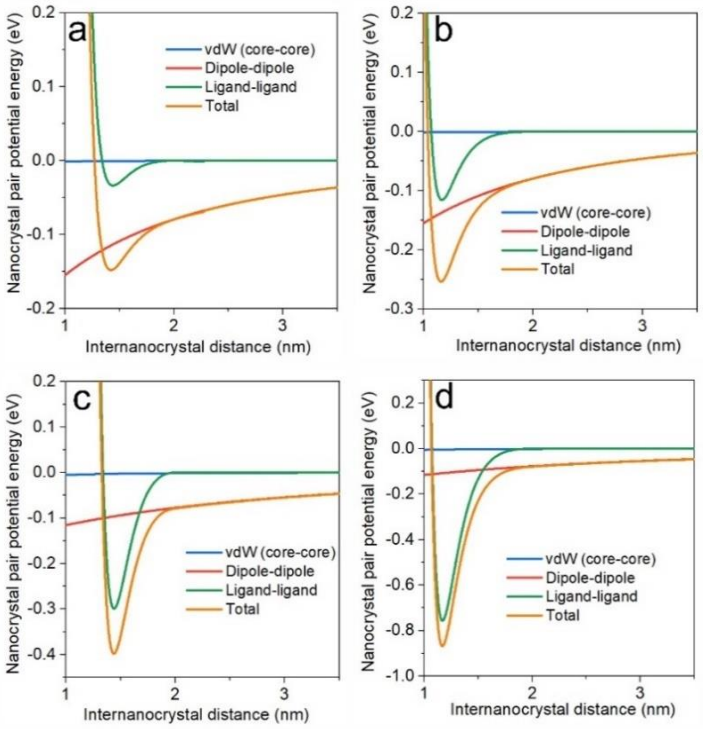

Figure 4.8 NC pair potential for 3nm PbS NC (a) thin film and (b) superlattice. NC pair potential for 6nm PbS NC (c) thin film and (d) superlattice. The NC pair potential energy comes from 3 major contributors: vdW attraction of NC cores (blue), dipole-dipole interaction of NC cores (red), and vdW interaction of neighboring ligands (red). And the total energy from all contributions are also shown (orange).

As shown in Figure 4.8c, d, the derived pair potential for 6nm PbS nanocrystals shows that ligand-ligand vdW attraction dominates the NCs' interaction near the equilibrium position. Hence the mechanical property of NC solids is also dominated by the ligand-ligand vdW attraction. This suggests NC solids should possess polymeric mechanical behavior, which is in line with previous reports. However, as indicated in

Figure 4.8a, b, for 3nm PbS nanocrystals, ligand-ligand vdW attraction becomes much smaller and becomes comparable to dipole-dipole interaction or even below that as a result of poor ligand-ligand alignment and interdigitation. In this case, both ligand-ligand vdW interaction and dipole-dipole interaction contribute to attraction of neighboring NCs. This explains why 3nm PbS NC thin films and NCSLs possess smaller Young's modulus than that of larger NC sizes. Lastly, we note that core-core vdW interaction is weakest in all the cases, which suggests that core-core vdW interaction contribute little to attraction between adjacent NCs and thus mechanical response of nanocrystal assemblies.

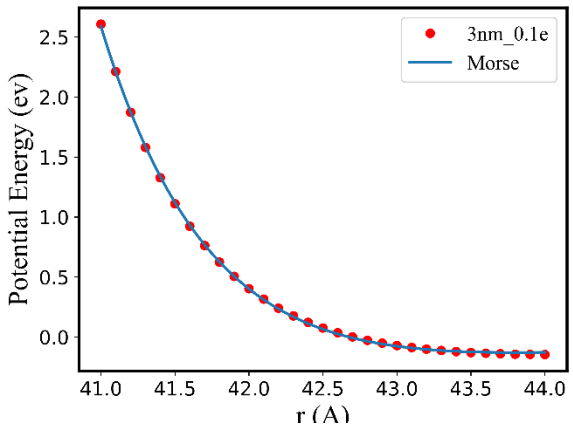

Figure 4.9 Morse fitting result for the pair potential of two 3nm NCs.

For simplicity, the derived pair potential was fitted with classical Morse format using the following expression:

$$E = D_0\left[e^{-2\alpha(r-r_0)} - 2e^{-\alpha(r-r_0)}\right], r < r_c$$

here r_c and r_0 are the potential cutoff and the equilibrium distance, respectively. D_0 are in energy unit, α is in 1/distance unit. However, to identify the impact of the permanent dipole-dipole interaction with r^3 term of the NC-OA system, a revised

Morse equation with a constant energy term D_1 added to the equation is used for well capture the overall energy landscape around the equilibrium. The revised equation is as follows:

$$E = D_0\left[e^{-2\alpha(r-r_0)} - 2e^{-\alpha(r-r_0)}\right] + D_1, r < r_c$$

Further, to ensure the accuracy of the fitted Morse model compared to the analytical result. The equilibrium position is identified. Following that the energy landscape is fitted at -5% to +5% range around the equilibrium point. This operation is feasible for studying the mechanical property of NC-OA system especially under small deformation (strain ~ 1%). As shown below in Figure 4.9, the example of the Morse fitting result for the 3nm NC-OA system.

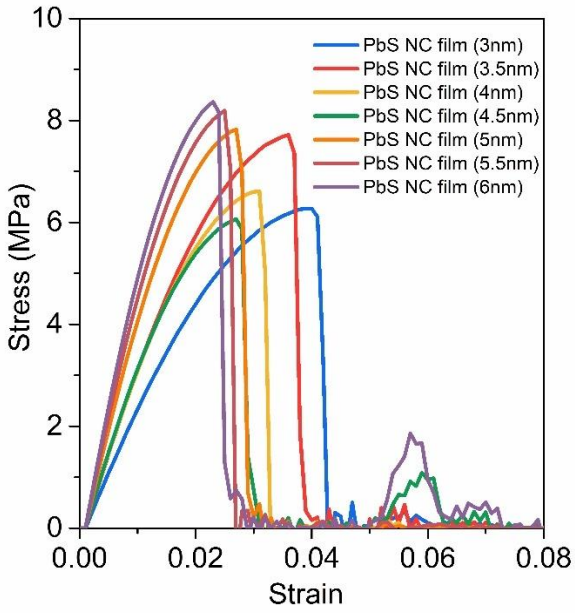

Figure 4.10 Representative stress-strain curves derived from MD simulations on PbS nanocrystal thin film coarse-grained model with a uniaxial tension strain applied along the <100> direction.

The concise expression of the Morse formula makes it feasible to study large NC system. Once the parameters in the Morse equation (above) is determined. We were able to build up NC superlattice model composed of over 100 thousand NCs and performed molecular dynamic simulations on the nanolattice unit cell bulk crystals of the NC-OA system to elucidate its elastic properties. Here, coarse-grained simulations are performed using LAMMPS package. Periodic boundary conditions (PBC) are applied along all three directions of the nanolattice cell. Initially, we performed the molecular dynamics simulations within the Isothermal-Isobaric (NPT) ensemble for 800ps with a time step of 1 fs. Such treatment is supposed to relax the system while letting the structure reaches its equilibrium state. During the equilibrium process, the total temperature was kept at 300 K and the pressure along all three axial directions were kept at zero. After that, the equilibrated structure was elongated along x-direction with a uniaxial tension strain up to 10% of the original length, while the pressure component on the y and z direction are controlled to maintain the uniaxial tension condition. The deformation-controlled strain rate of $10^{-9}s^{-1}$ were applied along the x direction. After analyzing the stress-strain relation, young's modulus is extracted by fitting the linear part (~ 0.002).

To systematically investigate the mechanical properties of NC-OA bulk crystals, elastic constants of NC-OA bulk crystals, young's modulus, bulk modulus, Poisson's ratio are calculated. In general, the elastic constants are obtained using the stress-strain method based on the generalized Hooke's law. As is shown in Figure 4.10 and Figure 4.2f, Young's modulus of PbS nanocrystal thin films exhibit a NC size dependence, which is in line with the experiments. Comparatively Young's modulus of PbS nanocrystal superlattices (Figure 4.11 and Figure 4.2f) exhibit a much more pronounced NC size dependence, which is also in good agreement with experiments.

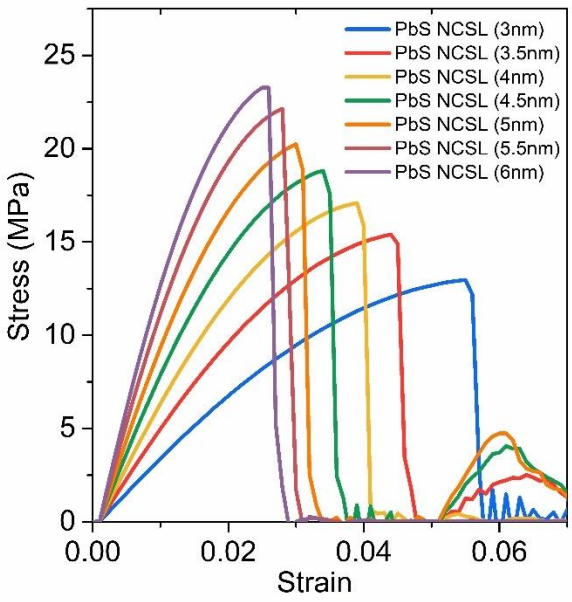

Figure 4.11 Representative stress-strain curves derived from MD simulations on PbS nanocrystal superlattice coarse-grained model with a uniaxial tension strain applied along the <100> direction.

Because of the symmetry of the crystal, the C_{11}, C_{22}, and C_{33} of face-centered cubic (FCC) NC assemblies are the same and the largest of all the compounds, which provides the evident that the NCA crystal is hard to be compressed under external uniaxial stress along the [100], [010], and [001] directions. C_{44}, C_{55} and C_{66} represent the shearing strength at (100), (010) and (001) crystal plane, respectively. The mechanical modulus, such as the bulk modulus (B) and the shear modulus (G) are evaluated with Viogt-Reuss-Hill (VRH) approximation[94] using the elastic constants for single bulk crystal. Young's modulus (E) and Poisson's ration (ϑ) are estimated by the following expressions:

$$E = 9BG/(3B + G)$$

$$\vartheta = (3B - 2G)/(6B + 2G)$$

The Poisson's ratios (ϑ) of all NCA crystals are close to 0.3 indicating they possess weak metallic characters. The obtained modulus values are listed in Figure 4.2f. Meanwhile, because the intrinsic hardness is proportional to the shear modulus, the stronger bond/interaction between the NCA crystals generally indicates the hardness is larger. This qualitatively explains why experimentally, the bigger size of the nanocrystal, the higher hardness.

4.5.3 Frequency Domain Thermoreflectance (FDTR) Measurements

4.5.3.1 *Basic principles*

FDTR is one of the pump-probe techniques for measuring thermal transport properties of bulk crystals, thin films and etc. Specifically, A modulated pump laser ($\lambda = 488\ nm$) heats the sample up and thus introduces a periodic temperature variation at the surface of the sample. On the other hand, an unmodulated probe laser ($\lambda = 532\ nm$) senses the temperature variation by corresponding reflectivity variation at the top gold layer. Phases of reflected pump and probe beams are collected by a photodiode. Eventually, we collect the phase lag between pump and probe beam frequencies ranging from 100 kHz and 50 MHz and use it to fit a theoretical heat transfer model, from which we can extract the sample thermal conductivity.

4.5.3.2 *Samples preparation for FDTR*

PbS NC thin films and NCSLs of various NC core sizes are coated with ~80nm gold via electron beam deposition. As shown in Figure 4.12, we observed a uniform and continuous gold transducer coating that covers the surface of both PbS nanocrystal superlattice and thin films. It is noteworthy that we saw some local roughness of gold film that arises from the surface roughness of the colloidal nanocrystal superlattice and thin films. 4.9 nm PbS NCSL exhibits highest surface roughness, which presents a challenge for our thermal transport measurement. Some nanocracks were also seen

in the gold films that deposited onto (m) 3nm and (p) 6.1 nm PbS nanocrystal thin films, respectively. This is different from gold films deposited onto bare Si substrates. The surface roughness change and presence of nanocracks can affect electronic and thermal conductivity of gold transducer film. Measurements and more detailed discussion will be covered in the next section.

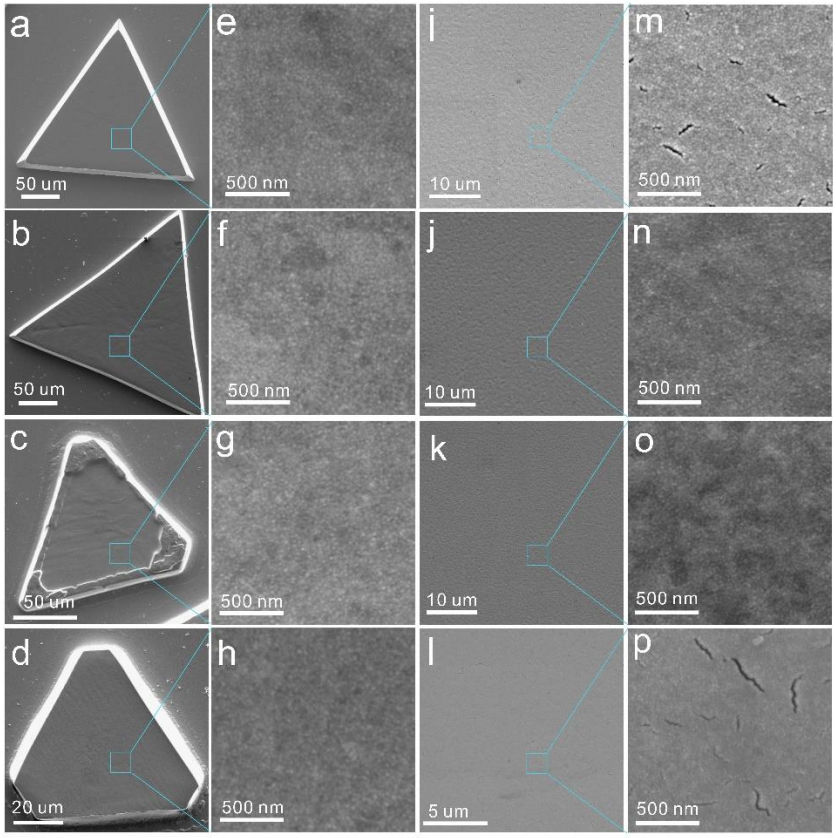

Figure 4.12 SEM characterizations of PbS nanocrystal superlattices and thin films of various core sizes after gold transducer deposition. (a-d) representative 3nm, 3.5nm, 4.9nm, and 6.1nm PbS nanocrystal superlattice with gold films on top, respectively. (e-h) high magnification SEM images of Au film on top of 3nm, 3.5nm, 4.9nm, and 6.1nm PbS nanocrystal superlattice show similar grain size of gold. (i-l) 3nm, 3.5nm, 4.9nm, and 6.1nm PbS nanocrystal thin films with gold films on top, respectively. (m-

p) high magnification SEM images of Au film on top of 3nm, 3.5nm, 4.9nm, and 6.1nm PbS nanocrystal thin films show similar grain size of gold.

4.5.3.3 ***Au film thermal conductivity***

Per our discussion above, Au film electronic and thermal conductivity can vary when deposited onto different substrates. We performed electronic conductivity measurements on gold films on top of PbS nanocrystal thin films of various core sizes utilizing both van der Pauw method and four-probe method (Kelvin technique). Then we convert electronic conductivity into thermal conductivity by applying Wiedemann-Franz law.

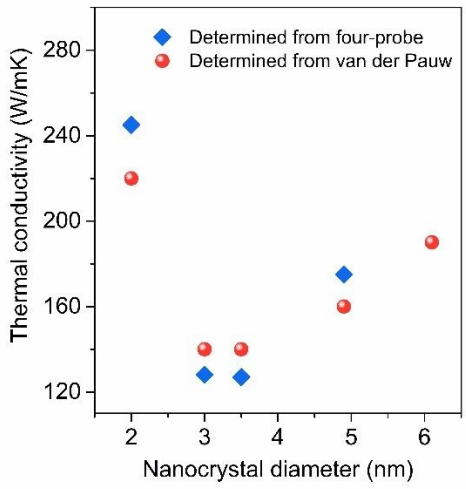

Figure 4.13 Electronic thermal conductivity of gold films deposited onto Si and PbS nanocrystal thin films.

Representative data is shown in Figure 4.13. Evidently gold film thermal conductivity can be affected by PbS nanocrystal surface morphology. It should be pointed out that this parameter is critical to our FDTR measurements as our sensitivity analysis already shows that the fitted thermal conductivity is very sensitive to gold film thermal conductivity. Specifically, thermal conductivity of gold films on top of PbS

nanocrystal thin films are 15-35% lower than that of Si bare substrates due to surface roughness, nanocracks, and possibly smaller grain sizes. Additionally, electronic and thermal conductivity of gold films on top of PbS nanocrystal superlattices are not measurable with either van der Pauw method or four-probe method due to the small size of the gold film. In this case, we employed a "MSE contour" method to find out the best combination of gold thermal conductivity and PbS NCSL thermal conductivity that matches the measurements best.

4.5.3.4 ***Data analysis***

The raw data collected from FDTR measurements was combined with a heat conduction model as well as some physical properties measured via experimental techniques (i.e. density, heat capacity) to derive the thermal conductivity of the sample.

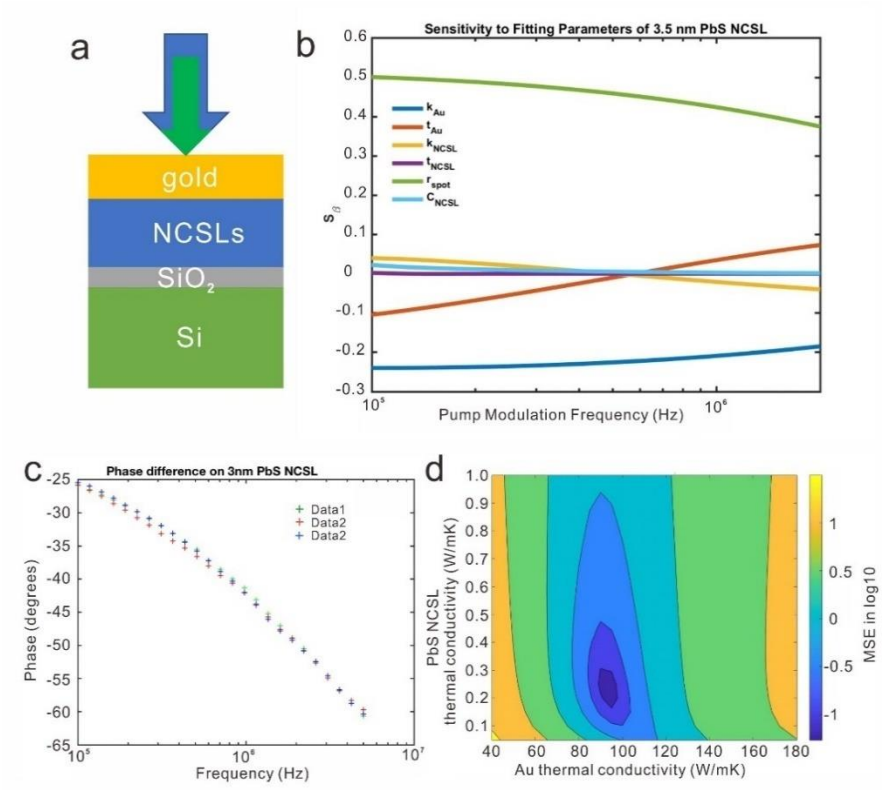

Figure 4.14 FDTR measurement details on PbS NCSLs. (a) sample configuration for pump-probe FDTR method. (b) sensitivity analysis of FDTR measurements on PbS nanocrystal NCSLs. (c) phase difference consistency from 3 separate measurements. (d) MSE contour as a function of Au thermal conductivity and PbS NCSL conductivity for 3nm PbS NCSL. This plot allows us to explore how various combination of these two parameters could produce models that are closest to experimental measurements.

To improve the fitting accuracy, we conducted a fitting parameters sensitivity analysis. All the physical properties of the material system that are involved in the heat conduction model is investigated. As shown in Figure 4.14a, physical properties of each layer play roles in the heat conduction model. By performing the sensitivity analysis, we can find out the parameters that affects the fitting results most. If we can lower the uncertainty of these parameters, we will be able to improve the fitting significantly. The model sensitivity to fitting parameters, S_β, can be expressed as

$$S_\beta = \frac{dln(\varphi)}{dln(\beta)} \sim \frac{\ln(\varphi)_{adjusted} - \ln(\varphi)_{nominal}}{\ln(\beta)_{adjusted} - \ln(\beta)_{nominal}}$$

Where φ is the phase lag, β is the physical properties (i.e. thickness, heat capacity).

As shown in Figure 4.14b, our model sensitivity to gold film thermal conductivity (k_{Au}) and laser spot size (r_{spot}) is highest. Additionally, our model also showed reasonable sensitivity to gold film thickness. Lastly, our model is insensitive to volumetric heat capacity (C_{NCSL}) and thickness (t_{NCSL}) of NCSL. In our experiments, the laser spot size was chosen to be ~3.2 um. Thus, accurate determination of gold film thermal conductivity becomes the main challenge here. Per our previous discussion, gold film thermal conductivity can vary when deposited to Si and nanocrystal thin films. Though we were not able to experimentally measure electronic conductivity of gold film on top of NCSL, we employed a "MSE contour" method that

allows us to find out the best combination of gold thermal conductivity and PbS NCSL thermal conductivity that matches the experimental measurement best. As is show in Figure 4.14d, in the case of 3nm PbS NCSL, we found out that NCSL and gold film have thermal conductivities of 0.25±0.5 W/mK and 90 W/mK, respectively. It is noteworthy that the gold thermal conductivity derived is lower than that of gold film on top of 3nm PbS NC thin films. We suspect this could be due to variance of heat dissipation during the deposition, but also acknowledge this merit further study. Lastly, we performed multiple measurements on different NCSLs and achieved good signal consistency (Figure 4.14c). The slight difference could be ascribed to: (1) laser spot size; (2) local difference of thermal conductivity of gold film. We further applied this method to interpretating the measurements on PbS NCSLs of various core sizes.

4.5.4 **Atomistic Molecular Dynamics Simulation**

To understand the mechanics and thermal transport of OA-OA interface at the atomistic scale, we built atomistic model of interdigitated OA-OA molecules and performed MD simulation to extract the mechanical properties using the LAMMPS package. The full atomistic investigations utilize the ReaxFF potential and a transferable force field as implemented in the LAMMPS (Large-scale Atomic/Molecular Massively Parallel Simulator) simulation package (http://lammps.sandia.gov/). The ReaxFF potential is previously developed for carbon-carbon interactions and hydrocarbon oxidation[95]. The first-principle based ReaxFF force field has been shown to provide an accurate account of the chemical and mechanical behavior of hydrocarbons, and carbon nanostructures[96, 97], while it is capable of treating thousands of atoms with near quantum-chemically accuracy. ReaxFF also allows for an explicit consideration of long-range and nonbonded interactions such as van der Waals, Coulombic, and hydrogen bond interactions, making it particularly suitable for our study of OA-OA ligand interaction. The time step was chosen to be on the order of a

fraction of femtoseconds (0.15×10^{-15}s) to ensure the stability of the simulations and reflect the relatively high vibrational frequency of the hydrogen atoms. All full atomistic simulations were subject to a microcanonical (NVT) ensemble, carried out at a temperature of 30K and 300 K. Temperature control was achieved using a Berendsen thermostat. Energy minimization runs of the system are performed using a conjugate-gradient (CG) algorithm with an energy-convergence criterion implemented in the LAMMPS code.

4.5.4.1 **Mechanics simulation**

A pair of interdigitated OA ligands with different overlap are created. The variance in ligand overlap can be easily seen from the difference in the length of the simulation cells on the x axis ($3.3nm \times 0.67nm \times 0.67nm$ and $2.6nm \times 0.67nm \times 0.67nm$). The models with more overlap and less overlap represent ligand-ligand interactions in ordered NCSL and disordered NC thin film, respectively. The ligand pairs were then equilibrated within the Isothermal-Isobaric (NPT) ensemble for temperature and pressure control, respectively, at a time step of 0.015 fs. The structure was first gradually heated from 10 to 300 K over a time span of 500 fs, then annealed at 300 K for 500 fs, and subsequently quenched to 30 K over a time span of 500 fs. Finally, the structure was further annealed at 300 K and zero pressure for the duration of 2 ps to ensure complete equilibration of the structure. Such treatment is supposed to relax the system to its equilibrium state. After this equilibration treatment, the ligand pair were replicated 5 times along y and z direction to simulate the overlapping region of two nanocrystal resulting 50 OA ligands and 2650 atoms in total. The O atoms at both ends along the x boundary are fixed on the y and z direction, which reduces the fluctuation and movements of the OA ligands. We also switched to an NVT ensemble at 30K in order to estimate the mechanical strength of the OA ligand system. At the meantime, x boundary condition is converted to be shrinkable boundary condition with a constant

expansion speed at 0.005 A/fs, while y and z boundary conditions are kept as periodic. The atomic displacement data were recorded at every 10-time steps to compute the displacement correlation functions. After analyzing the stress-strain relation, young's modulus is extracted by fitting the initiate linear part (~ 0.002).

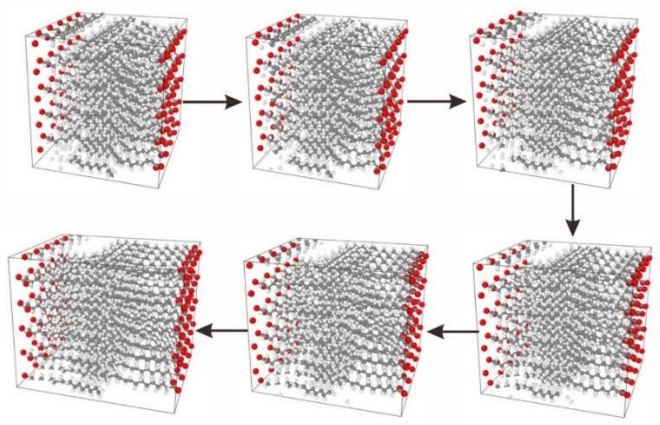

Figure 4.15 Snap-shorts of OA-OA bilayer upon applying a tensile stress in an atomistic MD simulation at 30K.

To study the mechanical properties of the OA-OA bilayer at room temperature (300K), the ligand pairs are first replicated along y and z direction for 5 times. The O atoms at both ends along x direction are fixed along x direction leaving y and z direction free to move, which is used to relax the inter ligand space but keeps the overlapping area fixed. The OA ligand models were then equilibrated within the Isothermal-Isobaric (NPT) ensemble for temperature and pressure control, respectively, at a time step of 0.015 fs. The structure was first gradually heated from 10 to 300 K over a time span of 500 fs, then the structure was annealed at 300 K and zero pressure for the duration of 2 ps to ensure complete equilibration of the structure. Such treatment is supposed to relax the system to its equilibrium state. After equilibration, we switched to an NVT ensemble at 300K in order to estimate the mechanical strength of the OA ligand system. At the meantime, x boundary condition

is converted to be shrinkable boundary condition with a constant expansion speed at 0.005 A/fs, while y and z boundary conditions are kept as periodic. The atomic displacement data were recorded at every 10-time steps to compute the displacement correlation functions. After analyzing the stress-strain relation, young's modulus is extracted by fitting the initiate linear part (~ 0.2%).

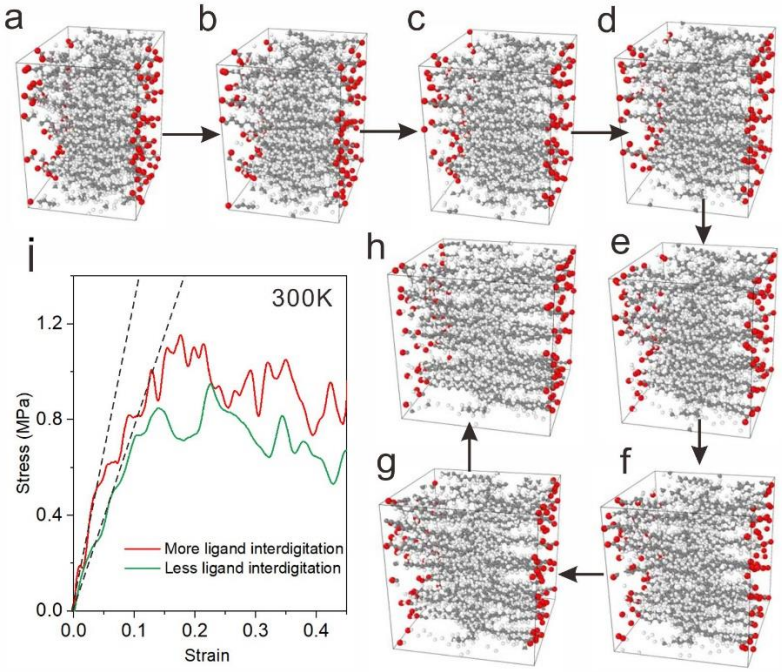

Figure 4.16 (a-h) Snap-shorts of OA-OA bilayer upon applying a tensile stress in an atomistic MD simulation at 300K. (i) Stress-strain curves derived from atomistic MD simulations upon OA-OA bilayer of various ligand interdigitation at 300 K.

Figure 4.15 shows the snap short of the interdigitated OA-OA bilayer model at different strain. The stress-strain curves obtained from these models are shown in Figure 4.2i. Evidently the OA-OA bilayer model of higher interdigitation volume leads to higher slope in its stress strain curve, which suggests a higher Young's modulus. This is in good agreement with experiments as well as theories. As is stated in Salem's theory[93], attraction between two saturated carbon chains is proportional to overlap

chain length, while is inversely proportional to fifth-power of distance between two parallel carbon chains. As in colloidal PbS nanocrystal superlattice, ligands from adjacent nanocrystals have a smaller internanocrystal spacing and this further leads to a stronger ligand-ligand attraction. Additionally, ligands within colloidal PbS nanocrystal superlattice are believed to be better aligned as they reach a thermodynamically stable state. This means the average distance between the adjacent ligand chains are smaller for nanocrystal superlattice, which further leads to stronger ligand-ligand attraction. For simplicity, this difference in ligand arrangement order is not explicitly accounted in our MD model.

At low temperature, ligands tend to maintain higher packing order due to weak thermal vibrations of the chain. However, at room temperature, ligands packing order disappear, which is shown in Figure 4.16. In this case, the attractive interactions between adjacent ligands also became weaker and further leads to smaller Young's modulus as compared to that of low temperature. Still, we were able to observe a higher Young's modulus for OA-OA bilayers of more ligand interdigitation.

4.5.5 **Mass-spring Model of PbS NCSL**

In a mass-spring model, the energy of phonon modes scale with $\sqrt{k(a)/m(a)}$, where k is the spring constant of the ligand-ligand interaction that links the neighboring NCs, and m is the mass of NC core mass plus the ligand shell mass. Specifically, $k(a)$ is determined as:

$$k(a) = \frac{d^2U(r_0)}{dr_0{}^2}$$

where $U(r)$ is the potential energy of a NC pair, r_0 is the equilibrium position. The truncated-octahedron PbS NCs are approximated as sphere with radius a, then m can be estimated as:

$$m(a) = 4/3\pi a^3 \rho_{PbS} + 4\pi a^2 \rho_{OA} m_{OA}$$

where ρ_{PbS} is the density of PbS, ρ_{OA} is the OA capping density, which is usually determined by thermogravimetric analysis, m_{OA} is the mass of one OA ligand. The expected ultimate acoustic transversal and longitudinal phonon energies can be calculated as follows:

$$E_{TA} = \hbar\omega_{TA} \sim 1.2\sqrt{\frac{k(a)}{m(a)}}$$

$$E_{LA} = \hbar\omega_{LA} \sim 2\sqrt{\frac{k(a)}{m(a)}}$$

Additionally, the phonon group velocity for a particular branch x, v_x can be estimated as:

$$v_x \approx \frac{\omega_x}{k_x} = \frac{\omega_x a_{SL}}{\pi}$$

where a_{SL} is the lattice constant of the NCSL. The lattice thermal conductivity, κ_{lat}, from the LA phonon mode normalized by phonon mean free path:

$$\kappa_{lat}/l = \frac{4k_B}{\pi^2}\frac{v_{LA}}{{a_{SL}}^3}\left(\frac{k_B T}{\hbar\omega_{LA}}\right)^3 \int_0^{\hbar\omega_{LA}/k_B T} \frac{x^4 e^x}{(e^x - 1)^2}\, dx$$

Where l is the phonon mean free path, k_B is the Boltzmann constant.

Using the equation above, we calculate the coherent phonon thermal conductivity per MFP for PbS NC thin film and NCSL and the results are listed in Figure 4.17a, b, respectively. Thermal conductivity per MFP of both PbS NC thin film and NCSL decrease with increase of NC sizes. This is due to the fact that coherent phonon energy and group velocity decreases with increase of NC sizes. To directly compare with experimental results, we convert thermal conductivity per MFP into thermal

conductivity by multiplying assumed average MFP of coherent phonon at room temperature. As shown in Figure 4.17c, d, coherent phonon thermal conductivity is not comparable to measurements when phonon MFP reaches 6um for 3.0-6.1nm PbS NCSL and NC thin films. And this is very unlikely as the coherent phonon would be strongly scattered by a variety of paths (defects, impurities, NC mass fluctuations, and non-coherent phonon) at room temperature. However, our modeling also indicates that coherent phonon could contribute to thermal transport in NCSLs if the coherent phonon energy and group velocity can be greatly improved by enhancing elastic coupling of NC or further decreasing the core size of NCs.

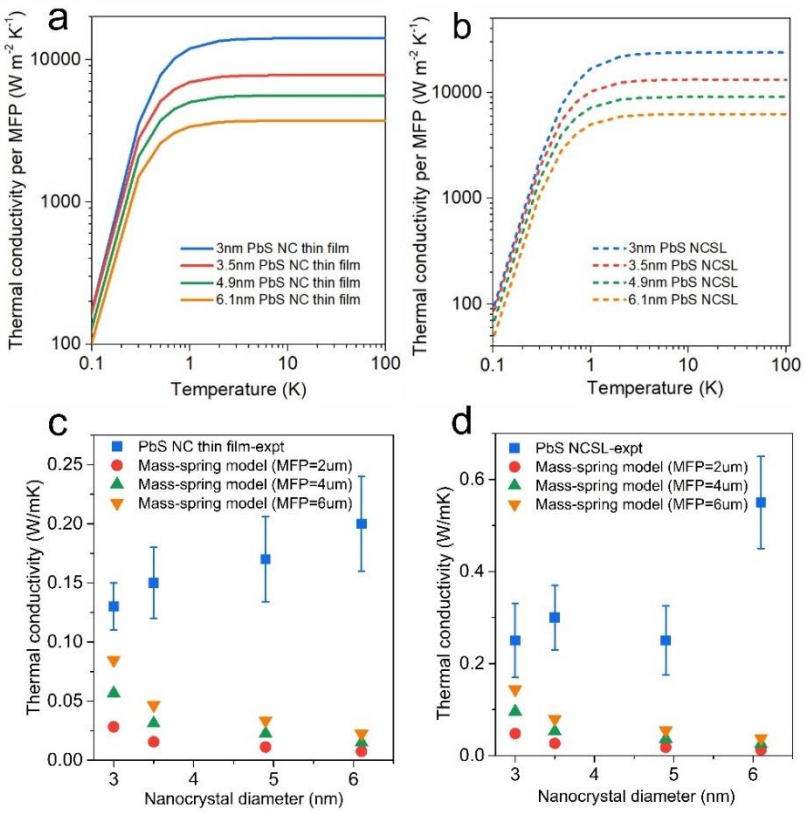

Figure 4.17 Thermal conductivity per phonon mean free path (MFP) originating from coherent phonons in colloidal nanocrystal (a) thin films and (b) superlattices using a simple mass-spring model. Comparison of experimental thermal conductivity and

predicted thermal conductivity from mass-spring model with assumed phonon mean free path for (c) NC thin film and (d) NCSL, respectively.

5 INORGANICALLY CONNECTED NANOCRYSTAL SOLIDS WITH EXCEPTIONAL MECHANICAL PROPERTIES

5.1 Abstract

Nanocrystalline materials exhibit unique mechanical properties due to presence of large grain boundary density. Colloidal nanocrystal (NC) serves as a promising building block for polycrystals of nanocrystalline grains. Additionally, assemblies of colloidal NCs are widely used in a variety of applications due to their unique electronic, optical, thermal, and magnetic properties. Hence, studying mechanics of colloidal NCs is of great importance for realization of nanocrystalline material of superior mechanical properties and robust devices. However, as-synthesized NC solids show a very limited range of elastic moduli (~1-10 GPa) and hardness (50-500 MPa), which presents a challenge for applications in which mechanical robustness is critical. The limited mechanical properties originate from the organic ligands that result in weak interparticle interactions in particle assemblies. In this work, we employed a coarse-grained model to understand the size-dependence and saturation of mechanical properties of organically capped NC solids. More importantly, we report the tremendous mechanical enhancement (a factor of ~60) achieved in CdSe NC solids through a simple ligand exchange process using $Sn_2S_6^{4-}$ ligands. After ligand exchange and drying, the short inorganic $Sn_2S_6^{4-}$ ligands dissociate into a few atomic layers of amorphous SnS2 at room temperature and interconnects the neighboring CdSe NCs. We observed softening of the composites as the size of CdSe NC decreases. We further identified the grain boundary as the mechanical bottleneck via atomistic simulations and analytical phase mixture modeling.

5.2 Introduction

The mechanical properties of nanocrystalline materials have been the subject of widespread research for the last two decades. Nanocrystalline materials are structurally characterized by a large volume fraction of grain boundaries, which significantly alters their mechanical properties. Compared to conventional polycrystalline materials, nanocrystalline materials may exhibit enhanced strength/hardness[98], improved toughness, enhanced mechanical and thermal stability[99] due to their unique structure. However, most synthesis of polycrystalline materials of nanometer size grains requires expensive and complicated techniques (i.e. inert gas condensation[100], mechanical alloying[101], electrodeposition[102], crystallization from amorphous material[103], and severe plastic deformation[104]). Furthermore, these techniques may have poor control over grain size distribution, interface structure, grain orientation etc, which presents a challenge for understanding and designing properties of nanocrystalline materials.

Colloidal NCs present great potentials for nanocrystalline materials with superior mechanical properties duo to their tightly controlled size, shape, faceted boundaries, surface chemistry, and low cost. This facile and versatile tunability allows their mechanical property to be designed and engineered. Apart from this, colloidal NC solids, which originates from the self-assembly of ligand passivated NCs, have demonstrated their potential in photovoltaics[105-107], thermoelectrics[54, 107, 108], transistors[107, 109], and optoelectronics[49, 107]. The successful bridging of length scales from nanoscale building blocks to macroscopic devices depends on the intrinsic thermomechanical robustness of the nanocomposites. Hence, understanding and engineering mechanical response of colloidal NC solids is crucial.

Unfortunately, as synthesized colloidal NC solids were identified to possess very poor mechanical property with a very limited range of elastic moduli (~1-10 GPa) and hardness (50-500 MPa). More recent measurements[110, 111] show that NC assemblies with organic ligands exhibited a facture toughness of ~50 kPa $m^{1/2}$, which reflects the brittle nature of these NC solids. This suggests that the soft organic ligands on top of inorganic core governs the overall mechanical response of colloidal NC solids. Researchers have developed several approaches, including ligand removal[41], ligand crosslinking[112], polymer grafts[42], and DNA grafts[44], to impart improvements to the mechanical robustness of colloidal NC solids. Nevertheless, these techniques either cannot be applied to chemically and thermal unstable NC systems (i.e. quantum dots) or lead to very limited range of mechanical enhancements.

In this work, we reported the enhanced mechanical properties (a factor of ~60) of CdSe NC solids through a thin tin disulfide layer in between the adjacent NCs. Short inorganic ligands or ions (i.e. metal chalcogenide complexes)[113] have been developed to replace the original organic ligands and thus enhanced the electronic coupling of NCs and further leads to improved charge transport properties. A more recent study by Scalise et al.[114] found that inorganic metal chalcogenide ligands dissociate into an amorphous passivation layer and bridge the neighboring NCs. Here, we found a few atomic layers of metal chalcogenide not only eliminate the soft organic ligands vdW contact but also improve the mechanical coupling of neighboring NCs. Specifically, after exchanging native long oleic acid ligand with $Sn_2S_6^{4-}$ ligands for 3.5 nm CdSe NC solids, its Young's modulus and hardness increase from 400 MPa and 50 MPa to 27 GPa and 1.6 GPa, respectively. Young's modulus and hardness of both organically and inorganically capped NC solids increase with increases of grain sizes. To understand this trend, we further performed computational studies to understand the mechanism in these two different systems. First, we employed a coarse-grained model to simulate

the organically capped NC solids. From this model we identified ligand-ligand vdW contacts as the mechanics bottleneck and further attributed the weak size dependence of NC solids' mechanical properties to NC surface curvature induced ligand interdigitation change when NC core size is varied. Second, we built fully atomistic models to simulate inorganically connected NCs. Our models successfully captured the reverse Hall-Petch relation of inorganically connected NCs. Further looking into the models allow us to conclude that the grain boundary activity and interfacial bonds are critical for determining their mechanical properties. Third, for both of the cases, analytical effective medium theory and phases mixture models were also utilized to understand the data of organically capped NC solids and inorganically capped NC solids, respectively. Our work motivates future experimental and computational work on mechanical properties of novel nanocrystalline materials originate from colloidal NCs.

5.3 Results and Discussion

We synthesized monodispersed 3-8 nm CdSe NC and ~1.5 nm CdS magic sized cluster (MSC) with organic (i.e. OA) and inorganic (i.e. $Sn_2S_6^{4-}$) ligands through a modification of literature recipes.[113, 115, 116] These synthesized NCs were carefully characterized with a combination of scanning electron microscopy (SEM), transmission electron microscopy (TEM), and scanning transmission electron microscopy (STEM) techniques. Figure 5.1a shows a representative TEM image of 3.5 nm CdSe-OA NC, where a wide spacing in-between the NCs is seen due to the presence of the thick OA ligand shell at the NC surface. As is vividly shown in Figure 5.1b, the organic ligands are believed to interdigitate with each other as a result of ligand-ligand attraction. On the other hand, as is shown in the STEM image (Figure 5.1d), CdSe-$Sn_2S_6^{4-}$ NCs were featured with very small interparticle spacing as a result of much smaller ligand molecule size and its self-driven dissociation into amorphous tin disulfides at room

temperature[114]. This was further demonstrated with a schematic shown in Figure 2e. UV-Vis spectrum shows that CdS MSC with OA and $Sn_2S_6^{4-}$ ligands possess absorption peaks within the UV range (Figure 5.5a), which suggests that their sizes are ~ 1.5 nm.[117] As a comparison, 3.5 nm CdSe NC with OA and $Sn_2S_6^{4-}$ ligands show an absorption peak of ~535 nm (Figure 5.5b). Eventually, we obtained smooth and thick (~3 um) films by simply drop-casting and drying concentrated NC and MSC solution onto silicon substrate, Figure 5.1c, f shows cross-sectional views of typical drop-casted 3.5 nm CdSe-OA and CdSe-$Sn_2S_6^{4-}$ NC solid films, respectively. To identify the interface structure and elemental distribution of CdSe-$Sn_2S_6^{4-}$ NCs, we performed STEM characterization. As is shown in figure 1g, evidently neighboring CdSe-$Sn_2S_6^{4-}$ NCs with different orientations feature a very thin gap. Further local EDS mapping on the NCs, as is demonstrated in Figure 5.1h-k, identifies the presence of a thin layer of amorphous tin disulfides on top of the crystalline CdSe core.

We continued to study mechanical properties and found CdSe-OA NC solids of various core sizes (3-8 nm) possess a very limited range of Young's modulus (0.3-2.5 GPa) and hardness (30-120 MPa). Schematic in Figure 5.2a illustrates the behavior of CdSe-OA NC solids during the nanoindentation tests, very small load is needed to break the vdW contacts of ligand molecules and displace the NCs. Representative load-displacement curves on 3.5nm CdSe-OA NC solids is shown in Figure 5.2b, and the inset of Figure 5.2b shows a representative clean indent on 3.5 nm CdSe-OA NC solids. The Young's modulus E was determined from the unloading slope. The hardness H of the film was determined as the ratio of the indentation force to the projected area of contact on the surface. Figure 5.2d, e shows Young's modulus and hardness of CdSe-OA NC solids as a function of NC core diameter, respectively. In general, CdSe-OA NC solids possess a Young's modulus of a few GPa and a hardness of a few tens MPa. Specifically, 3.5 nm CdSe-OA NC solids has Young's modulus and hardness of 0.4 GPa

and 35 MPa, respectively. Young's modulus and hardness of CdSe-OA NC solids increase with bigger NC core sizes, this was generally understood as a result of increased volume fraction of CdSe core along with the NC size increases.

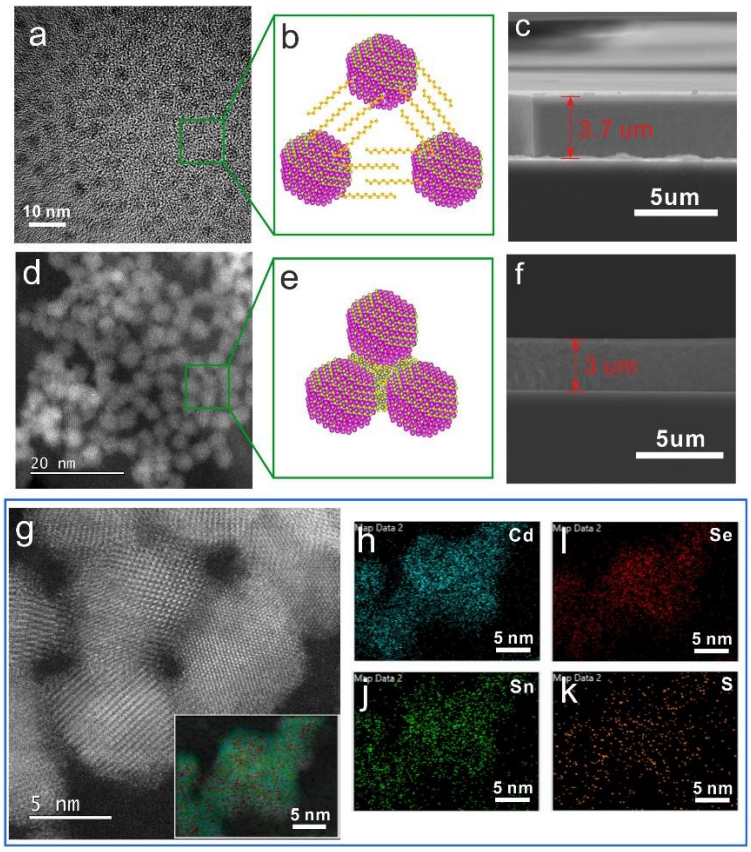

Figure 5.1 CdSe-OA NC and CdSe-SnS2 NC characterizations. (a) TEM image of 3.5 nm CdSe-OA NC; (b) schematic illustration of CdSe NCs with inter-digitated organic ligands; (c) cross-sectional view of deposited CdSe-OA NC solids film; (d) low magnification High-angle annular dark-field (HAADF)-STEM image of 3.5 nm CdSe-SnS2 NC; (e) schematic illustration of CdSe NCs with a thin layer of amorphous SnS2; (f) cross-sectional view of deposited CdSe-SnS2 NC solids film; (g) HAADF-STEM image of 7.2 nm CdSe-SnS2, the inset shows the combinational elemental mapping of a local NC region; (h-k) elemental mapping for Cd, Se, Sn, and S, respectively.

However, we noticed that Young's modulus and hardness of organically capped NC solids saturate at ~0.4 GPa and ~20 MPa at lower size ranges (<3.5nm). Composite models that assumes universal Young's modulus of organic matrix phase and inorganic dispersion phase failed to predict the trend of full range of sizes. Specifically, as is shown in Figure 5.2f, classical effective medium model underestimates the Young's modulus at higher size range while Halpin-Tsai model underestimates the Young's modulus at lower size ranges. There are already a few studies upon mechanical properties of organically capped NC solids materials both experimentally[38, 111, 118, 119] and theoretically[40, 120] in the literature. However, these works either employed empirical models (i.e. effective medium theory)[38] or rely on fully atomistic models (i.e. molecular dynamics simulation)[40] to interpret their results. We believe a more accurate and efficient model is still needed to understand the mechanics of NC solids of full-size ranges.

Here, we demonstrate that an analytical coarse-grained model built up with a pair potential can fit the entire NC size range. As is demonstrated in Figure 5.2c, we identify three major contributions to the attraction between the neighboring NCs: vdW attraction between the cores, dipole-dipole interactions between the cores, ligand-ligand vdW interactions. The vdW force between the inorganic cores can be adequately expressed as a function of NC core radius and interparticle distance (see section 5.5 of this chapter for detail). The presence of permanent dipole moment in CdSe NC core due to spontaneous polarization of CdSe wurtzite lattice leads to dipole-dipole interaction, and this interaction is described as a function of dipole moments and interparticle distance (see section 5.5 of this chapter for detail). However, it is extremely difficult to accurately quantify the strength of the short range vdW interactions between the organic ligands, on one hand, the neighboring ligands interdigitate near the equilibrium position, which is attractive and can be calculated

using Salem's theory[93]. Previous study[40] shows that neglection of ligand-ligand vdW attraction greatly underestimates mechanical properties of NC solids. On the other hand, once the ligand shells are too close to each other, the interaction become repulsive due to the stearic effect. In our case, we use classical Lennard-Jones potential form to represent both attractive and repulsive interactions of the ligands, and we further made an assumption that this interaction is proportional to the overlap volume between the ligand shells (see section 5.5 of this chapter for detail). We then obtain the pair-wise potential for two neighboring NCs by simply sum up all these three terms. As is indicated in Figure 5.6, ligand-ligand interaction dominates over both core-core vdW interaction and dipole-dipole interaction, which suggests the mechanical response in these CdSe-OA systems originate from their ligand-ligand vdW attraction. We anticipate stronger ligand interactions as the NC core increases. As the surface curvature is lowered with the increase of the NC core size, which indicates facilitated ligand interdigitation thus stronger ligand-ligand interaction. On the other hand, we anticipate a lower amorphous limit for ligand interactions in lower size range. Specifically, we let the energy parameter epsilon in Lennard-Jones potential to decrease with core size decrease and saturate at a core size of ~3nm. A face-centered cubic superlattice made up of 1500 NCs can be built up with this pair-wise potential (Figure 5.2c). To derive the mechanical properties of the system, we employed a classical "stress-strain" method (see section 5.5 of this chapter for detail). As is demonstrated in Figure 5.2d, e, using this coarse-grained model, we were able to fit the experimental data nicely in both magnitude and trend. Our measurements along with our model identify the ligand-ligand interface as the mechanics bottleneck, and further attribute the weak size-dependence of mechanical property to varied ligand-interdigitation as a result of surface curvature change. He et al.[85] drew similar conclusions from their mechanical studies on organically capped NC monolayer

membranes. Other important mechanical properties, such as yield strength, bulk modulus, shear modulus, and Poisson ratio of CdSe-OA NC solids is also derived and shown in Table 5.1(see detail in SI). The extremely low yield strength (i.e. 7.9 MPa for 3nm CdSe-OA NC) demonstrates that these CdSe-OA NC solids are very easy to fail upon applying stress. Classical mechanics theory[121] indicates that yield strength is related to the hardness by H/N, where N is typically 3 for metals, 1 for porous materials, 1.5 for oxide glasses, and 2 for polymers. In our case, as is demonstrated in Figure 5.2g, N was chosen to be ~2.5 to get a reasonable fit to our measurements.

Unlike organically capped CdSe NC solids, as shown in Figure 5.3b and sketched in Figure 5.3a, tin sulfide bridged CdSe NC solids requires much greater load to break NC interactions and displace the NCs, which suggests greatly enhanced mechanical properties. Representative load-displacement curve on 3.5 nm CdSe-$Sn_2S_6^{4-}$ NC solids was shown in Figure 5.3b, obviously, given the same indentation depth (200 nm), we obtained much greater peak load (~1400uN) as compared to 3.5 nm CdSe-OA NC solids, which suggests much greater mechanical strength of CdSe-$Sn_2S_6^{4-}$ NC solids. As is shown in Figure 5.3f, g, similarly as CdSe-OA NC solids, we monitored size-dependent mechanical properties of CdSe-$Sn_2S_6^{4-}$ NC solids. Specifically, with NC core size increases from 1.5 nm to 11 nm, the Young's modulus of inorganically capped NC solids increases from 18 GPa to 60 GPa, and hardness increases from 1.5 GPa to 4 GPa. Our results on inorganically capped NC solids show a typical reverse Hall-Patch relation, which has been predicted or observed on nanocrystalline metals[122], ceramics[123], and semiconductors[124]. There are two major contributors to this observed mechanical improvement. On one hand, ligand-ligand vdW contacts were eliminated and replaced with covalent inorganic bonding as a result of self-driven dissociation of $Sn_2S_6^{4-}$ ligands on top of inorganic NC. On the other hand, NC cores become much closer as compared to organically capped NC solids due to the small size of the $Sn_2S_6^{4-}$

ligand, this leads to enhanced vdW attraction and electrostatic (i.e. dipole-dipole) interaction. Further calculations indicate interaction energy originates from vdW and electrostatic interaction of NC cores is significantly smaller than that of covalent bond energy (see section 5.5 of this chapter for detail). This suggests that mechanical property enhancement arises from covalent nature of chemical bonds in CdSe-SnS2 NC solids.

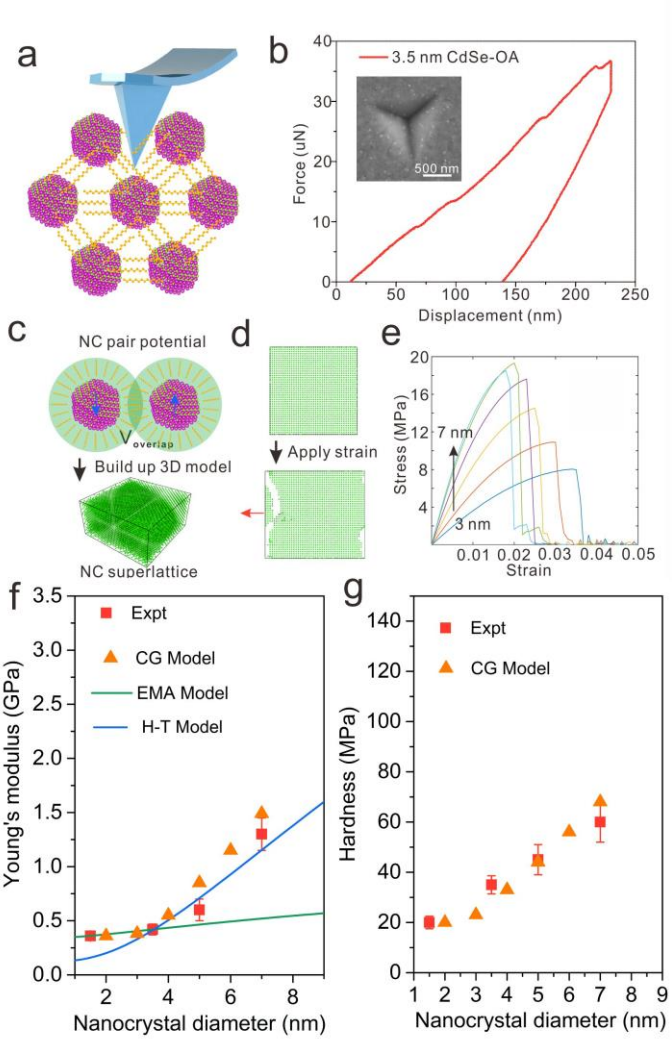

Figure 5.2 Nanoindentation results on CdSe-OA system and fitting with coarse-grained model based on NC pair potential. (a) Schematic illustration of poor mechanical

property of CdSe-OA NC solids; (b) Representative nanoindentation curves of the loading and unloading of indents on CdSe-OA NC solids, the inset shows the SEM image of one representative indent; (c) Up: Schematic of two interacting CdSe NCs with a core diameter of d and an organic ligand shell thickness of L, at equilibrium, the neighboring ligand shells will partially overlap with a volume of $V_{overlap}$; a permanent dipole is also considered in each CdSe NC core due to the spontaneous polarization of wurtzite CdSe lattice; Down: a 3D FCC model was built up with the pair potential; (d) a tensile stress was applied to the lattice along <100> direction, and the corresponding strain was recorded to get "Stress-strain" curves shown in (e); (f) Young's modulus of CdSe-OA NC solids as a function of NC core diameter, the fitted line was obtained from our coarse grained model; (g) hardness of CdSe-OA NC solids films as a function of NC diameter, the fitted line was derived using an empirical equation.

To quantitatively understand our measurements on CdSe-$Sn_2S_6^{4-}$ NC solids, we conducted atomistic molecular dynamics simulation. STEM image (Figure 5.1g) indicates that the interfacial SnS2 phase is indistinguishable from boundaries of polycrystalline CdSe. So, we treat CdSe-$Sn_2S_6^{4-}$ NC solids as nanocrystalline CdSe with interfacial atomic defects (i.e. Sn and S) in our atomistic model. We observed a reversed Hall-Petch relation in our atomistic MD simulations on nanocrystalline CdSe. This is in line with experimental measurements on CdSe-$Sn_2S_6^{4-}$ NC solids. Snap short of von Mises stress distribution at different strains (Figure 5.3d and Figure 5.11) suggests that grain boundaries (GB) activities (i.e. GB sliding) dominate the plastic deformation. The crack opening in all the polycrystalline CdSe models (Figure 5.11) indicates that the major fracture mode is intergranular fracture. We note that our polycrystalline CdSe model overestimates the Young's modulus and hardness of CdSe-$Sn_2S_6^{4-}$ NC solids. The variance could be due to the following reasons: (1) neglection

of interfacial S and Sn atoms; (2) neglection of defects (i.e. nano voids) (3) stress-strain curves are dependent on strain rate.

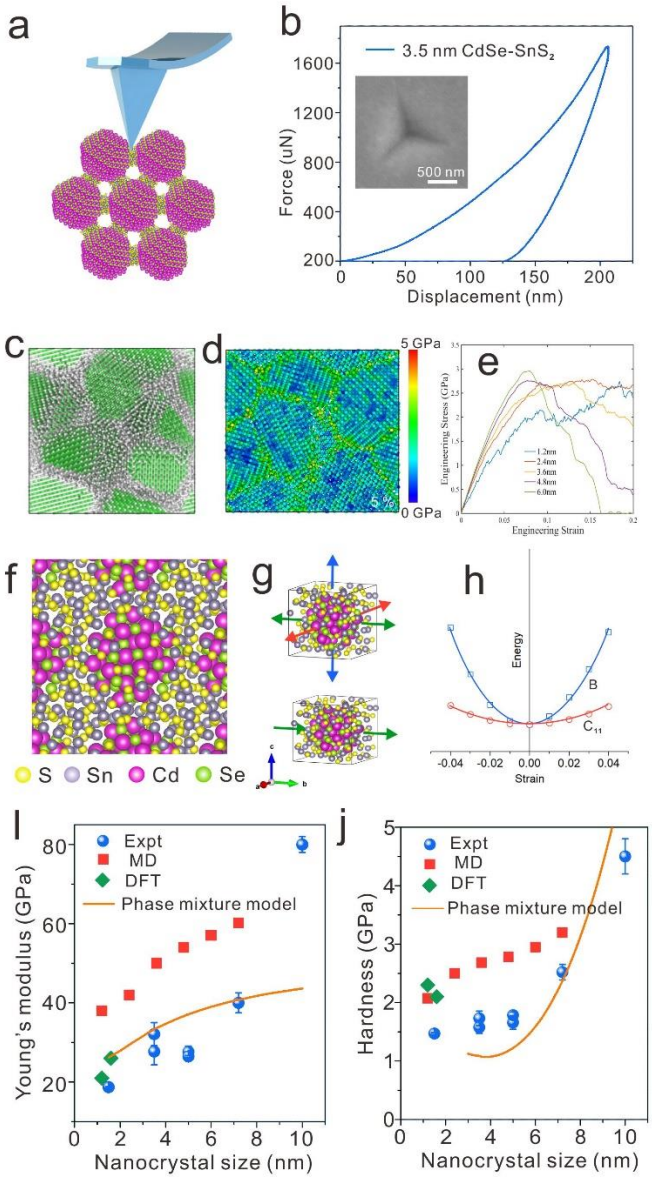

Figure 5.3 Nanoindentation results on CdSe-SnS2 system and fitting with atomistic models based on molecular dynamics (MD) and density functional theory (DFT) simulations. (a) Schematic illustration of superior mechanical property of CdSe-SnS2 NC solids, a high load was needed to break the interfacial bonds and displace the NCs;

(b) Representative nanoindentation curves of the loading and unloading of indents on CdSe-SnS2 NC solids, the inset shows the SEM image of one representative indent; (c) polycrystalline CdSe atomistic model with an average grain size of ~6nm; (d) snap short of polycrystalline CdSe shown in (c) at a tensile strain of 5%, color bar represents the von Mises stress magnitude; (e) Stress-strain curves of polycrystalline CdSe of various grain sizes upon applying tensile strain; (f) Schematic representation of a superlattice of $Cd_{42}Se_{45}$ NC embedded in a dilute amorphous tin sulfide matrix; Cd, magenta; Se, green; Sn, grey; S, yellow; (g) CdSe-SnS2 atomistic system energy versus strain, where the simulation box was deformed along all the axis (top) to derive B, while the simulation box was only deformed along one axis (bottom) to derive C_{11}; (h) Atomistic system energy evolution as a function of strain, parabolic fitting was applied to derive the independent force constants; Young's modulus (i) and hardness (j) of CdSe-SnS2 NC solids films as a function of NC diameter, a data point with a "NC" diameter of 1.5 nm corresponds to SnS2 capped CdS MSC.

We further utilized the ab initio approach to understand how the electronic structure affects the mechanical properties of CdSe-SnS2 NC solids. Specifically, we built atomistic core-shell model of CdSe-SnS2 with ab initio molecular dynamics (AIMD), performed density functional theory (DFT) energy calculations to derive the elastic constants, and eventually derived the mechanical properties (see section 5.5 of this chapter and Table 5.3). As was shown in Figure 5.3e, f, CdS MSC-SnS2 possess a Young's modulus of 19 GPa, which is fairly close to simulation result (21GPa) derived from our atomistic model. As was pointed out by Gao[125], hardness of covalent crystals is correlated to the electronic structure and thus bond density, bond length, and bond ionicity of the atomistic system (see section 5.5 of this chapter). We derive the hardness for our atomistic CdSe-SnS2 system by inputting all the parameters, which can be obtained from our DFT calculations, to Gao's model. As is indicated in Figure

3f, the estimations from our DFT model slightly overestimate the hardness but still within the same magnitude. This small variance could be explained as neglect of other possible plastic deformation mechanism (i.e. rotation and bending) other than bonds breaking in Gao's model. We again performed control DFT simulations on bulk amorphous SnS2 and wurtzite CdSe lattice, both of which possess a Young's modulus of 50-60 GPa, this makes us believe that CdSe/SnS2 interface is the mechanics bottleneck, this is confirmed by a "softening" of interfacial Cd-S/Se-Sn bonds in CdSe-SnS2 atomistic system (see section 5.5 of this chapter). Additional DFT simulations indicate Young's modulus and hardness of the system can be varied by modifying the core sizes and ligand compositions (see section 5.5 of this chapter).

The analytical phase mixture model (see section 5.5 of this chapter for detail) that averaging the contributions of crystalline CdSe phase and disordered boundary phase achieves decent fit for Young's modulus at lower size range, but underestimates the Young's modulus at higher size range (Figure 5.3e, f). Our atomistic MD simulations show that grain boundaries activities dominate the plastic deformation in CdSe-SnS2 NC solids, so we assume that dislocation plasticity breaks down and only consider crystallite and boundary diffusion mechanism for plastic flow. Evidently this phase mixture model for hardness yield similar trend as compared to experimental results.

We would like to point out that this technique can be widely used for mechanical reinforcement in colloidal NC materials and devices. Compared to other approaches that usually involves annealing and etching, inorganic functionalization chemistry would be more attractive to chemically and thermally unstable NC systems (i.e. quantum dots, noble metal NC).

5.4 Conclusion

In summary, inorganically functionalized colloidal NCs exhibit exceptional mechanical properties and thermal stability, which presents a promising route for realization of nanocrystalline material/devices of desired mechanical properties. We showed that as-synthesized organically capped NC solids possess poor mechanical property as a result of weak ligand-ligand vdW interaction. This ligand-ligand interaction depends on surface ligand capping density and ligand interdigitation. We further verified this using a coarse-grained model. After ligand exchange, the original soft ligand matrix made of long OA molecules was replaced with much shorter inorganic $Sn_2S_6^{4-}$ molecule that dissociates instantaneously into tin sulfide upon anchoring onto CdSe surface. This a few atomic layers of tin sulfide not only eliminates the weak vdW interaction but enhances mechanical coupling of neighboring NCs, both of which contribute to the mechanical reinforcement. We further proved that the boundaries can be further engineered to vary the mechanical properties via DFT simulations. We hope our study motivates future mechanical studies on colloidal nanocrystal systems with other inorganic functionalization methods[126-128]. Robust nanocrystalline thin films from solution processing are promising for mechanics coating purposes.[129] Colloidal chemistry presented here allows preparation of nanocrystalline material of well-controlled size, shape, and interfaces, which presents great potential for unique mechanical properties.

5.5 Method and Supporting Information

5.5.1 Materials Synthesis and Characterization

5.5.1.1 *CdSe nanocrystal (NC) synthesis*

For 3-8 nm CdSe-OA NC synthesis, we employed a modified "hot injection" method[115], we first prepared a selenium stock solution by heating a mixture of Se

powder (1.6 mmol, 99,99% Sigma Aldrich) in ODE (16 ml, 90% Sigma Aldrich) under nitrogen atmosphere at a temperature of 225 ℃ for 2h. After completion of dissolving, the mixture was cooled to room temperature, resulting in a stable yellow transparent solution. We then prepared the Cd precursor solution by mixing cadmium oxide (0.36 mmol, 99.99% Sigma Aldrich), oleic acid (3.6 mmol, 90% Sigma Aldrich), and ODE (12ml) in a 100 ml flask, degassing for 1h at 100 ℃ under N_2 and further heating to 250 ℃ until all CdO was dissolved. The solution was continued to be heated to 265 ℃, and then the Se stock solution was quickly injected. The temperature of the whole mixture dropped to 235 ℃ and the color of the solution turns slowly from yellow to burgundy, which suggests nucleation and growth of CdSe NCs. The reaction continued at this temperature for 11-30 min and then quenched to room temperature naturally.

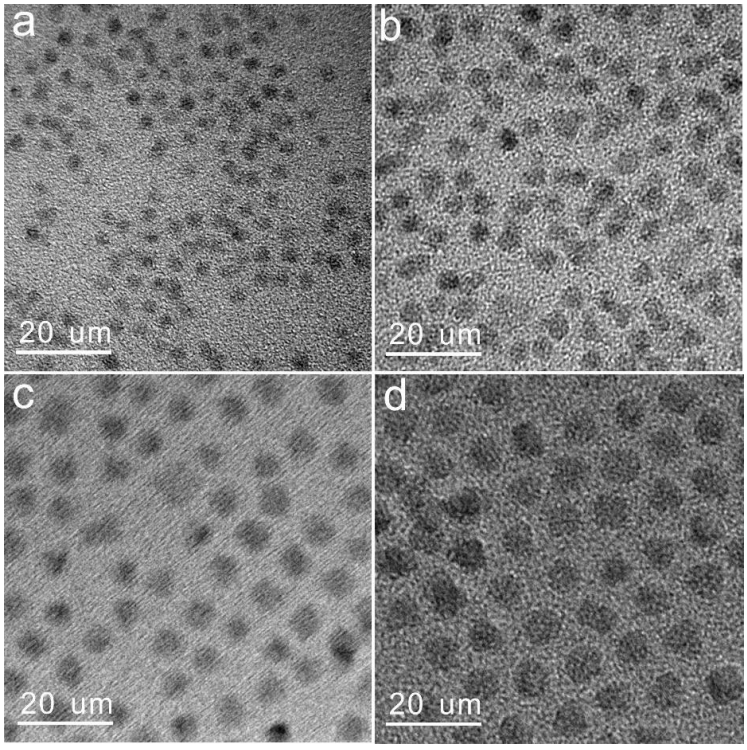

Figure 5.4 TEM images of as synthesized (a) 3.5nm (b) 5nm (c) 7nm and (d) 8nm CdSe NCs with surface capped oleic acid ligands.

For cleaning, equal volume of toluene and ethanol were added to the flask, the NCs are precipitated by centrifuging and then re-dispersed in toluene. Afterwards, the particle solution was further purified twice by repeating the precipitation and re-dispersing process.

Figure 5.4 shows representative TEM images of OA capped CdSe NCs of various core sizes (3-8 nm). CdSe NCs of all sizes are separated by a spacing, which suggests the presence of OA ligand on the surface of NC cores.

5.5.1.2 *CdS magic-sized cluster (MSC) synthesis*

We synthesized the CdS-OA MSC by referring to Zhu's recipe[130]. We first prepared Cd precursor Cd(OA)2 stock solution, a mixture of CdO, OA, and ODE was placed in a 50 ml flask, degassed for 1h, and continued to heat up to 220 ℃ to form a clear solution and then cooled down naturally under N2. The resulting Cd(OA)2 (0.15 mmol), elementary S (0.15 mmol), and ODE (4 g) were mixed in a 50 ml flask at room temperature. Followed by heating up to 190 ℃ and kept for 5 min under N_2. Then the mixture was cooled down to room temperature naturally. Lastly, 3 ml toluene was added to the resulting mixture at room temperature, the evolution of CdS-OA MSC took place slowly.

5.5.1.3 *Solution-phase ligand exchange*

For a typical $(N_2H_5)_4Sn_2S_6$ precursor synthesis, we used the recipe developed by Mitzi.[131] Specifically, Elemental tin (118.7 mg, 1mmol) and elemental sulfur (3 mmol) was dissolved in 4 ml N2H4, and the mixture was stirred at 130 ℃ for 2 days to form a nearly colorless (slightly yellow) transparent solution. Note that hydrazine is highly toxic and must be handled with great care.

We further performed solution-state ligand exchange on our NCs and MSCs with the MCC precursor.[113] In a typical example for CdSe-$Sn_2S_6^{4-}$ system, 5-25 ul of 0.25 M $(N_2H_5)_4Sn_2S_6$ solution were mixed with 2ml N_2H_4. Then 5-25 mg CdSe-OA NCs dispersed in toluene was mixed with MCC precursor solution. The whole mixture was vigorously stirred for 1-4 hours until the top organic phase became colorless and the bottom N_2H_4 phase turned red. This suggests the successful phase transfer of CdSe nanocrystals. The CdSe-$Sn_2S_6^{4-}$ NC can be further purified by precipitation with anhydrous acetonitrile and re-dispersing in pure N_2H_4. Similar procedure was used to functionalize CdS MSC with $Sn_2S_6^{4-}$ ligands.

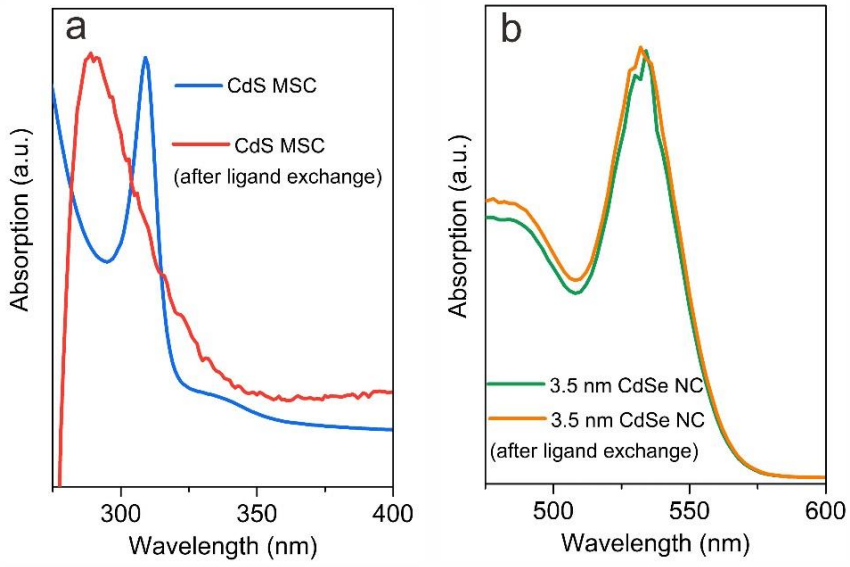

Figure 5.5 UV-Vis spectra of (a) CdS MSC and (b) 3.5 nm CdSe NC solution before and after $Sn_2S_6^{4-}$ ligand exchange.

5.5.1.4 ***NC and MSC films preparation***

~50 mg/ml CdSe NC or CdS MSC with organic ligand (OA) and inorganic ligand ($Sn_2S_6^{4-}$) are drop-casted onto pre-cleaned Si substrates. After drying of the solvent

at room temperature, the resulting thick film (>1 um) was further heated up to 180 ℃ for residual solvent removal and dissociation of $Sn_2S_6^{4-}$ ligands.

5.5.1.5 *Material characterizations*

Transmission Electron Microscopy (TEM) and Scanning Electron Microscopy (SEM): CdSe NC morphology and size were characterized using a FEI CM-200 TEM operated at 120 kV. This same TEM instrument was also used for HRTEM on samples before and after ligand exchange. To conduct HRTEM, the NC solution was drop-casted onto a carbon-coated TEM grid. The micro-morphology of the NC solid thin films was characterized using a FEI XL-30 SEM. Aberration-corrected Scanning Transmission Electron Microscopy (Aberration-corrected STEM): Aberration-corrected STEM was performed using a JEOL ARM200F. Elemental mapping on SnS2 capped CdSe NC was also obtained using the same instrument. Inductively coupled plasma mass spectrometry (ICP-MS): Elemental composition of SnS2 capped CdSe NC solids of various core sizes are determined via ICP-MS analysis. 5-10 mg of each sample was dried, collected and dissolved with acid solution for post analysis. The Cd, Se, and Sn mass concentration can be accurately determined using this technique. S concentration was estimated with an assumed molar ratio of Sn to S (1/2). Ultraviolet-visible spectroscopy (UV-Vis): Absorption spectra of CdS MSC and CdSe NC before and after $Sn_2S_6^{4-}$ ligand exchange was collected using a Perkin Elmer lambda 950 spectrometer.

5.5.2 Mechanical Measurements and Analysis

5.5.2.1 *Nanoindentation*

Hardness and young's modulus of the film were calculated using nanoindentation technique. Displacement controlled nanoindentation was carried out using TI 980 TriboIndenter with a Berkovich diamond tip of radius 150 nm. Indentation depth was

fixed at 200 nm which is within 10% of the film thickness. A three segment quasi-static loading profile with load, unload period and hold period of 10 s was utilized. More than 10 indents were used for each sample to get good statistical information. Each indent was spaced 10 μm apart to avoid overlap of their radial plastic zones.

5.5.2.2 *Composite model for OA capped CdSe NC solids*

We first considered a simple model of parallel oriented layers perpendicular to the loading direction, which has been used to describe the mechanical response of non-crosslinked and crosslinked iron oxide NC solids[112]. In this model, the following equation was used to correlate the Young's modulus of the composites to Young's modulus of each constituents and their corresponding volume fractions:

$$\frac{1}{E} = \frac{\varphi_{NC}}{E_{NC}} + \frac{1-\varphi_{NC}}{E_m}$$

Where:

E: is the modulus of the NC solid composite

E_m: is the modulus of the ligand matrix

E_{NC}: is the modulus of the NC core

φ_{NC}: is the volume fraction of the NC cores

We further use Halpin-Tsai theory, which is developed for polymer nanocomposites, to calculate the effective modulus of NC solids. Previous work[38] has successfully applied this theoretical model to a variety of NC systems. In accordance with Halpin-Tsai composite theory, we use the following two equations used to calculate the modulus of the ligand matrix:

$$\frac{E}{E_m} = \frac{1 + \delta\eta\varphi_{NC}}{1 - \eta\varphi_{NC}}$$

$$\eta = \frac{\frac{E_{NC}}{E_m} - 1}{\frac{E_{NC}}{E_m} + \delta}$$

Where:

E: is the modulus of the NC solid composite

E_m: is the modulus of the ligand matrix

E_{NC}: is the modulus of the NC core

δ: is the shape parameter for spherical fillers ($\delta = 2 + 40 * \varphi_{NC}$)

φ_{NC}: is the volume fraction of the NC cores

The Halpin-Tsai model was first applied to 3.5 nm CdSe-OA NC solids to derive a E_m that equals to 0.3 GPa. This value was further used to fit the Young's modulus of the NC solid of various core sizes.

5.5.2.3 ***Phase mixture model for polycrystalline CdSe***

In a phase mixture model[132] of nanocrystalline material, a cubic unit cell consists of crystallite (grain interior), grain boundary, triple line junction and quadratic node. Assume a grain size of d and grain boundary width of w, we can derive the volume fraction of each component as follows

$$f_{CR} = (d - w)^3/d^3$$

$$f_{GB} = 6(d - w)^2(w/2)/d^3$$

$$f_{TJ} = 12(d - w)(w/2)^2/d^3$$

$$f_{QN} = w^3/d^3$$

Where the subscripts CR, GB, TJ, and QN represent crystallite, grain boundary, triple line junction and quadratic node, respectively. w is assumed to be a constant (1 nm) for all the grain sizes. Porosity is also taken into account in this model, where the porosity is treated to be a constituent of zero strength. Thus, the bulk modulus and shear modulus for the pore are set to zero.

Budiansky's method[133] is used to estimate the properties of composite materials which consist of a random mixture of N isotropic constituents. The bulk modulus K and the shear modulus G of the composite are related to K_i and G_i of the i-th constituents by the following equations,

$$\frac{f_{CR}}{1-a+a\frac{K_{CR}}{K}} + \frac{f_{GB}}{1-a+a\frac{K_{GB}}{K}} + \frac{f_{TJ}}{1-a+a\frac{K_{TJ}}{K}} + \frac{f_{QN}}{1-a+a\frac{K_{QN}}{K}} + \frac{f_{PO}}{1-a} = 1$$

and

$$\frac{f_{CR}}{1-b+b\frac{G_{CR}}{G}} + \frac{f_{GB}}{1-b+b\frac{G_{GB}}{G}} + \frac{f_{TJ}}{1-b+b\frac{G_{TJ}}{G}} + \frac{f_{QN}}{1-b+b\frac{G_{QN}}{G}} + \frac{f_{PO}}{1-b} = 1$$

where

$$a = \frac{1}{3}\left(\frac{1+v}{1-v}\right)$$

$$b = \frac{2}{15}\left(\frac{4-5v}{1-v}\right)$$

And v is the Poisson's ratio of the composite, which can be in turn given by

$$v = \frac{3K-2G}{6K+2G}$$

The subscript in the equations above represents the porosity phase.

Hardness of the nanocrystalline material can be related to its Yield strength. Here, we employed the same phase mixture model to estimate the yield strength and hardness of CdSe-SnS2 NC solids. In this model[134], a simple mixture rule based on the volume fraction of each components is used for analysis of deformation behavior:

$$\sigma = f_{cr}\sigma_{cr} + f_{gb}\sigma_{gb}$$

Where the subscripts cr and gb refer to crystallite and grain boundary, respectively. We further assume that the strains in both phases are the same, which are equals to the macroscopic applied strain.

As for the crystallite phase, three deformation mechanism are considered: (i) dislocation glide mechanism, (ii) the lattice diffusion mechanism in which vacancies diffuse through the bulk of the crystallite, (iii) the boundary diffusion mechanism in which vacancies diffuse along the grain boundaries. The total plastic strain rate is obtained by adding the contributions from the individual mechanisms (i)-(iii):

$$\dot{\varepsilon}^p = \dot{\varepsilon}^p_{cr,d} + \dot{\varepsilon}^p_{cr,b} + \dot{\varepsilon}^p_{cr,l}$$

Where the subscripts cr refers to the crystallite phase and d, b and l stand for the dislocation model, the boundary diffusion mechanism[135] and the lattice diffusion mechanism[136], respectively.

The plastic strain rate of the crystallite phase associated with the lattice diffusion mechanism and boundary diffusion mechanism can be expressed as

$$\dot{\varepsilon}^p_{cr,l} = 14\frac{\Omega\sigma_{cr}}{kT}\frac{D^{sd}_{ld}}{d^2}$$

$$\dot{\varepsilon}^p_{cr,b} = 14\pi\frac{\Omega\sigma_{cr}}{kT}\frac{\omega D^{sd}_{bd}}{d^3}$$

Where d is the grain size, ω is the grain boundary width (~1nm), k is the Boltzmann constant, Ω is the atomic volume, D_{ld}^{sd} and D_{bd}^{sd} is the lattice diffusivity and the grain boundary diffusivity, respectively. It is generally accepted that dislocation plasticity will break down below a certain value of grain size. In our case, we are dealing with <10nm grain sizes. So, we made another assumption that only the diffusion mechanism is operative.

As for the grain boundary phase, a diffusion mechanism[137] for plastic flow of the grain boundary phase was considered. The plastic strain rate of the grain boundary is written as

$$\dot{\varepsilon}_{bd} = 2\frac{\Omega_b \sigma_{gb}}{kT}\frac{D_{ld}^{sd}}{d^2}$$

The phase mixture model described above was applied to polycrystalline CdSe-SnS2, and the results were compared to the experimental hardness measurements. The following parameter values were used in our model: $\dot{\varepsilon}_{bd}=\dot{\varepsilon}^p=10^{-2}$ s^{-1}, $\Omega=2.73^{-29}$ m^3, $\Omega_b=3^{-29}$ m^3, $\omega=1.0^{-9}$ m, $D_{ld}^{sd}=2.66^{-33}$ m^2s^{-1}, $D_{bd}^{sd}=4^{-21}$ m^2s^{-1}, and σ_{gb} saturates at 1.5 GPa.

5.5.3 **Coarse-grained Simulation**

CdSe NC-OA system was described using a coarse-grained model, where each nanocrystal plus the OA ligands are simplified as a spherical unit of diameter with a ligand shell of certain length. The pairwise interaction energy for nanocrystals can be expressed as follows:

$$U(r) = U_{vdw}(r) + U_{electrostatic}(r) + U_{L-L}(r)$$

Where r is the interparticle distance. The attractive van der Waals interaction between two spherical nanocrystal cores can be expressed as:

$$U_{vdw}(r) = -\frac{A}{6}[\frac{2a_1a_2}{r^2-(a_1+a_2)^2} + \frac{2a_1a_2}{r^2-(a_1-a_2)^2} + \ln(\frac{r^2-(a_1+a_2)^2}{r^2-(a_1-a_2)^2})]$$

Where A is the Hamaker constant and a_1, a_2 are radius of two nanocrystals, respectively. Specifically, for CdSe, we set A to be 0.3 eV based on previous literature.[91] The electrostatic interaction can be induced by charges, permanent and induced dipoles. CdSe nanocrystals were reported to possess a permanent dipole due to spontaneous polarization of bulk wurtzite CdSe lattice, and the magnitude is linearly related to the size of the CdSe nanocrystals.[138] Specifically, 5.8 nm CdSe NC has a dipole moment of 100D.[91] Thus, a dipole-dipole interaction energy was considered and calculated using equation below:

$$U_{dipole-dipole} = \frac{1}{4\pi\epsilon_0\epsilon_r r^3}[\boldsymbol{P_1}\cdot\boldsymbol{P_1} - 3(\boldsymbol{P_1}\cdot\boldsymbol{r})(\boldsymbol{P_2}\cdot\boldsymbol{r})]$$

Where $\boldsymbol{r}$ is the vector connecting two nanocrystals, $\boldsymbol{P_1}$ and $\boldsymbol{P_2}$ are dipole moments of nanocrystal 1 and 2. The ligand-ligand interaction can be described using the classical Lennard-Jones form, and is also assumed to be proportional to the overlap volume of two neighboring ligand shells:

$$U_{L-L} = 4\varepsilon[(\frac{\sigma}{r})^{12} - (\frac{\sigma}{r})^{6}]V_{overlap}\rho_L/M_L$$

$$V_{overlap} = \frac{\pi}{2}(2L-(r-2a))^2R + \frac{\pi}{6}\big(2L-(r-2a)\big)^2(2L+(r-2a)/2)$$

Where ε is the depth of the potential well, σ is the finite difference at which the inter-particle potential is zero, ρ_L is the density of ligand shell, L is the ligand shell thickness, and M_L is the molar weight of ligand matrix. To determine the parameters in the Lennard-Jones potential for describing ligand-ligand interaction, we used Salem's theory to calculate the attraction force between alkane chains at short distance:

$$W = A\frac{3\pi}{8\lambda^2}\frac{L}{D^5}$$

Where is λ and L the length of CH_2 and whole alkane chain, respectively. D is the distance between two adjacent alkane chains. In our case, D was related to ligand capping density ρ_c, which can be determined from thermogravimetric analysis (TGA) on the NC solids sample. Assuming a hexagonal array of interdigitated ligand molecules, D can be derived as $D = \sqrt{1/2\rho_c}$. In the end we calculated the molar-based attraction interaction of interdigitated ligand shells.

The derived pair potential shows that ligand-ligand vdW attraction dominates the NCs' interaction near the equilibrium position. Hence the mechanical property of NC solids is also dominated by the ligand-ligand vdW attraction. This suggests NC solids should possess polymeric mechanical behavior, which is in line with previous reports.[139]

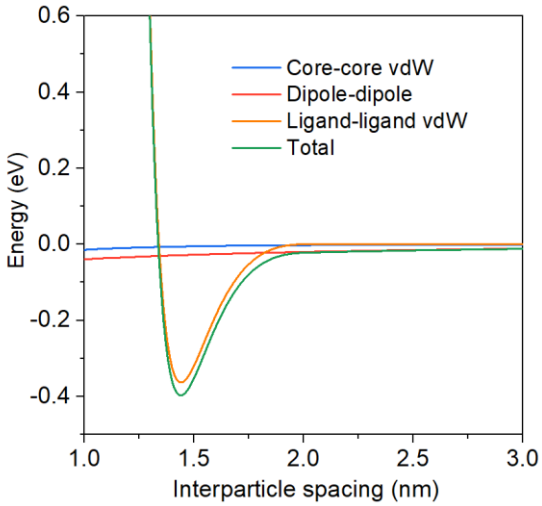

Figure 5.6 NC pair potential from 3 major contributors: vdW attraction of NC cores (blue), dipole-dipole interaction of NC cores (red), and vdW interaction of neighboring ligands (orange).

For simplicity, the derived pair potential was fitted with classical Morse format using the following expression:

$$E = D_0\left[e^{-2\alpha(r-r_0)} - 2e^{-\alpha(r-r_0)}\right], r < r_c$$

here r_c and r_0 are the potential cutoff and the equilibrium distance, respectively. D_0 are in energy unit, α is in 1/distance unit. However, to identify the impact of the permanent dipole-dipole interaction with r^3 term of the NC-OA system, a revised Morse equation with a constant energy term D_1 added to the equation is used for well capture the overall energy landscape around the equilibrium. The revised equation is as follows:

$$E = D_0\left[e^{-2\alpha(r-r_0)} - 2e^{-\alpha(r-r_0)}\right] + D_1, r < r_c$$

Further, to ensure the accuracy of the fitted Morse model compared to the analytical result. The equilibrium position is identified. Following that the energy landscape is fitted at -5% to +5% range around the equilibrium point. This operation is feasible for studying the mechanical property of NC-OA system especially under small deformation (strain ~ 1%). As shown below in Figure 5.7, the example of the Morse fitting result for the 3nm CdSe NC-OA system.

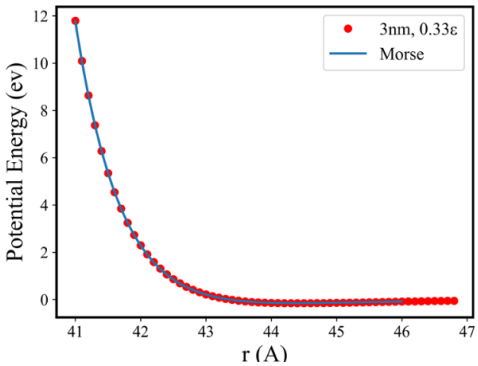

Figure 5.7 Morse fitting result for the pair potential of two 3nm CdSe NCs.

The concise expression of the Morse formula makes it feasible to study large CdSe NC system. Once the parameters in the Morse equation is determined. We built up CdSe NC superlattice model composed of over 100 thousand CdSe NCs and performed molecular dynamic simulations to elucidate elastic properties. Here, coarse grain MD simulations are performed using LAMMPS package. To study the mechanical properties anisotropy of the CdSe NC-OA superlattice structure, tensile stress was applied along both <100> and <111> directions of the superlattice. Periodic boundary conditions (PBC) are applied along all three directions of the simulation cell. Initially, we performed the molecular dynamics simulations within the Isothermal-Isobaric (NPT) ensemble for 800ps with a time step of 1 fs. Such treatment is supposed to relax the system while letting the structure reaches its equilibrium state. During the equilibrium process, the total temperature was kept at 300 K and the pressure along all three axial directions were kept at zero. After that, the equilibrated structure was elongated along x-direction with a uniaxial tension strain up to 10% of the original length, while the pressure component on the y and z direction are controlled to maintain the uniaxial tension condition. The deformation-controlled strain rate of $10^{-9}s^{-1}$ were applied along the x direction. After analyzing the stress-strain relation, young's modulus is extracted by fitting the linear part (~ 0.002).

As are shown in Figure 5.8 and 5.9, our results show that the mechanical response of the superlattice is anisotropic. Specifically, when the tensile strain was applied along <100> direction, the Young's modulus and yield strength of the 3 nm NC-OA superlattice model were derived to be 0.3 GPa and 30 MPa, respectively. While when the tensile strain was applied along <111> direction, the Young's modulus and yield strength were calculated to be 0.4 GPa and 40 MPa, respectively. We realized that difference in Young's modulus and yield strength is relatively small. We applied the tensile strain along <100> direction if not specified.

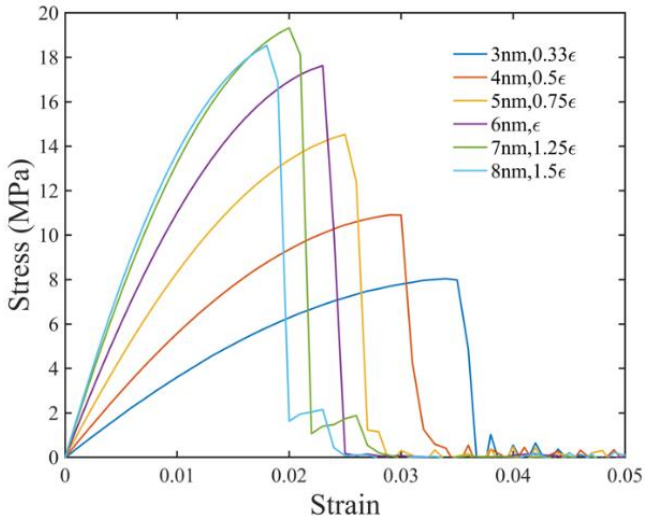

Figure 5.8 Representative stress-strain curves derived from MD simulations with a uniaxial tension strain applied along the <100> direction.

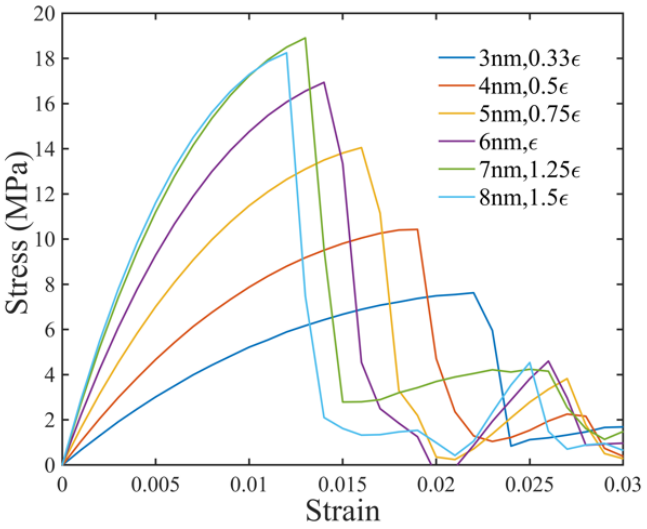

Figure 5.9 Representative stress-strain curves derived from MD simulations with a uniaxial tension strain applied along the <111> direction.

To systematically investigate the mechanical properties of NC-OA bulk crystals, elastic constants of NC-OA bulk crystals, young's modulus, bulk modulus, Poisson's

ratio are calculated. In general, the elastic constants are obtained using the stress-strain method based on the generalized Hook's law as summarized in Table 5.1 below.

Table 5.1 Calculated elastic constants (GPa), bulk modulus (GPa), shear modulus (GPa), Young's modulus (GPa), B/G values, Poisson's ration (ϑ), and Yield strength (MPa)

NC-OA	3nm	4nm	5nm	6nm	7nm	8nm
$C11$	0.696	1.013	1.482	1.979	2.432	2.586
$C44$	0.348	0.507	0.742	0.989	1.216	1.293
$C12$	0.348	0.507	0.742	0.989	1.216	1.293
B	0.463	0.676	0.99	1.32	1.62	1.72
G	0.279	0.405	0.593	0.79	0.973	1.03
B/G	1.659	1.669	1.669	1.671	1.665	1.670
E	0.696	1.01	1.48	1.98	2.43	2.58
ϑ	0.25	0.25	0.25	0.25	0.25	0.25
σ	7.89	10.9	14.53	17.62	19.33	22.54

The bond population is proportional to the strength of the bonding. However, temperature will increase the bond length due to high thermal energy. Therefore, it may be harmful for the mechanical properties of the lattice structure. Compared with the calculation in previous section considering temperature variation, the little deviation here can be attributed to the thermal dynamic effects on the crystal structure

during the experiments and different approximation methods for calculation. Here, the constants are determined using energy minimization to eliminate the temperature effect.

Because the symmetry of the crystal, the C_{11}, C_{22}, and C_{33} of cubic NCA are the same and the largest of all the compounds, which provides the evidence that the NCA crystal is hard to be compressed under external uniaxial stress along the [100], [010], and [001] directions. C_{44}, C_{55} and C_{66} represent the shearing strength at (100), (010) and (001) crystal plane, respectively. The mechanical modulus, such as the bulk modulus (B) and the shear modulus (G) are evaluated with Viogt-Reuss-Hill (VRH) approximation using the elastic constants. Young's modulus (E) and Poisson's ration (v) are estimated by the following expressions:

$$E = 9BG/(3B + G)$$

$$v = (3B - 2G)/(6B + 2G)$$

The Poisson's ratios (v) of all NCA crystals are close to 0.3 indicating they possess weak metallic characters. The obtained modulus values are listed in Table 5.1. The 9nm NC-OA model exhibits the largest B, which reveals that it's the most difficult one to be deformed under hydrostatic pressure. This result is in consistent with the experiment result. Meanwhile, because the intrinsic hardness is proportional to the shear modulus, the stronger bond/interaction between the NCA crystals generally indicates the hardness is larger. This qualitatively explains why experimentally, the bigger size of the nanocrystal, the higher hardness.

The Pugh ratio (B/G) listed in Table 5.1 characterizes the brittle or ductile property of materials. The critical value which separates ductile and brittle material is 1.75. Lower value (<1.75) was termed as brittle, whereas higher value (B/G>1.75) was

termed as ductile. The results reveal the brittle nature of NC-OA systems, which is also validated by our nanoindentation test.

5.5.4 **Comparison of NC interaction and covalent bond energy**

CdSe-SnS2 NC solids exhibit greatly enhanced mechanical properties. This is because the vdW OA-OA interaction was exchanged with covalent bonds (i.e. Cd-S&Sn-S). Apart from this, CdSe NC core-core interaction has also been enhanced as the interNC distance has been significantly decreased. To evaluate the contribution of enhanced NC core-core interaction on the observed mechanical enhancement, we compared the NC core-core interaction energy with bond energy of covalent bonds involved in CdSe-SnS2 NC solids.

Table 5.2 Comparison between CdSe NC interaction energy and chemical bond energy

NC core-core (kJ/mol)	Cd-Se (kJ/mol)	Cd-S (kJ/mol)	Sn-S (kJ/mol)
0.23	127.6[140]	208.5[140]	467[140]

NC core-core interaction energy, which is mainly composed of dipole-dipole interaction and vdW attraction, was calculated using the pair potential model proposed above. Specifically, using 3nm CdSe NC core as an example, we calculated the NC core-core interaction energy with a decreased NC gap (0.5 nm), which corresponds to the size of $Sn_2S_6^{4-}$ ligand upon dissociation. This calculation leads to CdSe NC core-core interaction energy of 0.23 kJ/mol. This value is significantly lower than bond energy of chemical bonds present in CdSe-SnS2 NC solids (Table 5.2). Consequently,

the covalent nature of chemical bonds unambiguously dominates the observed mechanical enhancement.

5.5.5 **Atomistic Molecular Dynamics Simulation**

Nanocrystalline structures with random distributed crystal orientations for the MD simulations are constructed by the Voronoi construction method. Periodic boundary is applied in all three directions. All samples contain 16 grains, and the average grain size varies from 1.2 to 8.4 nm. The variation of average grain size is controlled by changing the simulation domain dimensions while keeping the number and geometry of grains unchanged, obtaining self-similar samples. The simulation domain dimensions of each sample range from $30a_0$ (30.25 nm) to $120a_0$ (211.75 nm), in which a_0 demonstrates the lattice constant of platinum and a_0= 0.650 nm at 300 K, to provide mean grain sizes of 1.2-8.4 nm, respectively. The number of atoms in the samples varies from about 922 to 316774, which corresponds to the average grain size of 1.2 nm and 8.4 nm, respectively.

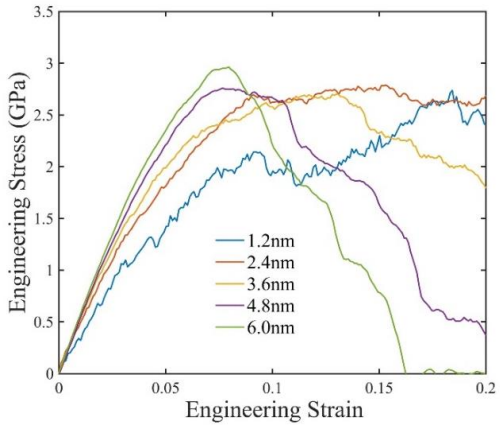

Figure 5.10 Stress-strain curves derived from atomistic MD simulations on polycrystalline CdSe of various grain sizes.

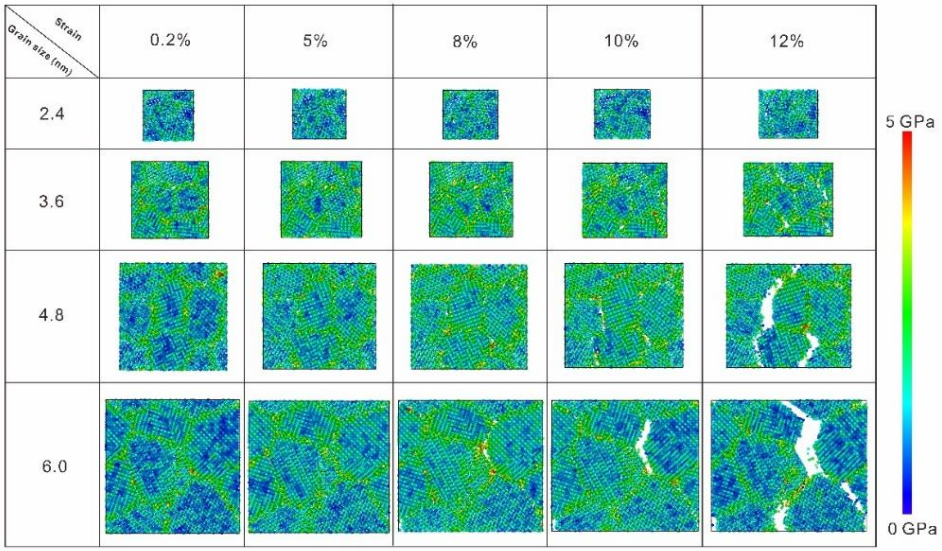

Figure 5.11 Snap shots of von-mises stress distribution of polycrystalline CdSe model at different strains. The simulation results clearly show that boundaries yield and break first.

Von-mises stress distribution of polycrystalline CdSe models at different strain is shown in Figure 5.11. This clearly indicates that, especially for polycrystalline CdSe of larger grain, higher Von-mises stress is predicted at the grain boundary. Thus, we saw that grain boundary yield and fail first as compared to the interior of the grain.

5.5.6 **Atomistic Density Functional Theory Simulation**

Density Functional Theory (DFT) calculations were performed with the Vienna Ab Initio Simulation package (VASP) under the Projector Augmented Wave (PAW) method and the Perdew-Burke-Ernzerhof (PBE) form of the generalized gradient approximation (GGA) for exchange and correlation. All the starting crystalline phase and structures were obtained from crystal data base material project. We set the kinetic energy cutoff in the planewave expansion to be 600 eV. For k point mesh, most of the time we were

using single Gamma point as our simulation involves hundreds of atoms and thus a large simulation box.

We built up the atomistic model of CdSe-SnS2 core shell structure through a combination of a CdSe crystalline phase and amorphous SnS2 shell. We first create the amorphous phase SnS2 using the "melt and quench" method through ab initio molecular dynamics (AIMD) simulations. In this approach, we started with a supercell of crystalline phase SnS2 (typically 100-200 atoms). The cell was heated to a temperature much larger than the melting temperature of the crystalline phase (2500K). Then the system was kept at this temperature for 1000 MD time steps (each time step equals to 1 fs). We obtained the amorphous structure by cooling the heated structure to room temperature at the rapid rate of 200K per 200 MD time steps. Then this structure was further relaxed to the ground state with an atomic force tolerance of 0.01 eV A^{-1}. We only allow the atomic coordinates to vary and kept the simulation box as unchanged during this relaxation. In the following, the center area of the resulting SnS2 amorphous structure was replaced with a crystalline CdSe phase. Again, we allowed the whole structure to relax with an atomic force tolerance of 0.01 eV A^{-1}. Similarly, we allow the atomic coordinates to vary and kept the simulation box as unchanged during the relaxation.

After relaxation, the whole system became amorphous-like structure due to the surface reconstruction of CdSe crystalline phase. Since amorphous structures are isotropic and are therefore characterized by two independent elastic constants, the bulk modulus B and the modulus C_{11}. Once these two elastic constants were calculated, we can further derive Young's modulus, shear modulus, and the Poisson's ratio based on relations between different elastic constants.

To derive the elastic constants B, we employed a "strain-energy" method. We use A_i to denote the basis lattice vectors of the simulation cell, after applying the deformation gradient ξ,

$$\xi = \begin{bmatrix} 1+\theta & 0 & 0 \\ 0 & 1+\theta & 0 \\ 0 & 0 & 1+\theta \end{bmatrix}$$

To the basis lattice vectors to obtain the deformed lattice vectors. Here, is the strain. The energy of the deformed cell was calculated and fitted to the equation $E(\theta) = E_0 + c\theta^2$, where E_0 is the undeformed cell. Then we can derive the bulk modulus using the formula:

$$B = \frac{2c}{9V_0}$$

Where V_0 is the volume of the unstrained cell and c is the coefficient of in the quadratic fit. To calculate the elastic constant C_{11}, we multiplied the basis lattice vector matrix with the deformation matrix, which was expressed as:

$$\xi' = \begin{bmatrix} 1+\theta & 0 & 0 \\ 0 & 1 & 0 \\ 0 & 0 & 1 \end{bmatrix}$$

Similarly, the deformed cell energy was calculated and fitted to equation $E(\theta) = E_0 + d\theta^2$. Then we can obtain elastic constant C11 using the formula:

$$C_{11} = \frac{2d}{V_0}$$

Finally, after the computation of B and C_{11}, then we can further calculate the shear modulus G, Young's modulus E, Poisson's ratio v of the system using the expressions:

$$G = \frac{3(C_{11} - B)}{4}$$

$$E = \frac{9B(C_{11} - B)}{C_{11} + 3B}$$

$$v = \frac{3B - C_{11}}{C_{11} + 3B}$$

5.5.7 **Intrinsic Hardness of Covalent Bonded Structure**

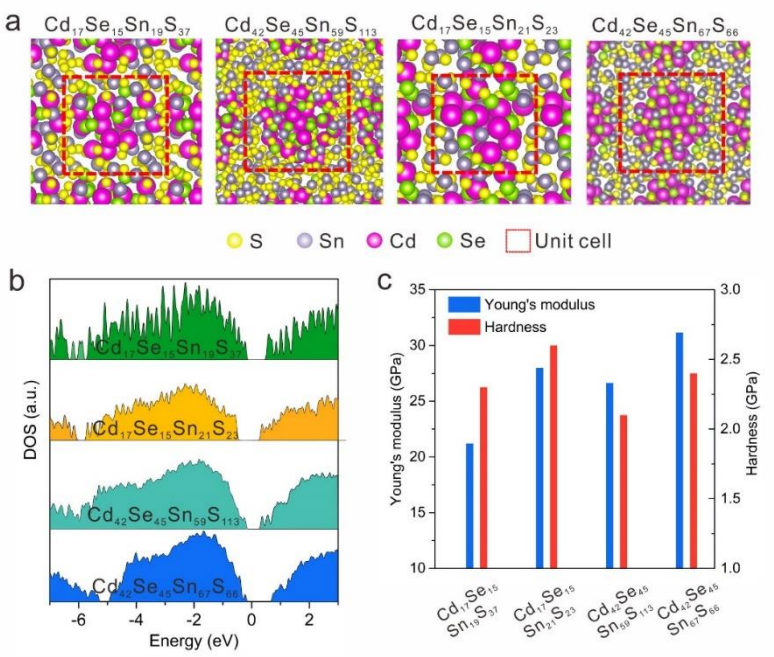

Figure 5.12 Density functional theory (DFT) calculations on atomistic CdSe-Sn_xS_y models. (a) Relaxed structures of CdSe-Sn_xS_y models of various core sizes and ligand composition. (b) Electronic density of states of CdSe-Sn_xS_y models of various core sizes and ligand composition. (c) Mechanical properties (Young's modulus and Hardness) of CdSe-Sn_xS_y models of various core sizes and ligand composition.

Hardness is defined as the resistance offered by a given material to external mechanical action. In covalent materials, the bonding is localized in electron spin pairs, which suggests hardness as an intrinsic property. Gao et al.[125] proposed a semi-empirical model that established a link between hardness and electronic structure. As

hardness depends strongly on plastic deformation of covalent crystals. This means electron-pair bonds must first be broken and then re-made. Breaking covalent electron-pair bond means excitation of two electrons from valence band to conduction band. Thus, the bond strength is correlated with band gap, Eg. The hardness of covalent crystals could be expressed as

$$H = AN_aE_g = 350\left[(N_e)^{2/3}\exp(-1.191f_i)\right]/d_b^{2.5}$$

Where A is a coefficient of proportionality, N_a is the covalent bond number per unit area, N_e is the number of valence electrons per cubic angstrom, d_b is the bond length in angstrom, f_i is the ionicity of given chemical bond type. This theory highlights bond density, bond length, and degree of covalent bonding as the three major determinative factors for the intrinsic hardness of a polar covalent crystal.

In addition, Gao et al.[125] further generalized the equation into expression of hardness for multicomponent compound system. Given the complex crystal system, the trend of breaking bonds will start from softer ones. Therefore, the hardness of multicomponent system was calculated by geometric average of all bonds as follows:

$$H = \left[\prod^{\mu}(H_v^{\mu})^{n^{\mu}}\right]^{1/\sum n^{\mu}}$$

Where is the hardness of binary compound composed of μ type bond, is number of μ type bond, is number of valence electrons of μ type bond per cubic angstroms, and is expressed as follows:

$$N_e^{\mu} = (n_e^{\mu})^*/v_b^{\mu}$$

$$(n_e^{\mu})^* = (Z_A^{\mu})^*/N_{CA} + (Z_B^{\mu})^*/N_{CB}$$

$$v_b^{\mu} = (d^{\mu})^3 \Big/ \sum_{\nu} [(d^{\nu})^3 N_b^{\nu}]$$

Where $(n_e^{\mu})^*$ is the number of valence electrons per μ type bond, Z_A^{μ} or Z_B^{μ} is the valence electron number of the A or B atom constructing μ type bond, respectively. v_b^{μ} is the bond volume, and N_b^{ν} is the bond number of type ν per unit volume.

Table 5.3 Elastic Constants and Mechanical Properties Derived from Atomistic CdSe-Sn_xS_y Models

	B (GPa)	C_{11} (GPa)	E (GPa)	G(GPa)	ν	H(GPa)
$Cd_{17}Se_{15}Sn_{19}S_{37}$	28.7	39	21.2	7.7	0.38	2.3
$Cd_{17}Se_{15}Sn_{21}S_{23}$	36.75	50.33	27.98	10.19	0.37	2.6
$Cd_{42}Se_{45}Sn_{59}S_{113}$	55.03	67.54	26.63	9.38	0.42	2.1
$Cd_{42}Se_{45}Sn_{67}S_{66}$	20.76	37.37	31.15	12.46	0.25	2.4

In our case, CdSe nanocrystal is capped with a thin atomic layer of amorphous SnS2 phase. The majority of covalent bonds involved here are Cd-Se bond, Sn-S bond, and interfacial bonds at the CdSe/SnS2 interface (including S-Cd, Se-Sn etc.). Most of the important parameters for determining the system hardness can be directly obtained via DFT calculations.

Specifically, given a $Cd_{42}Se_{45}$ NC core, its hardness increases from 2.3 GPa to 2.7 GPa when surface capped Sn_xS_y matrix is varied from SnS2 to SnS. Two possible reasons might be accounting for this, on one hand, our electronic band structure calculation indicates that the composites' band gap (E_g) increases increased Sn concentration, according to Gao's theory, a higher E_g suggests larger hardness as more energy is required to break the electron-pair bond and further displace the atoms; On

the other hand, the formation of sulfur chain[114] with increasing sulfur concentration softens the matrix and lead to a decrease in hardness.

Table 5.4 Elemental Composition Analysis via ICP-MS

CdSe size (nm)	Cd (wt%)	Se (wt%)	Sn (wt%)	S (wt%)	SnS2 concentration (g/cm^2)
3.5	52.71	22.66	5.22	2.82	3.62
5	50.46	24.25	4.25	2.29	4.25
7	52.70	28.94	4.35	2.35	5.18
8	52.90	31.49	2.42	1.30	3.51

6 FUTURE WORK: COLLOIDAL NANOCRYSTAL AND MAGIC-SIZED CLUSTER ASSEMBLIES AS PROMISING PHONONIC CRYSTALS

6.1 Introduction

As presented in this dissertation, we have systematically investigated the mechanical and thermal transport properties of colloidal nanocrystal and nanocluster assemblies. These studies lay foundations for future in-depth phononic properties on these material systems. As both mechanical and thermal transport properties can be correlated to its phononic structure. In this chapter, we will briefly show the promise of colloidal nanocrystal and nanocluster assemblies as phononic crystals with phononic band gap of larger frequency. We will also demonstrate a few powerful techniques can be potentially used towards this research direction. We hope this could inspire future experimental and computational efforts down this path.

Phononic crystal is defined as artificial crystals with a phononic band gap that forbids the propagation of phonons within the band gap frequency range. We know photonic crystals are periodically structured electromagnetic media, generally possessing photonic band gaps: ranges of frequencies in which light cannot propagate through the structure.[141-143] The band gap in a photonic crystal is caused by a periodic variation in the refractive index of an artificially structured material. Similarly, the bandgaps here for phonons was due to the periodic change of the material density and/or the elastic constant, that is, periodic change of the speed of sound.

To get an intuitive understanding of how band gaps form, one-dimensional crystal composed of alternating layers of two different materials is considered. At every interface an incoming wave transfers part of its energy into secondary, reflected waves, which then interfere with each other. Assuming the interference is constructive, all the energy of the original wave is reflected and the wave cannot propagate through

the crystal. On the other hand, if the interference is destructive, then all energy of the original wave is transmitted through the crystal. Therefore, constructive interference of the secondary waves results in the creation of a band gap while destructive interference leads to the formation of propagation bands. The condition for constructive interference is simply that the path differences between the interfering waves must be equal to an interger multiple of their wavelength, λ. Since the path difference is determined by the lattice parameter of the crystal, a, it is easy to see that constructive interference occurs when the lattice parameters are comparable to the wavelength. And since frequency is inversely proportional to wavelength, the frequency at the centre of the band gap, ω_g, is also inversely proportional to the lattice parameter: $\omega_g \sim 1/\lambda \sim 1/a$. As a result, we can create a band gap at any frequency we choose in a 1-dimensional crystal by simply changing the size of the unit cell. The width of the band gap is directly related to the ratio of the densities and sound velocities in the different layers: the large the ratio, the wider the gap.

To date, the phononics fields has focused mainly on kHz frequencies for sound manipulation, MHz frequencies for acoustic imaging, and GHz frequencies for optomechanics.[144, 145] Heat transporting phonons have frequencies over 100 GHz. This phonon regime as thus far evaded the phononics field because this frequency regime requires nanostructures with sub-10 nm size/precision. This size/precision requirements could not be achieved by standard fabrication technique, such as photolithography. But these nanoscale dimensions are naturally achieved with colloidal nanocrystals and molecular building blocks. Our group first evaluated the possibility of three-dimensional nanocrystal superlattice being phononic crystals using plane wave expansion modeling.[146] The simulation shows that the nanoscale periodicity of these superlattices yield phononic band gaps with very high center frequencies on the order of 100 GHz. In addition, based on simulation, the large acoustic contrast between the

hard nanocrystal cores and the soft ligand matrix lead to very large phononic band gap widths on the order of 10 GHz. All of these suggests that colloidal nanocrystal superlattices are promising candidates for use in high frequency phononic crystal applications.

To further push the phononic crystal band gap forward towards even higher frequencies, we suggest phononic crystals made of magic-sized nanoclusters. Compared to colloidal nanocrystals, magic sized nanocluster has unique atomic-precise core composition (sub-100 atoms) and similar surface chemistry as that of colloidal nanocrystals. This could lead to higher assembly order due to the disappearance of nanocluster core mass fluctuations. Additionally, a phononic band gap with higher center frequency (>100 GHz) is predicted as a result of smaller size of nanocluster core (sub 2nm) as compared to colloidal nanocrystals (>2nm).

6.2 **Phonon Spectroscopy**

Phonon spectroscopy is a promising technique for direct probing the phonon band gap. As is demonstrated in Figure 6.1, the phonon spectroscopy technique enables us to emit phonons of certain frequency range and detect the transmission phonons at the sample time. Ideally, we could directly observe the phononic band gap in the phonon transmission spectra of the nanocrystal superlattice.

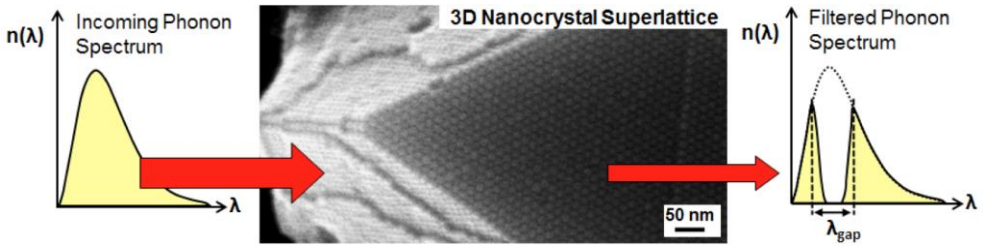

Figure 6.1 Colloidal nanocrystal superlattices can function as band-stop filters for high frequency, f, phonons due to their nanoscale periodicity.

6.2.1 **Experimental Setup**

Colloidal nanocrystal with crystalline inorganic core and soft organic ligand will first be synthesized and then self-assembled into close-packing supercrystals using a solvent-destabilization method. To test if these nanocrystal superlattices could be used for phononic crystals, phonon spectroscopy measurements done by earlier researches[147, 148] could be used to study frequency-resolved transport of phonons. The key tool in phonon spectroscopy measurement is the superconducting tunnel junctions (STJ), which consists of two superconductors separated by an insulation film (Al-insulator-Al). As we all know, metal become superconductors below their critical temperature, T_c, via formation of Cooper pairs. An energy gap of size Δ (typically 0.1-1 meV) separates the energy of these Copper pairs from other electronic states. STJs are the key tool in phonon spectroscopy because they can function as actively tunable monochromatic phonon generators and detectors.

6.2.1.1 ***Superconducting tunneling junction fabrication***

We conducted some preliminary work in the fabrication of STJ. We hope other researchers could benefit from our preliminary result. Specifically, we fabricated STJ using a bilayer photolithography and double-angle deposition method proposed in the literature[149]. The basic process involves the fabrication of an undercut structure in a resist bilayer to form a suspended "bridge", which was schematically demonstrated in Figure 6.3a. This was followed by two angle deposition of aluminum with an in-situ oxidation in between. Then, we obtained two overlapping wires separated by a thin layer of aluminum oxide, which is usually termed as Al-AlO_x-Al tunneling junction.

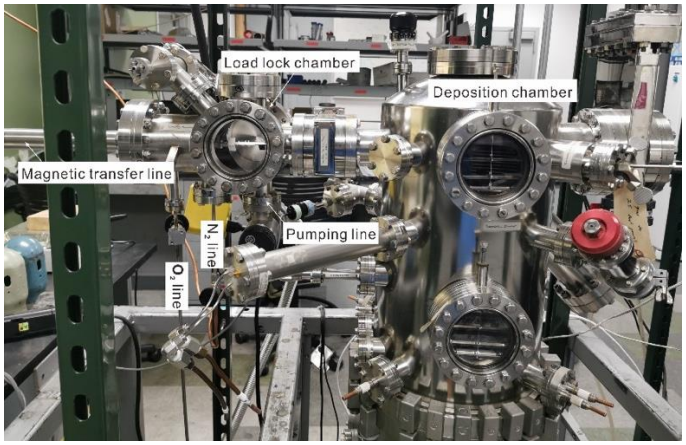

Figure 6.2 Home-built angular-dependent electron-beam deposition system for fabrication of superconducting tunneling junction.

Experimentally, we first fabricated the undercut structure using two distinct photoresists. Representative undercut structure was clearly seen in Figure 6.3b, where 6 patterns with suspended "bridges" were seen. The resulting bilayer structure was then amounted onto sample holder on the deposition system to perform the following depositions. To conduct angular dependent electron beam deposition, we utilized the magnetic transfer line that embedded onto our e-beam deposition system. Specifically, with the help of the magnetic transfer line, the sample substrate can be tuned at various angles. It should be pointed out that the quality and the thickness of the central oxide thin film is related to oxygen purity, pressure and exposure duration. As shown in Figure 6.2, our load lock chamber is equipped with high-purity oxygen line for in situ oxidation after first layer aluminum deposition. After the oxidation, the load lock was pumped to decent vacuum (10^{-6} mbar) through the pumping line before opening the gate valve between the load lock and main deposition chamber.

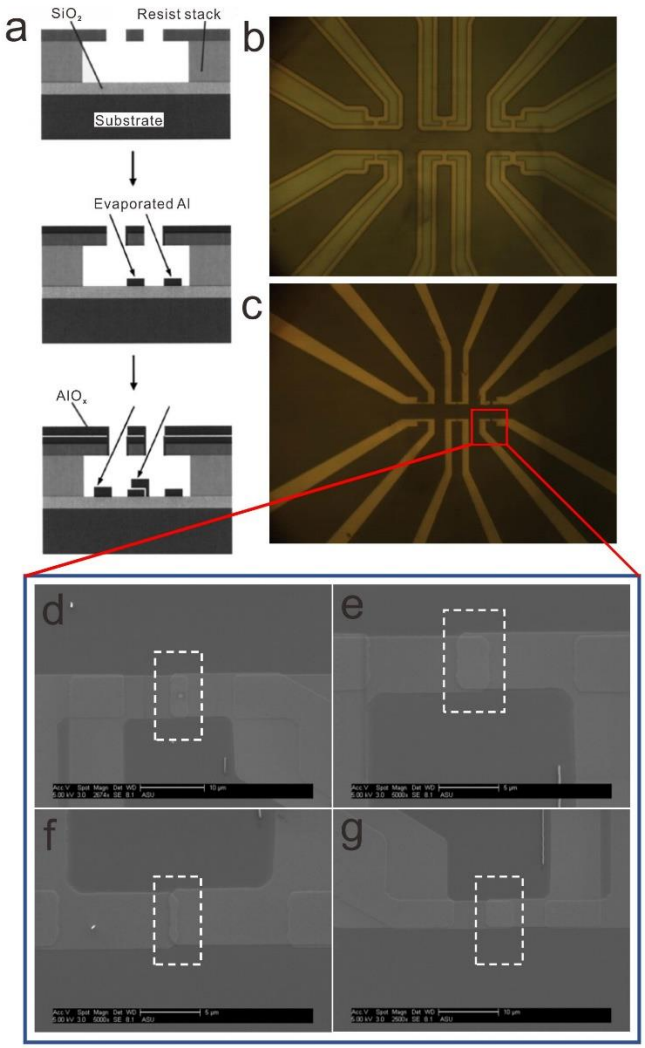

Figure 6.3 Fabrication of superconducting tunneling junction using bilayer photolithography and double angle deposition method. (a) Schematic illustration of Fabrication of Al-AlOx-Al superconducting tunneling junction using bilayer photolithography and double angle deposition method.[149] (b) photoresist pattern with undercut feature created with bilayer photolithography. (c) Optical image of Al-AlOx-Al superconducting tunneling junction along with the electrodes fabricated using this technique. (d-g) SEM images of the junction area of various dimensions. The overlap region highlighted are the tunneling junctions.

One optical microscope image of representative device fabricated using this home-built system was shown in Figure 6.3c. SEM images of the junction area shown in Figure 6.3d-g indicate that Al-AlO_x-Al tunneling junction can be fabricated with different dimensions. Additionally, the junction dimension can also be tuned by varying the deposition angles. It should be mentioned that the existing technique can be problematic when applied to soft colloidal nanocrystal assemblies. This is becoming even more challenging when colloidal nanocrystal of smaller sizes (3-6 nm) is used. Per our earlier discussion in this dissertation, colloidal nanocrystal of smaller sizes (3-6 nm) possesses very limited range of mechanical property as a result of weaker ligand-ligand interaction. Some of the methods (ligand crosslinking, inorganic functionalization) proposed earlier in this dissertation can be potentially used to address this problem.

6.2.1.2 ***Phonon generation and detection with STJ***

An STJ operates as a monochromatic phonon generator when a superimposed AC and DC voltage bias is applied across it (Figure 29 a). The energy and band width of the monochromatic phonons are tuned via the DC bias, $V_{0,gen}$, and the AC vias, δV_{gen}, respectively. When the DC bias exceeds $2\Delta_{gen}/e$, Copper pairs break and an electron current, i_{gen}, crosses through the STJ's insulating layer. On the opposite side of the insulator, the electrons relax back into cooper pairs and this relaxation energy is released by phonon creation. This creates a phonon generation spectrum as shown in Figure 29 c. The generation of monochromatic phonons with energy $eV_{0,gen} - 2\Delta_{gen}$ and bandwidth $\mathrm{e}\delta V_{gen}$ (hashed region in Figure 29 c) can be isolated by locking into the AC frequency with a lock-in amplifier.[147, 150]

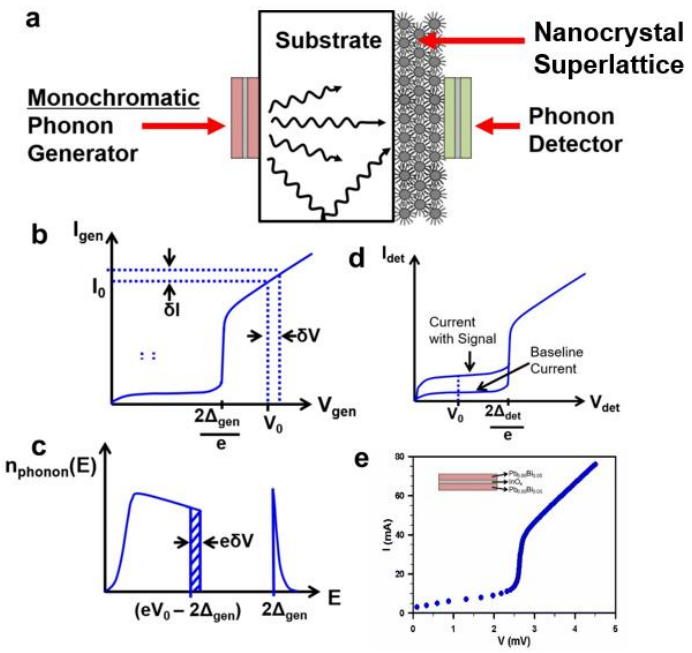

Figure 6.4 (a) Diagram of a phonon spectroscopy experiment that uses superconducting tunnel junctions as tunable monochromatic phonon generators and detectors. (b) The current-voltage plot of an Al superconducting tunnel junction (STJ). If a superimposed AC and DC voltage is applied, $V_{0,gen} + \delta V_{gen} \sin(\omega t)$, the STJ generates the phonon spectrum in (c). (d) Impinging phonons on STJ detector biased at $V_{0,det} < 2\Delta_{det}/e$ create an excess signal, i_{sig}, by breaking copper pairs and yielding extra tunneling electrons. (e) An IV curve for a $Pb_{0.95}Bi_{0.05}/InO_x/Pb_{0.95}Bi_{0.05}$ STJ at T equals to 4.2 K.

To operate the STJ phonon detector, a small voltage bias less than $2\Delta_{det}/e$ is applied. When phonons of energy greater than $2\Delta_{det}$ arrive from the generator, the detector current is augmented by an amount i_{sig} (Figure 8). This is the result of the impinging phonons having sufficient energy to break Cooper pairs and creating additional current. The detector's i_{sig} is related to the number of 2Δ phonons absorbed per unit time in the detector, n'_{ph}, by the equation:

$$i_{sig} = \left[\frac{\left(eV_{0,det} + \Delta_{det}\right)}{eR_{\infty}N_0\sqrt{\left(eV_{0,det} + \Delta_{det}\right)^2 - \Delta_{det}^2}} \frac{\tau_{eff}}{Ad} \right] n'_{ph}$$

Where $V_{0,det}$ is the nominal detector bias, A and d are the detector area and thickness, R_{∞} is the normal state resistance, N_0 is the electron density of states for one spin, and τ_{eff} is the life time for thermally excited electrons to recombine into cooper pairs. The values for A, d, R_{∞} and Δ come from basic characterization. N_0 is a known value for a given detector type. The value of τ_{eff} is determined via the time decay of the detector's signal in response to phonon pulses.

The phonon transmission spectrum is measured by systematically stepping through different $V_{0,gen}$ in the phonon generator and measuring the corresponding i_{sig} in the phonon detector. The upper frequency limit of a phonon spectrometer is maximized by using aluminum STJs, which can spectroscopically resolve phonons from 90 GHz – 3 THz.[151, 152]

6.3 Inelastic Neutron and X-ray Scattering

In addition to phonon spectroscopy technique presented above, there are other powerful techniques can be used to study the phononic properties of colloidal nanocrystal solids. Here we introduced two representative techniques (inelastic neutron and X-ray scattering) that has been utilized to uncover the vibrational density of states of colloidal nanocrystal assemblies. Some of the key finding of these studies are also included.

While requiring large amount of NC solid material, inelastic neutron scattering (INS) has the advantage of higher energy resolution. So, this technique is ideal for probing low frequency coherent phonons in NC assemblies given enough material. Yazdani et al.[90] conducted inelastic neutron scattering on large scale of PbS nanocrystal samples

(~8g) and successfully observed the presence of coherent phonon modes in disordered nanocrystal assemblies. Specifically, as shown in Figure 6.5a-d, Yazdani et al.[90] performed INS measurements on NC solids of various core size and ligands of various length. The energy corresponds to 1st peak of vibrational density of states scales with r^{-1}, which is in good agreement with predictions of mas-spring model presented in this work. Similarly, by varying the length of molecular ligands that bridge the neighboring nanocrystals, they can tune the stiffness of the organic ligand molecule. This further leads to similar energy shift of the 1st vibrational density of states that observed when tuning the nanocrystal sizes.

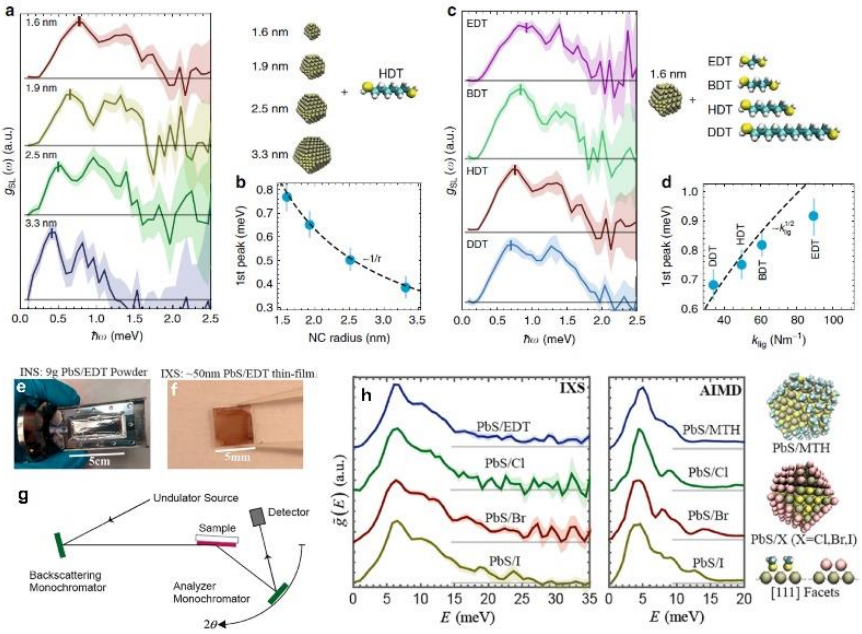

Figure 6.5 Phononic properties of colloidal nanocrystal solids detected via inelastic neutron and X-ray scattering techniques. (a) Extracted phonon density of states for NC solids fabricated with NCs of varying size from 1.6 nm to 3.3 nm, the shaded region indicates the error, the measurement was performed at 300 K. (b) the phonon energy of the 1st peak scales with r-1. (c) Extracted phonon density of states for NC solids fabricated with 1.6nm NCs with EDT, BDT, HDT, or DDT ligands measured at 300 K.

(d) A weak scaling of phonon energy of the 1st peak versus the force constants of the molecular ligands. Photographs of PbS NCs samples for both (e) inelastic neutron scattering and (f) inelastic X-ray scattering techniques. (g) Schematic of the set-up of the inelastic experiments. (h) The atomic structure factor weighted density of vibrational states, which is measured with IXS for PbS NC solid thin films with various surface termination. Computation results with AIMD was also shown as a comparison. The atomistic model of the AIMD simulations is shown in the right. Figures adapted from references[90, 153].

While not capable of detecting coherent phonon modes, inelastic X-ray scattering(IXS)[153] still can be used for studying the vibrations within the nanocrystal. And IXS measurements can be performed on a thin nanocrystal thin film (Figure 6.5f), which make it a lot easier for measuring nanomaterials of vary small quantities. A schematic of the IXS set-up is described in Figure 6.5g. The backscattering reflections of Si is employed to achieve a monochromatic beam at a wavelength of 0.6968 angstrom (17.8 keV). The X-ray beam impinges on the sample, scatters, and is analyzed by a second Si monochromator. Through varying the relative temperatures of two Si monochromators to tune their lattice constants and thereby the resulting diffraction angles, they are able to scan over photon-to-sample energy transfers. They performed measurements on three PbS/X NC thin films with different halide (X=Cl, Br, I) surface terminations and the result is shown in Figure 6.5h. As predicted by ab initio molecular dynamics (AIMD), different terminations will not change the number of the low frequency modes coming from the surface. This is in line with IXS measurements.

6.4 Future work

As mentioned earlier in this chapter, performing phonon spectroscopy on colloidal nanocrystal and nanocluster assemblies is promising, but also challenging. We suggest

starting with a polycrystalline nanocrystal thin film, which is comprised of many nanocrystal superlattice grains with varying grain size and orientation (Figure 6.6h). Polycrystalline superlattice can be made very quickly via drop-casting or spin-coating, which greatly simplifies alignment processes for the phonon-generator/detector used during phonon spectroscopy. It should be pointed out that phonon spectroscopy will probe an ensemble of grains because the phonon generator and detector are much larger than the superlattice grains. Despite probing an ensemble of superlattice grains, phononic band gap effects will still be observable during phonon spectroscopy measurements. This is because the phononic band gap occurs in all crystallographic directions, and hence phonon transmission will be insensitive to random grain orientations. Coinciding with the band gap will be a spectral gap in the phonon transmission spectrum. Phonon spectroscopy control measurements on amorphous nanocrystal solids (Figure 6.6i) will be used to confirm that the observed spectral features are due to the band gap. Amorphous control samples avia judicious selection of the deposition solvent as described by Urban.[154]

Although theoretical study indicates that the phononic band gap within nanocrystal assemblies should be isotropic and shouldn't be affected by grain boundaries, still, the phonon transmission, will be scattered by defects or boundaries within the assemblies. So, NCSL still serves as a more promising phononic crystal than short range ordered NC thin film considering the absence of boundaries in NCSL. However, as shown in Figure 6.6d-f, superlattices prepared with state-of-the-art techniques are limited to 20-200 um in lateral size, which presents a great challenge for fabricating tunneling junctions on top of them using standard lithography technique. Apart from that, colloidal nanocrystal superlattices still exhibit defects like vacancies and dislocations due to the polydispersity of colloidal nanocrystals (Figure 6.6d, g). Alternatively, supercrystals using atomic-precise magic sized cluster presents great potential for

defect-free superlattice. Very recently, supercrystals of gold nanoclusters with long range order and little defect was reported. However, the resulting supercrystals were still limited to ~20 um in size. Future efforts could be devoted to supercrystal growth out of magic-sized clusters to obtain supercrystals with bigger size and controlled surface orientation. On the other hand, nanofabrication techniques could be possibly modified to be applied to the tiny supercrystals out of either colloidal nanocrystals or magic-sized clusters to fabricate superconducting tunneling junctions on selective position on top of supercrystals.

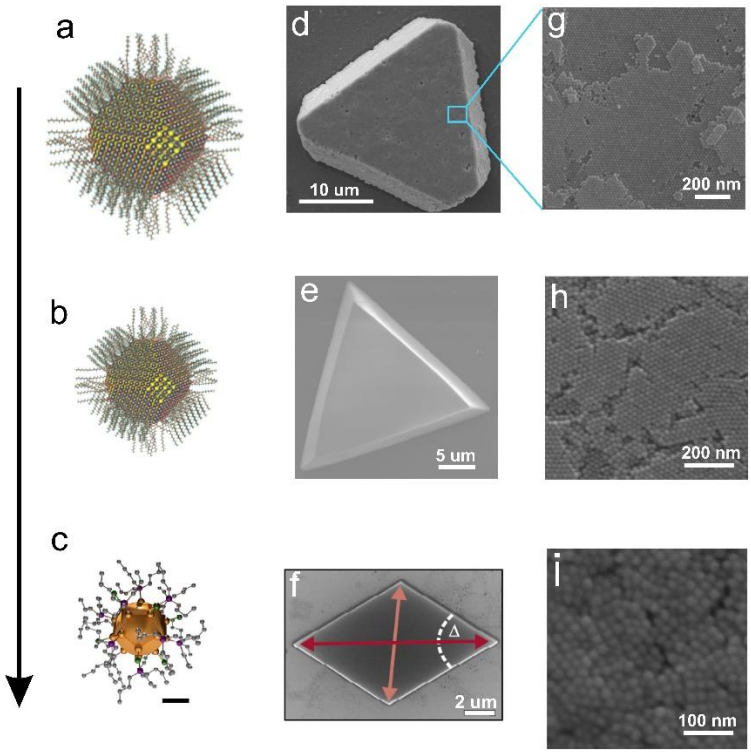

Figure 6.6 From colloidal nanocrystals to magic sized clusters: length scale and assembly order. (a-b) Schematic illustration of large (>10nm) and small (<10nm) PbS nanocrystals of oleic acid ligands, respectively. (c) Structural drawing of $Au_{32}(^{n}Bu_3P)_{12}Cl_8$ nanocluster.[155] (d-f) Supercrystals grown from building blocks shown

in (a-c). (g) A high magnification SEM picture of single domain nanocrystal superlattice shown in (d). High magnification SEM images shown (h) short-ranged ordered and (i) disordered nanocrystal thin films prepared with spin coating.

Alternatively, non-contact techniques like INS and IXS can be utilized for probing phononic properties of colloidal nanocrystal and nanocluster assemblies directly. However, INS and IXS suffer from large sample quantity and low energy resolution, respectively. Compared to colloidal nanocrystal superlattice, nanocluster superlattice possesses phononic band gap of higher center frequency. So, conducting IXS on nanocluster superlattice presents a promising way of decoding the phononic properties of nanocluster superlattices.

It would also be interesting to further study the role of coherent phonon transport in thermal transport in nanocrystal and nanocluster superlattices. Coherent thermal transport has been studied in epitaxially grown 1-D superlattice structures.[87, 88] Per our previous discussion in chapter 4, coherent phonons in colloidal nanocrystal superlattice are unlikely to contribute to thermal transport due to their low energy and low group velocity, and low mean free path due to scattering with defects or nanocrystal phonons. one obvious way of increasing the coherent phonon energy and their group velocity is to lower the core weight and/or and enhance the spring stiffness. Compared to colloidal nanocrystals, magic-sized nanoclusters are atomic-precise and much smaller in core size (sub 2 nm). Thus, we could achieve supercrystals with little defects which support excitation of coherent phonon of higher energy, group velocity, and longer mean free path. Study phononic properties of magic-sized clusters supercrystals can be of great importance for fundamental understanding and engineering of phonon transport in these unique structures.

REFERENCES

1. Park, J.; An, K. J.; Hwang, Y. S.; Park, J. G.; Noh, H. J.; Kim, J. Y.; Park, J. H.; Hwang, N. M.; Hyeon, T. *Nat Mater* **2004,** 3, (12), 891-895.

2. Puntes, V. F.; Krishnan, K. M.; Alivisatos, A. P. *Science* **2001,** 291, (5511), 2115-2117.

3. Tao, A. R.; Habas, S.; Yang, P. D. *Small* **2008,** 4, (3), 310-325.

4. Du, H.; Chen, C. L.; Krishnan, R.; Krauss, T. D.; Harbold, J. M.; Wise, F. W.; Thomas, M. G.; Silcox, J. *Nano Letters* **2002,** 2, (11), 1321-1324.

5. Smith, A. M.; Mohs, A. M.; Nie, S. *Nat Nanotechnol* **2009,** 4, (1), 56-63.

6. Song, Q.; Zhang, Z. J. *J Am Chem Soc* **2004,** 126, (19), 6164-6168.

7. Zherebetskyy, D.; Scheele, M.; Zhang, Y. J.; Bronstein, N.; Thompson, C.; Britt, D.; Salmeron, M.; Alivisatos, P.; Wang, L. W. *Science* **2014,** 344, (6190), 1380-1384.

8. Bodnarchuk, M. I.; Kovalenko, M. V., *Engineering Colloidal Quantum Dots*. Cambridge University Press: Cambridge: 2013.

9. Faraday, M. *Philos. Trans. R. Soc. London* **1846,** 136, 104.

10. Enustun, B. V.; Turkevich, J. *J Am Chem Soc* **1963,** 85, (21), 3317-+.

11. Sun, S. H.; Murray, C. B. *Journal of Applied Physics* **1999,** 85, (8), 4325-4330.

12. Wiley, B.; Sun, Y.; Mayers, B.; Xia, Y. *Chemistry* **2005,** 11, (2), 454-63.

13. Murray, C.; Norris, D. J.; Bawendi, M. G. *J Am Chem Soc* **1993,** 115, (19), 8706-8715.

14. Lee, J. S.; Kovalenko, M. V.; Huang, J.; Chung, D. S.; Talapin, D. V. *Nat Nanotechnol* **2011,** 6, (6), 348-52.

15. Choi, J.-H.; Wang, H.; Oh, S. J.; Paik, T.; Sung, P.; Sung, J.; Ye, X.; Zhao, T.; Diroll, B. T.; Murray, C. B. *Science* **2016,** 352, (6282), 205-208.

16. Boles, M. A.; Engel, M.; Talapin, D. V. *Chemical reviews* **2016,** 116, (18), 11220-11289.

17. Talapin, D. V.; Murray, C. B. *Science* **2005,** 310, (5745), 86-89.

18. Bigioni, T. P.; Lin, X.-M.; Nguyen, T. T.; Corwin, E. I.; Witten, T. A.; Jaeger, H. M. *Nat Mater* **2006,** 5, (4), 265.

19. Dong, A.; Chen, J.; Vora, P. M.; Kikkawa, J. M.; Murray, C. B. *Nature* **2010,** 466, (7305), 474.

20. Rupich, S. M.; Shevchenko, E. V.; Bodnarchuk, M. I.; Lee, B.; Talapin, D. V. *J Am Chem Soc* **2009,** 132, (1), 289-296.

21. Talapin, D. V.; Shevchenko, E. V.; Kornowski, A.; Gaponik, N.; Haase, M.; Rogach, A. L.; Weller, H. *Adv Mater* **2001,** 13, (24), 1868-1871.

22. Kaviany, M., *Heat transfer physics*. Cambridge University Press: 2014.

23. Ruan, X.; Bao, H.; Kaviany, M. In *Boundary-Induced Vibrational Spectra Broadening in Nanostructures*, ASME 2007 International Mechanical Engineering Congress and Exposition, 2007; American Society of Mechanical Engineers: pp 1181-1188.

24. Losego, M. D.; Grady, M. E.; Sottos, N. R.; Cahill, D. G.; Braun, P. V. *Nat Mater* **2012,** 11, (6), 502.

25. Hu, M.; Keblinski, P.; Schelling, P. K. *Phys Rev B* **2009,** 79, (10), 104305.

26. Prasher, R. *Applied Physics Letters* **2009,** 94, (4), 041905.

27. Hill, H. D.; Millstone, J. E.; Banholzer, M. J.; Mirkin, C. A. *ACS nano* **2009,** 3, (2), 418-424.

28. Jiménez, A.; Sarsa, A.; Blázquez, M.; Pineda, T. *The Journal of Physical Chemistry C* **2010,** 114, (49), 21309-21314.

29. Ong, W.-L.; Rupich, S. M.; Talapin, D. V.; McGaughey, A. J.; Malen, J. A. *Nature materials* **2013,** 12, (5), 410.

30. Hasselman, D.; Johnson, L. F. *Journal of composite materials* **1987,** 21, (6), 508-515.

31. Talapin, D. V.; Lee, J.-S.; Kovalenko, M. V.; Shevchenko, E. V. *Chemical reviews* **2009,** 110, (1), 389-458.

32. Liu, M.; Ma, Y.; Wang, R. Y. *ACS nano* **2015,** 9, (12), 12079-12087.

33. Lee, S.-M.; Jun, Y.-w.; Cho, S.-N.; Cheon, J. *J Am Chem Soc* **2002,** 124, (38), 11244-11245.

34. Powell Jr, B. R.; Youngblood, G.; Hasselman, D.; Bentsen, L. D. *Journal of the American Ceramic Society* **1980,** 63, (9-10), 581-586.

35. Hatta, H.; Taya, M. *Journal of applied physics* **1986,** 59, (6), 1851-1860.

36. Minnich, A.; Chen, G. *Applied Physics Letters* **2007,** 91, (7), 073105.

37. Li, X. D.; Bhushan, B. *Mater Charact* **2002,** 48, (1), 11-36.

38. Podsiadlo, P.; Krylova, G.; Lee, B.; Critchley, K.; Gosztola, D. J.; Talapin, D. V.; Ashby, P. D.; Shevchenko, E. V. *J Am Chem Soc* **2010,** 132, (26), 8953-8960.

39. Mueggenburg, K. E.; Lin, X. M.; Goldsmith, R. H.; Jaeger, H. M. *Nat Mater* **2007,** 6, (9), 656-660.

40. Zanjani, M. B.; Lukes, J. R. *J Chem Phys* **2013,** 139, (14).

41. Shaw, S.; Colaux, J. L.; Hay, J. L.; Peiris, F. C.; Cademartiri, L. *Adv Mater* **2016,** 28, (40), 8900-8905.

42. Gu, X. W.; Ye, X. C.; Koshy, D. M.; Vachhani, S.; Hosemann, P.; Alivisatos, A. P. *P Natl Acad Sci USA* **2017,** 114, (11), 2836-2841.

43. Dreyer, A.; Feld, A.; Kornowski, A.; Yilmaz, E. D.; Noei, H.; Meyer, A.; Krekeler, T.; Jiao, C.; Stierle, A.; Abetz, V. *Nature materials* **2016,** 15, (5), 522.

44. Lewis, D. J.; Carter, D. J. D.; Macfarlane, R. J. *J Am Chem Soc* **2020,** 142, (45), 19181-19188.

45. Choy, C. L.; Wong, Y. W.; Yang, G. W.; Kanamoto, T. *J Polym Sci Pol Phys* **1999,** 37, (23), 3359-3367.

46. Xie, X.; Yang, K. X.; Li, D. Y.; Tsai, T. H.; Shin, J.; Braun, P. V.; Cahill, D. G. *Phys Rev B* **2017,** 95, (3).

47. Ong, W. L.; O'Brien, E. S.; Dougherty, P. S. M.; Paley, D. W.; Higgs, C. F.; McGaughey, A. J. H.; Malen, J. A.; Roy, X. *Nat Mater* **2017,** 16, (1), 83-88.

48. Elbaz, G. A.; Ong, W.-L.; Doud, E. A.; Kim, P.; Paley, D. W.; Roy, X.; Malen, J. A. *Nano Letters* **2017,** 17, (9), 5734-5739.

49. Talapin, D. V.; Lee, J. S.; Kovalenko, M. V.; Shevchenko, E. V. *Chem Rev* **2010,** 110, (1), 389-458.

50. Oh, S. J.; Wang, Z. Q.; Berry, N. E.; Choi, J. H.; Zhao, T. S.; Gaulding, E. A.; Paik, T.; Lai, Y. M.; Murray, C. B.; Kagan, C. R. *Nano Letters* **2014,** 14, (11), 6210-6216.

51. Saran, R.; Curry, R. J. *Nat Photonics* **2016,** 10, (2), 81-92.

52. Tang, J.; Kemp, K. W.; Hoogland, S.; Jeong, K. S.; Liu, H.; Levina, L.; Furukawa, M.; Wang, X. H.; Debnath, R.; Cha, D. K.; Chou, K. W.; Fischer, A.; Amassian, A.; Asbury, J. B.; Sargent, E. H. *Nature Materials* **2011,** 10, (10), 765-771.

53. Yuan, M. J.; Liu, M. X.; Sargent, E. H. *Nat Energy* **2016,** 1.

54. Wang, R. Y.; Feser, J. P.; Lee, J. S.; Talapin, D. V.; Segalman, R.; Majumdar, A. *Nano Lett* **2008,** 8, (8), 2283-2288.

55. William, W. Y.; Falkner, J. C.; Yavuz, C. T.; Colvin, V. L. *Chemical Communications* **2004**, (20), 2306-2307.

56. Borca-Tasciuc, T.; Kumar, A.; Chen, G. *Review of scientific instruments* **2001,** 72, (4), 2139-2147.

57. Cahill, D. G. *Review of scientific instruments* **1990,** 61, (2), 802-808.

58. Lee, S. M.; Cahill, D. G. *J Appl Phys* **1997,** 81, (6), 2590-2595.

59. Slack, G. A. *Physical Review* **1962,** 126, (2), 427-&.

60. Pei, Y.-L.; Liu, Y. *Journal of Alloys and Compounds* **2012,** 514, 40-44.

61. Oliver, W. C.; Pharr, G. M. *J Mater Res* **1992,** 7, (6), 1564-1583.

62. Hay, J.; Crawford, B. *J Mater Res* **2011,** 26, (6), 727-738.

63. Rupich, S. M.; Shevchenko, E. V.; Bodnarchuk, M. I.; Lee, B.; Talapin, D. V. *J Am Chem Soc* **2010,** 132, (1), 289-296.

64. Reichmann, H. J.; Jacobsen, S. D. *Am Mineral* **2004,** 89, (7), 1061-1066.

65. Affdl, J. C. H.; Kardos, J. L. *Polymer Engineering & Science* **1976,** 16, (5), 344-352.

66. Kinsler, L. E., *Fundamentals of acoustics*. 4th ed.; Wiley: New York, 2000; p xii, 548 p.

67. Huang, D. H.; Simon, S. L.; McKenna, G. B. *J Chem Phys* **2005,** 122, (8).

68. Xie, X.; Li, D. Y.; Tsai, T. H.; Liu, J.; Braun, P. V.; Cahill, D. G. *Macromolecules* **2016,** 49, (3), 972-978.

69. Snow, C. L.; Shi, Q. A.; Boerio-Goates, J.; Woodfield, B. F. *J Phys Chem C* **2010,** 114, (49), 21100-21108.

70. Nsubuga, A.; Zarschler, K.; Sgarzi, M.; Graham, B.; Stephan, H.; Joshi, T. *Angewandte Chemie* **2018,** 130, (49), 16268-16272.

71. Deacon, G. B.; Phillips, R. J. *Coordin Chem Rev* **1980,** 33, (3), 227-250.

72. Ma, Y. Y.; Liu, M. L.; Jaber, A.; Wang, R. Y. *J Mater Chem A* **2015,** 3, (25), 13483-13491.

73. Ma, Y. Y.; Vartak, P. B.; Nagaraj, P.; Wang, R. Y. *Rsc Adv* **2016,** 6, (102), 99905-99913.

74. Wang, R. Y.; Feser, J. P.; Gu, X.; Yu, K. M.; Segalman, R. A.; Majumdar, A.; Milliron, D. J.; Urban, J. J. *Chem Mater* **2010,** 22, (6), 1943-1945.

75. Wang, R. Y.; Segalman, R. A.; Majumdar, A. *Appl Phys Lett* **2006,** 89, (17).

76. Harikrishnan, S.; Kalaiselvam, S. *Thermochimica Acta* **2012,** 533, 46-55.

77. Ong, W. L.; Rupich, S. M.; Talapin, D. V.; McGaughey, A. J. H.; Malen, J. A. *Nat Mater* **2013,** 12, (5), 410-415.

78. Liu, M. L.; Ma, Y. Y.; Wang, R. Y. *Acs Nano* **2015,** 9, (12), 12079-12087.

79. Wang, Z. Y.; Singaravelu, A. S. S.; Dai, R.; Nian, Q.; Chawla, N.; Wang, R. Y. *Angew Chem Int Edit* **2020,** 59, (24), 9556-9563.

80. Shen, S.; Henry, A.; Tong, J.; Zheng, R. T.; Chen, G. *Nat Nanotechnol* **2010,** 5, (4), 251-255.

81. Wang, Z. H.; Carter, J. A.; Lagutchev, A.; Koh, Y. K.; Seong, N. H.; Cahill, D. G.; Dlott, D. D. *Science* **2007,** 317, (5839), 787-790.

82. Hines, M. A.; Scholes, G. D. *Advanced Materials* **2003,** 15, (21), 1844-1849.

83. Lee, B.; Podsiadlo, P.; Rupich, S.; Talapin, D. V.; Rajh, T.; Shevchenko, E. V. *J Am Chem Soc* **2009,** 131, (45), 16386-+.

84. Milowska, K. Z.; Stolarczyk, J. K. *Phys Chem Chem Phys* **2016,** 18, (18), 12716-12724.

85. He, J.; Kanjanaboos, P.; Frazer, N. L.; Weis, A.; Lin, X. M.; Jaeger, H. M. *Small* **2010,** 6, (13), 1449-56.

86. Terrill, R. H.; Postlethwaite, T. A.; Chen, C. H.; Poon, C. D.; Terzis, A.; Chen, A. D.; Hutchison, J. E.; Clark, M. R.; Wignall, G.; Londono, J. D.; Superfine, R.; Falvo, M.; Johnson, C. S.; Samulski, E. T.; Murray, R. W. *J Am Chem Soc* **1995,** 117, (50), 12537-12548.

87. Ravichandran, J.; Yadav, A. K.; Cheaito, R.; Rossen, P. B.; Soukiassian, A.; Suresha, S. J.; Duda, J. C.; Foley, B. M.; Lee, C. H.; Zhu, Y.; Lichtenberger, A. W.; Moore, J. E.; Muller, D. A.; Schlom, D. G.; Hopkins, P. E.; Majumdar, A.; Ramesh, R.; Zurbuchen, M. A. *Nat Mater* **2014,** 13, (2), 168-172.

88. Luckyanova, M. N.; Garg, J.; Esfarjani, K.; Jandl, A.; Bulsara, M. T.; Schmidt, A. J.; Minnich, A. J.; Chen, S.; Dresselhaus, M. S.; Ren, Z. F.; Fitzgerald, E. A.; Chen, G. *Science* **2012,** 338, (6109), 936-939.

89. Poyser, C. L.; Czerniuk, T.; Akimov, A.; Diroll, B. T.; Gaulding, E. A.; Salasyuk, A. S.; Kent, A. J.; Yakovlev, D. R.; Bayer, M.; Murray, C. B. *Acs Nano* **2016,** 10, (1), 1163-1169.

90. Yazdani, N.; Jansen, M.; Bozyigit, D.; Lin, W. M. M.; Volk, S.; Yarema, O.; Yarema, M.; Juranyi, F.; Huber, S. D.; Wood, V. *Nat Commun* **2019,** 10.

91. Talapin, D. V.; Shevchenko, E. V.; Murray, C. B.; Titov, A. V.; Kral, P. *Nano Lett* **2007,** 7, (5), 1213-9.

92. Bertolotti, F.; Dirin, D. N.; Ibanez, M.; Krumeich, F.; Cervellino, A.; Frison, R.; Voznyy, O.; Sargent, E. H.; Kovalenko, M. V.; Guagliardi, A.; Masciocchi, N. *Nat Mater* **2016,** 15, (9), 987-994.

93. Salem, L. *J Chem Phys* **1962,** 37, (9), 2100-&.

94. Chung, D. H.; Buessem, W. R. *J Appl Phys* **1968,** 39, (6), 2777-2782.

95. Chenoweth, K.; Van Duin, A. C. T.; Goddard, W. A. *The Journal of Physical Chemistry A* **2008,** 112, (5), 1040-1053 %@ 1089-5639.

96. Medhekar, N. V.; Ramasubramaniam, A.; Ruoff, R. S.; Shenoy, V. B. *ACS Nano* **2010,** 4, (4), 2300-2306 %@ 1936-0851.

97. Van Duin, A. C. T.; Dasgupta, S.; Lorant, F.; Goddard, W. A. *The Journal of Physical Chemistry A* **2001,** 105, (41), 9396-9409 %@ 1089-5639.

98. Bringa, E. M.; Caro, A.; Wang, Y. M.; Victoria, M.; McNaney, J. M.; Remington, B. A.; Smith, R. F.; Torralva, B. R.; Van Swygenhoven, H. *Science* **2005,** 309, (5742), 1838-1841.

99. Li, X. Y.; Jin, Z. H.; Zhou, X.; Lu, K. *Science* **2020,** 370, (6518), 831-836.

100. Nieman, G. W.; Weertman, J. R.; Siegel, R. W. *Scripta Metall Mater* **1989,** 23, (12), 2013-2018.

101. Suryanarayana, C. *Progress in Materials Science* **2001,** 46, (1), 1-184.

102. Erb, U. *Nanostruct Mater* **1995,** 6, (5-8), 533-538.

103. Lu, K.; Wang, J. T.; Wei, W. D. *J Appl Phys* **1991,** 69, (1), 522-524.

104. Iwahashi, Y.; Wang, J. T.; Horita, Z.; Nemoto, M.; Langdon, T. G. *Scripta Mater* **1996,** 35, (2), 143-146.

105. Steinhagen, C.; Panthani, M. G.; Akhavan, V.; Goodfellow, B.; Koo, B.; Korgel, B. A. *J Am Chem Soc* **2009,** 131, (35), 12554-+.

106. McDonald, S. A.; Konstantatos, G.; Zhang, S. G.; Cyr, P. W.; Klem, E. J. D.; Levina, L.; Sargent, E. H. *Nat Mater* **2005,** 4, (2), 138-142.

107. Kagan, C. R.; Lifshitz, E.; Sargent, E. H.; Talapin, D. V. *Science* **2016,** 353, (6302).

108. See, K. C.; Feser, J. P.; Chen, C. E.; Majumdar, A.; Urban, J. J.; Segalman, R. A. *Nano Lett* **2010,** 10, (11), 4664-7.

109. Talapin, D. V.; Murray, C. B. *Science* **2005,** 310, (5745), 86-89.

110. Choi, J.; Hui, C. M.; Pietrasik, J.; Dong, H. C.; Matyjaszewski, K.; Bockstaller, M. R. *Soft Matter* **2012,** 8, (15), 4072-4082.

111. Tam, E.; Podsiadlo, P.; Shevchenko, E.; Ogletree, D. F.; Delplancke-Ogletree, M. P.; Ashby, P. D. *Nano Lett* **2010,** 10, (7), 2363-2367.

112. Dreyer, A.; Feld, A.; Kornowski, A.; Yilmaz, E. D.; Noei, H.; Meyer, A.; Krekeler, T.; Jiao, C. G.; Stierle, A.; Abetz, V.; Weller, H.; Schneider, G. A. *Nat Mater* **2016,** 15, (5), 522-+.

113. Kovalenko, M. V.; Scheele, M.; Talapin, D. V. *Science* **2009,** 324, (5933), 1417-1420.

114. Scalise, E.; Srivastava, V.; Janke, E.; Talapin, D.; Galli, G.; Wippermann, S. *Nat Nanotechnol* **2018,** 13, (9), 841-+.

115. Fritzinger, B.; Capek, R. K.; Lambert, K.; Martins, J. C.; Hens, Z. *J Am Chem Soc* **2010,** 132, (29), 10195-10201.

116. Qu, L. H.; Peng, Z. A.; Peng, X. G. *Nano Lett* **2001,** 1, (6), 333-337.

117. Yu, W. W.; Qu, L. H.; Guo, W. Z.; Peng, X. G. *Chem Mater* **2003,** 15, (14), 2854-2860.

118. Podsiadlo, P.; Lee, B.; Prakapenka, V. B.; Krylova, G. V.; Schaller, R. D.; Demortiere, A.; Shevchenko, E. V. *Nano Lett* **2011,** 11, (2), 579-588.

119. Yan, C.; Arfaoui, I.; Goubet, N.; Pileni, M. P. *Adv Funct Mater* **2013,** 23, (18), 2315-2321.

120. Liu, X. P.; Ni, Y.; He, L. H. *J Chem Phys* **2016,** 144, (14).

121. Marsh, D. M. *Proc R Soc Lon Ser-A* **1964,** 279, (1376), 420-+.

122. Schiotz, J.; Di Tolla, F. D.; Jacobsen, K. W. *Nature* **1998,** 391, (6667), 561-563.

123. Guo, D. Z.; Song, S. X.; Luo, R. C.; Goddard, W. A.; Chen, M. W.; Reddy, K. M.; An, Q. *Phys Rev Lett* **2018,** 121, (14).

124. Nair, S. S.; Khadar, M. A. *J Nanopart Res* **2009,** 11, (2), 485-490.

125. Gao, F. M.; He, J. L.; Wu, E. D.; Liu, S. M.; Yu, D. L.; Li, D. C.; Zhang, S. Y.; Tian, Y. J. *Phys Rev Lett* **2003,** 91, (1).

126. Dong, A. G.; Ye, X. C.; Chen, J.; Kang, Y. J.; Gordon, T.; Kikkawa, J. M.; Murray, C. B. *J Am Chem Soc* **2011,** 133, (4), 998-1006.

127. Nag, A.; Kovalenko, M. V.; Lee, J. S.; Liu, W. Y.; Spokoyny, B.; Talapin, D. V. *J Am Chem Soc* **2011,** 133, (27), 10612-10620.

128. Zhang, H.; Dasbiswas, K.; Ludwig, N. B.; Han, G.; Lee, B.; Vaikuntanathan, S.; Talapin, D. V. *Nature* **2017,** 542, (7641), 328-+.

129. Fotovvati, B.; Namdari, N.; Dehghanghadikolaei, A. *Journal of Manufacturing and Materials Processing* **2019,** 3, (1).

130. Zhu, T. T.; Zhang, B. W.; Zhang, J.; Lu, J.; Fan, H. S.; Rowell, N.; Ripmeester, J. A.; Han, S.; Yu, K. *Chem Mater* **2017,** 29, (13), 5727-5735.

131. Mitzi, D. B.; Kosbar, L. L.; Murray, C. E.; Copel, M.; Afzali, A. *Nature* **2004,** 428, (6980), 299-303.

132. Kim, H. S.; Bush, M. B. *Nanostruct Mater* **1999,** 11, (3), 361-367.

133. Budiansk.B. *J Compos Mater* **1970,** 4, 286-&.

134. Kim, H. S.; Estrin, Y.; Bush, M. B. *Mat Sci Eng a-Struct* **2001,** 316, (1-2), 195-199.

135. Coble, R. L. *J Appl Phys* **1963,** 34, (6), 1679-&.

136. Herring, C. *J Appl Phys* **1950,** 21, (5), 437-445.

137. Kim, H. S.; Estrin, Y.; Bush, M. B. *Acta Mater* **2000,** 48, (2), 493-504.

138. Blanton, S. A.; Leheny, R. L.; Hines, M. A.; Guyot-Sionnest, P. *Phys Rev Lett* **1997,** 79, (5), 865-868.

139. Lee, D.; Jia, S. G.; Banerjee, S.; Bevk, J.; Herman, I. P.; Kysar, J. W. *Phys Rev Lett* **2007,** 98, (2).

140. Luo, Y.-R.; Luo, Y.-R., *Comprehensive handbook of chemical bond energies*. CRC Press: Boca Raton, 2007; p 1655 p.

141. Lin, S.-y.; Fleming, J.; Hetherington, D.; Smith, B.; Biswas, R.; Ho, K.; Sigalas, M.; Zubrzycki, W.; Kurtz, S.; Bur, J. *Nature* **1998,** 394, (6690), 251.

142. Vlasov, Y. A.; Bo, X.-Z.; Sturm, J. C.; Norris, D. J. *Nature* **2001,** 414, (6861), 289.

143. Baba, T. *Nature photonics* **2008,** 2, (8), 465.

144. Lu, M.-H.; Feng, L.; Chen, Y.-F. *Materials today* **2009,** 12, (12), 34-42.

145. Olsson III, R. H.; El-Kady, I. *Measurement science and technology* **2008,** 20, (1), 012002.

146. Sadat, S. M.; Wang, R. Y. *RSC Advances* **2016,** 6, (50), 44578-44587.

147. Narayanaamurti, V. *Science* **1981,** 213, (4509), 717-723.

148. Dietsche, W. *Physical Review Letters* **1978,** 40, (12), 786.

149. Cord, B.; Dames, C.; Berggren, K. K.; Aumentado, J. *Journal of Vacuum Science & Technology B: Microelectronics and Nanometer Structures Processing, Measurement, and Phenomena* **2006,** 24, (6), 3139-3143.

150. Narayanamurti, V.; Störmer, H.; Chin, M.; Gossard, A.; Wiegmann, W. *Physical Review Letters* **1979,** 43, (27), 2012.

151. Koblinger, O.; Mebert, J.; Dittrich, E.; Döttinger, S.; Eisenmenger, W.; Santos, P.; Ley, L. *Phys Rev B* **1987,** 35, (17), 9372.

152. Burger, W.; Lassmann, K. *Phys Rev B* **1986,** 33, (8), 5868.

153. Yazdani, N.; Tra, N. T.; Yarema, M.; Lin, W. M. M.; Gao, R.; Yarema, O.; Bosak, A.; Wood, V. *J Phys Chem Lett* **2018,** 9, (7), 1561-1567.

154. Urban, J. J.; Talapin, D. V.; Shevchenko, E. V.; Murray, C. B. *J Am Chem Soc* **2006,** 128, (10), 3248-3255.

155. Fetzer, F.; Maier, A.; Hodas, M.; Geladari, O.; Braun, K.; Meixner, A. J.; Schreiber, F.; Schnepf, A.; Scheele, M. *Nat Commun* **2020,** 11, (1), 6188.